Understanding the biomechanical signature of pressurised tumour on the surrounding tissue
a modelling study

Fiorito, Marco

Awarding institution:
King's College London

Understanding the Biomechanical Signature of Pressurised Tumour on the Surrounding Tissue: a Modelling Study

Marco Fiorito

A thesis submitted in fulfillment of the requirements
for the degree of Doctor of Philosophy at the

-

School of Biomedical Engineering & Imaging Sciences
King's College London

First supervisor: Prof. Ralph Sinkus
Second supervisor: Dr. Gilbert Fruhwirth

March 2019

Abstract

Solid tumour growth is often associated to the accumulation of mechanical stresses acting on the surrounding host tissue. These forces alter the biomechanics of the adjacent tissue, which can be probed with propagating shear waves and quantified through MR-Elastography. The reconstructed shear modulus in the peri-tumoural region inherits a signature from the tumour expansion which depends on multiple factors, including the soft tissue constitutive law, stress/strain states in the ensemble and the local wave propagation direction. Here we have used analytical and experimental means based on a simple setup of the tissue-tumour ensemble to investigate the shifts in shear modulus associated to a spherical inflation as a way to bridge to *in vivo* tissue.

Due to tissue nonlinearity, the shear modulus of the tumour environment will change according to the local deformation created by the tumour forces, increasing when undergoing stretch and decreasing when compressed. Shear waves can sense the apparent stiffness along its propagation direction, hence probing a negative change, compared to the background modulus, at the leading edge of the inflated object and a positive variation along the lateral area.

In this thesis we have developed an analytical framework that associates the expected signature pattern to the radial stretch generated by the spherical inflation, using a thick-shelled sphere approximation and a specific hyperelastic strain energy density function. A phantom consisting of an inflatable Foley catheter inserted inside a soft tissue-mimicking cuboid was then built to reproduce the tissue-tumour ensemble and to validate the analytical findings. A measuring system based on a pressure sensor was used to quantify the radial stress applied by the inflated balloon onto the surrounding soft plastic material, while the associated strain was instead estimated through an implemented non-rigid image registration strategy, applied to high resolution MR images acquired at the various inflation states. A rheological characterisation of the chosen material confirmed the suitability of the constitutive equation employed in the development of the analytical formulation to model its stress/strain relationship.

Using the developed phantom, inflation experiment were carried out to empirically probe the apparent variation in shear modulus, generated at different balloon inflations, through MRE. The observed anisotropy displayed a satisfactory agreement with the predicted patterns, especially at higher strains, where the nonlinear response of the material was

more pronounced, and also showed a good correlation with the deformation sensed by the probing shear waves. A preliminary replicate of this experiment *ex vivo* also helped to identify the challenges expected in *in vivo* application.

Overall, we have demonstrated that MRE, in combination with non-linear mechanics, is capable to predict the apparent alteration of shear modulus of soft tissue generated by tumour expansion. These results are expected to provide a significant step towards the development of a noninvasive method to measure and monitor intra- and peri-tumoural stresses as a biomarker for tumour progression and treatment efficacy

Acknowledgements

This thesis is the result of the hard work and perseverance I put into this project over the last three years. It has been an extremely challenging and rewarding experience and I could not obtain this result on my own; therefore I am using this little space to say thank you to all the people that have shared with me the good times and bad times of this journey.

First of all, I would like to express my gratitude to Prof. Ralph Sinkus, for the direction he has given me throughout this PhD, for the support provided during the difficult moments encountered along the way and for continuously believing in me and in the work I have done. His experience and vast knowledge have always been a guidance and a source of inspiration for me. I would also like to thank Dr. Gilbert Fruhwirth for the very insightful discussions we had during the first part of this PhD and for his valuable feedback for the writing of this thesis, which allowed me to broaden my horizons which directly reflected in my research.

Equally important has been the team I worked with, under both a professional and a personal point of view. I have found in all of its members some incredible colleagues and true friends and I am extremely grateful for the good time spent together. In particular, I would like to thank Dan, for the precious help and support he offered, Pam, for sharing almost every day of the last two years with me, and Sweta, for the short but intense time we have been lucky to spend together.
And of course I must acknowledge all the other people in the School of Biomedical Engineering and Imaging Sciences for forming such an incredible community where to do a PhD. Here, I had the chance to meet many interesting and talented people through the EPSRC CDT program, allowing me to establish fruitful collaborations and close friendships, and I am especially grateful to Esther and Giovanna for having been there for me from the very beginning of this adventure.

Living in such a dynamic city as London, I had the chance to make so many new friends and I would like to extend my gratitude to all the people I met at Griffon's, for all the evenings spent in the common room and for the wonderful moment we shared over the summer. Special thanks go to Maria, Enrico, Daniel, Sharan, Valentini and Jure, who have been just incredible. Obviously I cannot forget all my friends from back in Italy, who have always supported me despite the distance and who will still do in the future.

Moving to London to commit to this program has been a big step in my life, and I could not do it without the constant support of my parents and my brother, who helped me get where I am right now.

Finally, I want to express my deepest gratitude to Dr. Jack Lee, for the never-ending discussions and for the invaluable help he provided. This achievement would have not been possible without him.

Marco Fiorito, March 2019

Conferences & Publications

Conferences

M. Fiorito, L. Jack. D. Fovargue, A. Capilnasiu, D. Nordsletten and R. Sinkus: "Understanding the Biomechanical Signature of Pressurised Tumour on the Surrounding Tissue: a Modelling Study". In *ISMRM Proceedings* (2019).

M. Fiorito, R. Sinkus, D. Fovargue, A. Capilnasiu, D. Nordsletten, and L. Jack: "Impact of Nonlinear Tissue Mechanics on Solid Tumour Surrounding Soft Tissue: a Phantom and in silico Investigation". In *BioMedEng18 Proceedings* (2018).

D. Fovargue, J. Lee, M. Fiorito, A. Capilnasiu, S. Sethi, S. Hoelzl, J. H. Runge, J. de Arcos, A. Purushotham, K. Satchithananda, D. Nordsletten, and R. Sinkus1: "Non-linear Mechanics Allows Non-invasive Quantification of Interstitial Fluid Pressure". In *ISMRM Proceedings* (2018).

D. Fovargue, J. Lee, A. Capilnasiu, M. Fiorito, D. Nordsletten and R. Sinkus: "Using non-linear tissue biomechanics to infer static forces within tissue: towards quantifying IFP". In *ISMRM Proceedings* (2017).

Publications

M. Fiorito, R. Sinkus, D. Fovargue, A. Capilnasiu, D. Nordsletten, and L. Jack: "Understanding the Biomechanical Signature of Pressurised Tumour on the Surrounding Tissue: a Modelling Study". Journal manuscript currently in preparation.

Table Of Contents

Abstract i

Acknowledgements iii

Conferences & Publications iv

Table Of Contents vi

List of Figures xi

List of Tables xx

List of Abbreviations xxii

1. Introduction 1

1.1. The Impact of Cancer . . . 1

1.1.1. Unmet Needs in Cancer . . . 1

1.2. Mechanical Properties of Soft Tissue Measured through MRE . . . 4

1.2.1. Mechanical Excitation of Soft Tissue . . . 6

1.2.2. Imaging the Propagating Waves . . . 7

1.2.3. Mechanical Parameter Estimation . . . 8

1.2.4. Macro-Deformations Introduce Bias . . . 11

1.3. Stress Distribution in the Tumour Environment . . . 12

1.3.1. The Tumour Microenvironment . . . 12

1.3.2. Measurement & Modelling of Tumour Stress Distribution . . . 15

1.4. Project Rationale & Goals . . . 20

2. Analytical Modelling 23

2.1. Preliminaries . . . 24

2.1.1. Displacement and strain . . . 24

2.1.2. Stress . . . 25

2.1.3. Field Equations . . . 26

2.2. Linearised Constitutive Laws of a Largely Deformed Viscoelastic Body Subjected to Small Perturbations . . . 31
2.3. Constitutive Relationships for Soft Tissue . . . 34
2.3.1. Analytical Formulation of Stress Tensors . . . 37
2.3.2. Derivation of Linearised Shear Modulus . . . 38
2.4. Wave Propagation in Thick-Shelled Sphere . . . 39
2.4.1. Thick-shelled Sphere Inflation: Kinematics . . . 39
2.4.2. Inflation Pressure . . . 40
2.4.3. Nonlinear Wave Propagation . . . 42
2.5. Discussion . . . 46

3. Inflation Experiment Using a Phantom **51**
3.1. Materials Employed to Mimic Mechanical Properties of Soft Tissue in Elastography . . . 52
3.2. Phantom Construction . . . 54
3.2.1. Material Selection . . . 54
3.2.2. Need for Scattered Particles to Track the Deformation . . . 54
3.2.3. Manufacturing Protocol . . . 56
3.2.4. Foley Catheter to Mimic Tumour-Generated Stress . . . 56
3.3. Pressure Measuring System . . . 57
3.3.1. Linear Subtraction of Balloon Resistance from Measured Pressure 59
3.3.2. Inflation range . . . 59
3.3.3. Inflation Volume Estimation . . . 60
3.3.4. Comparison with Theoretical Values . . . 62
3.4. Image acquisition . . . 63
3.4.1. MRE setup . . . 64
3.5. Discussion . . . 65

4. Strain Estimation **69**
4.1. Image Registration in Medical Imaging . . . 69
4.1.1. Overview of Existing Image Registration Methods . . . 69
4.1.2. Non-Rigid Image Registration . . . 71
4.2. Development of a Ground Truth *in Silico* Model . . . 73
4.2.1. Image Embedding . . . 74
4.2.2. Non-Rigid Image Registration Method and Optimisation . . . 74
4.2.3. Validation on Simulated Realistic Deformations of a Real Image . 77
4.3. Strain Estimation in Phantom, *in Vivo* Preclinical Images and Patient Data 81
4.3.1. Balloon Inflation . . . 81

4.3.2. Murine Tumour Compression . . . 82
4.3.3. Breast Fibroadenoma . . . 86
4.4. Discussion . . . 88

5. Phantom Material Characterisation **91**
5.1. Model Tissue Viscoelasticity . . . 92
5.1.1. Fractional Viscoelastic Models . . . 93
5.2. Rheological Data Acquisition & Processing . . . 95
5.2.1. Sample preparation . . . 95
5.2.2. Testing protocol . . . 95
5.2.3. Data Analysis and Modelling . . . 96
5.2.4. Parameter Fitting . . . 99
5.3. Scattered Tracking Particles Increase Material Nonlinearity . . . 100
5.3.1. Parameter Optimisation . . . 102
5.4. Mooney-Rivlin and Fung Models Can Predict the Viscoelastic Behaviour of the Material at Different PVC Concentrations . . . 104
5.4.1. Parameter Optimisation . . . 107
5.4.2. Model Simplification to Account for Parameter Coupling . . . 108
5.4.3. Linearised Shear Modulus . . . 110
5.5. Discussion . . . 113

6. Experimental Investigation **117**
6.1. MRE Reconstruction Method . . . 118
6.2. Circumferential Strain Generates Apparent Anisotropy in Phantoms . . . 119
6.2.1. Local Wave Propagation Determines the Probed Deformation . . . 119
6.2.2. Reconstructed Shear Modulus and Shear Modulus Variation from MRE Data . . . 122
6.3. Preliminary *Ex Vivo* Experiments Using Bovine Tissue Sample . . . 127
6.3.1. Experiment Implementation . . . 127
6.3.2. Initial Results . . . 128
6.4. Discussion . . . 131

7. Conclusions & Future Work **141**
7.1. Summary . . . 141
7.2. Clinical Impact . . . 143
7.3. Limitations and Future Directions . . . 146
7.4. Conclusions . . . 149

Appendices

A. The Material Derivative **151**

A.1. The Material Derivative of a Volume Integral 151

B. The Reynolds Transport Theorem **153**

C. Simplification to Linearised Elastic Wave Equations **155**

C.1. Linearisation of Perturbed PK1 Stress Tensor 155

C.2. Linearisation of Perturbed Jacobian 156

Bibliography **159**

List of Figures

1.1. Schematics of the typical work-up for cancer detection and treatment. Image taken from the WHO (2017) [8]. 2

1.2. Example of a gradient recalled-echo (GRE) MRE acquisition sequence. Image taken from Mariappan *et al.* (2010) [54]. 7

1.3. Schematics of the mechanical forces developed in the tumour microenvironment. Cancer cell proliferation and enhanced ECM protein deposition leads to the accumulation of solid stress in the tumour interior. This stress can compress or collapse tumour vasculature, which is normally leaky and irregular, reducing blood and lymph flow. Inefficient drainage of tumour interstitium results in an homogeneous rise in IFP throughout the tumour mass, with a quick drop at the periphery. These unbalanced stresses force the tumour to push against the host tissue, which in turn resists this deformation, restricting tumour expansion. Image taken from Jain *et al.* (2014) [88]. 14

1.4. Spatial distribution of IFP (A) and of the radial (B) and circumferential solid stress (C) through the tumour and in the surrounding normal tissue. The parameter θ directly correlates with the hyper-vascularity of a tumour and the leakiness of the blood vessels. Image A modified form Stylianopoulos *et al.* (2013) [127], images B and C modified from Voutouri *et al.* (2014) [130]. 15

1.5. A) Tumour stress generates a nonlinear tissue response. B) Radial compression results in a reduced apparent shear modulus, while circumferential tension generates an increased value. C) MRE probes material properties according to the direction of propagation of the shear waves, hence reconstructing an anisotropic pattern. D) Reconstructed shear modulus around an inflated balloon inside a plastic cuboid. 21

2.1. Example family of curves representing the inflating pressure obtained from the linear (left) and quadratic (centre) term of the modified Mooney-Rivlin law employed. The combined contributions generate a characteristic family of S-shaped curves (right). 42

2.2. The magnitude of the hydrostatic pressure is directly proportional to the radial stretch (a/A), fading to zero while moving away from the inner surface. Given a constant $\mu_1 = 1$, the second parameter, μ_2, has a relevant impact on the model at the interface between the inclusion and the surrounding material, however it does not affect the curve trend. 42

2.3. Wave propagation through the thick-shelled sphere. Due to the local spherical coordinate orientation, at Ⓐ, the wave will appear as θ-polarised, travelling in the radial direction. At Ⓑ, the opposite is found. 44

2.4. It can be seen that when the wave approaches the inner sphere head-on, inflation would lead to an apparent softening of the material, identified by the blue region. In contrast, along the peripheral interface of the inner sphere, a stiffening is detected, with the curves being constantly in the red region. Given a constant $\mu_1 = 1$, the parameter μ_2 shapes the curves differently in the two regions, especially in the case of larger deformations. 45

2.5. 2D representation of the shear modulus variation patterns generated by an inflated inner sphere as probed by plane waves propagating from left to right. 46

3.1. A) High resolution images of both wood shavings and silica gel uniformly distributed throughout the phantom. Both trackers provide sufficient contrast to follow their displacement during the phantom deformation. B) Top: reconstructed shear modulus of the central slice of three phantoms containing different concentrations of trackers. Bottom: histograms of the G' distribution over the selected region (highlighted in the white ROI). 55

3.2. Cross section of high resolution images of the balloon inserted inside the plastisol cuboid at different inflation states. The contrast between the bright plastic phantom and the dark water allows a good identification of the inclusion. The inflation of the employed balloon meets the sphericity requirement. 57

3.3. A) A Foley catheter was used to mimic tumour expansion. While water was injected inside the catheter, the generated radial stress was measured through a MPXV500DP pressure sensor. The sensor output is then read through an Arduino® Mega board and a connected laptop. B) Picture of the connection between the catheter and the pressure sensor 58

3.4. Two replicates of the same measurements (solid v dotted curves) show that the same injected volume produces comparable pressure measurements. After an initial peak, the relaxation of the viscoelastic material leads to a quick decrease in pressure, however a waiting period between 5 and 10 min is sufficient to ensure convergence. 58

3.5. A) In the absence of the material resistance, the measure pressure reaches a quicker convergence. B) Free inflation produces reproducible pressure measurements at different volumes. C) The subtraction of the balloon resistance from the pressure measured when the balloon is inflated inside the phantom returns the actual pressure experienced by the surrounding material. 60
3.6. A) High-resolution MR image showing how large balloon inflations lead to material rupture. B) A drop in the real inflating pressure indicates the loss of material integrity. These results were obtained for a phantom made using an 80 % concentration of plastisol 61
3.7. A) Segmentation of the balloon at the different inflation states from high-resolution MR images provides a better estimation of the volume of the inclusion. B) The segmented volume reveals an overestimation of the injected amount of liquid, leading to a shift of the pressure-volume curve. 61
3.8. Analytical prediction of inflation pressure curves. A) The modified Mooney-Rivlin model can fit the pressure data obtained from the three phantoms. B) Residual analysis for the three experiments. 62
3.9. Schematic representation of the developed mechanical transducer. Image modified from Capilnasiu *et al.* (2018) [86]. 65

4.1. Deformation of embedded image into mesh grid. A) COMSOL Multiphysics® ensured a good element quality throughout the mesh. B) A higher number of elements allows a better sampling of the image, for a more accurate preservation of the features. C) Using a sufficiently fine mesh, the process of embedding and re-interpolation of an image produces an average difference of ~10 % of the original one. D) The generation of a ground truth deformation involves the embedding of the original image into a mesh grid, which is deformed using a known deformation field; the warped image is then re-interpolated from the mesh into a voxel grid and used as objective image for the registration process. 75
4.2. The choice of the metric is an important component of the registration process. The use of different metrics leads to a better or worse matching to the objective image (first row). Based on the percentage difference between the L2-norm calculated for the ground truth deformation and that obtained from the estimated one, MI provides a better agreement between the objective and the warped moving image (second row). 76
4.3. The voxel spacing between each node of the B-Spline grid is crucial for an accurate recovery of the true deformation field. A too wide spacing could not be able to correctly capture the true deformation, while a too narrow spacing can lead to over-fitting. 77

4.4. Four different deformations were applied to the same liver tumour image to validate the implemented registration on a real contrast image. First column) Overlay between the original (green) and deformed (magenta) image. The red lines represent the applied deformation field. Second column) L2 norm of the true deformation field used to generate the objective image. Third column) Estimated deformation field provided by image registration. Fourth column) Percentage difference between the estimated and real deformation normalised over the latter. The location of the tumour mass is highlighted in all images. 79

4.5. First column) High resolution MR images of the inflated balloon overlaid on the corresponding image of the deflated state. Second column) The deflated balloon is warped to match each inflation state. The quality of the registration is confirmed by the low number of non-matching features in green and magenta. Third column) L2 norm of the deformation field estimated through the registration process. Fourth column) Circumferential strain calculated from the estimated deformation. Fifth column) Vectorial representation of the estimated deformation field. 82

4.6. Anatomical images used for the registration process to estimate the generated strain at the various levels of compression. Here c0 refers to the undeformed state while c1, c2 and c3 refer to the injection of 1 mL, 2 mL and 3 mL of air inside the balloon used to apply the compression. The top row shows the images obtained from Mouse 1, while in the second row are the images from Mouse 2. Size bar = 10 mm 83

4.7. A1,B1-top row) Overlay of the moving (green) and objective image (magenta) prior to the registration. A1,B1-bottom row): Overlay of the warped (green) and objective image (magenta) after the registration process. The columns correspond to the registration of the compressed state c0, c1 and c2 to match the subsequent state, respectively. A2,B2) The quality of the registration has been assessed calculating the correlation coefficient for both mice. The blue bars show the score obtained when comparing the objective image with the original one prior to the registration, while the orange bars refer to the same test applied to the objective and moving image after the registration. For this test, only the voxels inside the mask were considered. 84

4.8. To assess the incompressibility of the deformation fields estimated through the image registration, the determinant of the Jacobian matrix of the transformation was calculated for each voxel of the masked tumour and plotted as a histogram for all the registered states. A mean value of 1 and a small variance reflect a good fulfilment of the incompressibility hypothesis. Values are reported as mean ± s.d. 85

4.9. A,B-top row) Estimated deformation fields superimposed to the overlaid original (green) and objective images (magenta). A,B-bottom row) The corresponding maximum shear strain increases with the magnitude of the compression in a heterogeneous way throughout the tumour. 86

4.10. First row) estimated deformation field superimposed to the overlaid original (green) and objective images (magenta). Second row) Image registration dramatically reduces the amount of mismatching features. Third row) The voxel-wise calculation of the determinant of the Jacobian matrix associated to the estimated deformation field reveals the regions where the incompressibility assumption was not respected. Fourth row) Maximum shear strain pattern generated on the breast tissue by the applied compression. Each column refers to the registration of the original image and each of the subsequent compressed states. 87

5.1. Illustration of the experimental setup used for the viscoelastic characterisation of the phantom material (left). The moving plate was used to apply a fixed vertical compression on the sample and the load was measured through an integrated sensor. For each compression level, the phantom was subjected to four consecutive micro-oscillation and one macro-oscillation test (right). Each of those tests consisted in the application of a series of oscillatory compression cycles centred around the selected compression level at different frequencies, as presented in the zoomed panel. 97

5.2. Under the investigated level of compression, the traction data measured from sample B1, which contains motion trackers, show a higher material nonlinearity than sample A1 and A2. The different batch used for sample A2 produced a steeper curve than for sample A1, but a similar nonlinearity. The data are taken from the loading process that leads roughly to a 20 % compression. 102

5.3. The fractional derivative order that returned the minimised fitting error was investigated for both the Neo-Hookean (black) and the modified Mooney-Rivlin (red) model. While in the absence of trackers the two curves are identical, in their presence the latter provides a better fit of the rheological data. The minimum error in each curve is highlighted using a filled red symbol, however all the curves present a very shallow minimum region that goes roughly from $\alpha = 0.04$ to $\alpha = 0.2$. 103

5.4. Each sample was compressed to different levels and subjected to various sets of micro and macro-oscillations at different frequencies. Here, the data (red) obtained from the sample containing trackers were fitted to the modified Mooney-Rivlin model (black), with the best agreement obtained for the fractional derivative order $\alpha = 0.04$. Overall the model proved able to reproduce the induced oscillations even at the highest employed frequency. The nonlinear increase in traction was also captured, as well as the relaxation process visible over the explored time-frame. 104

5.5. Parameter trend at the variation of the fractional derivative order α in the absence (A1,A2) and presence (B1,B2) of trackers. The parameters that model the elastic and viscoelastic part of the two models show opposite and complementary trends. 105

5.6. The bar graph presents the best fitting parameters obtained from the tested samples in the presence and absence of trackers using both the Neo-Hookean and modified Mooney-Rivlin model. Each value, reported also in the table underneath, represents the average, over a fractional derivative order going from 0.04 to 0.2, of the mean value between the coupled parameters. The error bars show the range of values over the investigated α's. The same procedure is used to display the minimisation error. 106

5.7. The nonlinearity of the stress/strain response of the material increases with the plastisol concentration, as underlined by the increasing value of the parameter scaling the quadratic term of the fitting curve. Again, the data are taken from the loading process that leads to a compression slightly higher than 25 %. 106

5.8. Data from different PVC concentration are modelled by equally small fractional derivative orders. The best fit was obtained for a range of α values that roughly goes from 0.05 to 0.2 by both the modified Mooney-Rivlin (A) and the Fung hyperelastic law (B). The actual minimum α_{min} is indicated by a filled symbol. Both models show a good agreement with the data, with a fitting error smaller than 4 % in the selected region. 107

5.9. A) Using the Mooney-Rivlin model, the elastic and viscous parameters show opposite and complementary trends over the considered α range at different plastisol concentrations. B) With the Fung model, while μ_1 and δ_1 appear coupled, μ_2 and δ_2 display non-complementary trends: while the former keeps constant for all samples, the latter increases linearly with the fractional derivative order, with a slope directly proportional to the plastisol concentration 108

5.10. Estimated best parameters and corresponding fitting error at the three investigated PVC concentrations using the modified Mooney-Rivlin (left) and Fung law (right). In this case, given the non constant trend followed by the sum of the coupled parameters in the Fung model over the fractional order going from 0.04 to 0.2, only the estimates obtained at the fractional derivative order that minimised the error are considered. For the Mooney-Rivlin model, instead, the average value of the parameters and the fitting error are reported, with the error bars showing the range of values over the investigated αs. The parameter values and errors are also reported in the table underneath. 109

5.11. Best fractional order to model the traction data measured for the 70 %, 80 % and 90 % PVC samples using the simplified version of the modified Mooney-Rivlin law (A) and the Fung law (B). 109

5.12. Estimated best parameters and corresponding fitting error for the three investigated PVC concentrations using the simplified version of the modified Mooney-Rivlin (left) and Fung law (right). The associated fractional derivative order is also reported. The parameter values and errors are shown in the table underneath, together with their percentage variation with respect to the estimates in Fig.5.10. 110

5.13. All the four models generate a similar estimate of the linearised shear modulus of the three investigated samples, producing a similar quadratic dependence on the plastisol concentration. 112

5.14. All the four models generate a similar estimate of the linearised shear modulus of the three investigated samples, producing a similar quadratic dependence on the plastisol concentration. 115

6.1. The MR images of the wave displacement (A), the associate wave amplitude (B) as well as the local estimation of the k-vector (red arrows in C) is presented for each investigated inflation state. The green arrows represent the mean k-vector direction over the selected ROI. 120

6.2. A) Shear waves probe the material shear modulus along their direction of propagation, identified by the k-vector. This is comparable, in the case of a macro-deformation, to the projection of the deformation field onto the k-vector using $\boldsymbol{CK} \cdot \boldsymbol{K}$. B) For a spherical deformation, the angle between the deformation vector and the k-vector determines the magnitude of the probed material displacement and allows to differentiate between compression and tension. 121

6.3. Estimated macro-deformation using the implemented image registration strategy. The deformation field (red arrows, not to scale), relating the deflated balloon to each inflation state, shows a magnitude and directionality comparable with the spherical inflation of the inclusion. 121

6.4. In-plane Cartesian representation of the calculated $\boldsymbol{CK} \cdot \boldsymbol{K}$. The overlaid arrows represent the mean direction of propagation of the shear waves. 122

6.5. A) Reconstructed shear modulus at different inflations. B) Background shear modulus reported as mean ± s.d. C) Comparison between background shear modulus reconstructed for the deflated cases and the analytical calculations using the best estimate of the material parameters obtained by fitting the pressure curve associated to each experiment. In this case, the error bars correspond to the values obtained when fitting the highest and lowest pressures measured throughout the different replicas of each experiment, as presented in Table 3.2. 123

6.6. Relative change in shear modulus between the various inflated states and the deflated case. The overlaid arrows show the mean direction of the propagating waves. 124

6.7. Example of Cartesian representation of the inclusion where circular regions at different radial distances from the centre of the inclusion are showed with different colours (left). A better visualisation, independent on the mean direction of propagation of the waves, is obtained through the "unravelling" of the image following the perimeter of each circular region (right). 125

6.8. Polar representation of the probed deformation (left), calculated using the local k-vector estimated from the wave images, compared with experimental (middle) and analytical (right) relative shear modulus variation at the four inflation levels investigated through three replicas of the inflation experiment. The common elements in the generated patterns are highlighted with arrows. The balloon region is blacked out. 126

6.9. Unlike the other two samples, the bovine joint proved capable of sustaining the stress generated by the balloon inflation without rupturing. 128

6.10. The modified Mooney-Rivlin model provides a good fit of the pressure data acquired experimentally. 129

6.11. Top) Magnitude images of the inclusion at different inflation levels. Middle) Wave images acquired through MRE. Bottom) The wave amplitude fades quickly while moving away from the wave source. 130

6.12. The reconstructed shear modulus shows a heterogeneous distribution around the inclusion (A), as confirmed by the large standard deviation measured for each case (B). The mean value, however, remains roughly constant. A comparison between the reconstructed background G' and the value analytically calculated shows a good correlation. 131

6.13. The empirical $\boldsymbol{CK} \cdot \boldsymbol{K}$ (left) and G' variation (centre) show a very convoluted pattern, however some matching features are pointed out with arrows. The increasing softening in the -45°÷45° region also correlates with the analytical predictions (right). 132
6.14. Cartesian (A) and polar (B) representation of the two metrics devised to determine the local reliability of the measured variation in shear modulus at different inflation levels. In the polar representation, the less trustworthy regions (< 10 % and > 25 % respectively) are shaded out. 137

7.1. A) Assuming a radial inflation, the iterative search for the scaling parameter α that minimises the voxel variance around the inclusion can be used to undo the anisotropic shear modulus pattern and retrieve the associated pressure *in silico*. B) The application of this method on the MRE data acquired through the inflation experiments allowed the recovery of pressures similar to those measured experimentally. C) This method can represent a non-invasive biomarker to gauge metastatic potential in breast cancer. Images A and B adapted with permission from Fovargue *et al.* (2018) [162], image C adapted with permission from Fovargue *et al.* (2018) [263]. 145

List of Tables

2.1. 47

3.1. Trackers do not impact the reconstructed G' of the phantom matrix. 55
3.2. Inflating pressure (kPa) / radial stretch (-) measured from the three replicas of the inflation experiment. 63
3.3. Data fitting of the three replicas of the inflation experiment in phantom. 63
3.4. 66

4.1. Example of the components used for the non-rigid registration. 78
4.2. Quality of estimated deformation based on relative difference from ground truth. 80
4.3. List of the test carried out to assess the quality of the image registration in different settings. 81
4.4. 88

5.1. Sample details. 95
5.2. Details of the protocol used for the rheological tests. 96
5.3. 113

6.1. Inflating pressure (kPa) and radial stretch (-) measured from the bovine tissue sample 128
6.2. Bovine tissue sample pressure data fitting 128
6.3. 133

List of Abbreviations

ADC	Apparent diffusion coefficient
CAF	Cancer associated fibroblast
CC	Correlation coefficient
CT	Computer tomography
DCE-MRI	Dynamic contract-enhanced MRI
DWI	Diffusion-weighted imaging
EBS	Elastic body splines
ECM	Extra-cellular matrix
FE	Finite element
FEM	Finite element method
FFD	Free-form deformations
FOV	Field of view
GRE	Gradient recalled-echo
HCC	Hepatocellular carcinoma
IFP	Interstitial fluid pressure
LOX	Lysyl oxidase
MEG	Motion encoding gradient
MI	Mutual information
MMP	Matrix metalloproteinase
MPMRI	Multi-parametric MRI
MR	Magnetic resonance
MRE	Magnetic resonance elastography
MRI	Magnetic resonance imaging
MRSI	Magnetic resonance spectroscopy imaging
MSD	Mean squared difference
MVP	Micro-vascular pressure
NCD	Non-communicable disease
NMI	Normalised mutual information
NMR	Nuclear magnetic resonance
NSA	Number of signal averages
PK1	First Piola-Kirchhoff stress tensor

PK2	Second Piola-Kirchhoff stress tensor
PVA	Polyvinyl alcohol
PVC	Polyvinyl chloride
ROI	Region of interest
SNR	Signal-to-noise ratio
TE	Echo time
TGF-β	Trasnforming growth factor-β
TPS	Thin-plate spline
TR	Repetition time
US	Ultrasound, ultrasonography
VEGF	Vascular endothelial growth factor
WHO	World Health Organization

1. Introduction

1.1. The Impact of Cancer

According to estimates from the World Health Organization (WHO), in 2016 cancer was the second most common cause of premature death below the age of 70 in the world, accounting for 22 % of all non-communicable disease (NCD) deaths worldwide [1]. More than 15.5 million people in the United States had a history of cancer in 2016 [2]. These numbers increase rapidly, and 1.7 million new cases are expected in 2018, more than one third of which is predicted to be lethal [2]. Even worse figures are forecast in Europe, with an incidence more than twice as high and a nearly 50 % mortality [3]. Despite containing only less than one tenth of the world's population, in fact, Europe presents about 25 % of the global cancer cases [4]. Worldwide, the Global Cancer Observatory has estimated 9.6 million cancer deaths in 2018 over a total of 18.1 million new cases [5]. This incidence is expected to grow, making cancer the most important limitation to life expectancy in every country in the 21^{th} century [5]. The estimates predict also a global burden of 21.6 million new cases and 13 million deaths in 2030, caused by the sole growth and ageing of the population of the planet [2].

In addition to the impact on the quality of life of patients and their families, cancer has also an enormous social cost, involving the loss in human potential and the economic burden on the worldwide healthcare system, given by the treating and caring of the constantly increasing number of patients [6]. Estimates report oncology expenditures of more than $150 billion in 2020 [7], which are projected to increase by 70 % in the next 20 years [6].

The need for action to ensure healthy lives convinced the United Nations to define a set of targets to be achieved by 2030, including the reduction of NCD by one-third [7]. In this sense, the development of smarter technology for an improved healthcare at contained costs has become increasingly pressing and advancement in drug design must be accompanied by state-of-the-art techniques to diagnose, stage and monitor tumours, to maximise treatment efficacy and reduce expenses.

1.1.1. Unmet Needs in Cancer

The common work-up for cancer detection and treatment consists of three main stages, a schematic of which is presented in Fig.1.1. Awareness of specific cancer symptoms must

be the first alarm to access primary healthcare, where accurate diagnostic tests can confirm or disprove the suspicions. Staging and grading cancer spread and metastatic potential is then essential for the definition of an effective strategy for cancer treatment, which requires a constant monitoring through the following months and years to assess therapy efficacy and to monitor any sign of recurrence.

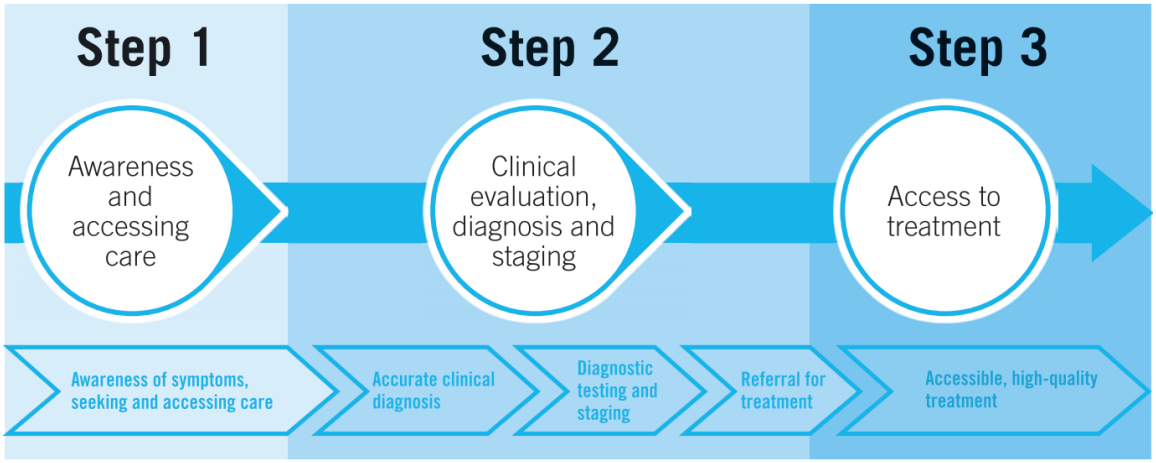

Figure 1.1.: Schematics of the typical work-up for cancer detection and treatment. Image taken from the WHO (2017) [8].

Early cancer diagnosis, combined with the access to effective treatments has proven to lead to improved cancer staging and decreased mortality [9]. A report from 1999, for instance, has associated a shortened delay in patient care to a greater survival rate from breast cancer, with a 7 % increase in 5-year survival for patients who experienced < 3 months delay compared to 3-6 months [10], while more than 50 % reduction in breast cancer mortality was reported in the UK in women under the age of 65 due to early diagnosis and adequate treatment [11].

Before proceeding with staging or treatment, sufficient evidence of cancer must be acquired, either with imaging modalities or laboratory tests. Magnetic resonance imaging (MRI) techniques targeted to specific hallmarks of cancer represent a powerful tool for the non-invasive tumour assessment; however they often present a low specificity in determining the tumour grade and in differentiating between benign and malignant lesions.

Dynamic contrast-enhanced MRI (DCE-MRI), used in oncology to assess angiogenesis and vascular permeability, showed a sensitivity that can reach almost 100 % for the detection of malignant breast lesions [12, 13]. This technique is especially useful in the case of patients with dense breast parenchyma, for which mammography and ultrasonography (US) are less sensitive [13]. Nevertheless, the non comparable specificity (37-97 %) represents an ongoing challenge, causing the diagnose of false positives and leading to unnecessary biopsies [14, 15].

Diffusion-weighted imaging (DWI), which aims at measuring the reduced diffusion of water molecules associated to the increased cellularity typical of cancer, has also become a popular imaging biomarker for the detection of primary and metastatic tumours, especially in brain. However, despite the sensitivity of this technique to tumour architecture, oedema and necrosis within the lesion can lead to a quantification of a higher apparent diffusion coefficient (ADC), hence limiting the specificity of this technique [16].
MR spectroscopy imaging (MRSI) provides metabolic information through the analysis of the chemical content of the tumour mass, which can be extremely beneficial for the differentiation between malignant and benign tumours. Nevertheless, MR spectroscopy is most widely used as a single-voxel technique, hence limiting the spatial resolution and allowing to evaluate only one lesion at a time [17].
Multi-parametric MRI (MPMRI) is an emerging tool which has found its main application in the identification and staging of prostate cancer. This technique combines standard anatomical T1-weighted or T2-weighted imaging to the presented functional sequences in order to improve the characterisation of the lesion. The integration of DCE-MRI, DWI and MRSI into a T2-weighted imaging modality has shown a better cancer prediction, with figures rising from 68 % to 98 % compared to the sole anatomical information [18].

The listed MR-based detection techniques are a few examples of the technical progresses made in oncology for tumour detection; nevertheless, in the case of breast cancer, manual palpation is still the technique of reference, as breast malign lesions are generally characterised by a higher stiffness with respect to benign ones and the normal surrounding tissue [19, 20]. Breast cancer accounts for the most frequently diagnosed cancer in women, representing the second main cause of death and an early diagnosis has shown to significantly increase the survival rate [21]; hence palpation has become a globally recommended routine for the self-detection of hard masses [22]. Nevertheless, tumour detection through manual palpation is very dependent on the experience of the physician and showed a sensitivity of only 54 % [22].
The association of altered mechanical properties to a pathological conditions is not only limited to breast tissue; a fibrotic liver has also been associated with a higher stiffness, the magnitude of increase of which directly correlates to the fibrosis stage [23]. A fibrotic state is a consequence of an inflamed liver and can lead to cirrhosis, which is responsible for a 50 % chance of death in 5 years [24]. Moreover, a cirrhotic liver can strongly lead to the development of hepatocellular carcinoma (HCC) [25], which represents the leading cause of mortality for patients suffering from cirrhosis [26]. Liver biopsy is the gold standard diagnose method to evaluate fibrosis, however sampling error and invasiveness are inherent problems of this approach [27], hence emphasising a significant need for accurate and non-invasive techniques to detect fibrosis and to determine the efficacy of the associated therapies.

Knowledge of the mechanical properties of brain can also help the characterisation of pathologies, such as Alzheimer's disease, multiple sclerosis, hydrocephalus and cancer [28, 29]. In particular, in the case of brain tumour, non-invasive stiffness measurement can provide further information about the neoplasm and its response to treatment.

Unfortunately, none of the standard techniques employed in the realm of medical imaging, i.e. MRI, US, computer tomography (CT), are capable of translating into images the mechanical properties probed through palpation, which, on the other hand, offers solely a qualitative and subjective assessment and is only applicable to superficial and easy to access organs. Elastography imaging techniques are emerging methods to quantitatively assess elasticity and make use of mechanical waves to probe the response of soft tissue. The ability to provide contrast between healthy and diseased tissue, combined with the suggestion of cell stiffness as a biomarker of metastatic potential [30], gives these techniques the potentiality to play a key role in the field of cancer research.
Magnetic resonance elastography (MRE) is an non invasive, flexible MRI-based technique that has proven capable of characterising the biomechanical properties of practically every organ [31, 23, 32, 33, 34, 35, 36, 37, 38, 39, 40, 41, 42, 43]. MRE has found its main employment in the detection and staging of liver fibrosis, due to a reasonable accuracy and reproducibility and can represent a significant alternative to biopsy [44]; nevertheless, this technique has the potential to be used in many more applications. An explanation of the steps involved in MRE data acquisition, together with encouraging results obtained in the diagnosis and staging of tumours and in its differentiation from healthy tissue will be presented in the next section. A final discussion of the limitations encountered when this technique employed on soft tissues subjected to large strains will provide a justification for the work carried out for this thesis.

1.2. Mechanical Properties of Soft Tissue Measured through MRE

MRE is an MRI-based technique that falls into a broader group of elasticity imaging methods, which include ultrasonography and optical imaging, developed to spatially map and measure the material properties of soft tissues. The response of soft tissue to mechanical excitation is very dependent on the rheology of the tissue itself, therefore an accurate modelling of its mechanical behaviour is required. Generally soft tissue shows anisotropic properties and is characterised by a nonlinear viscoelastic behaviour [45, 46]; however, for a simpler mathematical description, its behaviour is often modelled with an isotropic linear elastic Hookean constitutive law [47, 48, 49, 19, 50]. These assumptions have been found valid under the following conditions:

- The observations of potential anisotropy is dependent on the spatial scale at which elasticity is probed; for example, despite different types of tissues being found within the same organ, i.e. glandular, fat, normal, tumour, etc., the irregular architecture of tumour vasculature is such that, at a small scale, the tissue can be described by an isotropic model [51].

- While soft tissue shows both elastic and viscous response, most of the applied forces can be attributed to the former, hence a purely elastic idealisation is often employed [50].

- Finally, small deformations are generally not sufficient to cause a nonlinear stress/strain response of the tissue. Nevertheless, in the presence of endogenous or external macro-deformations, the nonlinear character of soft tissue must be accounted for [52].

Using these approximations, the relation between the applied mechanical stress and the resulting deformation is given by a set of elastic constants, the value of which is representative of the stiffness of the material. The parameter that determines the amount of longitudinal displacement is the Young's modulus, E, while the shear modulus, G, reflects the resistance of a body to undergo shear deformation under a shear stress. Finally the bulk modulus, K, is indicative of the compressibility of a body. Using an isotropic linear elastic approximation, any two of these constants are sufficient to fully describe the mechanical behaviour of soft tissue [53]. Another parameter descriptive of the elastic properties of materials is the Poisson's ratio, ν, which is given by the ratio of transverse to axial strains under compression along the axial direction. An incompressible material, i.e. water, assumes a Poisson's ratio of exactly 0.5. As soft tissues are composed mainly by water, with reported values ranging between 0.30 and 0.499, they are often considered incompressible or nearly incompressible and with a density ρ near $1000\,\mathrm{kg\,m^{-3}}$. In this case, the Young's and shear modulus are related by a simple scaling factor: $E = 3G$ [54]. Near-incompressibility also implies that the bulk modulus varies little among different tissues (less than 15 % from that of water [55]); on the other hand, the wide range of values assumed by shear modulus throughout various tissues and among different physiological and pathological states (around 5 orders of magnitude) make it the ideal parameter to provide sufficient contrast in the reconstructed images [54].
Imaging of shear modulus through MRE, like all other elasticity imaging methods, is based on three subsequent steps, each of which will be treated in more details in the following sections:

1. application of a mechanical stress capable of deforming the biological tissue. The stress can either be generated by an external force or by an internal mechanism, i.e. respiratory cycle, heart motion, tumour forces.

2. Monitoring of the associated strain response through an imaging technique (MRI in this case).

3. Local estimation of the mechanical parameter relating stress to strain through the application an inversion algorithm.

1.2.1. Mechanical Excitation of Soft Tissue

Depending on the type of applied mechanical stress, MRE can be divided into three categories: static, quasi-static and dynamic. Static and quasi-static elastography involve the application of either a single compression or of a cyclically repeated compressive force at low frequency (typically around 1 Hz), followed by the measurement of the resulting deformation field. Static MRE presents analogous limitations to those of manual palpation, making it generally suitable only for superficial or easy to access tissues. Such constraints have restricted its use to *ex vivo* studies [56], while quasi-static MRE has found applications both *ex vivo* [57, 58] and *in vivo*, although only in breast [59, 60].
Dynamic MRE was first introduced in 1995 by Muthupillai *et al.* [61] and aims at imaging the response of tissue to a continuous harmonic steady-state wave pattern. Wave propagation through even deep regions of the body make it the most suitable MRE method for *in vivo* applications. Shear waves, the propagation of which is governed by the shear modulus of the material, are the method of choice to mechanically excite soft tissue and are applied through the use of an external driver, or transducer. Thus far, several kinds of MRE transducers have been developed to generate the needed shear waves: they all rely on the conversion of a sinusoidal electrical signal created by a function generator into a mechanical vibration of a probe, which applies a dynamic pressure against the tissue to be imaged [62]. Among the most common approaches there is the use of a piezoelectric drive, where an external oscillating electric field is used to induce the desired mechanical deformation of a piezoelectric crystal [63]; another recurrent method found in the literature makes use of an electromagnetic driver, which generates the required vibration thanks to the motion imposed by the current flowing through a coil immersed in a magnetic field [64]. Driving systems based on everyday voice loudspeakers have also been employed, although they must be placed away from the scanner due to their own integrated magnet [65, 23]. Recently, our group has proposed a gravitational transducer based on a rotational eccentric mass, that can provide a cleaner vibration spectrum, limiting undesired frequencies [66]. The working frequency generally used in dynamic MRE ranges between 50 and 500 Hz and the corresponding spatial wavelength in soft tissues is in the order of millimetres to

centimetres, granting an image resolution between half and one-fifth of that achievable with the corresponding MRI sequence [54]. Generally, a wavelength comparable to the size of the feature of interest, i.e. tumour, is sought. The choice of the vibration frequency, however, is very dependent on the viscoelastic properties of the probed tissue and must be carefully selected depending on the application. The viscoelastic nature of soft tissue has also a non-negligible impact on wave propagation, which becomes more relevant when higher vibration frequencies are used [67], limiting penetration and hence the applicability of this technique only to superficial tissue investigations.

1.2.2. Imaging the Propagating Waves

In MRE, a phase-contrast MRI technique is used to map the harmonic displacement of the tissue generated through shear waves. This acquisition method makes use of motion-encoding gradients (MEGs) imposed along a specific direction to encode the shear waves into the phase of the MR images (Fig.1.2) [61]. Each spin inside the mechanically excited

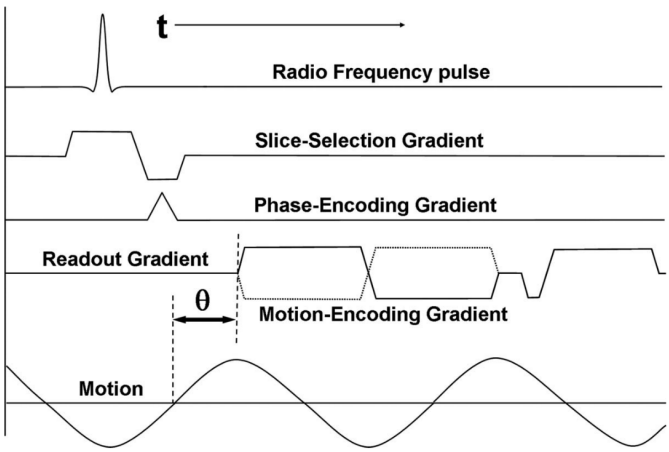

Figure 1.2.: Example of a gradient recalled-echo (GRE) MRE acquisition sequence. Image taken from Mariappan *et al.* (2010) [54].

tissue, in fact, is described by a position vector

$$\boldsymbol{r}(t) = \boldsymbol{r}_0 + \boldsymbol{\xi}(\boldsymbol{r}, t) \tag{1.1}$$

where $\boldsymbol{r}_0$ is the mean position and $\boldsymbol{\xi}(\boldsymbol{r}, t)$ defines a generic motion around the mean position. In the case of the harmonic motion generated by the shear waves, $\boldsymbol{\xi}$ is defined as

$$\boldsymbol{\xi}(\boldsymbol{r}, t) = \boldsymbol{\xi}_0 \cos(\boldsymbol{k} \cdot \boldsymbol{r} - \omega t + \theta) \tag{1.2}$$

where $\boldsymbol{\xi}_0$ is the displacement amplitude, $\boldsymbol{k}$ in the wave vector, ω is the angular frequency and θ is a phase offset. The polarity of the MEGs is adjustable and is set to switch at the

same frequency of the oscillating motion applied through the transducer. Under these conditions, the phase contribution to the MR image caused by the propagating shear waves is directly proportional to the scalar product of the motion-sensitising gradient $\boldsymbol{G}$ and the displacement vector $\boldsymbol{\xi}_0$ and is given by [61, 68]

$$\phi(\boldsymbol{r}, t) = \gamma \frac{NT(\boldsymbol{G} \cdot \boldsymbol{\xi}_0)}{2} \cos(\boldsymbol{k} \cdot \boldsymbol{r} + \theta) \tag{1.3}$$

The amount of phase-shift accumulated is also proportional to the period of the mechanical excitation T and the number of gradient cycles N, making this technique extremely sensitive even to small amplitude oscillatory motion [69]. Previous investigations have assessed the possibility to observe shear wave displacements as small as 100 nm [61]; nevertheless, MRE is only little more sensitive to non-synchronous physiologic motion than a conventional gradient recalled-echo (GRE) sequence [70]. γ is the gyromagnetic ratio of the nuclei, while the parameter θ in Eq.1.3 is a phase offset between the mechanical and magnetic oscillations and its variation permits the sampling of the waves at different time points, effectively allowing the acquisition of snapshots of the propagating waves. Typically, 4-8 equally spaced samples, or wave phases, are acquired covering one period of the wave motion. The obtained wave images represent the displacement of the spins in the medium due to acoustic shear waves governed by the local elasticity of the tissue; regions of the object with a higher shear modulus G are characterised by a longer wavelength λ, given the same vibration frequency ν, and vice versa, in agreement with the following basic relation for the propagation of shear waves in isotropic linear elastic materials [71]

$$\lambda = \frac{1}{\nu} \sqrt{\frac{G}{\rho}} \tag{1.4}$$

where ρ is density. The quantitative measurements of the displacement generated by the propagating waves are then used to reconstruct a map of the shear modulus of the tissue under investigation, as explained in the following section.

1.2.3. Mechanical Parameter Estimation

A linear viscoelasticity wave equation has been broadly considered as a good model of the small wave displacement $\boldsymbol{u}$ in soft tissue [72] and can be expressed starting from a constitutive equation that relates the stress tensor $\boldsymbol{\sigma}$ to the strain tensor $\boldsymbol{\varepsilon}$ and the strain rate $\partial\boldsymbol{\varepsilon}/\partial t$ through the fourth-order stiffness and viscosity tensor, $\boldsymbol{C}$ and $\boldsymbol{\nu}$ respectively

$$\boldsymbol{\sigma} = \boldsymbol{C}\boldsymbol{\varepsilon} + \boldsymbol{\nu} \frac{\partial \boldsymbol{\varepsilon}}{\partial t} \tag{1.5}$$

which can be written in Einstein's notation as

$$\sigma_{ij} = C_{ijkl}\varepsilon_{kl} + \nu_{ijkl}\frac{\partial \varepsilon_{kl}}{\partial t} \tag{1.6}$$

Eq.1.5 and Eq.1.6 are none other than the generalised Hooke's law for linear viscoelastic materials, with the Cartesian tensor C_{ijkl} containing 81 elastic coefficients that can be reduced to 36 components thanks to the symmetry of both the strain and stress tensors. In the particular case of an isotropic material, the number of independent elements that compose the elasticity tensor C_{ijkl} is further narrowed down, so that only two quantities, the Lamé parameters λ and μ, are sufficient to describe the stress/strain relations in all possible directions. The two parameters are related to the material parameters previously introduced through the following equations:

$$\lambda = \frac{\nu E}{(1+\nu)(1-2\nu)} \tag{1.7a}$$

$$\mu = \frac{E}{2(1+\nu)} = G \tag{1.7b}$$

It is to be noted that the second Lamé parameter is equivalent to the shear modulus.
An analogous process can be applied to the viscous part of Eq.1.5, hence relating stress and strain through the two viscous parameters ζ and η, which describe the viscosity of the compressional and shear waves, respectively. Eq.1.5 then becomes

$$\sigma_{ij} = 2\mu\varepsilon_{ij} + \lambda\delta_{ij}\varepsilon_{nn} + 2\eta\frac{\partial \varepsilon_{ij}}{\partial t} + \zeta\delta_{ij}\frac{\partial \varepsilon_{nn}}{\partial t} \tag{1.8}$$

where δ_{ij} is the Kronecker delta. According to the summation convention, the subscripts nn represent dummy indices, which take on all the possible values assumed by i and j (i.e. 11, 22 and 33 in a 3-dimensional system) and the resulting terms are summed. Using the definition of the strain tensor as a function of the harmonic wave displacement in the case of infinitesimal strain theory

$$\varepsilon_{ij} = \frac{1}{2}\left(\frac{\partial u_i}{\partial x_j} + \frac{\partial u_j}{\partial x_i}\right) \tag{1.9}$$

we can replace Eq.1.9 into Eq.1.8 and then into Eq.1.10 (which represents the Cauchy momentum equation in the absence of body forces and under the assumption of local material homogeneity and will be derived in Eq.2.28 of this dissertation)

$$\rho\frac{\partial^2 \boldsymbol{u}}{\partial t^2} - \nabla \cdot \boldsymbol{\sigma}^T = 0 \tag{1.10}$$

We then obtain the following partial differential equation [73]

$$\rho\frac{\partial^2\boldsymbol{u}}{\partial t^2} = \mu\nabla^2\boldsymbol{u} + (\lambda+\mu)\nabla(\nabla\cdot\boldsymbol{u}) + \eta\frac{\partial\nabla^2\boldsymbol{u}}{\partial t} + (\zeta+\eta)\frac{\partial\nabla(\nabla\cdot\boldsymbol{u})}{\partial t} \tag{1.11}$$

Assuming tissue incompressibility ($\nabla\cdot\boldsymbol{u}=0$), the term multiplied by ζ can be neglected, as the viscosity of the compressional wave can be safely ignored at the low frequencies employed in MRE [73]. The same process cannot be applied to the term multiplying λ as, under incompressibility, the Poisson's ratio tends to 0.5 and λ tends to infinity (see Eq.1.7b), compensating the zero given by the divergence of the deformation $\boldsymbol{u}$. The total term $\lambda\nabla\cdot\boldsymbol{u}$ represents the hydrostatic pressure p and is generally employed in the equation of motion for incompressible materials [74], returning

$$\rho\frac{\partial^2\boldsymbol{u}}{\partial t^2} = \mu\Big[\nabla^2\boldsymbol{u} + \nabla(\nabla\cdot\boldsymbol{u})\Big] + \eta\Big[\frac{\partial\nabla^2\boldsymbol{u}}{\partial t} + \frac{\partial\nabla(\nabla\cdot\boldsymbol{u})}{\partial t}\Big] + \nabla p \tag{1.12a}$$

$$\nabla\cdot\boldsymbol{u} = 0 \tag{1.12b}$$

Exploiting the following equalities: $\nabla^2\boldsymbol{u} + \nabla(\nabla\cdot\boldsymbol{u}) = \nabla\cdot\left(\nabla\boldsymbol{u} + \nabla\boldsymbol{u}^T\right)$ and $\nabla p = \nabla\cdot p\mathbb{1}$, where $\mathbb{1}$ is the second-order identity tensor, and recalling the linearity of differentiation, Eq.1.12 can be expressed as

$$\rho\frac{\partial^2\boldsymbol{u}}{\partial t^2} = \nabla\cdot\left[\mu\left(\nabla\boldsymbol{u} + \nabla\boldsymbol{u}^T\right) + \eta\frac{\partial\left(\nabla\boldsymbol{u} + \nabla\boldsymbol{u}^T\right)}{\partial t} + p\mathbb{1}\right] \tag{1.13a}$$

$$\nabla\cdot\boldsymbol{u} = 0 \tag{1.13b}$$

Under the further assumption of harmonic micro-displacement, generated by steady state waves characterised by an angular frequency of vibration ω, we can re-define $\boldsymbol{u}(\boldsymbol{x},t) = \boldsymbol{u}_\varepsilon(\boldsymbol{x})e^{i\omega t}$ and $p(\boldsymbol{x},t) = p_\varepsilon(\boldsymbol{x})e^{i\omega t}$. The equations of motion for an incompressible isotropic linear viscoelastic material, normally employed in MRE reconstruction, are then given by

$$\rho\omega^2\boldsymbol{u}_\varepsilon + \nabla\cdot\left[(G' + iG'')\left(\nabla\boldsymbol{u}_\varepsilon + \nabla\boldsymbol{u}_\varepsilon^T\right) + p_\varepsilon\mathbb{1}\right] = 0 \tag{1.14a}$$

$$\nabla\cdot\boldsymbol{u}_\varepsilon = 0 \tag{1.14b}$$

In this last set of equations, the material parameters have been replaced by the complex shear modulus $G^* = G' + iG''$, where the real part, G', also called storage modulus, reflects the elastic propagation of shear waves, and imaginary part, G'', known as loss modulus, describes the wave attenuation in a viscoelastic medium. While ω and the tissue density ρ are assumed to be known quantities in Eq.1.14a, and the gradient of displacement $\boldsymbol{u}_\varepsilon$ can be computed from the wave images, the shear modulus and the pressure term are

unknown. Elastography reconstruction methods attempt to solve Eq.1.14a for p and G^* given the measurement of $\boldsymbol{u}_\epsilon$, either directly or using iterative methods.

In this work, a state-of-the-art curl-based approach [73] was employed. While further details will be given in Chapter 6 of this dissertation, briefly, this reconstruction method assumes that G^* is locally constant and the curl operator is applied to remove the pressure term. Given the homogeneity assumption, the local curl-based approach falls into the group of direct local reconstruction methods, where many independent reconstructions of smaller areas are performed, covering the entire field of view (FOV) of the image. Direct global methods, despite considering spatial variability of the mechanical parameters, are generally computationally more expensive and require regularisation. Both the alternatives work using error minimisation and are inherently sensitive to data quality. Alternatively, iterative reconstruction techniques are less sensitive to noise but strongly depend on correct definition of the forward problem and their computational time is not suitable for clinical time scales. A comparison between iterative and direct techniques is proposed by Honarvar *et al.* (2016) [75] and an exhaustive review of the currently available reconstruction techniques can be found in Fovargue *et al.* (2018) [74].

1.2.4. Macro-Deformations Introduce Bias

To date, MRE has produced promising results in the breast cancer diagnosis, proving capable of differentiating malignant from benign lesions, as well as from healthy soft tissue, based on the characterisation of their material parameters [76, 77, 78, 51, 73]. The combination of MRE with MRI has also shown significant improvements in the characterisation of the lesion and in the accuracy of the diagnosis [79, 80, 81]. Venkatesh *et al.* (2007) have also reported a four-fold increase in the shear modulus, measured through MRE, of malignant tumours with respect to that of benign ones or normal tissue in liver [82]. Garteiser *et al.* (2013) have suggested the use of the loss shear modulus to distinguish between benign and malignant liver lesions, reporting a ~50 % increase in the latter case [83]. MRE has emerged as a promising technique for the assessment of brain tumour, too. The mechanical properties of meningioma, assessed by Xu *et al.* (2007) in six patients, showed a perfect correlation with the neurosurgeon's report [84]. A similar consistency between preoperative and surgical assessment was reported by Murphy *et al.* (2013) [32].

All these results assume measurements of the harmonic deformation $\boldsymbol{u}$ in the absence of external or endogenous forces, such that the linear viscoelasticity approximation made for the shear modulus reconstruction is satisfied. Nevertheless, an *ex vivo* study by Clarke *et al.* (2011) has revealed that, given the nonlinear viscoelastic nature of soft tissue, a 10 % linear compression is sufficient to generate a 47 % overestimation of the intrinsic storage shear modulus in bovine liver [85]. Endogenous and external forces can then lead to a biased estimation of the material properties of the investigated tissue. The implications

can be clinically relevant, as the measurement of an increased shear modulus can lead to erroneous diagnoses, while a decreased shear modulus caused by soft tissue deformation can mask the increased stiffness typical of certain tumours.
Recently, Capilnasiu *et al.* (2018) have investigated the loading bias generated by a pure uniaxial compression in polyvinyl alcohol (PVA) phantoms and have developed a mathematical framework to predict the apparent change in both G' and G'' given the knowledge of the applied deformation and of the constitutive law characterising the material [86]. In the presence of a nonlinear stress/strain response of tissue, the shear modulus will not only change according to the applied strain, but it will also affect the wave displacement and its gradient $\nabla \boldsymbol{u}$, hence the reconstructed values will depend on the direction of propagation of the probing waves as well. As a consequence, soft tissue can appear apparently anisotropic, with an apparent tissue softening measured when a compression is probed and an apparent stiffening in the case of tension.

Such work provides a new way to interpret MRE measurements, as a loading bias can be expected in many MRE applications: for example, breast MRE often requires the breast to be tightly fixed, which was found to lead to a loading bias [51], while respiratory motion applies a large strain of the liver, which can be exploited to make liver pathologies more apparent [87]. Tumour forces acting on the surrounding soft tissue can also compromise the estimation of the reconstructed shear modulus. The quantification of these forces, on the other hand, would represent a valuable biomarker to assess therapy efficacy. Measurement of the apparent anisotropy in the vicinity of the tumour through MRE, combined with modelling of tissue nonlinearity and estimation of the underlying deformation, could enable a direct non-invasive mapping and quantification of the stress exerted by the tumour onto the surrounding soft tissue. Elevated intra- and peri-tumoural forces, in fact, have been shown to modulate the behaviour of tumours, either when directly exerted on cancer cells or by indirectly increasing interstitial fluid pressure within the tumour core [88]. In the next section, the factors that lead to the accumulation of mechanical stresses in the tumour microenvironment will be presented, with an explanation of their impact on tumour progression. The definition of the two phases that characterise tumour stress, a solid and a liquid phase, will follow, together with the current understanding of the distribution of the two components and an overview of the techniques to quantify them.

1.3. Stress Distribution in the Tumour Environment

1.3.1. The Tumour Microenvironment

Solid tumours consist of a conglomerate of tumour and host cells, embedded in an extracellular matrix (ECM), for which nutrition and drainage is provided by an irregular blood and lymphatic vascular system [89]. Two of the main characteristic often found

in tumours, especially in breast and pancreatic cancer, are desmoplasia and increased stiffness, conditions that make lesions detectable through manual palpation or elastography techniques [88]. ECM composition is strongly regulated by fibroblasts, which are the main tissue cells present in the tumour microenvironment, which, in normal tissues, are characterised by a negligible activity [90, 91] In tumours, on the other hand, fibroblasts tend to become activated and acquire a malignant phenotype, undergoing a transformation into cancer associated fibroblasts (CAFs). In this state, CAFs have been found to enhance the production and remodelling of ECM proteins, mainly collagen I and fybronectin, hence contributing to ECM stiffening [90, 91]. The induced desmoplasia, combined with their release of growth factors, proteases and chemokines, can sustain tumour growth, invasion and angiogenesis [92, 93, 94]. Activation or over-expression of transforming growth factor-β (TGF-β) is one of the pathways that can cause precursor cells to convert into CAFs and trigger the associate ECM remodelling [90, 95], which in turn can further activate latent TGF-β, hence reinforcing the process [96, 97]. TGF-β can also increase ECM stiffening by regulating the production of matrix metalloproteinases (MMPs) and lysyl oxidase (LOX), enzymes responsible for the regulation of matrix protein synthesis and cross-linking and for the inhibition of matrix proteinase activity [98, 99, 100, 101].
The increased accumulation of cancer cells, stromal cells and ECM proteins in the tumour environment results in the development of a solid stress that applies both onto the tumour interior and its surroundings, which can stimulate cell migration and invasion during tumour growth [102].

Fluid stress, on the other hand, accounts for flow along tumour blood and lymphatic vasculature and in the tumour interstitial space. A deregulated fluid mechanics due to abnormalities in the tumour microenvironment can affect pressure gradients and lead to increased fluid stresses [103]. Hypoperfusion of many tumours is such that, with tumour growing in size, oxygen and nutrients cannot diffuse to the inner regions, which become hypoxic. This condition leads to the formation of a necrotic core and stimulates the sprouting of new blood vessels through the release of proangiogenic factors [104, 105]. Upregulation of vascular endothelial growth factors (VEGFs) has been found to be fundamental for this process, as they diffuse through the ECM and bind to the endothelial cells of nearby blood vessels, stimulating the formation of new ones, which follow the gradient of VEGFs towards the tumour's interior [103]. Tumour vasculature, however, is usually characterised by abnormal structure and functions: blood vessels inside the tumour are tortuous [106] and present large openings that favour the leaking of blood plasma into tumour interstitium [107], leading to an increased interstitial fluid pressure (IFP) [108]. Lymphatic vessels are also often recruited in tumours to drain the excessive accumulation of interstitial fluid [109]; however, compression due to elevated solid stress in the intratumoural region makes them non functional [110, 111], hence contributing to

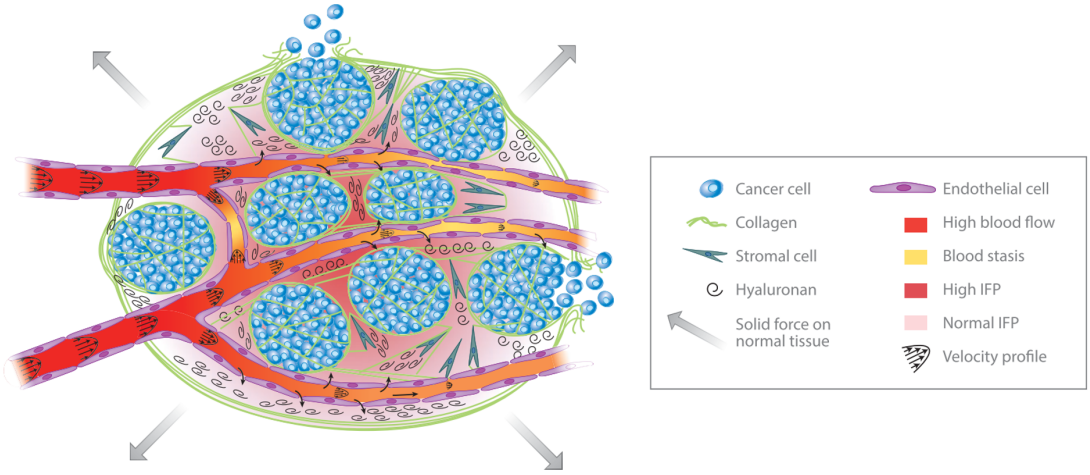

Figure 1.3.: Schematics of the mechanical forces developed in the tumour microenvironment. Cancer cell proliferation and enhanced ECM protein deposition leads to the accumulation of solid stress in the tumour interior. This stress can compress or collapse tumour vasculature, which is normally leaky and irregular, reducing blood and lymph flow. Inefficient drainage of tumour interstitium results in an homogeneous rise in IFP throughout the tumour mass, with a quick drop at the periphery. These unbalanced stresses force the tumour to push against the host tissue, which in turn resists this deformation, restricting tumour expansion. Image taken from Jain *et al.* (2014) [88].

a further increase in IFP. An increased lymph flow is instead observed at the periphery, which is sufficient for lymphatic metastasis [111, 112, 113]. A schematic of the stress and elevated IFP encountered in the tumour microenvironment is presented in Fig.1.3.

Both solid stress and IFP have been presented as hallmarks of cancer progression. Solid stress was found to be responsible for epithelial-to-mesenchymal transition in mouse mammary epithelial cells, which makes the cancer cells more motile and favours detachment from the primary tumour [114, 115]. These results were supported by the enhanced expression of metastasis-associated genes in glioblastoma and breast cancer cells subjected to compressive stress [116]. Kilarski *et al. (2009)* have shown how mechanical forces can mediate vascular growth, facilitating angiogenesis [117]. A recent study by Kalli *et al.* (2018) has associated solid stress to pancreatic fibroblast activation *in vitro* and has shown a consequent promotion of pancreatic cancer cell migration [118].
On the other hand, elevated IFP has been found to promote cell proliferation *in vitro* in osteosarcomas [119, 120], while a long-term lowering of IFP was found to reduce cell proliferation in two different tumours in mouse models [121]. Cell culture in a pressurised environment has also been revealed to regulate the release of angiogenic factors in osteosarcomas [122]. Altered flow conditions within the tumour can instead create biased gradients of cytokines, which guide cell migration towards the tumour periphery, in the direction of the functional lymph vessels [123]. These results, combined with an increased

peripheral lymph-flow, suggest that the lymphatic flow might play a fundamental role in the dissemination of carcinogenic cells. ECM density and solid stress can also lead to collapse of tumour micro-vessels, hence presenting a limitation to drug transport to the core of the tumour [124]

1.3.2. Measurement & Modelling of Tumour Stress Distribution

1.3.2.1. IFP

The fluid-phase stress includes IFP, micro-vascular pressure (MVP) and the shear stress that interstitial and intravascular flows exert on stromal and cancer cells, extracellular matrix, and on vessel walls. Interstitial flow is mediated by the hydrostatic and osmotic pressure generated between the tumour interstitial space and the vasculature. As explained earlier, the compressive forces present within the tumour mass, combined with the hyper-permeability of tumour vasculature, are responsible for a deregulated fluid mechanics. Blood and lymph vessel compression increases resistance to blood flow, hence impacting MVP and shear stress, and reduces interstitial fluid drainage, which, combined with an erratic transcapillary flow within the tumour interstitium, results then in an elevated IFP [125, 124]. Solid-phase stress has been accepted as a direct cause of an elevated IFP, as it can lead to intratumour vessel collapse, causing hypoxia and intestitial hypertension [126]. It has been proven, in fact, that IFP, being constantly lower or comparable with MVP, cannot be responsible for tumour blood and lymphatic vessel collapse, but is rather a consequence of such mechanism [127]. The loss of gradient between vessel walls and tumour interstitium caused by an increased IFP makes diffusion the main transport mechanism for extravasation, posing a significant obstacle to drug convective transport in many treatments [128, 129].

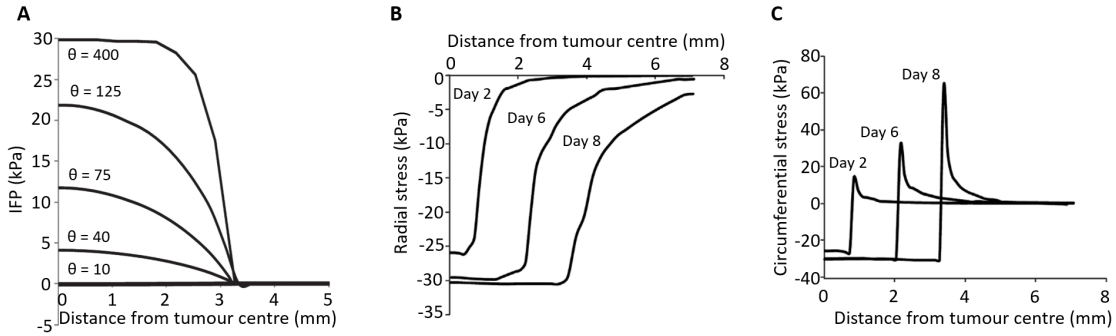

Figure 1.4.: Spatial distribution of IFP (A) and of the radial (B) and circumferential solid stress (C) through the tumour and in the surrounding normal tissue. The parameter θ directly correlates with the hyper-vascularity of a tumour and the leakiness of the blood vessels. Image A modified form Stylianopoulos *et al.* (2013) [127], images B and C modified from Voutouri *et al.* (2014) [130].

The first evidence of elevated IFP in tumours was reported in a study by Young *et al.* (1950) on rabbit models [131], however it was only in 1988 that the first mathematical model confirmed the uniform IFP distribution throughout the bulk of the tumour [132, 133] (see Fig.1.4-A). An abrupt drop to normal levels at the margins of the tumour was also reported. The generated steep pressure gradient causes fluid from the tumour interstitium, containing cancer cells and growth factors, to ooze into the surrounding normal tissue, facilitating tumour spread and metastasis [134].

In 1977, Fadnes *et al.* proposed for the first time the use of the wick-in-needle method, based on the use of a needle connected to a measuring device, to measure IFP [135]. This technique was employed for the first time in humans *in situ* by Boucher *et al.* (1991), reporting a mean value of 14.3±12.5 kPa in superficial metastatic melanomas [136], and still stands as a standard method for the measurement of IFP [108]. The pressure values can vary a lot depending on the tumour type and state, and a list of IFP measurements in various human tumours is given by Jain *et al.* (2007) [134], reporting values as high as ∼12 kPa in cervical carcinomas.
Piezoelectric pressure transducer catheters were employed to estimate IFP by Provenzano *et al.* (2012) in autochthonous pancreatic ductal adenocarcinomas in genetically engineered mouse models, with measurements ranging between ∼10 and 17 kPa [137]. This piezoelectric catheter was first proposed by Ozerdem and Hargens (2005) as a simplified method capable of providing more reliable IFP estimates [138] and was suggested by DelGiorno *et al.* (2014) to isolate solid stress from IFP measurements [139]; nevertheless Chauhan *et al.* (2014) have suggested that this method might not be able to effectively differentiate the two components, indicating the wick-in-needle technique as still more reliable [140].
Encouraging results were provided by the modified version of the piezoelectric pressure transducer probe proposed by Nieskoski *et al.* (2017), which, by adding a retractable cover around the catheter, proved capable to separately measure IFP and solid stress in the same tumour location [141]. Nevertheless, given the invasive nature of the instrument, an imaging technique able to measure the different stress components is currently sought and would potentially provide a better understanding and modelling of the mechanical processes involved. DCE-MRI [142, 143], through the monitoring and modelling of MR-contrast agent kinetics, and US contrast micro-bubbles [144, 145], with the sub-harmonic amplitude of scattered signal correlated to hydrostatic pressure, have shown the potential to be employed to non-invasively quantify IFP; nevertheless, the quest for the development of an imaging technique capable of accurately estimating tumour pressures to replace the standard invasive methods is still ongoing.

1.3.2.2. Solid stress

The solid-phase stress includes all the stresses carried by non-fluid components and can be divided into three categories characterised by different sources [146]:

- the externally applied stress, generated from the interaction of the growing tumour with the host tissue [127, 130];
- the swelling stress, developed by the electrostatic repulsive forces among closely spaced hyaluronian chains [147, 148];
- the residual or growth-induced stress, which is accumulated into the matrix and cells of the tumour tissue during tumour progression [149].

Externally applied stress arises from tumour growth and expansion: the higher stiffness compared to that of the hosting tissue is such that the tumour exerts mechanical forces onto the surrounding tissue that allow its growth in size. In response, the host tissue will resist such expansion, hence generating compressing forces applied on the tumour mass [149, 127]. A stiffer hosting tissue results in a higher magnitude of the external solid stress, hance making the mechanical properties of both the tumour and the surrounding tissue crucial to define the state of stress of the tumour [130]. *In vitro* studies on avascular tumour spheroids embedded in an agarose matrix have shown how their growth is increasingly reduced or inhibited when subjected to higher solid stress levels [150]. These results were found consistent throughout different tumour cell line and differentiation states. The generated compressive external forces can suppress cancer cell proliferation and trigger apoptosis through the mitochondrial pathway, with cancer cells growing preferentially in the regions subjected to less stress [151]. These processes have been found to be reversible once the stress is removed.

The high expression of the hyaluronan chains in the interstitial space of many malignant tumours, i.e. pancreatic ductal adenocarcinoma [152], gives rise to the swelling solid stress [153]. The negative charge of the closely spaced hyaluronic acids generates repulsive electrostatic forces responsible for the stress. The collagen content has been found to play a role too: while a higher hyaluronan to collagen area fraction has been associated to an increased swelling stress, a higher collagen content correlates to an increased tissue stiffness that opposes swelling [148, 154]. Collagen interaction with deposited hyaluronan also correlates to blood vessel compression and reduced vessel perfusion [155]. *In vitro* experiments on breast, ovarian and prostate cells spheroids have revealed that cancer cells can also contribute to swelling pressure [147]: when subjected to compressive stress, in fact, intracellular tonicity is reduced through sodium efflux to modulate osmotic pressure, leading to tumour swelling. Nevertheless, the cell-associated contribution to swelling stress appears negligible compared to that given by the electromagnetic repulsion among

hyaluronan chains [148]. The identification of swelling stress as a component of the solid stress instead of the IFP, however, is still debated [137, 141].
Finally, residual stress is caused by the proliferation of cancer and stromal cells during tumour progression, which is stored within the tumour even when it is excised. The magnitude of the stress was shown to correlate with tumour volume and hence tumour progression [149]. At the same time, a higher residual stress has been associated to a reduced tumour growth, potentially because of the increased apoptotic death and suppressed proliferation of cancer cells [149, 151].

Given the limited amount of techniques to calculate the total solid stress and its different components *in vivo*, many studies have developed mathematical models of tumour growth to quantify the stress distribution within a solid tumour [156, 157]. These models agree on an heterogeneous distribution of residual solid stress through the tumour mass and its surroundings: while this stress acts compressively in all directions at the centre of the tumour (Fig.1.4-B), a smooth transition of the circumferential stress from compressive to tensile has been modelled moving towards the periphery (Fig.1.4-C). A stress between 0 and 1.3 kPa was calculated from avascular tumour spheroid data using a linear poro-elasticity model [156].
A technique to quantify the residual solid stress was proposed by Stylianopoulos *et al.* (2012) using excised tumours that are allowed to relax by making a cut along their longest axis: the swelling of the centre and the simultaneous retraction of the boundaries become then visible and can be incorporated into a mathematical model relating the measured deformation to the applied stress. Measurements of tissue relaxation following the cut of excised tumours have reported residual stress levels in the range of 2.2 to 19.0 kPa and 0.37 to 8.0 kPa in the interior of different types of human and murine tumours, respectively [149]. On the basis of experimental data, using the phenomenological Gompertzian equation [158] to model tumour growth, the residual solid stress was estimated to account only for 30 % of the total solid stress [127]; however these numbers might be affected by the residual presence of the swelling stress. *In vitro* experiments on different cancer cell spheroids, coupled with mathematical modelling, measured no swelling stress for isotonic and hypertonic environments and a stress ranging between 2.1 and 10.0 kPa for hypertonic tumour micro-envionments, showing a linear correlation with the ratio of hyaluronan to collagen area fraction [148]. Nia *et al.* (2017) have also recently proposed three techniques to map residual solid stress from the measurement of the stress-relaxing deformation through ultrasonography and optical microscopy, both in excised tumours and *in situ*. In the former case, maximum values of 0.21 kPa and 7 kPa in brain and pancreatic tumours were reported, while, interestingly, in the case of small deformations, a maximum radial stress of 0.1 kPa was estimated from a murine brain tumour *in situ* compared to 0.02 kPa observed *ex vivo*. [159]. This last result highlights the importance of the tumour-host

tissue interaction in the definition of the state of stress of the tumour and sets a limit in the proposed method to isolate the various components of the solid stress.
The major component of the solid-phase stress is in fact given by the resistance of the surrounding normal tissue to tumour expansion. In the absence of experimental validation, by modelling both tumour and host tissue through an isotropic nonlinear elastic constitutive law, Stylianopoulos *et al.* (2013) have estimated values of the externally applied stress to be as high as 40 kPa, clearly the largest contribution to solid-phase stress and sufficient to collapse intra-tumoural vasculature [127]. This value, however, is strictly dependent on the mechanical properties of the surrounding tissue, which, as a consequence, can also impact tumour growth in volume [130]. *In vitro* experiments on cancer cell spheroids have provided evidence of the role of the tumour-host tissue mechanical interaction, reporting stress values ranging from 3.7 to 16.0 kPa, estimated from tumour spheroids embedded in matrices characterised by different stiffness [160, 151].

1.3.2.3. MRE to Measure Tumour Stress

Despite a clear distinction between the mechanical processes behind the generation of the solid and the liquid stresses, to date the measurement of one component excluding the other one is still challenging. Furthermore, both solid stress and IFP have arisen as hallmarks of the mechanical environment of solid tumours [105], and their increased magnitude has been associated to tumour progression [100], making their local noninvasive estimation a biomarker for the clinical assessment of therapy efficacy.
In this sense, a consortium of international partners has joined forces in the FORCE (Imaging the Force of Cancer) project, sponsored by the European Union, which aims to address a fundamental need in planning and monitoring of cancer treatment using MRE to measure the forces active in cancer [161]. The employment of the latest developments in MRE, combined with 3D strain imaging and a correct modelling of the viscoelastic behaviour of soft tissue can be used to assess the stiffness load relation of tissue, hence giving the possibility to retrieve a map of the stress and pressure distribution within tumours. This innovative multi-modal MR-based approach presents itself as the first imaging technique capable of measuring cancer forces *in vivo* and to determine their spatial distribution in a noninvasive manner. Developments of the FORCE project could open new avenues for cancer therapy, providing a new paradigm for predicting metastatic potential, gauging the efficacy of drug delivery for cancer therapy, and clinically observing therapy progression through imaging.
The work presented in this thesis falls within the objectives of this project and aims at investigating the apparent change of the mechanical properties of the host tissue generated by tumour-associated stresses, as measured through MRE. Details of the hypotheses at the basis of this project and the associated objectives are reported in the next section.

1.4. Project Rationale & Goals

In the previous sections we have explained that elevated IFP and solid stress are defining characteristic of solid tumour progression and they both contribute to tumour expansion in size, leading to the mechanical deformation of the surrounding environment. With the generated stress and the resulting applied strain strongly dependent on the mechanical properties of the host tissue, a correct modelling of its rheological behaviour becomes extremely important. It has been established that soft tissue presents a nonlinear stress/strain response, leading to variations in its mechanical properties even when subjected to small deformations. While the material parameters of soft tissue can be measured through MRE, the wave equation employed in the reconstruction process normally assumes linear viscoelasticity, making the local estimation of the shear modulus biased by the presence of tumour-associated forces. Previous mathematical considerations have shown that tissue compression, associated to a shortened wavelength, leads to an apparent decrease in shear modulus, while the opposite is seen under tension. As a consequence, assuming a radial expansion of the tumour (Fig1.5-A), an apparent radial softening is predicted, while the circumferential tension is expected to cause a measured softening in the same direction (Fig1.5-B). Nevertheless, we have also made clear that the directionality of the shear waves plays a fundamental role in the material properties estimation in the case of underlying nonlinear deformations. Under the assumption of plane waves, characterised by a unique direction of propagation, we expect the force-associated bias to lead to an apparent softening on the leading and trailing edges of the tumour, where a compression is sensed, and an apparent stiffening where circumferential tension is probed (Fig1.5-C). While previous findings have shown this signature apparent anisotropic pattern in phantoms [162] (Fig1.5-D), a clear experimental and mathematical framework that confirms this theory has not been presented yet.

The main goals of this project thus comprise of

- providing an analytical formulation that describes the impact of the nonlinear properties of soft tissue on its shear modulus estimation through MRE when subjected to a spherical deformation similar to that generated by a pressurised tumour;

- developing a phantom setup that reproduces the nonlinear behaviour of soft tissue under compression to investigate the signature shear modulus pattern produced by a mimicked tumour;

- implementing an inflation experiment where MRE is used to experimentally assess the shift in shear modulus produce by radial deformations characterised by different magnitudes;

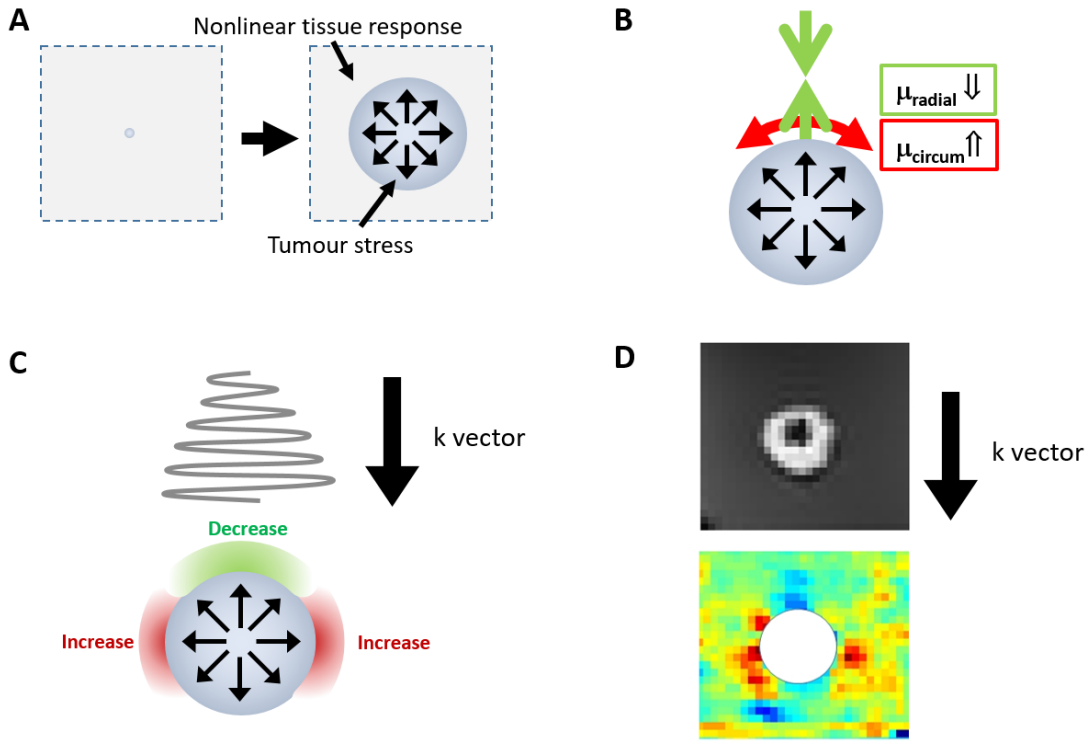

Figure 1.5.: A) Tumour stress generates a nonlinear tissue response. B) Radial compression results in a reduced apparent shear modulus, while circumferential tension generates an increased value. C) MRE probes material properties according to the direction of propagation of the shear waves, hence reconstructing an anisotropic pattern. D) Reconstructed shear modulus around an inflated balloon inside a plastic cuboid.

- defining a method to measure the generated stress and strain distributions to set a bridge between the mathematical framework and the experimental findings.

These objectives will be addressed throughout this manuscript, which follows the organisation presented here. In Chapter 2, a mathematical framework to describe the effect of a macro-deformation on the wave equation normally employed in MRE reconstruction under the assumption of linear viscoelasticity will be presented. We will then focus on the particular case of the inflation of a thick-shelled sphere, modelled with an incompressible isotropic hyperelastic material law, and produce an analytical formulation of the variation in shear modulus probed in elastography using plane waves. Chapter 3 will then provide the protocol to carry out the inflation experiment using a phantom, focusing on its different constituents and explaining the method implemented to measure the stress generated by the mimicked tumour onto its surroundings. Finally, the details of the setup used for the MRE data acquisition and of the imaging sequences will be provided. The implementation of a nonrigid image registration strategy and its *in silico* validation using simulated deformations of real images similar to those applied by a solid tumour will be introduced

in Chapter 4. Here, the reliability of this method to estimate the strains generated in the inflation experiment was then investigated, and further tests on compressed murine tumours and in fibroadenomas in patients were carried out to define its reliability in a preclinical and clinical setting and to identify its limitations. Chapter 5 will focus on the rheological characterisation of the material used to simulate the nonlinear behaviour of soft tissue. Two nonlinear viscoelastic models were used to fit the experimental data, providing additional insights on the required composition of the material used to build the phantom and validating the use of the constitutive equation employed to develop the analytical framework presented in Chapter 2. The results obtained from three replicates of the inflation experiment in phantom will be reported in Chapter 6. This chapter will investigate the impact of the local shear wave propagation direction on the expected variation in apparent shear modulus and will provide an alternative way to compare the experimental results with the analytical predictions. Preliminary results obtained from the attempt to extend the inflation experiment to an *ex vivo* setting will follow. Finally, a discussion of the reliability of the measurements and on the challenges associated with the use of real tissue samples will be provided. Final conclusions will close this thesis, revisiting the assumption at the basis of the analytical work, remarking the limitations identified from the experimental findings and examining the implications of the developed framework in a clinical scenario.

2. Analytical Modelling

In Chapter 1, the possible impact of tumour-associated forces on the mechanical properties of the surrounding soft tissue has been discussed. Prior investigations have shown that the nonlinear response to macro-deformations, typical of soft tissues, is not accounted for in the wave equation employed in the state-of-the-art MRE reconstruction methods, hence the variation in wavelength caused by tissue compression/tension is interpreted as wave propagation through a softer/stiffer medium. This leads to the reconstruction of an apparent anisotropic shear modulus distribution, which depends on the direction of propagation of the shear waves relative to the applied deformation.
In this chapter, a modified version of Cauchy's equations of motion, introduced in Section 1.2, describing an incompressible nonlinear viscoelastic material and accounting for macro-deformations will be proposed, to elucidate the connection between applied kinematics and intrinsic material properties in MRE. Perturbation analysis was employed to simplify the presented governing equations and to determine the impact of a large-scale deformation on harmonic wave propagation. This theoretical derivation yelled an expression of the apparent stiffness and viscosity moduli, $\mathcal{G}'$ and $\mathcal{G}''$, of the material, dependent on the magnitude and direction of the applied deformation, and to clarify how the estimation of the shear moduli, G' and G'', depends on the direction of propagation of the probing waves. The particular case of the impact of the stress generated by a radially expanding tumour onto the MRE estimation of the material properties of the host tissue will then be examined.

In detail, Section 2.1 will provide the mathematical background to derive Cauchy's equations of motion in both the Eulerian and Lagrangian configuration. Section 2.2 will present the perturbation theory employed to simplify Cauchy's equation of motion for a deformed viscoelastic material affected by a harmonic perturbation and will reveal the dependence of the material properties on the applied deformation gradient. Following that, a brief overview of the hyperelastic models employed to describe soft tissue nonlinear stress/strain behaviour will be given; the specific case of an hyperelastic material described by a polynomial strain energy density function will be considered and the corresponding analytical formulation of the stress tensors will be calculated in Section 2.3. The proposed Cauchy stress tensor will then be used to produce a linearised version of the shear modulus in the case of a simple shear deformation, under the assumption of small strain. In Section

2.4, the proposed theoretical framework will be applied to an idealised peri-tumoural tissue exposed to tumour-generated stress. Using a thick-shelled sphere approximation and a modified Mooney-Rivlin constitutive equation, the associated shift in G' probed through plane wave propagation will be investigated. A numerical representation of the expected reconstructed images will also be provided. A final discussion over the developed mathematical framework and the presented data is given in Section 2.5.

2.1. Preliminaries

2.1.1. Displacement and strain

In continuum mechanics, the points of a deformable body in their reference/original configuration, Ω_0, are described by their position $\boldsymbol{X}$ at time $t = 0$. When an external force is applied, it causes the body to deform, hence displacing each point to a new location $\boldsymbol{x}$ at time $t = T$. Under the assumption of a unique mapping from $\boldsymbol{X}$ to $\boldsymbol{x}$, a Lagrangian description of the motion, made in terms of the fixed referential coordinates in the reference domain, defines the new point location as a function of the initial one, $\boldsymbol{x} = \boldsymbol{x}(\boldsymbol{X})$; hence the displacement relative to the original position is given by $\boldsymbol{U}(\boldsymbol{X}) = \boldsymbol{x}(\boldsymbol{X}) - \boldsymbol{X}$. An Eulerian configuration, instead, focuses on the current domain Ω, expressing the generated displacement as $\boldsymbol{u}(\boldsymbol{x}) = \boldsymbol{x} - \boldsymbol{X}(\boldsymbol{x})$. Accordingly with this notation, in the following discussion the subscript 0 on a variable will be used to refer to the initial configuration.
In the reference configuration, the particle positions before and after the deformation are related by the deformation gradient:

$$\boldsymbol{F} = \frac{d\boldsymbol{x}}{d\boldsymbol{X}} = \nabla_X \boldsymbol{U} + \mathbb{1} \tag{2.1}$$

where ∇_X denotes the gradient of the deformation field mapped in Ω_0. In the case of large deformations, the finite strain generated by the displacement $\boldsymbol{U}$ is given by the Green strain tensor

$$\boldsymbol{E} = \frac{1}{2}(\boldsymbol{F}^T\boldsymbol{F} - \mathbb{1}) \tag{2.2}$$

where the diagonal components refer to normal strain and the off-diagonal elements are related to shear strain. The product $\boldsymbol{C} = \boldsymbol{F}^T\boldsymbol{F}$ is called the right Cauchy-Green deformation tensor, along with the left Cauchy-Green deformation tensor (or Finger tensor) $\boldsymbol{B} = \boldsymbol{F}\boldsymbol{F}^T$.The two tensors are related simply by a rotation, so they share the same invariants:

$$\begin{aligned} I_{\mathrm{C}} &= tr(\boldsymbol{C}) = \lambda_1^2 + \lambda_2^2 + \lambda_3^2 \\ II_{\mathrm{C}} &= \frac{1}{2}\left[tr(\boldsymbol{C})^2 - tr(\boldsymbol{C}^2)\right] = \lambda_1^2\lambda_2^2 + \lambda_2^2\lambda_3^2 + \lambda_3^2\lambda_1^2 \\ III_{\mathrm{C}} &= det(\boldsymbol{C}) = J^2 = \lambda_1^2\lambda_2^2\lambda_3^2 \end{aligned} \tag{2.3}$$

Here λ_1, λ_2 and λ_3 are the eigenvalues of $\boldsymbol{F}$, also called principal stretches. Notably, in the case of an isotropic material, its deformation gradient can be expressed solely in terms of the principal stretches or of the invariants of the Cauchy-Green deformation tensors.In the definition of the third invariant, $J \triangleq det(\boldsymbol{F})$ is the Jacobian of the deformation and describes the change of a volume element. For incompressible bodies, a volume element keeps is volume constant throughout the deformation, hence we have $J = dV/dV_0 = 1$. In the case of a slightly incompressible material it is useful to decompose the deformation gradient into the product of:

- a volume preserving, or isochoric, component $\hat{\boldsymbol{F}}$
- a volume-changing, or volumetric, component $J^{\frac{1}{3}}$

This concept can be carried on to $\boldsymbol{C}$ and $\boldsymbol{B}$, such that their isochoric component can be written as:

$$\hat{\boldsymbol{C}} = J^{-\frac{2}{3}}\boldsymbol{C} \qquad \hat{\boldsymbol{B}} = J^{-\frac{2}{3}}\boldsymbol{B} \tag{2.4}$$

The invariants of the isochoric tensors are called unimodular invariants and are also a volumetric scaling of the original invariants:

$$\begin{aligned} I_{\hat{\mathrm{C}}} &= J^{-\frac{2}{3}} I_{\mathrm{C}} & I_{\hat{\mathrm{B}}} &= J^{-\frac{2}{3}} I_{\mathrm{B}} \\ II_{\hat{\mathrm{C}}} &= J^{-\frac{4}{3}} II_{\mathrm{C}} & II_{\hat{\mathrm{B}}} &= J^{-\frac{4}{3}} II_{\mathrm{B}} \\ III_{\hat{\mathrm{C}}} &= 1 & III_{\hat{\mathrm{B}}} &= 1 \end{aligned} \tag{2.5}$$

2.1.2. Stress

When a body is subjected to an external surface force, each infinitesimal particle of the body will experience a stress corresponding to the amount of force exerted per unit area

$$\boldsymbol{T}^{\hat{\boldsymbol{n}}} = \lim_{\Delta\Gamma \to 0} \frac{\Delta \boldsymbol{f}}{\Delta\Gamma} = \frac{d\boldsymbol{f}}{d\Gamma}$$

Here $\boldsymbol{T}^{\hat{\boldsymbol{n}}}$ is the stress vector, or traction, pointing towards the direction of the normal vector $\hat{\boldsymbol{n}}$, while $\boldsymbol{f}$ is the force acting on the surface Γ. According to Cauchy's stress theorem, the traction $\boldsymbol{T}^{\hat{\boldsymbol{n}}}$ can be expressed as a linear function of the area vector $\hat{\boldsymbol{n}}$ through

$$d\boldsymbol{f} = \boldsymbol{T}^{\hat{\boldsymbol{n}}} d\Gamma = \boldsymbol{\sigma}^T \hat{\boldsymbol{n}} d\Gamma \qquad \text{or} \qquad \boldsymbol{T}^{\hat{\boldsymbol{n}}} = \boldsymbol{\sigma}^T \hat{\boldsymbol{n}} \tag{2.6}$$

where the symmetric tensor $\boldsymbol{\sigma}$ is called the Cauchy stress tensor and is used to define the physical state of stress at a point in the current configuration.
The corresponding stress tensor relating the areas $d\Gamma_0 \hat{\boldsymbol{n}}_0$, defined in Ω_0, to the forces

applied in the current domain Ω is the first Piola-Kirchhoff stress tensor (PK1), defined as

$$d\boldsymbol{f} = \boldsymbol{T}^{\hat{\boldsymbol{n}}} d\Gamma = \boldsymbol{P} d\Gamma_0 \hat{\boldsymbol{n}}_0 \qquad \text{or} \qquad \boldsymbol{T}_0^{\hat{\boldsymbol{n}}} = \boldsymbol{P}\hat{\boldsymbol{n}}_0 \tag{2.7}$$

which can be expressed in terms of the Cauchy stress tensor as

$$\boldsymbol{P} = J\boldsymbol{\sigma}\boldsymbol{F}^{-T} \tag{2.8}$$

Unlike $\boldsymbol{\sigma}$, $\boldsymbol{P}$ is in general a non-symmetric tensor;* however, another symmetric tensor, the second Piola-Kirchhoff stress tensor (PK2), is introduced to pull back the force $d\boldsymbol{f}$ to the reference configuration Ω_0

$$d\boldsymbol{f}_0 = \boldsymbol{F}^{-1} d\boldsymbol{f} = \boldsymbol{F}^{-1}\boldsymbol{P}\hat{\boldsymbol{n}}_0 d\Gamma_0 = \boldsymbol{S}^T \hat{\boldsymbol{n}}_0 d\Gamma_0 \qquad \text{or} \qquad \boldsymbol{F}^{-1}\boldsymbol{T}_0^{\hat{\boldsymbol{n}}} = \boldsymbol{S}^T \hat{\boldsymbol{n}}_0 \tag{2.9}$$

which directly relates to the other tensorial quantities through

$$\boldsymbol{S} = \boldsymbol{F}^{-1}\boldsymbol{P} \qquad \text{and} \qquad \boldsymbol{S} = J\boldsymbol{F}^{-1}\boldsymbol{\sigma}\boldsymbol{F}^{-T} \tag{2.10}$$

Following the approach used for the deformation gradient, it is sometimes useful to decompose the Cauchy stress tensor into a deviatoric component $\boldsymbol{\sigma}'$ and a spherical component containing the hydrostatic pressure $p = tr(\boldsymbol{\sigma})/3$

$$\boldsymbol{\sigma} = \boldsymbol{\sigma}' + p\mathbb{1} \tag{2.11}$$

where $\boldsymbol{\sigma}'$ is such that $tr(\boldsymbol{\sigma}') = 0$. A similar decomposition can also be established for PK1 and PK2:

$$\boldsymbol{P} = \boldsymbol{P}' + pJ\boldsymbol{F}^{-T} \tag{2.12}$$

$$\boldsymbol{S} = \boldsymbol{S}' + pJ\boldsymbol{C}^{-1} \tag{2.13}$$

2.1.3. Field Equations

2.1.3.1. The Equation of Continuity

Eulerian Form

In continuum mechanics the equation of continuity is used to express the conservation of mass during the time of the deformation. Given the mass of an entire body characterised by volume V_t at time t

$$m(t) = \int_{V_t} \rho(\boldsymbol{x}, t)\, dV \tag{2.14}$$

*Note to self from Jack: because it's a two point tensor with a base each in reference and current configs

the conservation of mass requires that $\frac{Dm}{Dt} = 0$, where $\frac{D}{Dt}$ represents the material derivative (see Appendix A), hence giving

$$\begin{aligned}\frac{Dm}{Dt} &= \frac{D}{Dt}\left[\int_{V_t} \rho(\boldsymbol{X}, t)\, dV\right] = \\ &= \int_{V_t} \left[\frac{\partial \rho}{\partial t} + \nabla_{\boldsymbol{x}} \cdot \rho \boldsymbol{v}\right] dV = 0\end{aligned}$$

where $\boldsymbol{v}$ is the velocity vector field. Since the equality holds for an arbitrary volume V_t, we obtain the Eulerian form of the equation of continuity

$$\frac{\partial \rho}{\partial t} + \nabla_{\boldsymbol{x}} \cdot \rho \boldsymbol{v} = 0 \tag{2.15}$$

Lagrangian Form

A collection of particles retains the same mass regardless of the chosen configurations, hence we can write

$$m = \underbrace{\int_{V_t} \rho(\boldsymbol{x}, t)\, dV}_{\text{CURRENT CONFIGURATION}} = \underbrace{\int_{V_{t=0}} \rho_0(\boldsymbol{X}, t)\, dV_0}_{\text{REFERENTIAL CONFIGURATION}} \tag{2.16}$$

Since $\boldsymbol{x} = \boldsymbol{x}(\boldsymbol{X}, t)$ and given that $dV = J\, dV_0$, we can write the term in the current configuration in the referential form, obtaining

$$m = \underbrace{\int_{V_{t=0}} \rho(\boldsymbol{X}, t) J\, dV_0}_{\substack{\text{CURRENT CONFIGURATION} \\ \text{IN REFERENTIAL FORM}}} = \underbrace{\int_{V_{t=0}} \rho_0(\boldsymbol{X}, t)\, dV_0}_{\text{REFERENTIAL CONFIGURATION}} \tag{2.17}$$

Collecting the terms, we get the following equality

$$\int_{V_{t=0}} \left[\rho(\boldsymbol{X}, t) J - \rho_0(\boldsymbol{X}, t)\right] dV_0$$

which holds for an arbitrary $V_{t=0}$, hence

$$\rho J - \rho_0 = 0 \tag{2.18}$$

where the dependency on $\boldsymbol{X}$ and t has been omitted. Again, the conservation of mass is expressed by $\frac{Dm}{Dt} = 0$, which gives

$$\frac{\partial \rho_0}{\partial t} = \frac{\partial (\rho J)}{\partial t} = 0 \tag{2.19}$$

For an incompressible material, defined by $J = 1$, the density must stay constant at all times for the selected volume $V_{t=0}$, hence

$$\rho = \rho_0 \tag{2.20}$$

and the equation of continuity in the Lagrangian form is given by

$$J - 1 = 0 \tag{2.21}$$

2.1.3.2. The Cauchy Momentum Equation

Eulerian Form

To derive the Cauchy momentum equation in the Eulerian form, it is convenient to start from the Newton's second law of motion: $\Sigma_i \boldsymbol{f}_i = m\frac{d\boldsymbol{v}}{dt}$. The sum of both the surface forces, $\boldsymbol{T}^{\hat{\boldsymbol{n}}}$ (N/m^2), acting over the surface of the body, and the body forces, $\boldsymbol{b}$ (N/m^3), acting on its volume at a time t during the deformation can be written as

$$\boldsymbol{f} = \sum_i \boldsymbol{f}_i = \oint_{\Gamma_t} \boldsymbol{T}^{\hat{\boldsymbol{n}}}\, d\Gamma + \int_{V_t} \rho \boldsymbol{b}\, dV \tag{2.22}$$

Using Eq.2.6, we can apply the Gauss theorem to convert the surface integral into a volume integral and to group the terms together:

$$\begin{aligned} \boldsymbol{f} &= \int_{V_t} \nabla_{\boldsymbol{x}} \cdot \boldsymbol{\sigma}^T\, dV + \int_{V_t} \rho \boldsymbol{b}\, dV = \\ &= \int_{V_t} \left[\nabla_{\boldsymbol{x}} \cdot \boldsymbol{\sigma}^T + \rho \boldsymbol{b}\right]\, dV \end{aligned} \tag{2.23}$$

We can re-write Newton's second law using the material derivative:

$$\frac{D}{Dt}\left[\int_{V_t} \rho \boldsymbol{v}\, dV\right] = \int_{V_t} \left[\nabla_{\boldsymbol{x}} \cdot \boldsymbol{\sigma}^T + \rho \boldsymbol{b}\right]\, dV \tag{2.24}$$

where the integral on the left-hand side of the equality is named the linear momentum of the body. If we now focus only on the resultant force f_z in the z-direction, by the Reynolds transport theorem (see Appendix B) we can take the time derivative of the term on the left-hand side of the above equality inside the integral:

$$\begin{aligned} \frac{D}{Dt}\left[\int_{V_t} \rho v_z\, dV\right] &= \int_{V_t} \rho \left(\frac{\partial v_z}{\partial t} + v_x \frac{\partial v_z}{\partial x} + v_y \frac{\partial v_z}{\partial y} + v_z \frac{\partial v_z}{\partial z}\right) dV = \\ &= \int_{V_t} \rho \frac{Dv_z}{Dt}\, dV \end{aligned} \tag{2.25}$$

Substituting Eq.2.25 in the z-component of Eq.2.24 and assuming an arbitrary volume V_t we obtain the Eulerian form of the equation of motion in the z-direction

$$\rho\left(\frac{\partial v_z}{\partial t}+v_x\frac{\partial v_z}{\partial x}+v_y\frac{\partial v_z}{\partial y}+v_z\frac{\partial v_z}{\partial z}\right)=\frac{\partial \sigma_{xz}}{\partial x}+\frac{\partial \sigma_{yz}}{\partial y}+\frac{\partial \sigma_{zz}}{\partial z}+\rho b_z$$

The same procedure can be applied to the x- and y-component of the resultant force, generating the entire set of equations of motion

$$\begin{aligned}
\rho\left(\frac{\partial v_x}{\partial t}+v_x\frac{\partial v_x}{\partial x}+v_y\frac{\partial v_x}{\partial y}+v_z\frac{\partial v_x}{\partial z}\right)&=\frac{\partial \sigma_{xx}}{\partial x}+\frac{\partial \sigma_{yx}}{\partial y}+\frac{\partial \sigma_{zx}}{\partial z}+\rho b_x\\
\rho\left(\frac{\partial v_y}{\partial t}+v_x\frac{\partial v_y}{\partial x}+v_y\frac{\partial v_y}{\partial y}+v_z\frac{\partial v_y}{\partial z}\right)&=\frac{\partial \sigma_{xy}}{\partial x}+\frac{\partial \sigma_{yy}}{\partial y}+\frac{\partial \sigma_{zy}}{\partial z}+\rho b_y\\
\rho\left(\frac{\partial v_z}{\partial t}+v_x\frac{\partial v_z}{\partial x}+v_y\frac{\partial v_z}{\partial y}+v_z\frac{\partial v_z}{\partial z}\right)&=\frac{\partial \sigma_{xz}}{\partial x}+\frac{\partial \sigma_{yz}}{\partial y}+\frac{\partial \sigma_{zz}}{\partial z}+\rho b_z
\end{aligned} \tag{2.26}$$

which can be concisely grouped into the vector form of the Cauchy momentum equation in the Eulerian coordinate system

$$\rho\left(\frac{\partial \boldsymbol{v}}{\partial t}+(\boldsymbol{v}\cdot\nabla)\boldsymbol{v}\right)=\nabla_{\boldsymbol{x}}\cdot\boldsymbol{\sigma}^T+\rho\boldsymbol{b} \tag{2.27}$$

or, writing the Eulerian velocity $\boldsymbol{v}$ in terms of the Eulerian displacement $\boldsymbol{u}$,

$$\rho\left(\frac{\partial^2 \boldsymbol{u}}{\partial t^2}+\left(\frac{\partial \boldsymbol{u}}{\partial t}\cdot\nabla\right)\frac{\partial \boldsymbol{u}}{\partial t}\right)=\nabla_{\boldsymbol{x}}\cdot\boldsymbol{\sigma}^T+\rho\boldsymbol{b} \tag{2.28}$$

Lagrangian Form

To derive the Cauchy momentum equation in the Lagrangian form, we can use the same approach employed in Eq.2.22 and rewrite the resultant force acting on the body during the deformation in the Eulerian configuration as the correspondent resultant in the Lagrangian XYZ-coordinate system

$$\boldsymbol{f}_0=\oint_{\Gamma_{t=0}}\boldsymbol{P}\hat{\boldsymbol{n}}_0\,d\Gamma_0+\int_{V_{t=0}}\rho_0\boldsymbol{b}\,dV_0 \tag{2.29}$$

By Gauss theorem, we find that

$$\boldsymbol{f}_0=\int_{V_{t=0}}\left[\nabla_X\cdot\boldsymbol{P}+\rho_0\boldsymbol{b}\right]dV_0 \tag{2.30}$$

Naming $\boldsymbol{V}$ the velocity expressed in the Lagrangian configuration, using Newton's second law we can write the following equality

$$\frac{D}{Dt}\left[\int_{V_{t=0}} \rho_0 \boldsymbol{V}\, dV\right] = \int_{V_{t=0}} \left[\nabla_{\boldsymbol{X}} \cdot \boldsymbol{P} + \rho_0 \boldsymbol{b}\right] dV_0 \tag{2.31}$$

Once again, focusing on the z-component of the linear momentum of the body, we can use the Reynolds transport theorem (see Appendix B) to rewrite the integral on the left of the above equation as

$$\frac{D}{Dt}\left[\int_{V_{t=0}} \rho_0 V_Z\, dV_0\right] = \int_{V_{t=0}} \rho_0 \frac{DV_Z}{Dt}\, dV_0 = \int_{V_{t=0}} \rho_0 \frac{\partial V_Z}{\partial t}\, dV_0 \tag{2.32}$$

where for the last equality we have expressed the material derivative in the Lagrangian form (see Appendix A). Newton's law for the z-component of the resultant force hence assumes the following version

$$\int_{V_{t=0}} \rho_0 \frac{\partial V_Z}{\partial t}\, dV_0 = \int_{V_{t=0}} \left(\frac{\partial P_{ZX}}{\partial X} + \frac{\partial P_{ZY}}{\partial Y} + \frac{\partial P_{ZZ}}{\partial Z} + \rho_0 b_Z\right) dV_0 \tag{2.33}$$

Such equality must hold for any arbitrary volume $V_{t=0}$, so that, if we extend the discussion to the x- and y-component of the resultant force, we obtain the set of equations of motion in the Lagrangian configuration

$$\begin{aligned}
\rho_0 \frac{\partial V_X}{\partial t} &= \frac{\partial P_{XX}}{\partial X} + \frac{\partial P_{XY}}{\partial Y} + \frac{\partial P_{XZ}}{\partial Z} + \rho_0 b_X \\
\rho_0 \frac{\partial V_Y}{\partial t} &= \frac{\partial P_{YX}}{\partial X} + \frac{\partial P_{YY}}{\partial Y} + \frac{\partial P_{YZ}}{\partial Z} + \rho_0 b_Y \\
\rho_0 \frac{\partial V_Z}{\partial t} &= \frac{\partial P_{ZX}}{\partial X} + \frac{\partial P_{ZY}}{\partial Y} + \frac{\partial P_{ZZ}}{\partial Z} + \rho_0 b_Z
\end{aligned} \tag{2.34}$$

which can be written in vector notation as

$$\rho_0 \frac{\partial \boldsymbol{V}}{\partial t} = \nabla_{\boldsymbol{X}} \cdot \boldsymbol{P} + \rho_0 \boldsymbol{b} \tag{2.35}$$

The Laplacian form of the Cauchy momentum equation is finally given in terms of the Laplacian displacement $\boldsymbol{U}$ by

$$\rho_0 \frac{\partial^2 \boldsymbol{U}}{\partial t^2} = \nabla_{\boldsymbol{X}} \cdot \boldsymbol{P} + \rho_0 \boldsymbol{b} \tag{2.36}$$

2.2. Linearised Constitutive Laws of a Largely Deformed Viscoelastic Body Subjected to Small Perturbations

In the case of an incompressible body under non-static equilibrium, we can describe the effect of a finite deformation over the time interval $[0, T]$ using the Cauchy momentum equation 2.36 and the equation of continuity 2.21 in the Lagrangian form, as derived in Section 2.1:

$$\rho J(\boldsymbol{U})\frac{\partial^2 \boldsymbol{U}}{\partial t^2} - \nabla_X \cdot \boldsymbol{P}(\boldsymbol{U}) = 0 \tag{2.37a}$$

$$J(\boldsymbol{U}) - 1 = 0 \tag{2.37b}$$

where the dependency of J and $\boldsymbol{P}$ on the Lagrangian $\boldsymbol{U}$ is left explicit and body forces are ignored.
In the field of MRE, we rely on the propagation of shear waves through the body to probe its material properties. Considering periodic waves in time acting in a time domain $I \subset [0, T]$ and under the assumption of steady state, the generated micro-deformation and associated hydrostatic pressure are expressed as

$$\boldsymbol{u}_\varepsilon(\boldsymbol{x}, t) = \mathrm{Re}\{\boldsymbol{u}_\mathbb{C}(\boldsymbol{x})e^{i\omega t}\} \qquad \text{and} \qquad p_\varepsilon(\boldsymbol{x}, t) = \mathrm{Re}\{p_\mathbb{C}(\boldsymbol{x})e^{i\omega t}\} \tag{2.38}$$

where $\boldsymbol{u}_\mathbb{C}(\boldsymbol{x}) = \boldsymbol{u}_r(\boldsymbol{x}) + i\boldsymbol{u}_i(\boldsymbol{x})$ and $p_\mathbb{C}(\boldsymbol{x}) = p_r(\boldsymbol{x}) + ip_i(\boldsymbol{x})$ are complex-valued function of space. For a nonlinear viscoelastic material such as soft tissue, the presence of a macro-deformation $\boldsymbol{U}$ will affect the wave propagation, leading to an apparent variation of the mechanical properties of the material, and must be accounted for in the equations of motion. Under the assumption that the micro-deformation produced by the low frequency low amplitude waves normally employed in MRE is much smaller than the pre-applied macro-deformation: $\boldsymbol{u}_\varepsilon \ll \boldsymbol{U}$, the former can be regarded as a perturbation of the latter. As a consequence, the combination of the micro- and macro-deformation field and of their associated hydrostatic pressure is given, in the time domain I, by $\boldsymbol{u} = \boldsymbol{U} + \boldsymbol{u}_\varepsilon$ and $p = P + p_\varepsilon$
Here we will use perturbation theory to analytically develop a set of equations governing low amplitude wave propagation in a deformed nonlinear viscoelastic medium, starting from the perturbed version of the equations of motion

$$\rho J(\boldsymbol{U} + \boldsymbol{u}_\varepsilon)\left(\frac{\partial^2 \boldsymbol{U}}{\partial t^2} + \frac{\partial^2 \boldsymbol{u}_\varepsilon}{\partial t^2}\right) - \nabla_X \cdot \boldsymbol{P}(\boldsymbol{U} + \boldsymbol{u}_\varepsilon) = 0 \tag{2.39a}$$

$$J(\boldsymbol{U} + \boldsymbol{u}_\varepsilon) - 1 = 0 \tag{2.39b}$$

or, more compactly

$$\rho J(\boldsymbol{u})\frac{\partial^2 \boldsymbol{u}}{\partial t^2} - \nabla_X \cdot \boldsymbol{P}(\boldsymbol{u}) = 0 \tag{2.40a}$$

$$J(\boldsymbol{u}) - 1 = 0 \tag{2.40b}$$

where $\boldsymbol{u}$ and p are defined in the following way

$$\boldsymbol{u}(\boldsymbol{X}, t) = \begin{cases} \boldsymbol{U}(\boldsymbol{X}, t), & t \in [0, T] \backslash I \\ \boldsymbol{U}(\boldsymbol{X}, t) + \boldsymbol{u}_\varepsilon(\boldsymbol{X}, t), & t \in I \end{cases} \tag{2.41a}$$

$$p(\boldsymbol{X}, t) = \begin{cases} P(\boldsymbol{X}, t), & t \in [0, T] \backslash I \\ P(\boldsymbol{X}, t) + p_\varepsilon(\boldsymbol{X}, t), & t \in I \end{cases} \tag{2.41b}$$

A linearisation of these equations can be obtained through the use of directional derivative [163] for a function f of $\boldsymbol{U}$ in the direction of $\boldsymbol{u}_\varepsilon$:

$$D[f][\boldsymbol{u}_\varepsilon] = \lim_{h \to 0} \frac{f(\boldsymbol{U} + h\boldsymbol{u}_\varepsilon) - f(\boldsymbol{U})}{h} \tag{2.42}$$

where h is a parameter used to scale the increment along $\boldsymbol{u}_\varepsilon$.
The linearisation of the perturbed PK1, $\boldsymbol{P}(\boldsymbol{U} + \boldsymbol{u}_\varepsilon)$, and of the Jacobian of the deformation, $J(\boldsymbol{U} + \boldsymbol{u}_\varepsilon)$, is carried out in Appendix C and returns the following expressions:

$$\boldsymbol{P}(\boldsymbol{U} + \boldsymbol{u}_\varepsilon) \approx \boldsymbol{P}(\boldsymbol{U}) + \nabla_F \boldsymbol{P}(\boldsymbol{U}) : \nabla_X \boldsymbol{u}_\varepsilon + \nabla_{\frac{\partial F}{\partial t}} \boldsymbol{P}(\boldsymbol{U}) : \nabla_X \frac{\partial \boldsymbol{u}_\varepsilon}{\partial t} + p_\varepsilon J(\boldsymbol{U}) \boldsymbol{F}^{-T} \tag{2.43a}$$

$$J(\boldsymbol{U} + \boldsymbol{u}_\varepsilon) \approx J(\boldsymbol{U}) \tag{2.43b}$$

which lead to a new expression of the equations of motion:

$$\rho \left(J + J\nabla_{\boldsymbol{x}} \cdot \boldsymbol{u}_\varepsilon\right) \left(\frac{\partial^2 \boldsymbol{U}_\varepsilon}{\partial t^2} + \frac{\partial^2 \boldsymbol{u}_\varepsilon}{\partial t^2}\right) - \nabla_X \cdot \left(\boldsymbol{P} + \nabla_F \boldsymbol{P} : \nabla_X \boldsymbol{u}_\varepsilon + \nabla_{\frac{\partial F}{\partial t}} \boldsymbol{P} : \nabla_X \frac{\partial \boldsymbol{u}_\varepsilon}{\partial t} + p_\varepsilon J \boldsymbol{F}^{-T}\right) = 0 \tag{2.44a}$$

$$J\nabla_{\boldsymbol{x}} \cdot \boldsymbol{u}_\varepsilon = 0 \tag{2.44b}$$

where the dependence on $\boldsymbol{U}$ is implied. After rearranging, Eq.2.44 become

$$\left(\rho J \frac{\partial^2 \boldsymbol{U}}{\partial t^2} - \nabla_X \cdot \boldsymbol{P}\right) + \left(\rho J \nabla_{\boldsymbol{x}} \cdot \boldsymbol{u}_\varepsilon \left(\frac{\partial^2 \boldsymbol{U}}{\partial t^2} + \frac{\partial^2 \boldsymbol{u}_\varepsilon}{\partial t^2}\right)\right) + \left(\rho J \frac{\partial^2 \boldsymbol{u}_\varepsilon}{\partial t^2} - \nabla_X \cdot \left(\nabla_F \boldsymbol{P} : \nabla_X \boldsymbol{u}_\varepsilon + \nabla_{\frac{\partial F}{\partial t}} \boldsymbol{P} : \nabla_X \frac{\partial \boldsymbol{u}_\varepsilon}{\partial t} + p_\varepsilon J \boldsymbol{F}^{-T}\right)\right) = 0 \tag{2.45a}$$

$$J\nabla_{\boldsymbol{x}} \cdot \boldsymbol{u}_\varepsilon = 0 \tag{2.45b}$$

The first term in parentheses in Eq.2.45a vanishes as it represents the equilibrium equation in the unperturbed case (see Eq.2.37a), and so does the second term in parentheses, as $J\nabla_{\boldsymbol{x}} \cdot \boldsymbol{u}_\varepsilon = 0$ from Eq2.45b. The final system of equations of motion is therefore given by

$$\rho J \frac{\partial^2 \boldsymbol{u}_\varepsilon}{\partial t^2} - \nabla_X \cdot \left(\nabla_{\boldsymbol{F}} \boldsymbol{P} : \nabla_X \boldsymbol{u}_\varepsilon + \nabla_{\frac{\partial \boldsymbol{F}}{\partial t}} \boldsymbol{P} : \nabla_X \frac{\partial \boldsymbol{u}_\varepsilon}{\partial t} + p_\varepsilon J \boldsymbol{F}^{-T} \right) = 0 \tag{2.46a}$$

$$J\nabla_{\boldsymbol{x}} \cdot \boldsymbol{u}_\varepsilon = 0 \tag{2.46b}$$

Using the equivalences $(\nabla_X \mathcal{A})\boldsymbol{F}^{-1} = \nabla_{\boldsymbol{x}} \mathcal{A}$ and $\nabla_X \cdot \left(J\mathcal{A}\boldsymbol{F}^{-T} \right) = \nabla_{\boldsymbol{x}} \cdot \mathcal{A}$, and the property of the tensor contraction, $\mathcal{A} : \mathcal{B}\boldsymbol{F} = \mathcal{A}\boldsymbol{F}^T : \mathcal{B}$, we can transform the derivatives calculated in the above equation in the reference state Ω_0 into derivatives in the current configuration Ω, obtaining the final linearised version of the perturbed Cauchy momentum equation and of the equation of continuity for a viscoelastic material:

$$\rho \frac{\partial^2 \boldsymbol{u}_\varepsilon}{\partial t^2} - \nabla_{\boldsymbol{x}} \cdot \left(\boldsymbol{C} : \nabla_{\boldsymbol{x}} \boldsymbol{u}_\varepsilon + \boldsymbol{\mathcal{V}} : \nabla_{\boldsymbol{x}} \frac{\partial \boldsymbol{u}_\varepsilon}{\partial t} + p_\varepsilon \mathbb{1} \right) = 0 \tag{2.47a}$$

$$\nabla_{\boldsymbol{x}} \cdot \boldsymbol{u}_\varepsilon = 0 \tag{2.47b}$$

The fourth-order stiffness $\boldsymbol{C}$ and viscosity $\boldsymbol{\nu}$ tensor are given by

$$\boldsymbol{C} = \frac{1}{J} \nabla_{\boldsymbol{F}} \boldsymbol{P} \boldsymbol{F}^T \boldsymbol{F}^T \qquad \text{or} \qquad C_{ijkl} = \frac{1}{J} \frac{\partial P_{is}}{\partial F_{kn}} F_{ln} F_{js} \tag{2.48}$$

and

$$\boldsymbol{\mathcal{V}} = \frac{1}{J} \nabla_{\frac{\partial \boldsymbol{F}}{\partial t}} \boldsymbol{P} \boldsymbol{F}^T \boldsymbol{F}^T \qquad \text{or} \qquad \mathcal{V}_{ijkl} = \frac{1}{J} \frac{\partial P_{is}}{\partial (\partial F_{kn}/\partial t)} F_{ln} F_{js} \tag{2.49}$$

Substituting the periodic motion generated at steady state by the propagating waves (Eq.2.38) into Eq.2.47, we obtain a new set of equations describing the propagation of elastic waves through a macroscopically deformed viscoelastic object:

$$\begin{aligned} &\rho\omega^2 \boldsymbol{u}_{\mathbb{C}} + \nabla_{\boldsymbol{x}} \cdot (\boldsymbol{C} : \nabla_{\boldsymbol{x}} \boldsymbol{u}_{\mathbb{C}} + \boldsymbol{\mathcal{V}} : \nabla_{\boldsymbol{x}} (i\omega \boldsymbol{u}_{\mathbb{C}}) + p_{\mathbb{C}} \mathbb{1}) = \\ &\rho\omega^2 \boldsymbol{u}_{\mathbb{C}} + \nabla_{\boldsymbol{x}} \cdot ((\boldsymbol{C} + i\omega \boldsymbol{\mathcal{V}}) : \nabla_{\boldsymbol{x}} \boldsymbol{u}_{\mathbb{C}} + p_{\mathbb{C}} \mathbb{1}) = \\ &\rho\omega^2 \boldsymbol{u}_{\mathbb{C}} + \nabla_{\boldsymbol{x}} \cdot ((\boldsymbol{\mathcal{G}}' + i\boldsymbol{\mathcal{G}}'') : \nabla_{\boldsymbol{x}} \boldsymbol{u}_{\mathbb{C}} + p_{\mathbb{C}} \mathbb{1}) = 0 \end{aligned} \tag{2.50a}$$

$$\nabla_{\boldsymbol{x}} \cdot \boldsymbol{u}_{\mathbb{C}} = 0 \tag{2.50b}$$

Here, Eq.2.50b indicates the incompressibility of the material subjected to the deformation $\boldsymbol{u}_{\mathbb{C}}$, while the wave equation 2.50a determines the dynamic behaviour of the propagating shear waves through the real $\boldsymbol{\mathcal{G}}' = \boldsymbol{C}$ and imaginary $\boldsymbol{\mathcal{G}}'' = \omega \boldsymbol{\mathcal{V}}$ components of the complex

stiffness tensor $\boldsymbol{\mathcal{G}}^* = \boldsymbol{\mathcal{G}}' + i\boldsymbol{\mathcal{G}}''$.
For a viscoelastic material described by a hyperelastic constitutive equation, we can introduce a strain energy density function $W = W(\boldsymbol{F}, \partial_t \boldsymbol{F}, p)$ that will permit us to establish the nonlinear relationship between the stress tensor $\boldsymbol{P}$ and the deformation gradient $\boldsymbol{F}$, hence defining an analytical formulation for both $\boldsymbol{\mathcal{G}}'$ and $\boldsymbol{\mathcal{G}}''$. An overview of the hyperelastic constitutive equations reported in the literature to model soft tissue rheology will be provided in the next section of this chapter. Based on the choice of a specific strain energy density function, an analytical expression relating the PK1 stress tensor, as well as PK2 and the Cauchy stress tensor, to the applied deformation will be developed.

While the variation in the mechanical properties of the material associated to the macro-deformation in contained in $\boldsymbol{\mathcal{G}}'$ and $\boldsymbol{\mathcal{G}}''$, the micro-displacement produced by the waves is embodied in $\nabla_{\boldsymbol{x}} \boldsymbol{u}_{\mathbb{C}}$; the double contraction with the gradient of the harmonic micro-deformation provides a measurement of the apparent storage and loss shear modulus, G' and G'' as reconstructed through MRE, which represents the component or the combination of components of the two fourth-order elasticity tensors probed by the propagating shear waves. This effectively corresponds to solving the wave equation in a softer/stiffer medium, depending on the direction of propagation of the shear waves with respect to that of the deformation field. This topic will be treated in Section 2.4, where the apparent shift in shear modulus caused by an axisymmetric deformation of a hyperelastic thick-walled hollow sphere, used as an idealisation of peri-tumoural tissue, will be investigated. For the analytical framework developed in this section, we have chosen to focus only on the expression of the apparent changes generated by the spherical deformation on the stiffness modulus $\boldsymbol{\mathcal{G}}'$, hence assuming a purely elastic material. This assumption will be recalled and discussed in the following chapters, which will show that, despite the fact that this simplification may not be ideal to capture the viscous properties of soft tissue, it can be regarded as a reasonably accurate model of the viscoelastic behaviour of the material employed to experimentally validate the developed analytical formulation.

2.3. Constitutive Relationships for Soft Tissue

As mentioned previously, in Section 2.1 a definition of the stress and strain tensors has been given, while Section 2.2 has highlighted, starting from the equations of motion governing wave propagation in a nonlinear viscoelastic material, the dependence of both components of the dynamic shear modulus on the applied macro-deformation; nevertheless a constitutive law that relates stress with strain still needs to be defined. The empirical formulation of such relationships changes with different materials and must be independent of the chosen coordinate system. The intrinsic nonlinear mechanical response of soft tissue has often been modelled using hyperelastic constitutive laws [45], which assume the existence of a strain density energy function that depends on the deformation gradient

associated to the deformation: $W = W(\boldsymbol{F})$. To maintain it independent of any rigid rotation in the current configuration, W is often expressed as a function of either the right or left Cauchy-Green tensor. For isotropic materials, the strain energy function depends only on the first three invariants of $\boldsymbol{C}$:

$$W = W(I_{\mathrm{C}}, II_{\mathrm{C}}, III_{\mathrm{C}}) \tag{2.51}$$

Under the further assumption of incompressibility, III_{C} keeps spatially constant and equal to 1, making W only dependent on I_{C} and II_{C}.

Under the assumption of a purely elastic material, several hyperelastic models have been proposed in the literature to describe incompressible isotropic soft tissue, applied both in *ex vivo* tests and medical imaging techniques, and a recent study by Voutouri *et al.* (2014) on the modelling of the evolution of solid stress in tumours has underlined the crucial importance of the correct description of the mechanical properties of the surrounding soft tissue *in vivo* over those of the solid tumour itself [130]. The simplest hyperelastic constitutive law is Neo-Hookean, which is a function of only the first strain invariant I_{C} and is characterised by one single material parameter which represents the shear modulus.

$$W = C_1(I_{\mathrm{C}} - 3) \tag{2.52}$$

Despite being the most widely used constitutive equation for modelling soft tissue, this strain energy density function is not ideal to describe soft tissue nonlinearity, as it is effectively an extension of the elastic stress/strain relation to a larger deformations.
With a mathematical formulation similar to that of the Neo-Hookean model, polynomial constitutive laws in their incompressible form have largely been employed to approximate soft tissue rheology [57, 164, 165, 166].

$$W = \sum_{i,j=0}^{N} C_{ij}(I_{\mathrm{C}} - 3)^i + (II_{\mathrm{C}} - 3)^j \tag{2.53}$$

Here $C_{ij} \geq 0$ are the hyperelastic constraints determined empirically, while $C_{00} = 0$. The first two terms of Eq.2.53 return the popular Mooney-Rivlin model [167, 168]:

$$W = \frac{C_1}{2}(I_{\mathrm{C}} - 3) + \frac{C_2}{2}(II_{\mathrm{C}} - 3) \tag{2.54}$$

The Yeoh model has also been used in numerical studies on breast tissue [164] and, unlike the polynomial strain energy density functions, has the advantage of eliminating the dependence on the second strain invariant II_{C}, which has been reported to produce a

better prediction of tissue behaviour [164].

$$W = \sum_{i=0}^{3} C_{i0}(I_C - 3)^i \tag{2.55}$$

Exponential models have been suggested as optimal to describe certain kinds of soft tissue [169, 170, 171]. Furthermore, Krouskop *et al.* (1998) and Wellman *et al.* (1999) have reported that cancer tissue shows a more pronounced nonlinearity than benign tumours and healthy tissue in breast, highlighting the need for a strain energy density function capable of modelling a steeper stress increase with the applied strain [19, 50]. The Veronda-Westmann exponential constitutive law [52] was successfully used to model large soft tissue deformation for elastography techniques [172, 173].

$$W = \mu \left(\frac{e^{\gamma(I_C - 3) - 1}}{\gamma} - \frac{II_C - 3}{2} \right) \tag{2.56}$$

Among the reasons behind the popularity of the Veronda-Westmann law is the small number of material parameters involved. Here, the material parameter μ denotes the shear modulus of the material in the absence of strain, while γ determines its nonlinearity. Fung's exponential strain energy density function, based on the single invariant IC, was also proposed in the literature as an accurate model to describe soft tissue subjected to large deformations [45]. The constitutive equation is given by

$$W = q + c(e^Q - 1) \tag{2.57}$$

where $q = a_{ijkl}\mathbf{E}_{ij}\mathbf{E}_{kl}$, $Q = b_{ijkl}\mathbf{E}_{ij}\mathbf{E}_{kl}$ and c are the material parameters and $\boldsymbol{E}$ is the Green-Lagrange strain tensor. This model, developed for preconditioned incompressible soft tissues, can be simplified under isotropic assumption:

$$W = a(I_C - 3) + c\left(e^{b(I_C - 3)} - 1\right) \tag{2.58}$$

where a, b and c are constants.
Alternatively, logarithmic formulations can also be found [174].
The Ogden power law [175] has also been a popular choice to fit isotropic tissues:

$$W(\lambda_1, \lambda_2, \lambda_3) = \sum_{r=1}^{N} \frac{\mu_r}{\alpha_r} \left(\lambda_1^{\alpha_r} + \lambda_2^{\alpha_r} + \lambda_3^{\alpha_r} - 3 \right) \tag{2.59}$$

Unlike the other presented models, in this case the strain energy density function depends directly on the principal stretches λ_i instead of the invariants. N, μ_r and α_r are the material

parameters to be determined from the experiments. For particular values of the constant α, the Ogden model can be reduced into Neo-Hookean and Mooney-Rivlin form.

For reasons that will become more apparent in the following sections of this chapter and in the next chapters, in this study we have used a modified version of the Mooney-Rivlin equation of the form

$$W = \frac{1}{2}\mu_1(I_{\hat{C}} - 3) + \frac{1}{2}\mu_2(II_{\hat{C}} - 3)^2 \tag{2.60}$$

This constitutive law was successfully employed to model the rheological behaviour of PVA phantoms [86], however we expected it to provide an accurate representation of soft tissue rheology as well. With respect to the conventional Mooney-Rivlin strain energy density function presented in Eq.2.54, here the quadratic dependence on the second unimodular invariant $II_{\hat{C}}$ should help to better capture the nonlinear stress/strain response of soft tissue subjected to the deformations generated by a pressurised tumour. Rheological tests carried out on PVC phantoms, built to reproduce the viscoelastic properties of soft tissue, will also show the ability of this modified Mooney-Rivlin law to model the mechanical behaviour of the employed material, as presented in Chapter 5. Finally, the use of a polynomial law, with respect to an exponential one, can lead to a simpler mathematical formulation, which is presented in the next section of this chapter.

2.3.1. Analytical Formulation of Stress Tensors

The use of a governing strain energy density function which is a direct function of the deformation gradient or of its invariants allows us to introduce the following models to calculate PK1 and PK2 directly from $W(I_C, II_C)$:

$$\boldsymbol{P} = \frac{\partial W}{\partial \boldsymbol{F}} \qquad \text{and} \qquad \boldsymbol{S} = 2\frac{\partial W}{\partial \boldsymbol{C}} \tag{2.61}$$

Eq.2.61 can be expanded, so that the dependency on the invariants is explicitly written. For simplicity, we can use the tensor decomposition presented in Eq.2.11-2.13 and express the stress tensors in terms of the unimodular invariants $I_{\hat{C}}$ and $II_{\hat{C}}$ contained in the incompressible strain energy density function. PK1 can be expressed as

$$\begin{aligned}\boldsymbol{P} &= \frac{\partial W(I_{\hat{C}}, II_{\hat{C}})}{\partial \boldsymbol{F}} + pJ\boldsymbol{F}^{-T} = \frac{\partial W}{\partial I_{\hat{C}}}\frac{\partial I_{\hat{C}}}{\partial \boldsymbol{F}} + \frac{\partial W}{\partial II_{\hat{C}}}\frac{\partial II_{\hat{C}}}{\partial \boldsymbol{F}} + pJ\boldsymbol{F}^{-T} = \\ &= \underbrace{-2\left[\frac{\partial W}{\partial I_{\hat{C}}}\frac{I_{\hat{C}}}{3} + \frac{\partial W}{\partial II_{\hat{C}}}\frac{2II_{\hat{C}}}{3}\right]\boldsymbol{F}^{-T}}_{①} + \underbrace{2J^{-\frac{2}{3}}\left[\frac{\partial W}{\partial I_{\hat{C}}} + \frac{\partial W}{\partial II_{\hat{C}}}I_{\hat{C}}\right]\boldsymbol{F}}_{②} - \underbrace{2\left[\frac{\partial W}{\partial II_{\hat{C}}}J^{-\frac{4}{3}}\boldsymbol{F}\boldsymbol{C}\right]}_{③} + pJ\boldsymbol{F}^{-T}\end{aligned} \tag{2.62}$$

where the numbering ①, ②, ③ have been introduced for later use.
PK2 is instead given by

$$\begin{aligned}\boldsymbol{S} &= 2\frac{\partial W}{\partial \boldsymbol{C}} + pJ\boldsymbol{C}^{-1} = \boldsymbol{F}^{-1}\boldsymbol{P} = \\ &= 2\frac{\partial W}{\partial I_{\hat{\mathrm{C}}}} J^{-\frac{2}{3}} \left[-\frac{I_{\mathrm{C}}}{3}\boldsymbol{C}^{-1} + \mathbb{1}\right] + 2\frac{\partial W}{\partial II_{\hat{\mathrm{C}}}} J^{-\frac{4}{3}} \left[-\frac{2II_{\mathrm{C}}}{3}\boldsymbol{C}^{-1} + I_{\mathrm{C}}\mathbb{1} - \boldsymbol{C}\right] + pJ\boldsymbol{C}^{-1}\end{aligned} \tag{2.63}$$

Finally, the Cauchy stress tensor is equal to

$$\begin{aligned}\boldsymbol{\sigma} &= J^{-1}\boldsymbol{F}\boldsymbol{S}\boldsymbol{F}^{T} = \\ &= 2\frac{\partial W}{\partial I_{\hat{\mathrm{C}}}} J^{-\frac{5}{3}} \left[-\frac{I_{\mathrm{C}}}{3}\mathbb{1} + \boldsymbol{B}\right] + 2\frac{\partial W}{\partial II_{\hat{\mathrm{C}}}} J^{-\frac{7}{3}} \left[-\frac{2II_{\mathrm{C}}}{3}\mathbb{1} + I_{\mathrm{C}}\boldsymbol{B} - \boldsymbol{B}^{2}\right] + p\mathbb{1}\end{aligned} \tag{2.64}$$

where the last term accounts for the hydrostatic pressure.

2.3.2. Derivation of Linearised Shear Modulus

The intrinsic shear modulus of the material is usually derived from considering a simple shear deformation and the engineering shear strain. A simple shear deformation, described by

$$\begin{aligned} x_1 &= X_1 + aX_2 \\ x_2 &= X_2 \\ x_3 &= X_3 \end{aligned}$$

where $a << 1$ assuming small strain, leads to

$$\boldsymbol{F} = \begin{bmatrix} 1 & a & 0 \\ 0 & 1 & 0 \\ 0 & 0 & 1 \end{bmatrix} \qquad \boldsymbol{B} = \begin{bmatrix} 1+a^2 & a & 0 \\ a & 1 & 0 \\ 0 & 0 & 1 \end{bmatrix} \qquad \boldsymbol{B}^{-1} = \begin{bmatrix} 1 & -a & 0 \\ -a & 1+a^2 & 0 \\ 0 & 0 & 1 \end{bmatrix} \tag{2.65}$$

In the case of a hyperelastic material, we can rewrite the Cauchy stress tensor derived in Eq.2.64 replacing $\boldsymbol{B}^2$ using the Cayley-Hamilton theorem

$$\boldsymbol{B}^3 - I_{\mathrm{C}}\boldsymbol{B}^2 + II_{\mathrm{C}}\boldsymbol{B} - III_{\mathrm{C}}\boldsymbol{I} = \boldsymbol{0}, \qquad \text{or} \qquad \boldsymbol{B}^2 = I_{\mathrm{C}}\boldsymbol{B} - II_{\mathrm{C}}\boldsymbol{I} + III_{\mathrm{C}}\boldsymbol{B}^{-1}$$

to produce an alternative expression in terms of $\boldsymbol{B}^{-1}$

$$\boldsymbol{\sigma}^{\flat} = 2\frac{\partial W}{\partial I_{\hat{\mathrm{C}}}} J^{-\frac{5}{3}} \left[-\frac{I_{\mathrm{C}}}{3}\mathbb{1} + \boldsymbol{B}\right] + 2\frac{\partial W}{\partial II_{\hat{\mathrm{C}}}} J^{-\frac{7}{3}} \left[\frac{II_{\mathrm{C}}}{3}\mathbb{1} - J^2\boldsymbol{B}^{-1}\right] + p\mathbb{1}$$

It is further possible to produce an alternative definition by absorbing all terms multiplied by $\mathbb{1}$ into p, which is then renamed $\tilde{p}$, leaving

$$\boldsymbol{\sigma}^{\natural} = 2\left[\frac{\partial W}{\partial I_{\hat{\mathrm{C}}}} J^{-\frac{5}{3}}\boldsymbol{B} - \frac{\partial W}{\partial II_{\hat{\mathrm{C}}}} J^{-\frac{1}{3}}\boldsymbol{B}^{-1}\right] + \tilde{p}\mathbb{1} \tag{2.66}$$

which, using Eq.??yields the shear stress component

$$\begin{aligned}\sigma_{12} &= 2\left[J^{-\frac{5}{3}}\frac{\partial W}{\partial I_{\hat{\mathrm{C}}}} B_{12} - J^{-\frac{1}{3}}\frac{\partial W}{\partial II_{\hat{\mathrm{C}}}} B_{12}^{-1}\right] = \\ &= 2\left[\frac{\partial W}{\partial I_{\hat{\mathrm{C}}}} a + \frac{\partial W}{\partial II_{\hat{\mathrm{C}}}} a\right]\end{aligned}$$

The shear strain can be calculated from the Green strain tensor in Eq.2.2

$$\boldsymbol{C} = \begin{bmatrix} 1 & a & 0 \\ a & a^2+1 & 0 \\ 0 & 0 & 1 \end{bmatrix} \qquad \boldsymbol{E} = \frac{1}{2}\begin{bmatrix} 0 & a & 0 \\ a & a^2 & 0 \\ 0 & 0 & 0 \end{bmatrix} = \begin{bmatrix} \gamma_{11} & \frac{\gamma_{12}}{2} & \frac{\gamma_{13}}{2} \\ \frac{\gamma_{21}}{2} & \gamma_{22} & \frac{\gamma_{23}}{2} \\ \frac{\gamma_{31}}{2} & \frac{\gamma_{32}}{2} & \gamma_{33} \end{bmatrix} \tag{2.67}$$

Therefore, the linearised shear modulus is

$$\mu = \lim_{a\longrightarrow 0}\frac{\sigma_{12}}{\gamma_{12}} = \lim_{a\longrightarrow 0} 2\left(\frac{\partial W}{\partial I_{\hat{\mathrm{C}}}} + \frac{\partial W}{\partial II_{\hat{\mathrm{C}}}}\right) \tag{2.68}$$

2.4. Wave Propagation in Thick-Shelled Sphere

2.4.1. Thick-shelled Sphere Inflation: Kinematics

To find the Cauchy stress generated by an expanding tumour onto the surrounding tissue, we consider an idealisation of a thick-walled sphere made of an incompressible isotropic hyperelastic material [176], a cross section of which is shown below

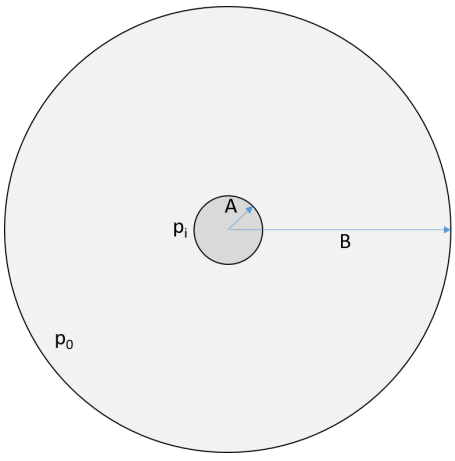

where

$$A \leq R \leq B \qquad 0 \leq \Theta \leq 2\pi \qquad 0 \leq \Phi \leq \pi$$
$$a \leq r \leq b \qquad 0 \leq \theta \leq 2\pi \qquad 0 \leq \varphi \leq \pi$$

Here, denoting with $\boldsymbol{X} = \boldsymbol{X}(R, \Theta, \Phi)$ and $\boldsymbol{x} = \boldsymbol{x}(r, \theta, \varphi)$ the location of a material particle in the reference and current configuration, we can describe a spherical deformation state with

$$\boldsymbol{F} = \begin{bmatrix} \frac{dr}{dR} & & \\ & \frac{r}{R} & \\ & & \frac{r}{R} \end{bmatrix} \tag{2.69}$$

where r is a pure function of R at each point and $\theta = \Theta$ and $\varphi = \Phi$ due to symmetry. We further assume that the tissue is incompressible, which leads to:

$$R^3 - r^3 = A^3 - a^3 = B^3 - b^3 \tag{2.70}$$

thus yielding $\frac{dr}{dR} = \frac{R^2}{r^2}$ such that

$$\boldsymbol{F} = \begin{bmatrix} \frac{R^2}{r^2} & & \\ & \frac{r}{R} & \\ & & \frac{r}{R} \end{bmatrix} \qquad \boldsymbol{B} = \boldsymbol{C} = \begin{bmatrix} \frac{R^4}{r^4} & & \\ & \frac{r^2}{R^2} & \\ & & \frac{r^2}{R^2} \end{bmatrix} \qquad \boldsymbol{B}^2 = \boldsymbol{C}^2 = \begin{bmatrix} \frac{R^8}{r^8} & & \\ & \frac{r^4}{R^4} & \\ & & \frac{r^4}{R^4} \end{bmatrix} \tag{2.71}$$

2.4.2. Inflation Pressure

The Cauchy stress tensor for an incompressible isotropic hyperelastic material is given in Eq.2.64. To evaluate the radial stress component, i.e. the inflating pressure, we apply the Cauchy equation 2.27, at equilibrium in the spherical coordinate system,

$$\frac{d\sigma_{rr}}{dr} + 2\frac{\sigma_{rr} - \sigma_{\theta\theta}}{r} = 0 \tag{2.72}$$

to Eq.2.64 and use Eq.2.71, yielding

$$\frac{d\sigma_{rr}}{dr} = -\frac{4}{rJ}\left[J^{-\frac{5}{3}}\left(\frac{\partial W}{\partial I_{\hat{\mathrm{C}}}} + I_{\hat{\mathrm{C}}}\frac{\partial W}{\partial II_{\hat{\mathrm{C}}}}\right)\left(\frac{R^4}{r^4} - \frac{r^2}{R^2}\right) - J^{-\frac{7}{3}}\frac{\partial W}{\partial II_{\hat{\mathrm{C}}}}\left(\frac{R^8}{r^8} - \frac{r^4}{R^4}\right)\right] \tag{2.73}$$

which can be integrated between $r \in [a, b]$ using the boundary conditions $\sigma_{rr}(r = a) = p_i$ and $\sigma_{rr}(r = b) = 0$, where p_i represents the inflating pressure exerted by the tumour on

the inner surface of the tissue:

$$p_i = \int_a^b \frac{d\sigma_{rr}}{dr} dr \tag{2.74}$$

Evaluating this integral requires the prescription of a specific constitutive law. In the following sections a modified Mooney-Rivlin formulation is considered.

Modified Mooney-Rivlin Law

The constitutive law that we chose to employ is of the form

$$W = \frac{1}{2}\mu_1(I_{\hat{\mathrm{C}}} - 3) + \frac{1}{2}\mu_2(II_{\hat{\mathrm{C}}} - 3)^2 \tag{2.75}$$

which yields

$$\frac{\partial W}{\partial I_{\hat{\mathrm{C}}}} = \frac{\mu_1}{2} \tag{2.76}$$

$$\frac{\partial W}{\partial II_{\hat{\mathrm{C}}}} = \mu_2(II_{\hat{\mathrm{C}}} - 3) \tag{2.77}$$

Applying these derivatives to Eq.2.74, we get

$$p_i = \frac{R}{5r^4}\Bigg[-5\left(a^3 - A^3\right)(\mu_1 + 4\mu_2) + 25(\mu_1 + 4\mu_2)r^3 - 8\mu_2\frac{(a^3 - A^3)r^6}{R^6} - 28\mu_2\frac{r^6}{R^3} + 60\mu_2\frac{r^2(a^3 - A^3 + r^3)}{R^2}\Bigg]_{r=a}^{r=b} \tag{2.78}$$

where, following Eq.2.70, R is a function of r:

$$R = (A^3 - a^3 + r^3)^{1/3}$$

An example curve of the pressure-radial stretch (a/A) relation is shown in Fig. 2.1. Here we show that, in the absence of μ_2, the modified Mooney-Rivlin constitutive law is reduced to the simpler Neo-Hookean case and the parameter μ_1 works as a scaler of the pressure generated by the inflation, but does not modify its trend. In this case, using Eq.2.68, the linearised shear modulus is given by $\mu_{NH} = \mu_1$. On the other hand, μ_2 acts on the shape of the pressure-radius curve, as well as on its behaviour at higher levels of inflation. This parameter however does not play a role in the definition of the linearised shear modulus in the modified Mooney-Rivlin case, and $\mu_{MR} = \mu_1$ like in the Neo-Hookean case.

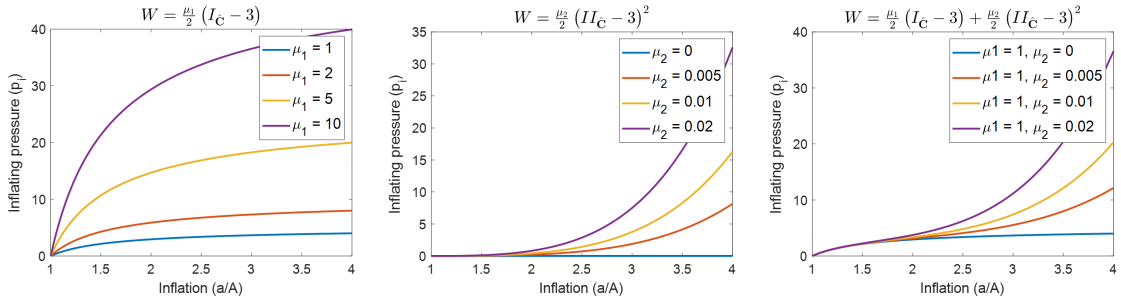

Figure 2.1.: Example family of curves representing the inflating pressure obtained from the linear (left) and quadratic (centre) term of the modified Mooney-Rivlin law employed. The combined contributions generate a characteristic family of S-shaped curves (right).

Hydrostatic Pressure

In order to obtain a complete analytic expression for the Cauchy stress tensor, we must calculate the hydrostatic pressure p. This can be derived by comparing the two expressions for σ_{rr} given by Eq.2.64 and Eq.2.74, yielding

$$p = \frac{\mu_1 R^6(-10r^6 + 9r^4R^2 + R^6) + \mu_2(r-R)^2(r+R)^2(r^2+2R^2)(5r^6 + 9r^2R^4 + 34R^6)}{6r^4R^8} \tag{2.79}$$

As an example, the hydrostatic pressure distribution away from the inner surface is shown in Fig. 2.2.

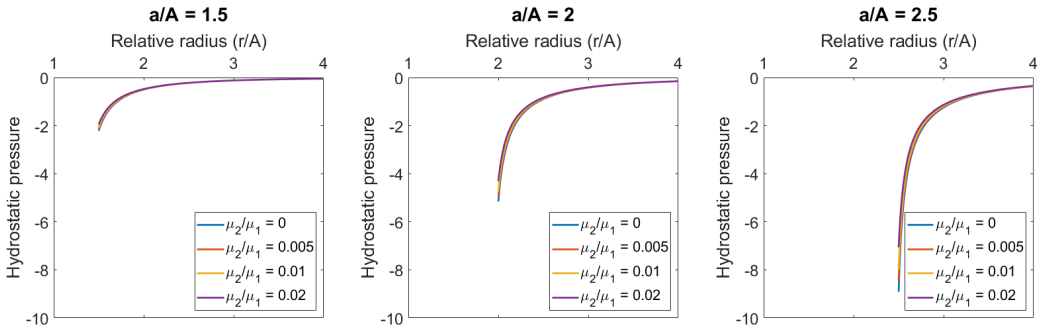

Figure 2.2.: The magnitude of the hydrostatic pressure is directly proportional to the radial stretch (a/A), fading to zero while moving away from the inner surface. Given a constant $\mu_1 = 1$, the second parameter, μ_2, has a relevant impact on the model at the interface between the inclusion and the surrounding material, however it does not affect the curve trend.

2.4.3. Nonlinear Wave Propagation

We have seen in Section 2.2 that the wave propagation in a nonlinear hyperelastic material is given by Eq.2.47a, obtained superimposing small-amplitude elastic waves on top of a macroscopic deformation. As shown in Eq.2.48, the derivation of the stiffness tensor, $\boldsymbol{C}$ or $\boldsymbol{\mathcal{G}}'$, requires the derivative $\partial P_{is}/\partial F_{kn}$ to be evaluated. Below, we evaluate

term-by-term the derivatives of PK1 from Eq.2.62 for the modified Mooney-Rivlin law:

$$\frac{\partial W}{\partial I_{\hat{\mathrm{C}}}} = \frac{\mu_1}{2}, \qquad \frac{\partial}{\partial F_{kn}}\left(\frac{\partial W}{\partial I_{\hat{\mathrm{C}}}}\right) = 0 \tag{2.80}$$

$$\frac{\partial J^c}{\partial F_{kn}} = cJ^c F^{-1}_{nk} \tag{2.81}$$

$$\frac{\partial I_{\mathrm{C}}}{\partial F_{kn}} = 2F_{kn} \tag{2.82}$$

$$\frac{\partial I_{\hat{\mathrm{C}}}}{\partial F_{kn}} = -\frac{2}{3} I_{\hat{\mathrm{C}}} F^{-1}_{nk} + J^{-\frac{2}{3}} \frac{\partial I_{\mathrm{C}}}{\partial F_{kn}} \tag{2.83}$$

$$\frac{\partial W}{\partial II_{\hat{\mathrm{C}}}} = \mu_2 (II_{\hat{\mathrm{C}}} - 3), \qquad \frac{\partial}{\partial F_{kn}}\left(\frac{\partial W}{\partial II_{\hat{\mathrm{C}}}}\right) = \mu_2 \frac{\partial II_{\hat{\mathrm{C}}}}{\partial F_{kn}} \tag{2.84}$$

$$\frac{\partial II_{\hat{\mathrm{C}}}}{\partial F_{kn}} = \frac{\partial}{\partial F_{kn}}\left(J^{-\frac{4}{3}} II_{\mathrm{C}}\right) = J^{-\frac{4}{3}} \frac{\partial II_{\hat{\mathrm{C}}}}{\partial F_{kn}} - \frac{4}{3} F^{-1}_{nk} II_{\hat{\mathrm{C}}} \tag{2.85}$$

$$\frac{\partial II_{\mathrm{C}}}{\partial F_{kn}} = 2I_{\mathrm{C}} F_{kn} - 2F_{na} F_{an} F_{nk} \tag{2.86}$$

$$\frac{\partial (FC)_{is}}{\partial F_{kn}} = \delta_{ik} F_{bn} F_{bs} + F_{in} F_{ks} + \delta_{sn} F_{ia} F_{ka} \tag{2.87}$$

$$\frac{\partial F_{is}}{\partial F_{kn}} = \delta_{ik} \delta_{sn} \tag{2.88}$$

$$\frac{\partial F^{-1}_{si}}{\partial F_{kn}} = -F^{-1}_{ni} F^{-1}_{sk} \tag{2.89}$$

The derivatives of the three terms in brackets in Eq.2.62, i.e. ① ② and ③, are given by the following equations:

$$\frac{\partial}{\partial F_{kn}}\left(\frac{\partial W}{\partial I_{\hat{\mathrm{C}}}}\frac{I_{\hat{\mathrm{C}}}}{3} + \frac{\partial W}{\partial II_{\hat{\mathrm{C}}}}\frac{2II_{\hat{\mathrm{C}}}}{3}\right) = \qquad ①$$

$$= -\frac{\mu_1}{9} I_{\hat{\mathrm{C}}} F^{-1}_{nk} + \frac{\mu_1}{3} J^{-\frac{2}{3}} F_{kn} + \frac{2}{3}\left(J^{-\frac{4}{3}} \frac{\partial II_{\mathrm{C}}}{\partial F_{kn}} - \frac{4}{3} F^{-1}_{nk} II_{\hat{\mathrm{C}}}\right)\left[\mu_2 II_{\hat{\mathrm{C}}} + \frac{\partial W}{\partial II_{\hat{\mathrm{C}}}}\right] \tag{2.90}$$

$$\frac{\partial}{\partial F_{kn}}\left(J^{-\frac{2}{3}}\left(\frac{\partial W}{\partial I_{\hat{\mathrm{C}}}} + \frac{\partial W}{\partial II_{\hat{\mathrm{C}}}} I_{\hat{\mathrm{C}}}\right)\right) = \qquad ②$$

$$= -\frac{2}{3} J^{-\frac{2}{3}} F^{-1}_{nk}\left[\frac{\partial W}{\partial I_{\hat{\mathrm{C}}}} + \frac{\partial W}{\partial II_{\hat{\mathrm{C}}}} I_{\hat{\mathrm{C}}}\right] + \mu_2 J^{-2} I_{\hat{\mathrm{C}}}\left[\frac{\partial II_{\mathrm{C}}}{\partial F_{kn}} - \frac{4}{3} F^{-1}_{nk} II_{\mathrm{C}}\right] + J^{-\frac{4}{3}} \frac{\partial W}{\partial II_{\hat{\mathrm{C}}}}\left[\frac{\partial I_{\mathrm{C}}}{\partial F_{kn}} - \frac{2}{3} I_{\mathrm{C}} F^{-1}_{nk}\right] \tag{2.91}$$

$$\frac{\partial}{\partial F_{kn}}\left(\frac{\partial W}{\partial II_{\hat{\mathrm{C}}}} J^{-\frac{4}{3}} \mathbf{FC}\right) = \qquad ③$$

$$= \mu_2\left[J^{-\frac{4}{3}} \frac{\partial II_{\mathrm{C}}}{\partial F_{kn}} - \frac{4}{3} F^{-1}_{nk} II_{\hat{\mathrm{C}}}\right] J^{-\frac{4}{3}} (FC)_{is} - \frac{\partial W}{\partial II_{\hat{\mathrm{C}}}}\left[\frac{4}{3} J^{-\frac{4}{3}} F^{-1}_{nk}\right](FC)_{is} + \frac{\partial W}{\partial II_{\hat{\mathrm{C}}}} J^{-\frac{4}{3}}\left[\frac{\partial (FC)_{is}}{\partial F_{kn}}\right] \tag{2.92}$$

Using these results, finally the analytic expressions for $\boldsymbol{\mathcal{G}}'$ and the stress-like tensor $\boldsymbol{\mathcal{G}}' : \nabla_{\boldsymbol{x}} \boldsymbol{u}_\varepsilon$ have been derived. Given a plane-wave travelling through the object as shown in Fig. 2.3, we consider two sets of displacements found at the leading and peripheral interfaces of the inner sphere, such that a θ-polarised r-propagating wave is characterised by

$$\text{Ⓐ} \qquad \nabla \boldsymbol{u}_\varepsilon = \begin{bmatrix} 0 & 0 & 0 \\ \delta u & 0 & 0 \\ 0 & 0 & 0 \end{bmatrix} \tag{2.93}$$

and an r-polarised θ-propagating wave is described by

$$\text{Ⓑ} \qquad \nabla \boldsymbol{u}_\varepsilon = \begin{bmatrix} 0 & \delta u & 0 \\ 0 & 0 & 0 \\ 0 & 0 & 0 \end{bmatrix} \tag{2.94}$$

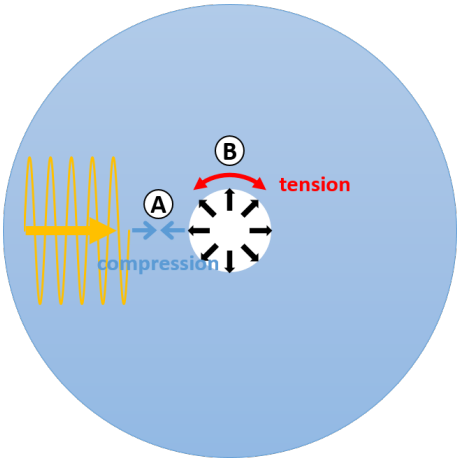

Figure 2.3.: Wave propagation through the thick-shelled sphere. Due to the local spherical coordinate orientation, at Ⓐ, the wave will appear as θ-polarised, travelling in the radial direction. At Ⓑ, the opposite is found.

The apparent shear modulus G' measured through MRE is then obtained through the double contraction between the stiffness tensor and the gradient of the wave micro-deformation, effectively quantifying the component of $\boldsymbol{\mathcal{G}}'$ sensed by the propagating waves. The apparent variation of G' relative to its intrinsic value, as a function of the relative radial position at different radial stretches, is plotted in Fig.2.4. As it shows, the apparent modulus softens when a compression is present in the propagating direction (case Ⓐ), and stiffens when tension is sensed (case Ⓑ). The factor by which the apparent modulus undergoes change is significantly larger in the latter case than in the former. However, the modelled curves are almost symmetrical on a logarithmic scale, especially at low deformations. This is true only for low μ_2 values, as, while the increase of this parameter leads to steeper trends in the case of radially-propagating waves, the opposite

happens in the case of compression, with the stiffness variation becoming less pronounced.

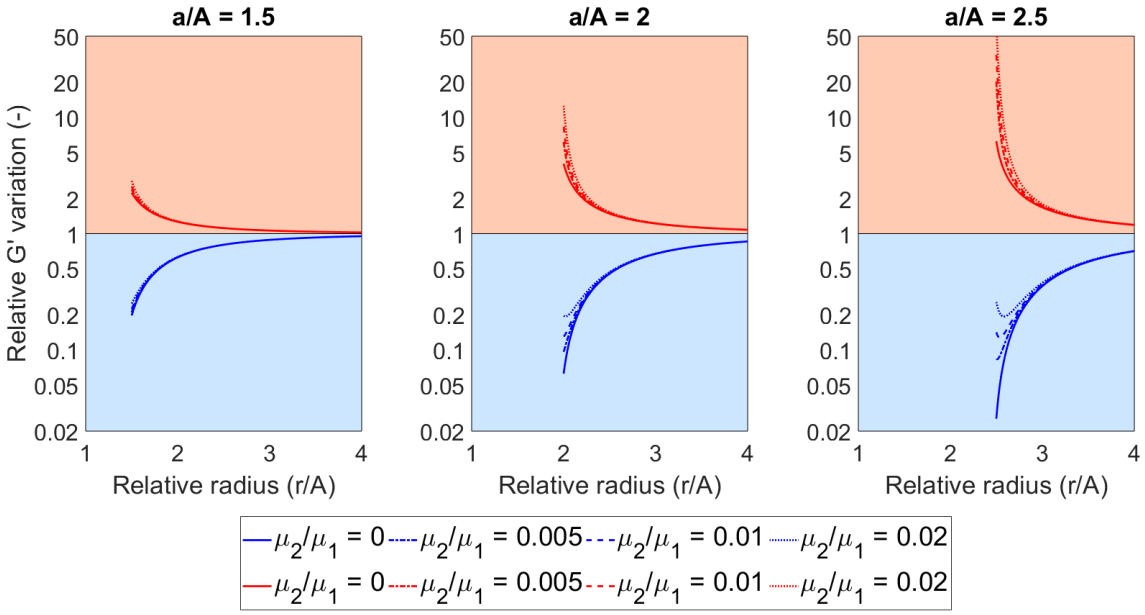

Figure 2.4.: It can be seen that when the wave approaches the inner sphere head-on, inflation would lead to an apparent softening of the material, identified by the blue region. In contrast, along the peripheral interface of the inner sphere, a stiffening is detected, with the curves being constantly in the red region. Given a constant $\mu_1 = 1$, the parameter μ_2 shapes the curves differently in the two regions, especially in the case of larger deformations.

Such analytical considerations were used to numerically calculate the patterns representing the relative shift in tangent stiffness around the inclusion at different inflations (Fig.2.5). Again, it is clear how the extent of the deformation impacts the magnitude of the generated

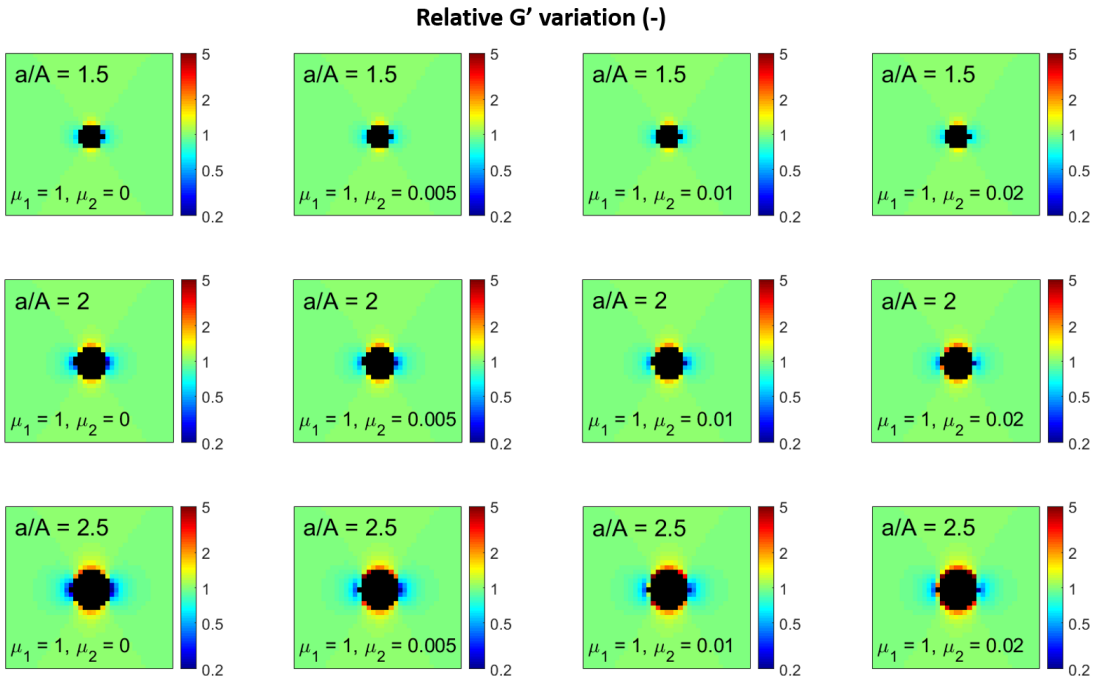

Figure 2.5.: 2D representation of the shear modulus variation patterns generated by an inflated inner sphere as probed by plane waves propagating from left to right.

variation in G', which, given the simple form of the probing shear waves, generates a symmetric pattern around the inclusion.

2.5. Discussion

A list of the main results reported in this chapter is presented in Table 2.1

In this chapter we have developed a mathematical framework to show how an incompressible spherical deformation of a thick-shelled sphere, representative of that applied by a pressurised tumour onto the surrounding nonlinear soft tissue, can generate an apparent anisotropic shear modulus distribution around the inner sphere, with the pattern depending on the direction of propagation of the probing shear waves. After presenting an analytical formulation that defines the impact of a macro-deformation on the real and elastic part of the complex stiffness tensor $\mathcal{G}^*$, here we have idealised soft tissue as purely elastic, hence limiting the analysis to the real component $\mathcal{G}'$. This assumption is supported by the mild viscoelastic behaviour observed in the rheological tests carried out in a tissue-mimicking phantom material presented in Chapter 5. In addition, although studies have proposed the loss shear modulus measured through MRE as a better differentiators

Main results
For the case of an incompressible material, subjected to a macro-deformation superimposed to a harmonic micro-deformation, an analytic expression for $\mathcal{G}'$ and $\mathcal{G}''$ was derived through the linearisation of the wave equation.
A family of curves, representing the relationship between inflation and generated pressure, was identified using a modified version of the Mooney-Rivlin hyperelastic equation. While the linear term of the model was found to simply scale the curve, the quadratic part is responsible for its behaviour at higher levels of inflations, which generates a characteristic S-shape.
The different local deformations sensed by the propagating probing waves lead to an anisotropic distribution of the apparent shear modulus G' reconstructed in elastography. In the case of plane waves travelling through an inflated thick-shelled sphere, a specific pattern was identified, symmetric with respect to the wave propagation direction.

Table 2.1.

between malignant and benign tumour [177], the estimation of G' from experimental wave data relies only on the knowledge of the associated wavelength, obtained through the computation of the second-order derivative in space of the generated displacement, while the evaluation of G'' needs further information on the wave attenuation, making its MRE reconstruction more prone to errors.

A second-order polynomial form of the employed modified Mooney-Rivlin strain energy density function was used to model the nonlinear relationship between stress and strain of soft tissue. With this constitutive equation, we have demonstrated that, while the linear term purely scales the inflating pressure-radial stretch curve, without impacting its general trend, the quadratic term controls the magnitude of the generated pressure at higher levels of inflation, generating a characteristic S-shape. It is also noticeable that the value of the parameter μ_2 is limited to several orders of magnitude less than the value of μ_1. Other hyperelastic laws, showing an exponential growth of stress with the applied strain, can be found in the literature to describe the rheological behaviour of soft tissue, however, given the challenges to analytically calculate the integral in Eq.2.74 using such forms, we have limited our discourse to the chosen polynomial function. Instead, we have seen that a simpler formulation, like the one provided by the use of a Neo-Hookean model, is sufficient to produce a similar shear modulus variation pattern around the inclusion. Nonetheless, with respect to the modified Mooney-Rivlin law, the Neo-Hookean model

does not exhibit the nonlinear increase in the pressure-radius relation at larger inflations which is observed in real tissue [173].

Interestingly, we showed that, despite changing by a similar order of magnitude, the absolute variation in the apparent shear modulus is less prominent when the direction of the propagating shear waves is along a compression, while a much greater apparent shift is detected in the case of tension. Given the simple shear waves employed in the analytical derivation, this yields a more pronounced pattern at the sides of the inclusion than at the leading and trailing edge. Such condition is a direct consequence of the incompressibility assumption and can be compared to the explicative example presented by Capilnasiu *et al.* (2018) for the case of a uniaxial compression of a simple incompressible isotropic Neo-Hookean material [86]. Briefly, given a simple macroscopic compression defined in Eq.2.95,

$$\boldsymbol{C} = \begin{bmatrix} \frac{1}{\lambda} & & \\ & \frac{1}{\lambda} & \\ & & \lambda^2 \end{bmatrix} \qquad \text{with} \quad \lambda < 1 \qquad \text{and} \quad J = 1 \tag{2.95}$$

plannar waves propagating along or perpendicularly to the direction of compression will probe a decreased or increased intrinsic elastic modulus of the medium, $\mu_\perp = \mu/\lambda$ and $\mu_\parallel = \lambda^2\mu$ respectively, where the invariants of the right Cauchy-Green stress tensor work as scalers. While this simple example highlights how the magnitude of the shift in shear modulus depends on the directionality of the waves with respect to the deformation field, the situation becomes more complex in the case of a more intricate wave motion.
Noticeably, in addition to a different magnitude, the relative shear modulus variation shows different trends with different material parameters as well. While a higher μ_2 correlates to an increased material stiffening at the surface of the inner sphere in the case of tension, the same increased parameter value reduces the extent of the softening in the immediate proximity of the inclusion in the case of compression. This effect is particularly evident at sufficiently large deformations, nevertheless, as expected from the family of curves presented in Fig.2.1, the impact of μ_2 becomes less relevant further away from the inner sphere, where the radial stretch is lower. Although clearly unrealistic in the context of soft tissue rheology, we have assessed that values of μ_2 comparable with μ_1 intensify the trend already found in the case of larger inflation radii, leading to a stiffening in the immediate vicinity of the boundary between inner and outer sphere even in the case of compression, followed by material softening farther away from the interface (data not shown).
It is also to be noted that a variation in the material parameters, as well as in the inflation level, only minimally affect the radial extension of the shift in apparent shear modulus, which is limited to the very immediate proximity of the inclusion, with a quick convergence to the background value. Although different material laws could extend the impact of the

inflation pressure to farther regions, these results are consistent with existing models based on measurements from excised tumours, showing a rapid decrease in both the absolute radial and circumferential solid stress as a function of the distance from the tumour-host tissue border [127] (see Fig.1.4). Nevertheless, such changes, given the quick convergence to the background shear modulus, could prove to be experimentally difficult to detect and will depend both on the size of the inclusion and on the resolution of the imaging technique.

Finally, the simple patterns shown here have been numerically generated under the assumption of simple shear waves characterised by a unique direction of propagation and a constant polarisation. The reproduction of such results in a phantom might present some challenges as, while an approximation of the spherical inflation could be experimentally achieved, such simple shear waves are more complicated to generate. The consequent deformation and the associated shear modulus variation will be strongly dependent on the local directionality of the propagating waves. In addition, wave attenuation will play a role in these settings, making the stiffness estimation at the trailing edge of the inclusion less reliable. We will look into these effects in a phantom experiment presented in Chapter 6, where we will present a comparison between the analytically predicted variation in shear modulus as measured through elastography and the experimentally estimated patterns.

3. Inflation Experiment Using a Phantom

In Chapter 2 we have provided an analytical framework to describe the expected change in the mechanical properties of a hyperelastic material when subjected to a spherical macro-deformation, representative of the tumour-generated stress onto the host tissue, as probed by propagating shear waves like those employed in MRE. In the context of elastography, we have analytically predicted that the nonlinear stress/strain response of the material, in our case modelled by the proposed modified Mooney-Rivlin hyperelastic law, will result in the detection of a anisotropic shear modulus distribution which depends on the local direction of the k-vector associated to the probing waves. In this study we have attempted to experimentally reproduce the mathematical results using a phantom representation of a pressurised tumour pushing against its surrounding environment. This requires the use of a material capable to replicate the nonlinear viscoelastic stress/strain behaviour of soft tissue modelled in Chapter 2. An inflatable spherical inclusion must be located inside the phantom to reproduce the strain generated by a pressurised tumour at different sizes. The measurement of the inflating pressure can allow a comparison with the theorised stress/strain behaviour. An inclusion with a size comparable to that of a real tumour will also assess the ability to detect variations in stiffness commensurable with those obtained in real cases.
An MRE setup, consisting of an MR scanner and a mechanical transducer, will then be employed to propagate shear waves through the phantoms and to reconstruct the generated variation in shear modulus. At the same time, a nonrigid registration of high resolution MR images of the inclusion at different inflation states will provide an estimate of the applied deformation field. In this sense, the addition of motion trackers to the otherwise featureless phantom material is a fundamental requirement. For reproducibility and to account for technical difficulties, three replicates of the proposed experiment will be carried out.

This chapter will initially provide an overview of the materials described in the literature exhibiting mechanical properties similar to those of soft tissue and used in the field of elastography. Section 3.2 will focus on the identification of a suitable phantom material and of trackers capable to estimate a detailed map of the local deformation field without impacting the material properties of the phantom. A protocol for the manufacturing, based on those available in the literature, will be provided. The use of a Foley catheter to reproduce a pressurised tumour will then be discussed. Section 3.3 will present the details

of the employed pressure measuring system, together with its limitations. A comparison between the experimental observations and the expected values will follow. In Section 3.4, the specifics of the MR image acquisitions and a description of the MRE setup used to generate shear waves will be presented. A final discussion over the obstacles faced to implement the experimental setup and observations on the similarities with a real tumour case will conclude the chapter.

3.1. Materials Employed to Mimic Mechanical Properties of Soft Tissue in Elastography

In the field of medical imaging, phantoms are often employed to investigate the performance of new and existing imaging techniques in a controlled and simpler setting. Phantoms containing objects characterised by different sizes and contrasts are commercially available for US, X-ray and MR imaging systems, however their availability is more limited when it comes to elastography techniques [178].

Changes in tissue stiffness are often associated to underlying pathological conditions [48] and many cancers correlate to a hardening of the surrounding soft tissue [19], making elastography an attractive technique for tumour detection and staging. The characterisation of the nonlinear stress/strain behaviour of both healthy and abnormal tissue would be extremely valuable for their mathematical modelling and under a diagnostic point of view; however, this task can be extremely complicated to perform, either *in vivo* or *in vitro*, due to the presence of underlying forces that can alter the mechanical properties of soft tissue, making it difficult to distinguish from a lesion [179]. In this sense, the development of phantoms capable to mimic the nonlinear rheological behaviour of soft tissue has become essential in the field of MR elastography, to investigate the limitations of such a technique in a controlled environment and can provide a crucial understanding of the impact of the above-mentioned forces.

In addition to a similar nonlinear behaviour, tissue mimicking materials should possess a stiffness comparable to that of tissue. Young's modulus can present a significant variability throughout different types of tissue for both normal and cancerous cases, with reported values ranging between 18 ± 7 kPa for breast fatty tissue to 106 ± 32 kPa for invasive and infiltrating ductal carcinoma in breast with 5 % pre-compression, as well as values up to 230 ± 34 kPa for prostate cancer with a similar pre-compression [19]; hence, ideally the mechanical properties of the phantom material should be controlled during the manufacturing process, allowing to reproduce the mechanical conditions more suitable for the desired investigation. In MR elastography, similar nuclear magnetic resonance (NMR) properties to those of soft tissue would permit a standard MR characterisation. Finally, for reproducibility purposes, the material must posses long-term stability, so that its elastic

and NMR properties do not change over time, and should remain unaltered even if one or more inclusions are added to the matrix.

Water-based gels, also known as hydrogels, have been extensively employed to reproduce the elastic properties of soft tissue in US studies, thanks to a well developed manufacturing technology over years [180, 181, 182]. These gels consist of cross-linked polymer chains in a water solution. Homogeneous gels of agar or gelatin are among the most widely employed materials in strain imaging, as they offer a good control over the phantom Young's modulus, dependent on the concentration of each of the two elements [183]. Parker *et al.* (1990) [184] have presented that the Young's modulus of agar and gelatin mixtures lies in the range of some human and animal soft tissue, as reported by Sarvazyan *et al.* (1995) [47]. While gelatin exhibits an almost linear stress/strain behaviour for strain lower than 10 % [183], agar is well known for producing nonlinear stress/strain curves [183, 179], making it more suitable to reproduce soft tissue properties under larger strains, although the nonlinearity can be too pronounced at higher concentrations [183, 185]. Agar phantoms, however, are usually brittle, while the Young's modulus of gelatin gels has been shown to increase over time [183]. The two material have also been employed together both in a mixture or in heterogeneous phantoms, with the agar concentration tuned to control the material stiffness and the gelatin providing more stable bondings with inclusions and a better geometrical stability [186]. Despite the extensive employment in US elastography, little attention has been given to the NMR properties of these materials [186].

PVA-cryogel is as another tissue-mimicking material proposed for MR imaging applications [187, 188], which gelifies when immersed into an aqueous solution and is exposed to freeze/thaw cycles [189, 190]. Depending on the cryogenic treatment, wave speed through the phantom can be tuned to assume values within the range of soft tissue [187]; NMR properties can be controlled in the same way [187, 188]. Studies have shown that PVA phantoms exhibit a nonlinear stress/strain response [191], which is determined by the number of freezing cycles, in the same way as the Young's modulus of the material [192, 193], making the manufacturing technique more lengthy and the reproducibility more complicated [194]. Unlike other materials, however, PVA cryogel has become particularly appealing for the possibility to produce anisotropic phantoms, reproducing the orthotropic mechanical behaviour typical of tendons and muscels [195].

Phantoms manufactured with a mixture of copolymer and mineral oil have proven to cover a wide range of Young's modulus values, from 2.2 to 150 kPa, nevertheless they showed densities significantly lower than those expected from soft tissue and a large linear viscoelastic domain[185].

Soft polyvinyl chloride (PVC) phantoms are made from a liquid suspension of PVC particles in a plasticiser which, when brought to a temperature above 170 °C, interact and

polymerise. While cooling down, the mixture assumes a gel form with increasing viscosity until solidification. The elastic modulus of this polymer gel, also known as plastisol, can vary between a few to hundreds of kPa, according to the plasticiser concentration in the mixture [196] and presents a long-time stability both in terms of elastic and viscous properties [197]. The stress/strain curves measured for different phantom compositions by Hungr *et al.* (2012) showed a hysteresis typical of viscoelastic materials, while the nonlinear response increased with the increase in PVC concentration [196]. A linear behaviour could be approximated for a strain less than 10-15 %, consistently with the behaviour expected from soft tissue.

3.2. Phantom Construction

3.2.1. Material Selection

To reproduce the viscoelastic behaviour of the compressed soft tissue, we necessitate a material exhibiting a nonlinear stress-strain relation, i.e. hyperelastic, without undergoing non-reversible changes in shape or yielding when subjected to the macro-deformations generated by an inflated inclusion used to mimic a pressurised tumour. These requirements are needed to probe the apparent change in shear modulus under the application of sufficient strain. Furthermore, the ideal medium will have an intrinsic shear modulus similar to that of a typical soft tissue. PVC-based phantoms can cover a wide range of elastic moduli and present different degrees of stress/strain nonlinearity depending on the employed mixture [196], permitting to control the material mechanical properties to resemble those of soft tissue. Furthermore, the large elastic limit of the polymerised material, experimentally assessed, made it an ideal choice to sustain the strain generated by the inclusion, larger than 100 % in its immediate proximity, as presented in Section 4.3 of this thesis. For our purpose we have used a liquid plastic plastisol (Lure-solutions, UK), sold under the commercial name Luresol, which is available in three stiffness grades: firm, medium and soft, and its elastic modulus can be further tuned with the addition of a softener (non-phthalate plasticiser).

3.2.2. Need for Scattered Particles to Track the Deformation

In order to correlate the variation in shear modulus, as measured through MRE, to the applied strain and to model the expected tissue response, we needed to quantify the generated macro-deformation to reproduce a tumour expansion. This could be estimated through the nonrigid registration of anatomical images of the phantom acquired at various expansion states of the inclusion, from the strain-free situation to the maximum extension investigated. Nevertheless, in order to track the pixel-wise deformation of the material, the presence of contrasting particles, or trackers, scattered within the otherwise featureless

phantom matrix, is mandatory. These trackers must be small enough to finely map the deformation, but large enough to be resolved in the MR images and must exhibit different NMR properties from the PVC mixture to offer a sufficient image contrast, hence allowing an easy detection by the registration program. It is also important that the trackers are sufficiently distributed in the vicinity of the inclusion, where the expected change in G' is expected. Finally, the trackers must interact with the PVC matrix in a way that does not alter the shear modulus isotropic distribution and must be MR compatible.

Silica gel particles, as well as wood shavings, had the required size and granted a good T2 contrast in the light of their short transverse relaxation time compared to that of plastisol (see Fig.3.1-A). Maps of the shear modulus distribution of three phantoms made with

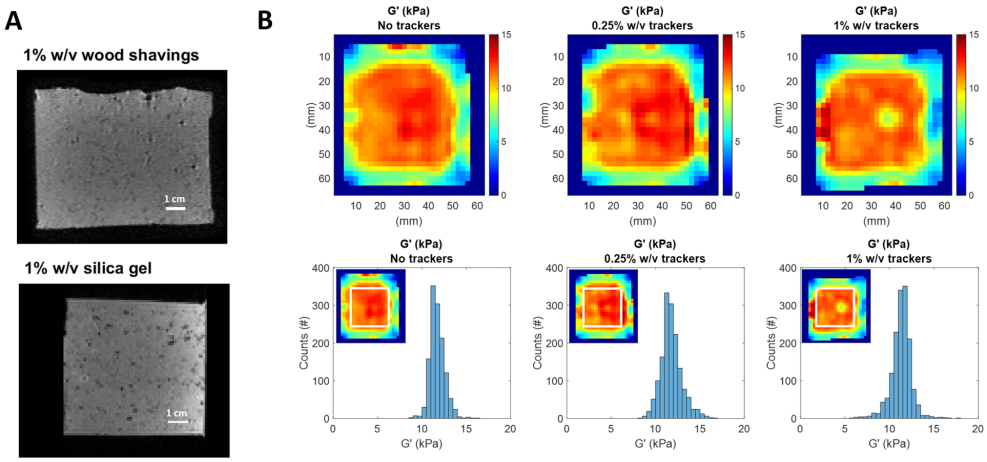

Figure 3.1.: A) High resolution images of both wood shavings and silica gel uniformly distributed throughout the phantom. Both trackers provide sufficient contrast to follow their displacement during the phantom deformation. B) Top: reconstructed shear modulus of the central slice of three phantoms containing different concentrations of trackers. Bottom: histograms of the G' distribution over the selected region (highlighted in the white ROI).

80 % plastisol and 20 % softener and containing a 0 %, 0.25 % and 1 % w/v concentration of trackers were reconstructed from MRE data acquired using a 140 Hz vibration frequency (Fig.3.1-B). To exclude the impact of boundaries from the reconstructed storage modulus, G', the mean value and its standard deviation were calculated over the central region of the 3D images. The values, reported in Table 3.1, show no significant difference among the three tested concentrations.

Tracker concentration	0 % w/v	0.25 % w/v	1 % w/v
G′ (mean ± s.d.)	11.7 ± 0.8 kPa	11.8 ± 1.2 kPa	11.3 ± 1.1 kPa

Table 3.1.: Trackers do not impact the reconstructed G' of the phantom matrix.

3.2.3. Manufacturing Protocol

The phantoms employed in our experiment were composed of 80 % of soft-grade Luresol and 20 % of additional softener. The protocol for the making of the phantom had been adapted from Hungr *et al.* (2012) [196] and Leclerc *at al.* (2012) [197]. 700 mL of the mixture were placed in a beaker on a magnetic stirrer at 300 °C. When the temperature of the solution reached ~170 °C, it was poured into a $86 \times 86 \times 115\,\mathrm{mm}^3$ tin cuboidal mould (Tinware Direct Ltd, Bedford, UK) and left to solidify at room temperature. The use of tracking particles added an extra step in the phantom-making protocol, such that, when the polymerisation had started but the material was still in a semi-liquid state, the trackers were scattered into the mixture and homogeneously distributed through gentle stirring. In the case of wood shavings, after the stirring, the mould containing the PVC solution was placed into a vacuum chamber for 3÷5 min. Stirring and vacuuming was repeated two or three times to eliminate air bubbles that could generate artefacts in the data acquisition. To avoid any damage to the integrity of the phantom caused by carving an access for the inclusion, a metallic tube with the diameter of the catheter was inserted in the matrix during the curing period and gently removed afterwards. The entire procedure takes up to 1 h 30 min to make one phantom, which was left to set for a minimum of 12 h. Afterwards, the phantom was gently removed from the mould using oil to facilitate the process. While curing, plastisol polymerises more quickly around the walls of the mould than in the centre, resulting in the formation of a meniscus on the open side of the mould, which was cut off to preserve the cuboidal geometry.

3.2.4. Foley Catheter to Mimic Tumour-Generated Stress

To reproduce the stress caused by a pressurised tumour expansion, a CH6 Foley catheter (The Vet Store, Bradford, UK) was inserted inside the pre-made hole inside the phantom and inflated to different levels (see Fig.3.2). This urinary catheter normally used for animal treatments consists of a thin silicone tube with a 1.5 mL compliant balloon at its extremity. Unlike other tested balloon-tipped catheters, this one retained its elastic behaviour when kept inflated for the time necessary for the MR data acquisition. The inflation with water satisfies the assumption of incompressibility made for the analytical model, while the use of a SOFT-JECT® Luer syringe ensured a better experimental control regarding the injected volume. In one of the three replicates of the inflation experiment, gadolinium (Gadovist®) was diluted in water to a 0.3 mM concentration to provide a better contrast from the PVC phantom. With respect to larger tested balloons, the one we employed also grants a sufficiently spherical inflation, hence approximating the idealised deformation modelled in Section 2.4.1. Under the assumption of a spherical inflation, the balloon diameter and the highest nominal injected volume was less than 20 mm, more than five times smaller than the phantom size to simulate the absence of boundary conditions modelled in Section

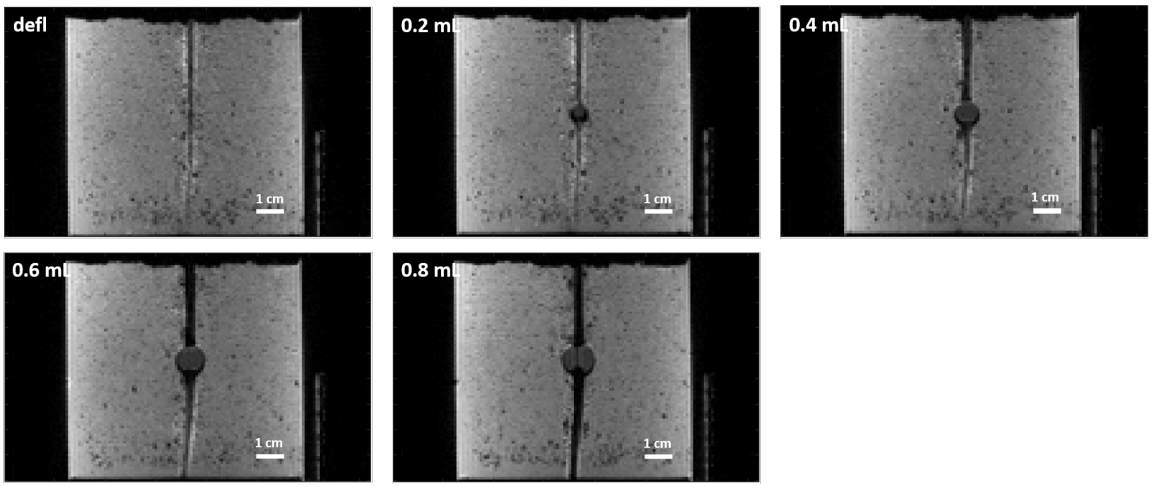

Figure 3.2.: Cross section of high resolution images of the balloon inserted inside the plastisol cuboid at different inflation states. The contrast between the bright plastic phantom and the dark water allows a good identification of the inclusion. The inflation of the employed balloon meets the sphericity requirement.

2.4 once positioned at the centre of the plastisol cuboid. In order to minimise viscous wave attenuation, however, the pre-made channel for the catheter insertion had to be located close enough to the side of the phantom in contact with the shear wave source used for the MRE data acquisition.

With the developed procedure to produce the soft tissue-tumour ensemble, three replicates of an inflation experiment were carried out, consisting in the subsequent inflation of the balloon catheter with increasing volumes of water to probe the induced variation in the apparent shear modulus of the material through MRE. A pressure measuring device was also connected to the catheter to record the magnitude of the generated radial strain, while MR images of the inflated balloon were also acquired at each inflation state. These measurements were used to relate the experimental findings to the analytical results obtained through the formulation developed in Chapter 2 and details on their acquisition are given in the following sections.

3.3. Pressure Measuring System

To measure the internal pressure exerted on the phantom material surrounding the inclusion, an MPXV5100DP integrated silicon pressure sensor was connected to the catheter through a series of 3-way tap stop cocks. The output is read through an Arduino® Mega board and saved on a laptop as an ASCII file. The measured inflating pressure corresponds to the average radial stress σ_{rr}, analytically calculated in Eq.2.74. A schematic of the measuring setup is presented in Fig.3.3. Once inserted into the pre-made hole in the plastisol cuboid, the balloon is inflated in steps until reaching the maximum chosen volume. For each inflation, the pressure is recorded until a steady state is reached, to account for the

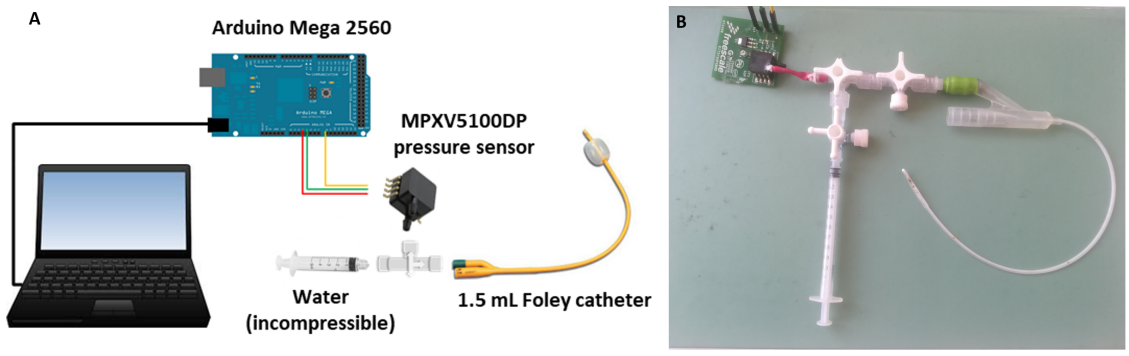

Figure 3.3.: A) A Foley catheter was used to mimic tumour expansion. While water was injected inside the catheter, the generated radial stress was measured through a MPXV500DP pressure sensor. The sensor output is then read through an Arduino® Mega board and a connected laptop. B) Picture of the connection between the catheter and the pressure sensor

time-dependent stress relaxation typical of viscoelastic solids. This behaviour was clearly visible from the pressure measurements (Fig.3.4), which show a decrease of the applied radial stress under a fixed strain until a plateau is reached. A waiting period between 5

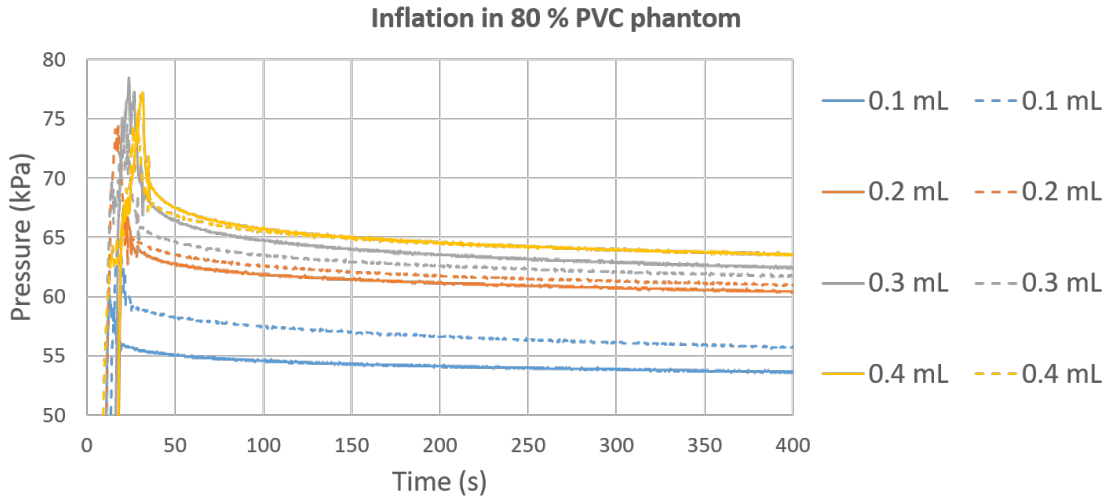

Figure 3.4.: Two replicates of the same measurements (solid v dotted curves) show that the same injected volume produces comparable pressure measurements. After an initial peak, the relaxation of the viscoelastic material leads to a quick decrease in pressure, however a waiting period between 5 and 10 min is sufficient to ensure convergence.

and 10 min proved sufficient to have the pressure converging to a plateau, with an average drop of 4.1 ± 0.7 % measured after 7 min relative to the 1 min recording. The data acquired over that time interval were also fitted to an exponential equation in the form $p = ae^{bt} + c$, where a, b and c are the fitting parameters, with the latter representing the equilibrium pressure: the average extrapolated drop in pressure after 7 min until convergence was by

0.26 ± 0.07 kPa, corresponding to an average further decrease of 0.4 ± 0.1 %. Fig.3.4 also shows the reproducibility of the pressure measurements, especially at volumes higher than 0.1 mL, where a similar uncertainty over the injected amount of water has a smaller impact on the inflation radius and hence on the applied radial stretch.
During the imaging process, the valve that connects the catheter to the adjacent stop cock was closed after each measurement, the measuring sensor was disconnected to avoid the generation of unwanted currents, and the MR data were acquired. For the entire duration of the inflation experiment, the time interval during which the balloon was kept inflated at the different volumes was recorded, so that the data points could be acquired again under the same conditions for reproducibility.

3.3.1. Linear Subtraction of Balloon Resistance from Measured Pressure

The pressure measured when the balloon is inflated inside the phantom corresponds to the combination of the pressure exerted by the balloon walls on the phantom itself, i.e. real inflating pressure, and of the pressure necessary to expand the compliant material that makes the balloon, i.e. balloon resistance. The latter contribution must then be removed from the total pressure measurement to extract the radial stress actually experienced by the PVC cuboid. To this aim, the employed catheter was characterised and the pressure generated at different inflation volumes was measured leaving the balloon free to expand. Fig.3.5-A shows that, in the absence of the viscoelastic response of the phantom material, the measured pressure converged much more quickly to an equilibrium value. Also, the pressure-volume curve was perfectly reproducible (Fig.3.5-B), removing one source of uncertainty from the estimation of the actual radial stress experienced by the PVC phantom in the region of the inclusion. The initial peak in pressure at lower volumes followed by a quick decrease and a subsequent slower pressure rise is typical of the spherical inflation of incompressible rubber-like balloons and can be described by several material models present in the literature [198]. Given the simple interaction between the inclusion and the phantom, with the balloon wall pushing against the surrounding material, we have modelled the real inflating pressure as the linear subtraction of the corresponding balloon resistance from the pressure measured when the balloon is inflated inside the phantom. An example of a pressure-volume curve measured with the pressure sensor, the corresponding balloon resistance obtained from the free balloon inflation and the difference between the two is given in Fig.3.5-C.

3.3.2. Inflation range

The real inflating pressure was also a good indication of the integrity of the phantom; the material, in fact, could only withstand a certain level of inflation before rupturing, as we could see when the catheter was removed and images of the holes in the phantoms at

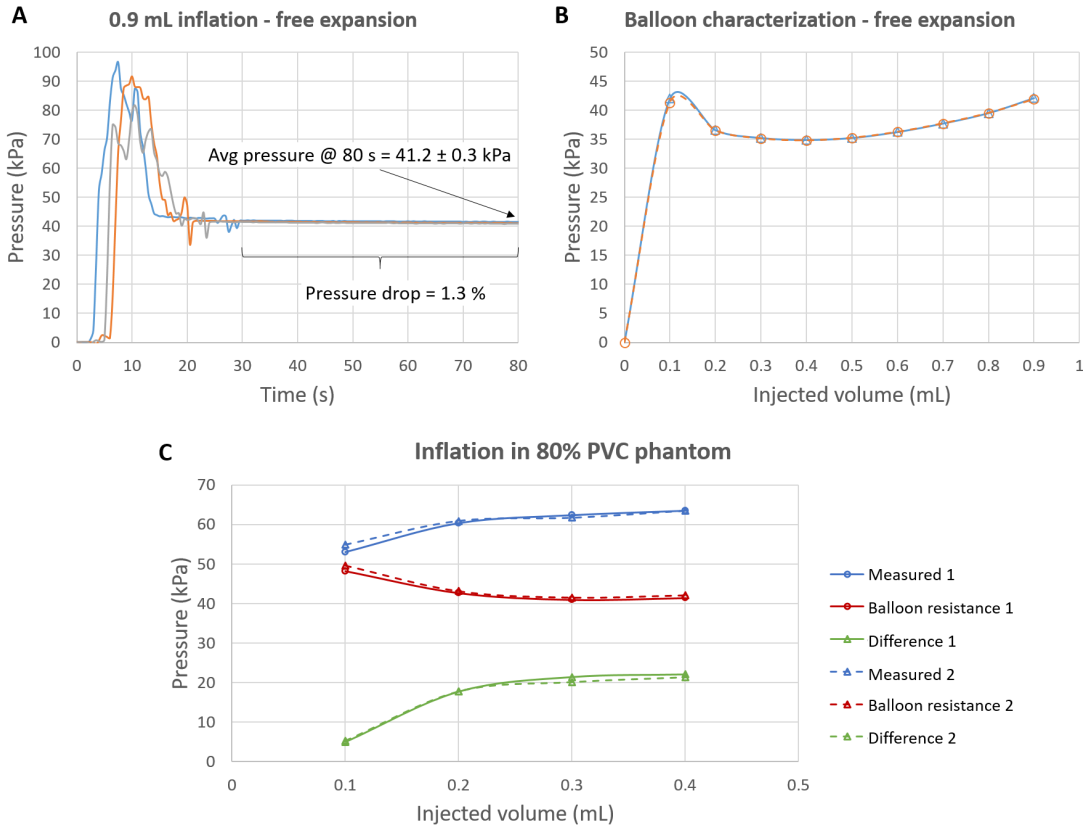

Figure 3.5.: A) In the absence of the material resistance, the measure pressure reaches a quicker convergence. B) Free inflation produces reproducible pressure measurements at different volumes. C) The subtraction of the balloon resistance from the pressure measured when the balloon is inflated inside the phantom returns the actual pressure experienced by the surrounding material.

the position of the inclusion were acquired (Fig.3.6-A). The pressure curves analytically calculated in Section 2.4.2, in fact, present a monotonic dependence on the inflating volume; therefore a drop in the stress applied by the balloon wall on the surroundings is not to be expected and can be ascribed to a loss in the structural integrity of the soft plastic material, as presented in Fig.3.6-B. At the selected plastisol-to-softener ratio, the maximum injection volume to ensure the phantom integrity and still apply a sufficient strain was found to be 0.4 mL.

3.3.3. Inflation Volume Estimation

The injected volume, as measured from the syringe, was found to be an imprecise estimate of the size of the inflated balloon; although the employed syringe provided a 0.05 mL uncertainty over the injected volume, the high resolution MR images of the inclusion showed that the balloon did not inflate consistently to the same volume given the same injected amount of water throughout different experiments. The intensity-

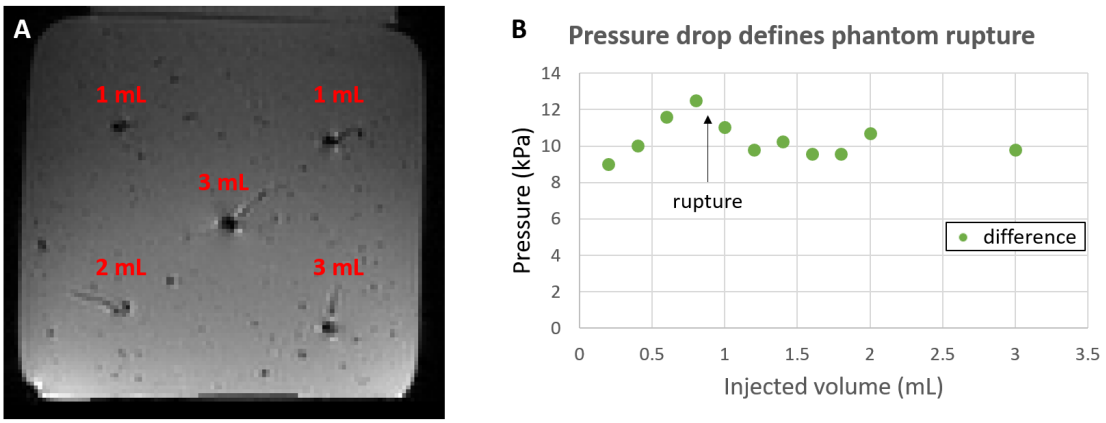

Figure 3.6.: A) High-resolution MR image showing how large balloon inflations lead to material rupture. B) A drop in the real inflating pressure indicates the loss of material integrity. These results were obtained for a phantom made using an 80 % concentration of plastisol

based segmentation of the balloon from the anatomical MR images, carried out using the Matlab function `regionprops3` for volumetric regions, reported different sizes at the same inflation state throughout different replicates of the inflation experiments (see Fig.3.7-A and -B). For each instance, the volume extracted from the segmented image of

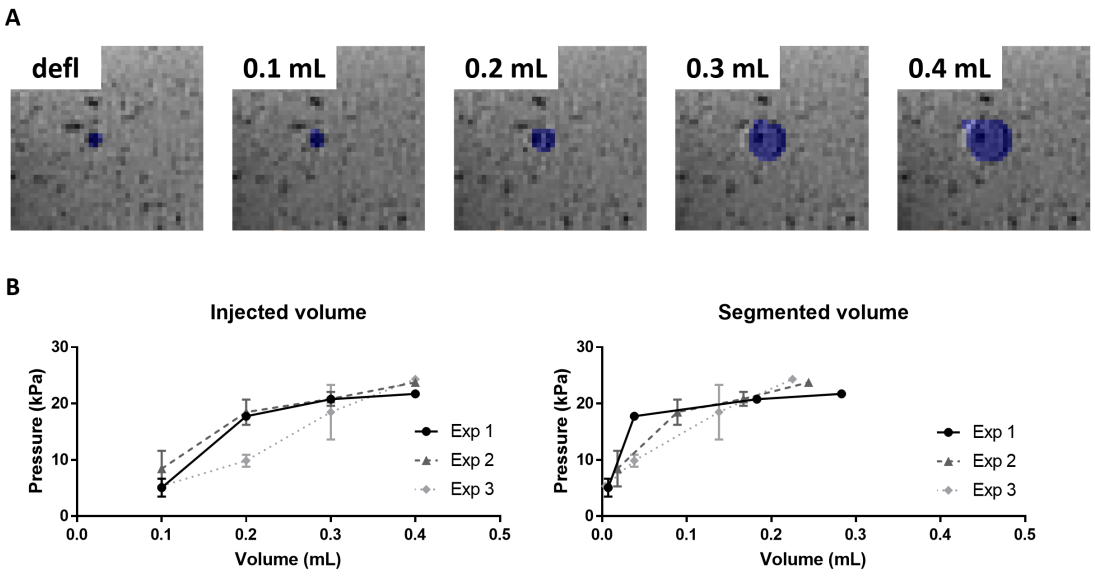

Figure 3.7.: A) Segmentation of the balloon at the different inflation states from high-resolution MR images provides a better estimation of the volume of the inclusion. B) The segmented volume reveals an overestimation of the injected amount of liquid, leading to a shift of the pressure-volume curve.

the balloon in the deflated state was subtracted from that of the other inflation states, to

account only for the actual inflation ΔV. The shift of the pressure curves using this volume measurements indicates that not all the injected water was used to inflate the balloon.

3.3.4. Comparison with Theoretical Values

The experimentally measured radial stress applied by the inflated balloon onto the surrounding phantom was plotted against the relative balloon radius (a/A), calculated as the mean of the two most similar lengths of the major axes of the segmented balloon, idealised as an ellipsoid, to draw a characteristic stress-strain curve for the investigated system (Fig.3.8-A). The values are displayed in Table 3.2, too. Each replica of the inflation

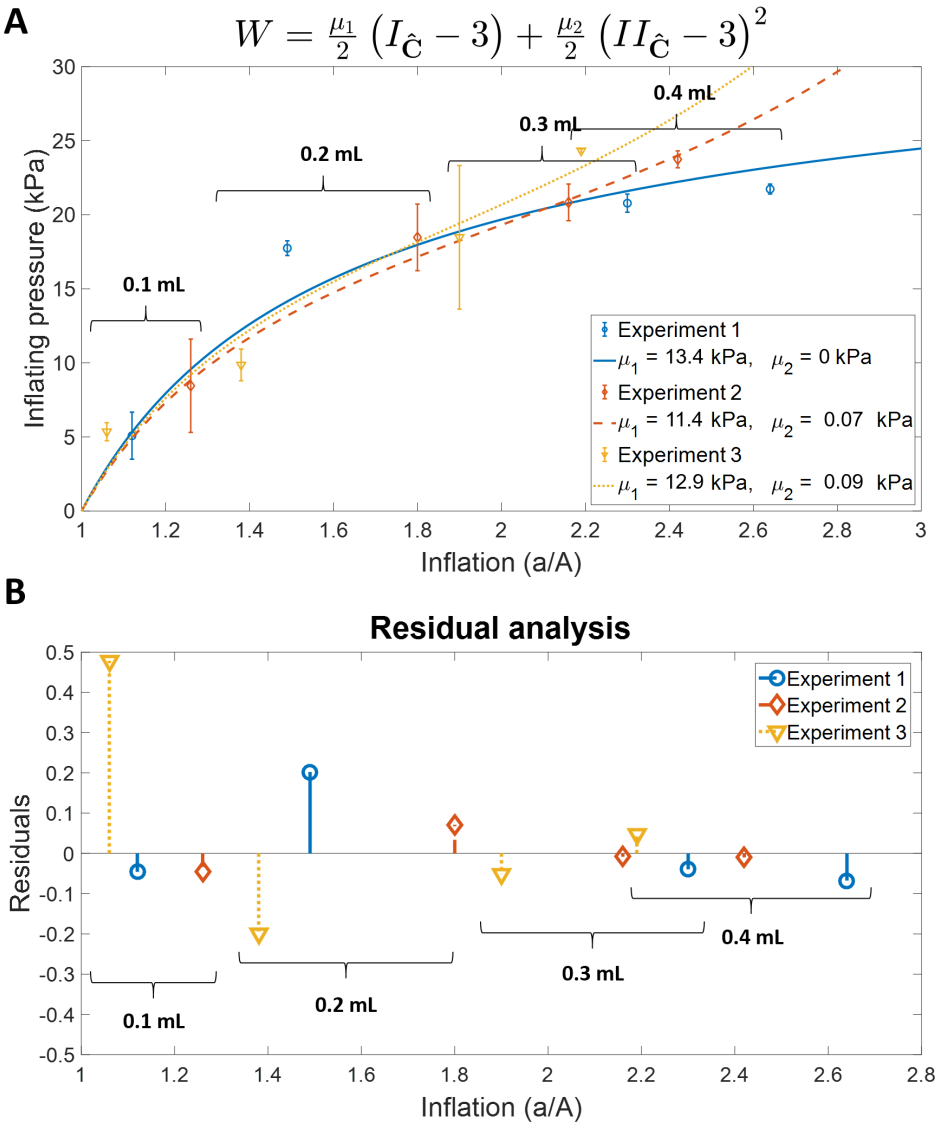

Figure 3.8.: Analytical prediction of inflation pressure curves. A) The modified Mooney-Rivlin model can fit the pressure data obtained from the three phantoms. B) Residual analysis for the three experiments.

experiment was repeated twice, the second time in the laboratory, outside of the MR scanner, so that the pressure measurements are reported as the mean values and the uncertainties reflect the range of values covered by the two measurements. The radial stretch, instead, was obtained from the single set of images acquired only for the first repetition of each replica of the inflation experiment. The data points obtained from three

	0.1 mL	0.2 mL	0.3 mL	0.4 mL
Experiment 1	5.1 ± 1.6 kPa / 1.12	17.7 ± 0.5 kPa / 1.49	20.8 ± 0.6 kPa / 2.30	21.7 ± 0.3 kPa / 2.64
Experiment 2	8 ± 4 kPa / 1.26	18 ± 3 kPa / 1.80	20 ± 2 kPa / 2.16	22.8 ± 1.5 kPa / 2.42
Experiment 3	6.0 kPa / 1.06	9.9 ± 1.1 kPa / 1.38	19 ± 5 kPa / 1.90	24.2 ± 0.1 kPa / 2.19

Table 3.2.: Inflating pressure (kPa) / radial stretch (-) measured from the three replicas of the inflation experiment.

phantoms were then fitted to the proposed modified Mooney-Rivlin model in order to find the correlation between the analytical predictions and the experimental data. A purely elastic version of the material law was used, as it was assumed that any residual viscoelastic relaxation of the material had reached asymptote at the time of the measurement. A non-constrained fit was obtained, using a nonlinear solving method based on the Generalized Reduced Gradient algorithm (Microsoft Excel), by only imposing a physical meaning to the parameters and forcing them to be greater than zero. The model produced a good correlation with the data, with an r^2 of 0.96, 0.99 and 0.97 for the first, second and third experiment respectively. A residual analysis revealed that the model offers a better estimate of the values measured at higher inflation states (Fig.3.8-B). The best estimate of the material parameters, Pearson's r^2 and squared sum of residuals (SSR) associated to the fit are given in Table 3.3

	μ_1 (kPa)	μ_2 (kPa)	r^2	SSR
Experiment 1	13.4	0	0.96	0.049
Experiment 2	11.4	0.07	0.99	0.007
Experiment 3	12.9	0.09	0.97	0.274

Table 3.3.: Data fitting of the three replicas of the inflation experiment in phantom.

3.4. Image acquisition

MR images of the deflated and inflated states were acquired with a 3T Philips Achieva Multi-Transmit scanner (Philips Healthcare, Best, Netherlands). The phantom was positioned on a supporting stage, located at the centre of the bore, and kept in position by a back wall and top plate with adjustable height. All contact surfaces were coated with oil to reduce the adhesiveness of the PVC. The catheter insertion direction was perpendicular to the sagittal imaging plane. To generate the mechanical waves required for elastography imaging we used a custom-made electromagnetic transducer described in Section 3.4.1.

High resolution images of the phantoms were acquired in the sagittal plane using a spin echo sequence (TR: 1394 ms*, TE: 13 ms). The scan resolution was 144×144 voxel^2 and the number of slices was arbitrarily set equal to 80 or 90. The image resolution was $0.889 \times 0.889 \times 0.89$ mm^3/voxel with no gap between slices. A double SENSE Flex Large coil was used for signal enhancement.
MR wave images, instead, were acquired using a GRE sequence [199] with motion encoding gradients along the phase (p), frequency (m) and slice (s) encoding directions, using a vibration frequency of 210 Hz. The reconstruction method proposed by Sinkus *et al.* (2005) [51, 73] and presented in Section 6.1 of this thesis, was then used to reconstruct the corresponding 3D set of MRE data, showing the shear modulus distribution around the inclusion. 13 sagittal slices with a 2 mm isotropic resolution were acquired, each one covering an in-plane FOV of 128×128 mm^2 centred on the inclusion. 8 time points were sampled along the wave cycle. A number of signal averages (NSA) of 4 was used for the acquisition to improve the signal-to-noise ratio (SNR) of the images, leading to a scan time of ~25 min for each inflation state.

3.4.1. MRE setup

The transducer developed for this study was based on the principle that an object exhibiting a magnetic moment $\boldsymbol{m}$ and immersed in a magnetic field $\boldsymbol{B}$ experiences a torque $\boldsymbol{\tau}$ that forces the object to rotate along its axis (Eq.3.1), so that its magnetic moment aligns to the external magnetic field lines

$$\boldsymbol{\tau} = \mathbf{m} \times \mathbf{B} \tag{3.1}$$

In our setup the magnetic moment was generated through an electric current running through a solenoid and is proportional to the applied current i, the surface area of the solenoid S as well as the ratio between the number of turns and the axial length of the coil N/l

$$\mathbf{m} = \frac{N}{l} i\mathbf{S} \tag{3.2}$$

The application of an alternating current, rather than direct current, results in the oscillation of the solenoid around the rotational axis, with amplitude and frequency dependent on the parameters of the waveform, on the geometry of the solenoid and on the intensity of the external magnetic field. The generated torque is transmitted to the phantom through a connecting push-pull rod linked to a piston, the motion of which is limited to the z-axis of the bore through Lego supports. A schematic representation of the transducer is shown in Fig.3.9. The sinusoidal input current was generated by means of a AFG3000C Arbitrary/Function Generator (Tektronix) through which it was possible to adjust the

*1239 ms for the third phantom experiment

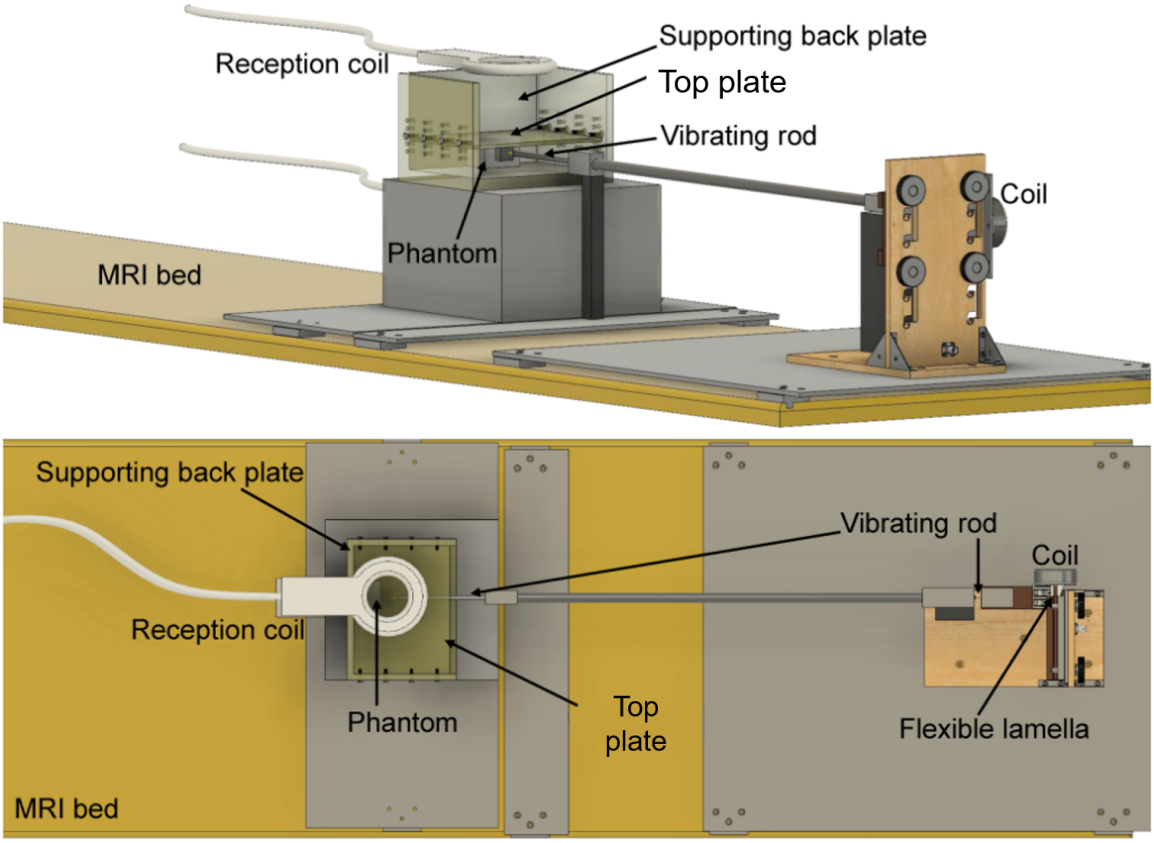

Figure 3.9.: Schematic representation of the developed mechanical transducer. Image modified from Capilnasiu *et al.* (2018) [86].

frequency and amplitude of the waveform. The output passed through a 600 W STA-500 power amplifier (Stage Line) before being fed to the coil in the actuator.

3.5. Discussion

A list of the main results reported in this chapter is presented in Table 3.4
In this chapter we have provided the details of the experimental setup used for the phantom investigation of the variation in shear modulus generated by a pressurised inclusion onto the surrounding simulated soft tissue. Different types of phantom materials used to mimic the mechanical properties of human soft tissue for both MRE and ultrasound validations have been described in the literature, most of them carrying limitations either to provide a realistic option for elastography studies or because of long-term instability. For this work we have initially attempted to use an agar-gelatin mixture following the findings of Pavan *et al.* (2010) [200], as well as paraffin wax and silicon elastomer. In both cases the produced cuboid did not satisfy the requirements necessary for our experiments: the agar-gelatin gel was too brittle and fractured even at moderate strains, while the paraffin mixture did not show the desired nonlinear stress/strain behaviour. Plastisol, on the other hand, proved

Main results
A soft plastic material, capable of mimicking soft tissue nonlinear mechanics, was identified.
A CH6 Foley catheter, inserted into a plastisol cuboid, was used to reproduce tumour growth. The generated pressure was measured through a pressure sensor connected to the catheter.
The hyperelastic material model developed in Ch.2 could fit the inflating pressure produced by the balloon pushing again the surrounding soft plastic material.
Silica particles were added to help tracking the deformation generated by the inflated balloon. In a concentration of 1 % w/v, they were found not to impact the shear modulus of the material, reconstructed from MRE data acquired in the absence of macroscopic strains.

Table 3.4.

capable of sustaining the strain generated by a spherical inclusion with a diameter $\lesssim$1 cm, comparable with the size of a small primary tumour [201]. MRE tests on plastisol phantoms presented in the literature have reported similar elastic and viscoelastic properties to that of healthy soft tissue, both in terms of stiffness and nonlinear strain-stress relationship [197], making this material an ideal choice for our experiment. Furthermore, the simple manufacturing permitted a better reproducibility of the phantom mechanical properties through different replicates of the experiment. A deeper characterisation of the material at different plastisol-to-softener ratios is reported in Ch.5. Madsen *et al.* (2003) underlined a higher wave attenuation, compared to that of soft tissue, in a plastisol sample at the frequency range employed in US elastography [202]; although less relevant, given the lower working frequency, we experienced a similar issue at with 210 Hz shear waves, which forced us to locate the inclusion closer to the surface in contact with the transducer, at a distance of ~20 mm. The problem could not be addressed by reducing the vibration frequency, as the corresponding wavelength was too long to correctly resolve the inclusion and to reconstruct the shear modulus around it.

The addition of silica gel or wood shavings to the PVC mixture, with their sub-millimetre size and different contrast from that of the phantom matrix, provided additional features to facilitate the image registration. In addition to those, we have also attempted to use other particles normally employed in phantoms used for US applications, such as agar-droplets, according to the oil-in-agar/gelatin dispersion preparation procedure described by Mardsen *et al.* (2003) [202] or glass beads, as employed by Li *et al.* (2015) [203] in soft PVC material.

Both trackers, however, were less suitable than the chosen ones: the agar-droplets due to a more complicated manufacturing process, while the glass beads because of their large diameter (~0.7 mm), which hindered the fine mapping of the deformation field. At the investigated concentrations, the employed scattered particles also did not appear to affect the shear modulus of the matrix as measured through MRE in a strain-free situation, granting homogeneous mechanical properties throughout the phantom. Compression of inhomogeneous media, in fact, would produce a different deformation field from the expected one, creating unusual strain patterns [183]. Chapter 5, however, will show that motion trackers do impact the nonlinearity of the stress-strain response of the phantom matrix at higher strain.

A CH6 Foley catheter inflated with water was used to mimic the tumour expansion and the generated stress. The maximum inflation volumes, provided that an access hole for the catheter was pre-made during the phantom matrix polymerisation, was limited to 0.4 mL, to prevent the risk of material ruptures. The use of water over air was chosen to satisfy the assumption of incompressible deformation made for the analytical modelling. To this end, prior to the inflation, the catheter line and all connections were pre-filled with water, to make sure that all the injected volume was used to inflate the balloon. Nevertheless, the segmented high resolution MR images revealed that the balloon size was not constant at a fixed inflation volume, which, in addition, was always overestimated; this could be ascribed to factors such as the presence of residual air bubbles that get compressed during the water injection, as well as to the slight expansion of the mildly compliant catheter line, which reduce the actual volume used to inflated the balloon.
Finally, the real inflating pressures associated to the investigated inflation volumes have been obtained by subtracting the resistance offered by the balloon membrane from the measured pressure values. The agreement with the predicted theoretical behaviour supports the validity of the assumption of the linear contribution of the two terms for the explored strain range.

Under the assumption of a spherical inflation, the radial stretch was calculated from the segmentation of the balloon at different inflation states from the acquired high resolution MR images; a more accurate estimate of the deformation field, however, can be obtained through non-rigid registration of the same images. Knowledge of the local directionality and intensity of the deformation can help correlate the compression/tension probed by the shear waves used in elastography with the experimentally detected apparent shift in the material parameters, as explained in Chapter 6 of this dissertation. Details of the strategy employed to non-rigidly register the acquired images, of its *in silico* validation and examples of strain estimates obtained from phantom data as well as *in vivo* will be presented in the following chapter.
A viscoelastic characterisation of the tissue-mimicking plastisol material will instead be

presented in Chapter 5 of this thesis, to assess the nonlinear stress/strain behaviour of the employed mixture. The identification of a suitable strain energy density function, capable of capturing the rheological response of different PVC samples when subjected to macro-deformations as well as harmonic micro-deformations comparable to those generated by the probing shear waves in MRE, will also determine the possibility to apply the analytical framework developed in Chapter 2 to the chosen material.

4. Strain Estimation

A reliable estimation of the strain in and around tumours is required for computing the forces and pressures involved. The analytical findings presented Chapter 2 suggest that, due to nonlinear tissue rheology, the strain generated by a pressurised tumour can alter the mechanical properties of its surroundings, leading to a variation in the shear modulus as measured through MRE. Knowledge of the deformation field generated by the expanding mass allows accounting for those alterations and enables an indirect quantification of the underlying static forces. In the realm of medical imaging, such deformation can be retrieved from the post-processing of the acquired images of the undeformed and deformed object. Registration of the two images is normally used to define the spatial transformation that connects the two images, allowing the calculation of the corresponding displacement and strain fields.
In this chapter we will initially give an overview of the existing image registration methods, focusing on non-rigid registration techniques and their applications in medical imaging. A ground truth *in silico* model, consisting of a high resolution MR image of the liver embedded into a tetrehedral mesh was developed to apply realistic deformations to real contrast image and will be presented in Section 4.2. This model was employed to optimise the chosen registration strategy and to test its ability to recover realistic deformations similar to those expected in a pressurised tumour environment. The estimation of the strain generated by an inflated balloon inside a soft tissue-mimicking cuboid, as well as around solid tumours subjected to external compression in murine and human cases, will follow in Section 4.3. A final discussion on the limitations of the registration strategy in the investigated cases is provided in Section 4.4.

4.1. Image Registration in Medical Imaging

4.1.1. Overview of Existing Image Registration Methods

Image registration is the process of warping of one or more images to match another one. The goal of image registration is to determine a spatial relation between each voxel of the deformed image, or moving image $I_M(\boldsymbol{X})$, and the corresponding position in the fixed image $I_F(\boldsymbol{x})$. Mathematically, the registration problem consists in finding the displacement $\boldsymbol{U}(\boldsymbol{X})$ that defines the transformation $\boldsymbol{T}(\boldsymbol{X}) = \boldsymbol{X} + \boldsymbol{U}(\boldsymbol{X})$ such that the deformed moving

image $I_M(\boldsymbol{T}(\boldsymbol{X}))$ best approximates $I_F(\boldsymbol{x})$ by some specified metric.
The concept of image matching and the best registration methodology to employ are greatly dependent upon the information needed from the registration process and the characteristics of the input images. Depending on the application, one can seek structural correspondence between the same anatomical structures, or functional correspondence, where functionally equivalent areas are aligned [204]. The task is relatively simple in the case of a rigid body undergoing a rigid displacement, however it can become extremely complicated in the case of a non-rigid deformation of elastic and deformable objects, where an ideal transformation that produces a perfect matching is rarely achievable. By definition, a rigid transformation is a combination of a rotational and translational motion and, in a 3D space, is defined by 6 parameters. Historically, this transformation was successfully employed for the registration of multi-modal images of the same patient, where a rigid body approximation was usually sufficient to compensate for the little displacement [205, 206]. The affine transformation is the simplest example of a non-rigid deformation, which adds global shear and scaling properties to the rigid object. With the exception of a few rigid structures, however, the deformation of the anatomical parts of the human body cannot be described by such approximations [207]; therefore, nowadays, rigid and affine transformations are only used for the registration of bones [208] or as pre-registration to obtain a better initial alignment prior to a curve registration [209, 210]. Given the low resolution and the high level of noise, affine registrations are sometimes also used with ultrasound images [211].
The majority of the registration algorithms used in medical imaging, on the other hand, are now based on curvilinear transformations, to adapt to the non-rigid behaviour of human soft-tissues during imaging or surgery [212]. Obviously, much work is still being done to optimise and improve the performances of registration algorithms that rely on non-rigid transformations, which are generally characterised by: 1) a longer computation time compared to their rigid counterparts, due to the comparatively high number of parameters to be estimated; 2) an asymmetric resulting transformation, which describes only the pixel-wise warping of the moving image to match the fixed one and not the inverse; 3) the possible existence of more than one deformation field that returns an equally good alignment, especially when the registration is based on geometrical features [204].
The definition of the model used to describe the transformation is only one part of the implementation of a registration algorithm; a similarity measurement, to evaluate the quality of the alignment between the two images, and an optimisation process to iteratively find the parameters that minimise the cost function are also essential requirements. Traditionally, similarity measurements operate in the spatial domain of the images and can either be geometric based, where the anatomical information provided by sparse features contained in the image is used, or match the voxel characterised by a similar intensity in

the so-called intensity-based methodologies. Commonly, these methods are based on the correspondence between control points that are manually or automatically selected in the images to be matched. The deformation of the regions around the control points is propagated by interpolation. Of course, a finer control point grid results in a more accurate registration, at the expense of its computing time [213, 214]. Rigid or affine registration algorithms based on voxel intensity have shown robust alignment in multi-modality image registration [215], although the same results are hard to achieve with non-rigid transformations, due to the common assumption of constant intensity between the two images included in most algorithms based on elastic or fluid deformations [216, 217, 218, 219]. Alternative methodologies operating in the frequency domain have also been developed, achieving optimal results with simple transformations [220].

4.1.2. Non-Rigid Image Registration

Most of the real-world applications of image registration in clinics focus on the use of non-rigid transformations [204]. These techniques are necessary as the deformations are normally complex and will not be able to be represented by simpler transformations, such as rigid or affine. In general, image registration algorithms can be divided into two categories according to the non-rigid transformation employed: in the case of guided transformations, material properties are assigned to the various structures in the moving image, so that the deformation is guided by a physical model; on the contrary, in the case of free-form deformations (FFD), no physical constriction is enforced and any deformation is permitted.

Among the most used transformations employed over the last two decades is the family of splines. Spline-based algorithms have been developed in various forms, all of which make use of spline functions to maximise the correspondence of those points away from the control points. Thin-plate spline (TPS) [221] is a guided coordinate transformation based on deformable solid properties [222]. In the algorithms that make use of TPS interpolation, the similarity measurement is regularised by a bending energy term [223]. TPS-based registrations are global, as a perturbation in the position of one of the control points has an effect on the whole deformation; this is one of the issues with TPS, as it limits the complexity and the variability of the control point grid [204]. It has also been argued that the use of TPS models might be more appropriate in the design of metal plates rather than for medical imaging problems [214], although an extensive use has been made in the field of schizophrenia brain imaging [224, 225, 226].

Elastic models based on elastic body splines (EBS) represent an outgrowth from TPS and are developed following a similar procedure [214]. Unlike TPS, however, the development of which was based on the bending of a thin metal sheet, EBS technique treats the content of the 3D image as a homogeneous, linear-elastic solid subjected to deformation forces

obtained from the similarity measurement [227]. Linear elasticity can provide a good description of the mechanical behaviour of many tissues in the human body [214], although this approximation is only valid for small image differences and hence is not ideal for large deformations. The propagation of the transformation in the neighbourhood of the control points is then guided by the equations of Navier until the deformation forces opposed to the internal elastic ones reach an equilibrium [228]. This, like for TPS, is a consequence of the minimisation of an associated elastic energy [228, 229]. EBS is best used for the recovery of the deformation applied to a phantom/patient and there is no reason to use it when no deformation is involved, as in the alignment of multi-modal images. Of course, the quality of the registration can be affected by the assumptions of homogeneity and linear elasticity, which often do not apply to body tissues. EBS also requires the specification of the Poisson's ratio for the calculation of the internal forces, which is not needed for TPS. Lastly, given the coupling of the deformation equations in all three directions, solving the registration problem requires increased computation and storage capabilities compared to TPS.
Similar to EBS, other elastic registrations based on finite element (FE) models divide the moving image into cells and assign a description of the physical properties to each of them [212, 230]. Although these models allow a better control of localised deformations, they are usually difficult to evaluate and can suffer the inter-subject variability of the elastic parameters of tissues [213]. Nevertheless, they have been successfully applied in the field of head surgery [212, 231].

Other guided non-rigid registration techniques treat the registration problem as a diffusion problem. This is the case of the algorithms based on optical flow [232], where the structures in the moving image deform to match those contained in the fixed image, leading to a minimisation of the energy in the physical model employed. A well-known registration technique inspired by the optical flow is the demons algorithm [216]. This non-rigid algorithms is based on Maxwell's demons, introduced to solve the Gibbs paradox in thermodynamics, in the sense that the motion of the content of the moving image is regulated by entities (demons) that act according to local characteristics of the images. The role of polarity becomes crucial in this diffusion model, as the boundaries of the objects in the fixed image are treated as semi-permeable membranes, and the diffusion of the model points through them depends on their inside-outside position. Unlike elastic models, fluid-based transformation allow larger deformations and are sometimes used after elastic registrations [217]. Like the other optical flow techniques, the demons method is fast and can provide very good results, although it also shares the limitation given by the assumption of constant intensity between the images, often broken in the use of medical images. Moreover, the theoretical basis of this algorithm has not been totally understood yet, making it difficult to predict its failures and their reasons [233].

As mentioned earlier, FFD curved transformations allow any deformation and do not rely on the guidance of physical models. This kind of registration usually aims to deduce the displacement of a grid of control points to produce a smooth transformation. The deformation is locally defined, as each individual control point moves following an optimal direction; hence, the scale of the registration is defined by the selected spacing in the grid. The transformation of the regions around the control points is propagated by interpolation: linear interpolation can be found in the literature [234], although B-splines are probably the most popular interpolators [235]. As a consequence, the total transformation of the image is given by the coefficients that determine the combination of the basis function B-splines that optimise the similarity measurement. The great advantage of the registrations based on free-form B-splines, compared to other non-rigid algorithms that make use of control points, like TPS or EBS, is that the deformation is locally supported, which means that the perturbation of a control point affects the transformation only in its vicinity. This property makes B-splines particularly efficient under a computational point of view, although it introduces the necessity for an initial alignment of the images to correct for global misregistrations [213]. On the downside, this technique can require special measures to prevent folding, which can become more difficult at finer resolutions [204].

For the inflation experiment developed and presented in Chapter 3, we require a nonrigid image registration technique to map and quantify the strain generated by the simulated pressurised tumour onto its surroundings. The image registration strategy must be able to handle the large inflations required to probe the nonlinear behaviour of the plastic material chosen to mimic the mechanical properties of soft tissue. A local approach is preferable, especially to account for the more complex deformations that can be encountered in an *in vivo* or clinical scenario, when additional endogenous and external forces come into play. The chosen registration strategy, together with its optimisation and validation through the use of a ground truth *in silico* model is presented in the following section.

4.2. Development of a Ground Truth *in Silico* Model

In order to implement an image registration strategy capable of estimating the strain generated by an expanding tumour, we developed a ground truth *in silico* model where a high resolution image was subjected to realistic deformations. Such an image was embedded into a mesh grid that can be deformed according to physical constraints using numerical methods. This would provide a ground truth deformation field to be compared with the one estimated from the image registration process. Furthermore, the use of an anatomical MR image of a tumour mass allows to optimise the registration process on a real contrast image, hence granting improved performances in clinical cases. This section

will present the details of the implemented image registration process and its validation using the developed ground truth model.

4.2.1. Image Embedding

To apply a realistic deformation to a high resolution anatomical image, we embedded the selected image into a tetrahedral mesh grid using Matlab's interpolation algorithm `griddata`. The element quality as well as the number of tetrahedral elements are important characteristics of the mesh grid, as they define the quality and computational time of the interpolation process. The tetrahedral grids employed for the *in silico* model were produced using the modelling software COMSOL Multiphysics®, which ensured a good element quality, an example of which is given in Fig.4.1-A. A higher number of elements results in a better sampling of the embedded image and in a higher resolution of the grid (Fig.4.1-B): in our case we have used ~2.9 node/voxel for each interpolated image, regardless of its resolution, leading to a sub-voxel sampling. The intensity of each node can then be re-interpolated into a voxel grid using the Gauss-Legendre quadrature. Fig.4.1-C shows the comparison between the original image, I1, and the same image after interpolation into a mesh grid and re-interpolation into a voxel grid, I2; the percentage difference between the voxel-wise intensity of the two images, given as

$$\text{Difference}_{\%} = 100 \times \frac{1}{N} \sum_{vox=1}^{N} \frac{\text{I1}_{vox} - \text{I2}_{vox}}{\text{I1}_{vox}} \tag{4.1}$$

reveals that the whole process produces an average error of ~10 %, with higher values in correspondence of the darkest regions and where edges are more pronounced. Image embedding into a mesh grid allows to include the physics of the deformation into the model and to test and optimise the image registration method onto 3D images characterised by real contrast. An example of all the steps, involving the interpolation of the original image into a mesh grid, its re-interpolation into the previous voxel grid after the application of a deformation field and the final registration process is presented in Fig.4.1-D.

4.2.2. Non-Rigid Image Registration Method and Optimisation

Medical image registration technology has been around for about three decades and a large number of open source software solutions have been proposed (see Oliveira & Tavares (2014) for a comprehensive list [235]). Widely-used open source image registration software packages include ITK [236] and Elastix [237, 238], both coded in C++. We explored the use of SimpleElastix [239], a free open-source extension of the software package SimpleITK (based on the ITK library) that includes the collection of registration algorithms contained in Elastix. SimpleElastix provides two types of curved transformations: one based on B-Splines and one on TPS. In light of its enhanced applicability for non-rigid registration in

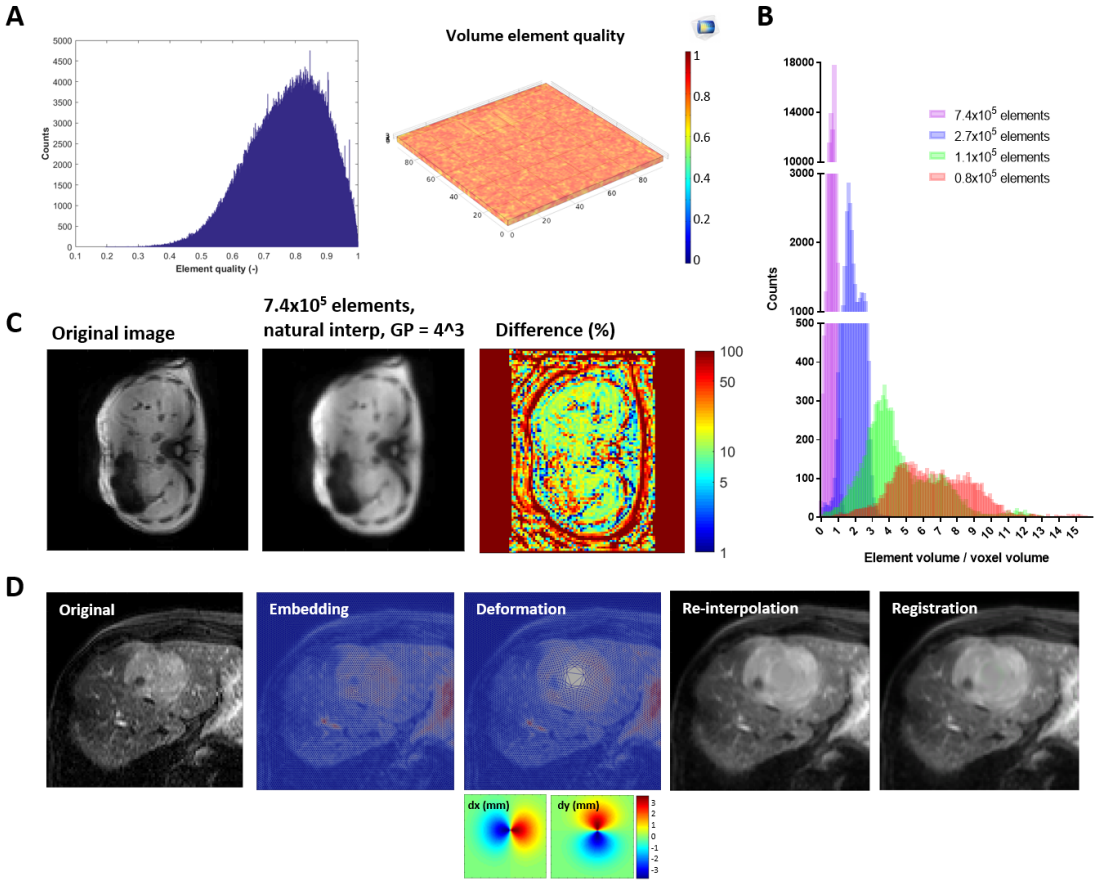

Figure 4.1.: Deformation of embedded image into mesh grid. A) COMSOL Multiphysics® ensured a good element quality throughout the mesh. B) A higher number of elements allows a better sampling of the image, for a more accurate preservation of the features. C) Using a sufficiently fine mesh, the process of embedding and re-interpolation of an image produces an average difference of ~10 % of the original one. D) The generation of a ground truth deformation involves the embedding of the original image into a mesh grid, which is deformed using a known deformation field; the warped image is then re-interpolated from the mesh into a voxel grid and used as objective image for the registration process.

the context of medical imaging and given the need of a transformation capable of correctly estimating the local displacement generated around the inflated balloon, we decided to use the "BSplineTransform", which is based on the B-Splines FFD algorithm presented by Rueckert *et al.* (1998) [213]. This performs a non-rigid registration between two datasets and returns a displacement field which relates the two images. The corresponding Green-Lagrangian strain tensor $\mathbf{E}$ can then be calculated using Eq.2.2. To iteratively find the optimal transformation parameters, the Adaptive-Stochastic Gradient Descent optimisation algorithm [240] was employed, which represents a more robust version of the standard gradient descent. The non-rigid registration algorithm was optimised on a 3D high resolution MR dataset of a liver tumour with a $0.983 \times 0.983 \times 4\,\mathrm{mm}^3$/voxel

resolution and covering a field of view of $137.62 \times 117.96 \times 24\,\mathrm{mm}^3$ with a 1 mm slice gap. The image was artificially warped applying an in-plane radial outward deformation in the form $r' = r + A\,e^{\left(-r^2/(2\sigma^2)\right)}$ centred roughly at the position of the centroid of the tumour. Here r and r' refer to each voxel position prior to and after the deformation, while A and σ are two parameters that scale and shape the deformation field.

Among the many possible components offered by SimpleElastix that can be tuned to optimise the quality of the registration outcome, we have identified a couple of crucial ones to obtain good results in a reasonable computation time. The first one would be the choice of the similarity measure used to iteratively guide the registration. We have investigated the use of four different metrics offered by elastix [237]: mean squared difference (MSD), normalised correlation coefficient (CC), mutual information (MI) and normalised mutual information (NMI). The first row of Fig.4.2 presents the overlay between the objective image and the warped moving image obtained integrating the various similarity measures into the registration process. In the second row, the percentage difference between the

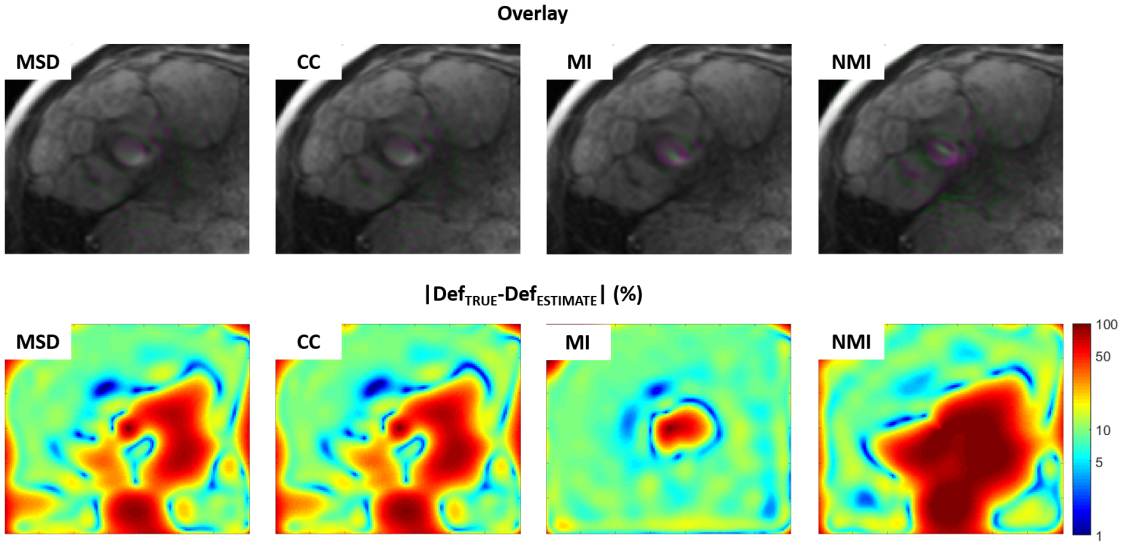

Figure 4.2.: The choice of the metric is an important component of the registration process. The use of different metrics leads to a better or worse matching to the objective image (first row). Based on the percentage difference between the L2-norm calculated for the ground truth deformation and that obtained from the estimated one, MI provides a better agreement between the objective and the warped moving image (second row).

L2-norm of the ground truth deformation and that of the registration estimate shows the local quality of the registration process. The use of the two intensity-based measures, MSD and CC, yields very similar results, with higher percentage errors in the region characterised by a poorer contrast. MI provides a better matching between the warped and objective image, with high errors only in the immediate centre of the radial deformation field and a general difference lower than 10 %. NMI, on the other hand, showed a very

lengthy convergence, obliging to reduce the sampling used to iteratively calculate the similarity measure by a factor of 10. Nevertheless, despite making the computational time comparable with that achieved with the other metrics, the limited sampling produced convergence issues, leading to large errors throughout most of the 3D image. Overall, the use of MI proved to combine an accurate registration to a reasonable convergence time for clinical applications.

The spacing of the grid of control points used in the B-Spline based non-rigid transformation was found to be a second crucial component to determine the quality of the registration. Using the chosen similarity metric, we could see how a too large voxel spacing between the support grid nodes leads to an excessively smooth deformation field, while a too close distance between the control points makes the registration process too sensitive to noise, hence producing an over-fitting (Fig.4.3). The use of more than one resolutions

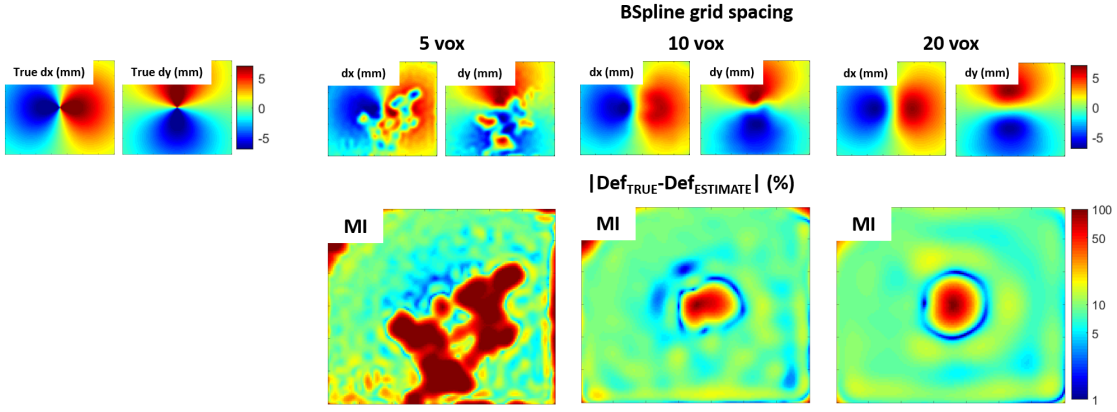

Figure 4.3.: The voxel spacing between each node of the B-Spline grid is crucial for an accurate recovery of the true deformation field. A too wide spacing could not be able to correctly capture the true deformation, while a too narrow spacing can lead to over-fitting.

with an increasing grid density helps matching subsequently smaller structures up to the final precision.

Many other components need to be carefully tuned to successfully perform the non-rigid registration and some chosen examples are presented in Table 4.1. For an explanation of the meaning of each parameter, the Elastix manual should be consulted [237].

4.2.3. Validation on Simulated Realistic Deformations of a Real Image

To validate the implemented non-rigid image registration scheme, we have applied a range of realistic deformations to a different high resolution T2-weighted anatomical MR image of a solid liver tumour embedded into a tetrahedral mesh. The ability to recover the ground truth deformation will provide an insight into the potential and the limitations of the registration process. To simplify and accelerate the testing protocol, the extent of the

Component	Choice	Component	Choice
Registration	MultiResolutionRegistration	Transform	BSplineTransform
Metric	AdvancedMattesMutualInformation	BSplineTransformSplineOrder	3
NumberOfHistogramBins	128	FinalGridSpacingInVoxels	5
ImageSampler	RandomSparseMask	GridSpacingSchedule	6.0 2.5 1.0
NumberOfSpatialSamples	1000 5000 15000	Optimizer	AdaptiveStochasticGradientDescent
MaximumNumberOfSamplingAttempts	8	NumberOfSamplesForExactGradient	4096
NewSamplesEveryIteration	true	MaximumNumberOfIterations	4000 4000 8000
Interpolator	BSplineInterpolator	NumberOfResolutions	3
BSplineInterpolationOrder	5	FixedImagePyramid	FixedShrinkingImagePyramid
Resampler	DefaultResampler	MovingImagePyramid	MovingShrinkingImagePyramid
ResampleInterpolator	FinalBSplineInterpolator	ImagePyramidSchedule	6 6 6 2 2 2 1 1 1
FinalBSplineInterpolationOrder	5		

Table 4.1.: Example of the components used for the non-rigid registration.

chosen dataset in the transverse plane was limited to 3 voxels. The total FOV covered by the image was $192 \times 192 \times 12.8\,\mathrm{mm}^3$ with a resolution of $2 \times 2 \times 4\,\mathrm{mm}^3$/voxel and a slice gap of 0.4 mm. Each applied deformation was limited to be in-plane and repeated at each slice. The SimpleElastix registration software was then employed to warp the moving image to match the objective one through a multi-resolution B-Spline approach that follows the implementation presented in the previous section and to extract an estimate of the true deformation field. A mask was applied to focus the registration on the regions of interest. Synthetic phantoms of increasing complexity in strain field were constructed as follows:

1. We initially tested the registration on a 2D affine transformation of the image, involving rotation and shear. This simple case was chosen to gain an understanding of how well the registration software can deal with a global deformation.

2. We then applied a radial inflation to the underlying mesh, centred in the mid-position of the tumour. This deformation was thought to reproduce an ideal spherical expansion of the core of a tumour due to internal pressures.

3. Incompressibility was then included in a finite element method (FEM) simulation of a uniaxial deformation of the embedded image in a tetrahedral grid using COMSOL Multiphysics®. Zero displacement was imposed to one side of the mesh and a load resulting in a 10 % compression to the other. Linear elasticity was assumed, with an isotropically distributed Young's modulus of 1 kPa, density of $1000\,\mathrm{kg\,m}^{-3}$ and Poisson's ration of 0.499. The numerical solution of the physical problem defined by such conditions aimed to provide a simulation of macroscopically compressed soft tissue.

4. Finally, we tested the registration on a more complex local deformation, where the same five randomly selected points in each slice were subjected to a random in-plane displacement between 3 and 5 mm; the deformation was then propagated to the rest of the image through TPS. Zero displacement was imposed on the four corners of each slice. No physical constraint was applied in this case.

For each deformation, the overlay between the original and deformed images is shown in the first column of Fig.4.4. The second and third columns present a comparison between the

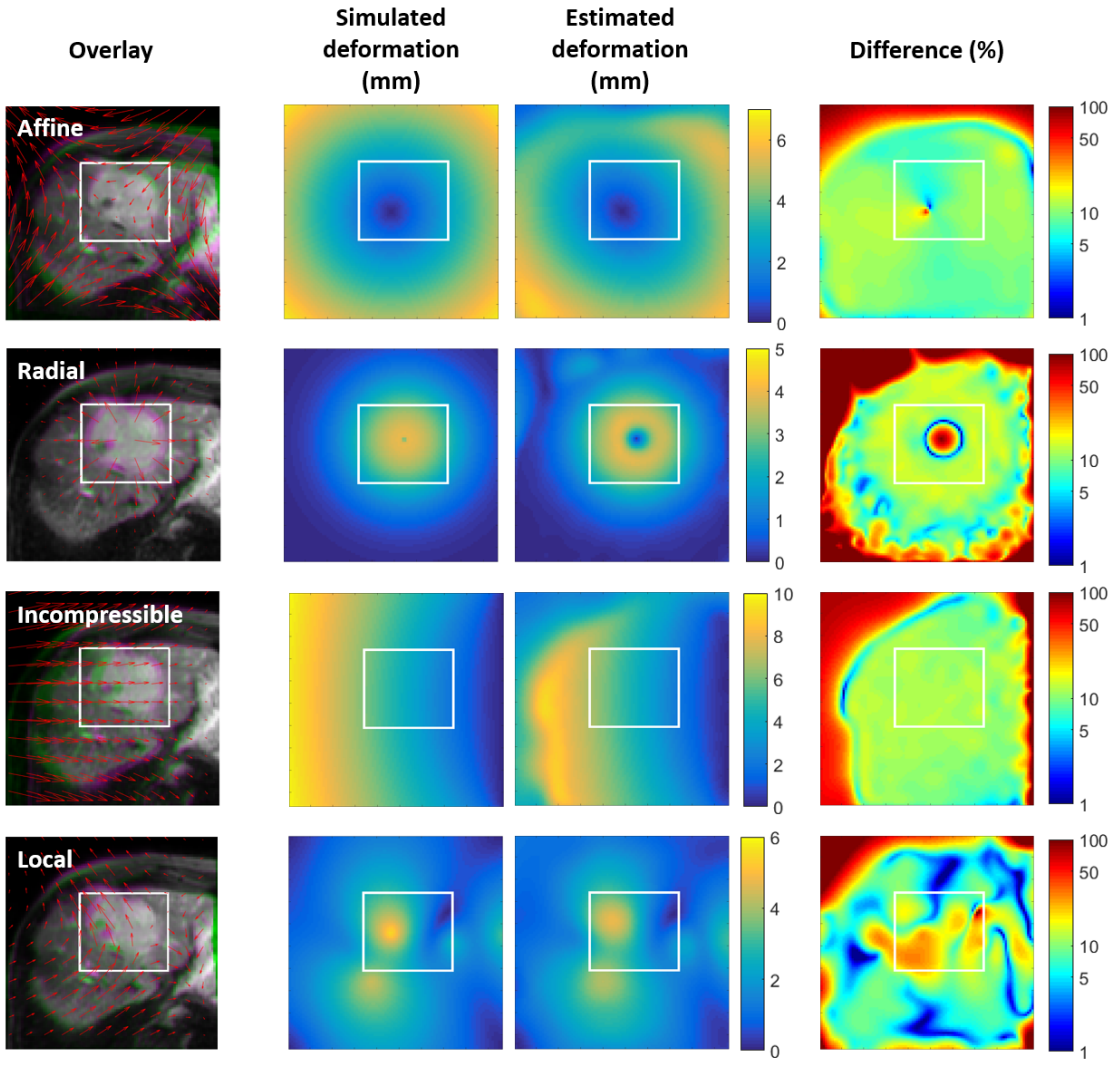

Figure 4.4.: Four different deformations were applied to the same liver tumour image to validate the implemented registration on a real contrast image. First column) Overlay between the original (green) and deformed (magenta) image. The red lines represent the applied deformation field. Second column) L2 norm of the true deformation field used to generate the objective image. Third column) Estimated deformation field provided by image registration. Fourth column) Percentage difference between the estimated and real deformation normalised over the latter. The location of the tumour mass is highlighted in all images.

L2 norm calculated for the true and the estimated deformation fields, while the percentage difference with respect to the true deformation is shown in the fourth column. This percentage difference represents the pixel-wise error in the estimation of the true image deformation and is the chosen metric to indirectly assess the quality of the registration process in this particular context. A good estimation is particularly important in the

3-dimensional region of interest (ROI) where the tumour is located, which is highlighted in all the images in Fig.4.4; moreover, a quantification of the fraction of pixels in the ROI with an error of less than 10 %, 15 % and 20 % is provided in Table 4.2. In all four cases,

Deformation	**No. Voxels < error threshold**		
	thresh = 10 %	**thresh = 15 %**	**thresh = 20 %**
$\text{Affine}_{\text{ROI}}$	52.9 %	97.2 %	99.2 %
$\text{Radial}_{\text{ROI}}$	19.2 %	90.1 %	92.0 %
$\text{Incompressible}_{\text{ROI}}$	1.1 %	99.9 %	100 %
$\text{Local}_{\text{ROI}}$	25.5 %	50.4 %	71.8 %

Table 4.2.: Quality of estimated deformation based on relative difference from ground truth.

the registration manages to retrieve the general trend of the deformation. From Table 4.2, however, it is evident that the registration presents some limitations in the accuracy of the estimation, with only a small fraction of the voxels having an error lower than 10 % in three out of four cases. Only in the case of the affine transformation is the quality of the estimation clearly better, with around half of the voxels contained in the ROI having a deformation difference lower than 10 % and with 97.2 % of the voxels falling below the 15 % threshold. The registration of the radially deformed image also presents similar figures for the 15 % error threshold in the tumour region and its immediate surroundings. Due to the nature of this transformation, however, the registration software fails to produce a correct estimate of the deformation in the few mm around the centre of the simulated inflation, with the estimated deformation differing by more than 50 % from the ground truth; nevertheless, connecting this case to the phantom experiment we developed, a good estimation is particularly important at the interface between the balloon and the outside plastic material. This location corresponds to the position of the tumour rim, where the solid and liquid stress components act on the hosting soft tissue, which here lies in proximity of the edges of the ROI. In such regions the errors are clearly lower than 15 %. The implemented registration can also reliably handle the more realistic case provided by the FEM simulation of an incompressible deformation, with a roughly uniform percentage variation over the entire image and with the totality of the pixels in the ROI falling below the 20 % error threshold. The voxel-wise calculation of the determinant of the Jacobian matrix of the deformation field returns an estimation of the local preservation of the volume: the average value in the highlighted ROI is 1.05 ± 0.03 (mean ± s.d.), confirming a good recovery of the incompressibility of the deformation. As regards the last case, despite a still good correlation between the fixed and the warped moving image ($\text{CC}_{\text{ROI}} = 0.9984$), the registration is not quite able to recover the underlying deformation correctly. Compared to the other deformations, in this case half of the pixels in the ROI present a percentage error in the estimated deformation equal or greater than 15 %. This result

identifies a limit to the capability of the implemented registration to deal with contrived complex deformations, especially if involving local displacements in different directions.

4.3. Strain Estimation in Phantom, *in Vivo* Preclinical Images and Patient Data

The implemented image registration method was then used to estimate the deformation generated by the inflated catheter balloon during the inflation experiment. The obtained strain would allow a direct correlation between the applied deformation probed by the shear waves and the variation in shear modulus experimentally measured through MRE. Preliminary tests on *in vivo* preclinical and clinical images of lesions subjected to different macro-compressions were also carried out to assess the employability of this registration scheme in more complex cases, where additional external forces come into play. A list of these tests is reported in Table 4.3.

Phantom	***In vivo***	**Patient**
Foley catheter inside 80 % plastisol cuboid	Subcutaneous tumour in murine model	Breast fibroadenoma
4 levels of radial inflation	3 levels of uniaxial compression from one side	3 levels of external compression
	Images from collaborators at LBI, INSERM, Paris (F)	Images from collaborators at KCL, London, (UK)

Table 4.3.: List of the test carried out to assess the quality of the image registration in different settings.

4.3.1. Balloon Inflation

For the inflation experiment, the balloon was inflated with four different volumes of water and MR images of each state were acquired. Non-rigid image registration was carried out to warp the image of the deflated balloon to match that of each inflation state. Overlay of the central slice of the images before and after the registration, presented in the first and second columns of Fig.4.5 showed an adequate alignment in all cases. The estimated displacement, reported in the third column, is close to zero in the first two inflated states; this can be ascribed to the uncertainty in the injected volume discussed in Section 3.3.3, as the segmented volume was much lower than the injected one (0.02 and 0.07 mL instead of 0.1 and 0.2 mL). The deformation obtained for the two other states reveals a favourite direction of inflation of the balloon and reports a generated displacement up to ~4 mm. A vectorial representation of the deformation field is presented in the fifth column. Given the spherical nature of the deformation, the use of polar coordinates is more appropriate for the estimation of the generated strain. The fourth column reports the circumferential strain induced by the growing inclusion onto the surrounding material. As expected the

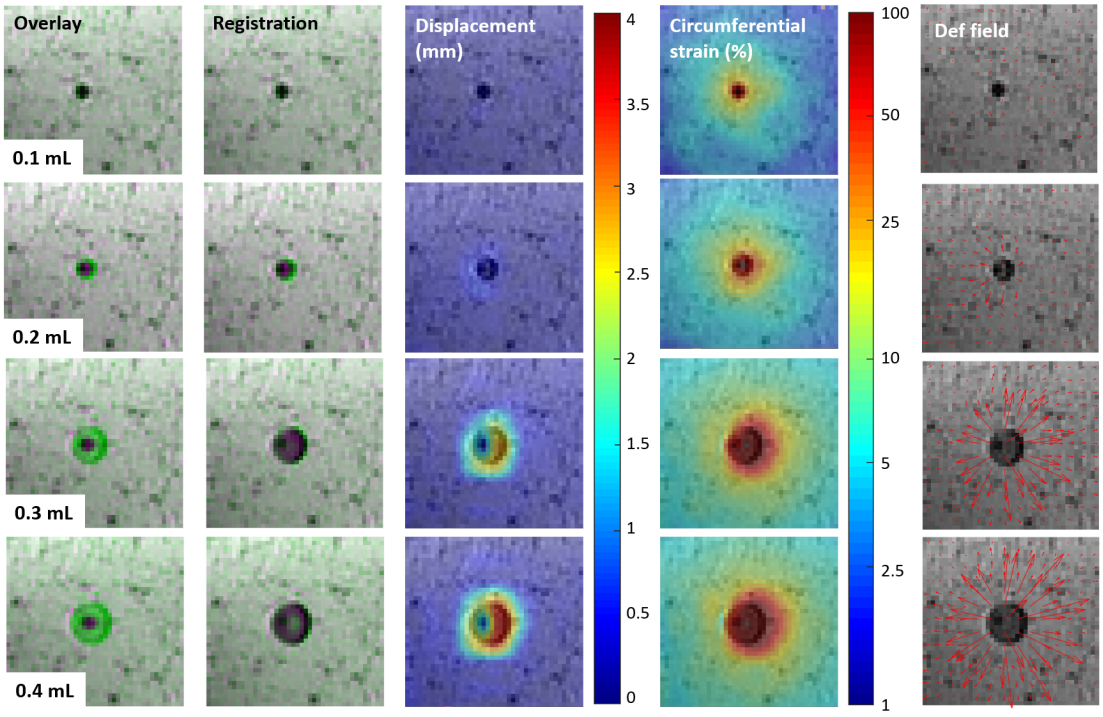

Figure 4.5.: First column) High resolution MR images of the inflated balloon overlaid on the corresponding image of the deflated state. Second column) The deflated balloon is warped to match each inflation state. The quality of the registration is confirmed by the low number of non-matching features in green and magenta. Third column) L2 norm of the deformation field estimated through the registration process. Fourth column) Circumferential strain calculated from the estimated deformation. Fifth column) Vectorial representation of the estimated deformation field.

strain gets more intense with the amount of water injected inside the balloon and, in line with the results obtained in Section 2.4, fades quickly to less than 10 % just a few mm away from the edge of the inclusion, which can however represent a limitation for the detection of the associated shift in shear modulus in the phantom investigation.

4.3.2. Murine Tumour Compression

The implemented image registration strategy was further tested on *in vivo* MR images of subcutaneous tumours implanted in a murine model (provided by LBI, Université Paris Diderot, Sorbonne Paris Cité, Inserm). The tumour masses were subjected to several levels of uniaxial compression, leading to the generation of complex strain patterns due to the heterogeneous biomechanics of the malignancy and of the surrounding soft tissue. A reasonable strain estimation could be useful to investigate the rheology of the lesion and of its host tissue and, in combination with MRE data, to explore the associated impact on their biomechanical properties.

Here, two datasets were employed: the first mouse dataset (Mouse 1) contains 130 ×

$100 \times 130\,\text{voxel}^3$ images with a $0.2 \times 0.2 \times 0.197\,\text{mm}^3$/voxel resolution. The images from the second dataset (Mouse 2) have the same resolution but a different size: $130 \times 100 \times 150\,\text{voxel}^3$. The anatomical images are presented in Fig.4.6. Here, c0 refers to the uncompressed case, while c1, c2 and c3 refer to the compression generated with a 1, 2 and 3 mL inflation of the employed balloon. For both datasets, the registration produced

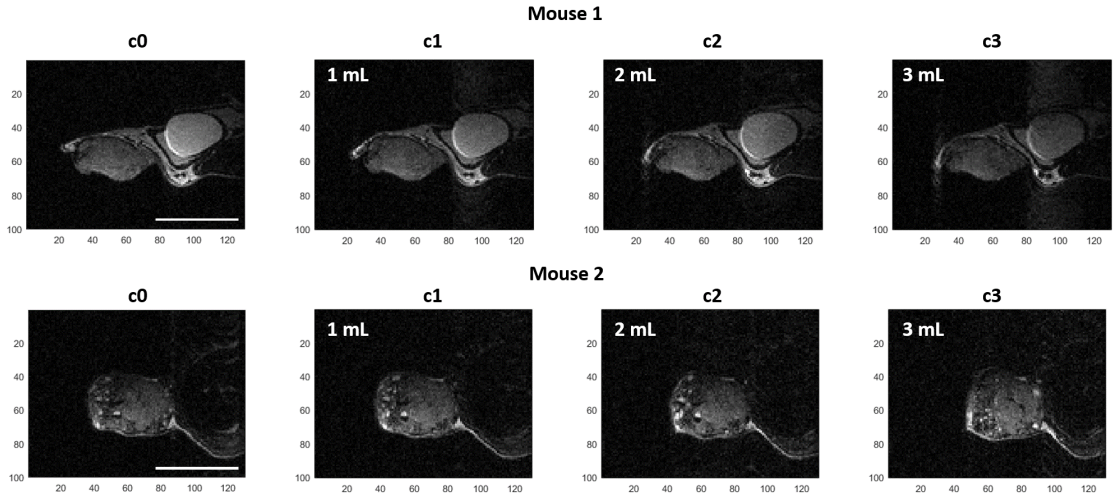

Figure 4.6.: Anatomical images used for the registration process to estimate the generated strain at the various levels of compression. Here c0 refers to the undeformed state while c1, c2 and c3 refer to the injection of 1 mL, 2 mL and 3 mL of air inside the balloon used to apply the compression. The top row shows the images obtained from Mouse 1, while in the second row are the images from Mouse 2. Size bar = 10 mm

more accurate results when attempting to register each state to the subsequent one (e.g. c0 to c1, c1 to c2, etc.), hence estimating a smaller deformation, rather than warping the uncompressed state to match all the others. The overlay between the image of each state (moving image) and the subsequent one (objective image) are presented in the first row of Fig.4.7-A1 and -B1 for Mouse 1 and Mouse 2 respectively, while the second row shows the overlay obtained after the non-rigid registration. For all cases, it is immediately apparent that the number of non-matching features dramatically diminishes with the warped images, confirming the quality of the registration scheme when applied to this case. The quality of the registration was quantitatively assessed calculating CC over the tumour region: this test has been carried out using the original images together with the objective ones and comparing the results with those obtained using the registered images, warped using the estimated deformation field, and the objective ones (Fig.4.7-A2 and -B2). While in Mouse 1 the first comparison (blue bars) produces roughly the same score throughout all 3 compression cases, the amount of overlaid features decreases dramatically in the c1toc2 and c2toc3 cases of Mouse 2, where the applied deformation is larger, as visible from the overlaid images. In the light of a smaller deformation, the registration produces a better

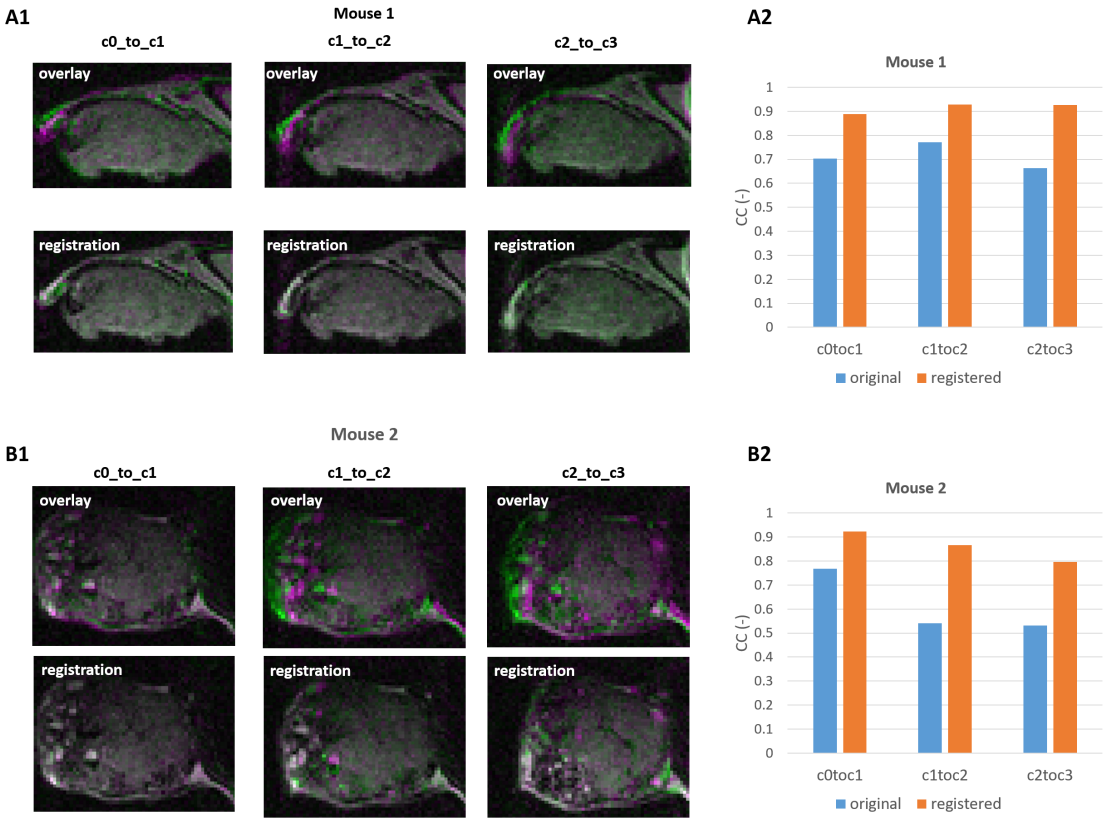

Figure 4.7.: A1,B1-top row) Overlay of the moving (green) and objective image (magenta) prior to the registration. A1,B1-bottom row): Overlay of the warped (green) and objective image (magenta) after the registration process. The columns correspond to the registration of the compressed state c0, c1 and c2 to match the subsequent state, respectively. A2,B2) The quality of the registration has been assessed calculating the correlation coefficient for both mice. The blue bars show the score obtained when comparing the objective image with the original one prior to the registration, while the orange bars refer to the same test applied to the objective and moving image after the registration. For this test, only the voxels inside the mask were considered.

score (orange bars) in the Mouse 1 case, with an average CC of 0.91, than in the Mouse 2 case, where the average CC is 0.86. Nevertheless, the improvement in the image matching is more evident in the latter, where CC improves by 20, 60 and 50 % in the c0toc1, c1toc2 and c2toc3 cases, compared with the 27, 20 and 40 % of Mouse 1.

We also assessed how accurately the registration process could handle the assumption of incompressible soft tissue through the pixel-wise calculation of the determinant of the Jacobian matrix associated to each estimated deformation field. The obtained histograms for Mouse 1 and Mouse 2 are shown in Fig.4.8. All histograms are normally distributed around 1 with a reasonably small standard deviation from the mean value and no outliers, confirming the validity of the incompressibility assumption. As expected, the distribution

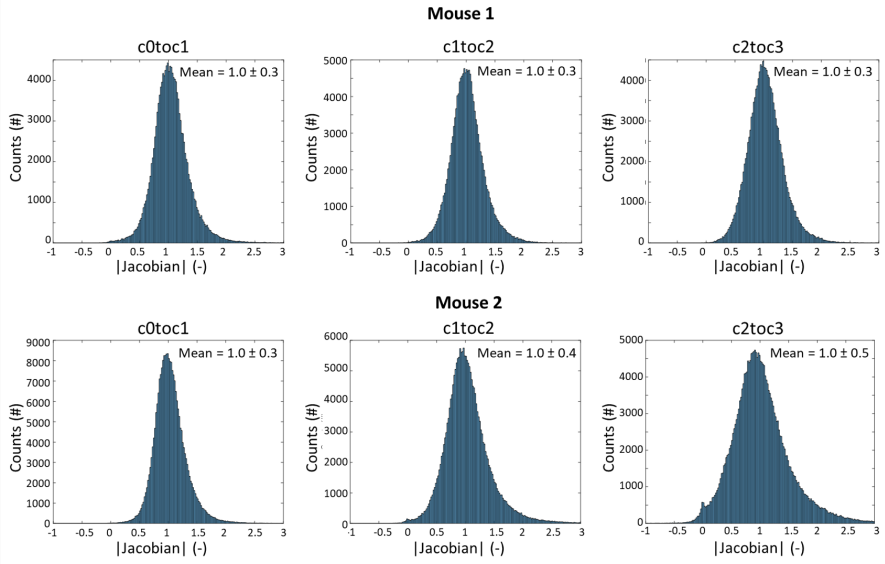

Figure 4.8.: To assess the incompressibility of the deformation fields estimated through the image registration, the determinant of the Jacobian matrix of the transformation was calculated for each voxel of the masked tumour and plotted as a histogram for all the registered states. A mean value of 1 and a small variance reflect a good fulfilment of the incompressibility hypothesis. Values are reported as mean ± s.d.

gets slightly broader in Mouse 2 in the c1toc2 and c2toc3 cases, where the deformation is larger and hence more difficult to be correctly estimated.

The deformation field extracted from the image registration of the various states is presented in the first row of Fig.4.9-A for Mouse 1 and in Fig.4.9-B for Mouse 2. In the c0toc2 and c0toc3 cases, the deformation field has been obtained combining the deformations estimated from the registration of the previous states. The arrows clearly confirm the uniaxial compression of the tumour in both datasets, directed from the left-hand side of the images to the opposite side. It is also evident how the intensity of the estimated deformation rises at higher compression levels. The maximum shear strain $E_{\mathrm{mss}} = (E_{\max} - E_{\min})/2$ was obtained from the difference between the maximum and minimum eigenvalue of the Green strain tensor $\boldsymbol{E}$ and is presented in the last row of Fig.4.9-A,B.As expected, no strain is generated at the lowest level of compression. As for the other two compressions, in Mouse 1 a maximum of 15 % shear strain is generated at the tumour border, especially in the region where the deformation is more intense. On the other end, in the Mouse 2 case the shear strain is more homogeneously distributed throughout the tumour, reaching peaks of 25 %. The implantation of the tumours in close proximity to the skin of the mice, however, made it impossible to get a clear estimation of the strain generated on the soft tissue surrounding the lesion.

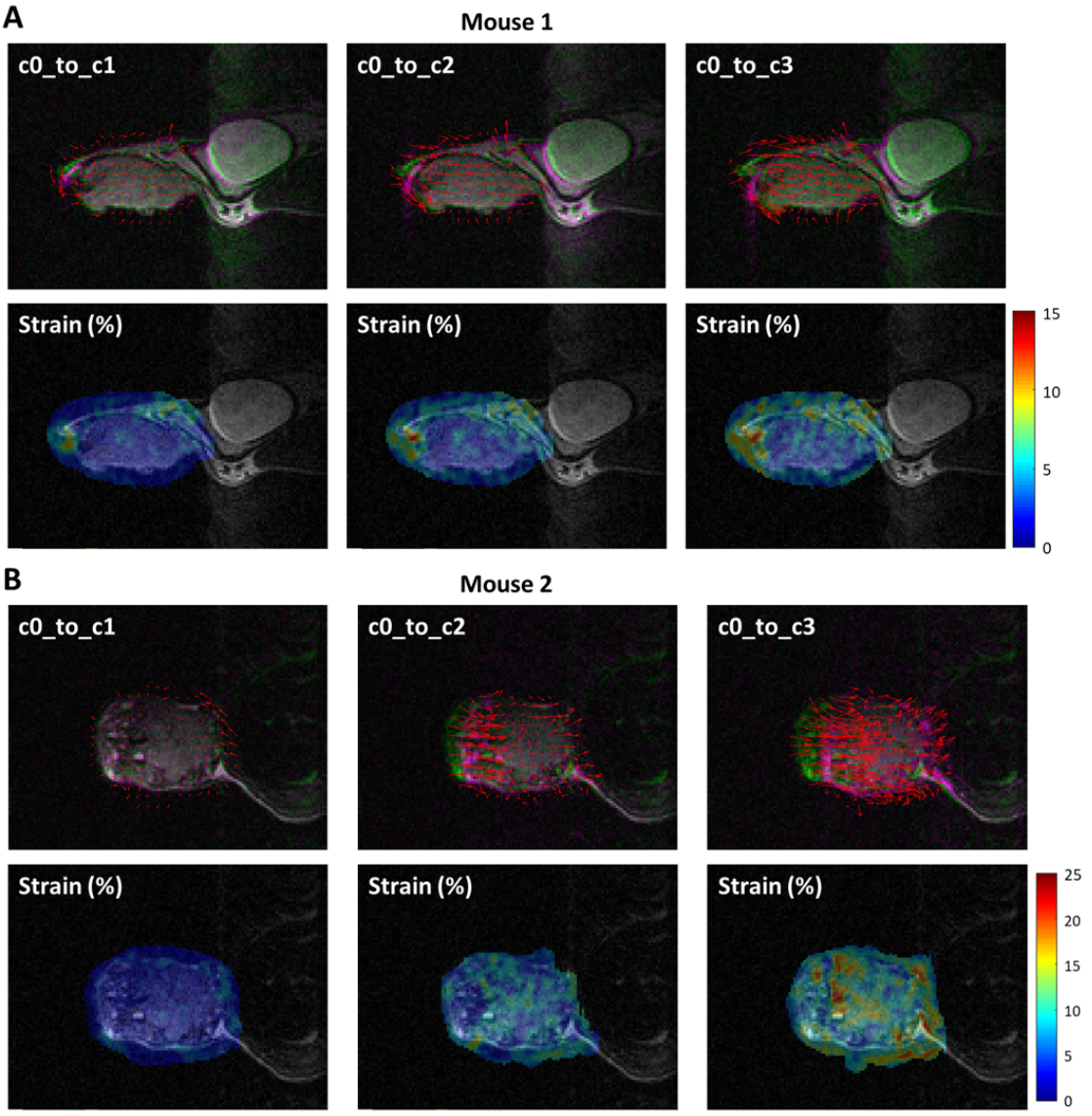

Figure 4.9.: A,B-top row) Estimated deformation fields superimposed to the overlaid original (green) and objective images (magenta). A,B-bottom row) The corresponding maximum shear strain increases with the magnitude of the compression in a heterogeneous way throughout the tumour.

4.3.3. Breast Fibroadenoma

Finally we have tested the implemented registration scheme on patient data. In this case, T1-weighted MR images of a breast fibroadenoma in its undeformed state (c0) and when subjected to three different levels of compression (c1, c2 and c3), generated using a specific setup developed in our lab, have been acquired by our collaborators using the same 3 T MR scanner employed for the inflation experiment. The dataset covered a FOV of $142.3 \times 97.9 \times 84\,\mathrm{mm}^3$ and had a spatial resolution of $0.644 \times 0.644 \times 3\,\mathrm{mm}^3$/voxel with no gap between slices. As suggested by Rueckert *et al.* (1999) [213], a global rigid

transformation was integrated in the registration process to ensure the initial alignment and to facilitate the registration process. The mismatch between the rigidly registered images and each subsequent state is presented in the first row of Fig.4.10. The deformation

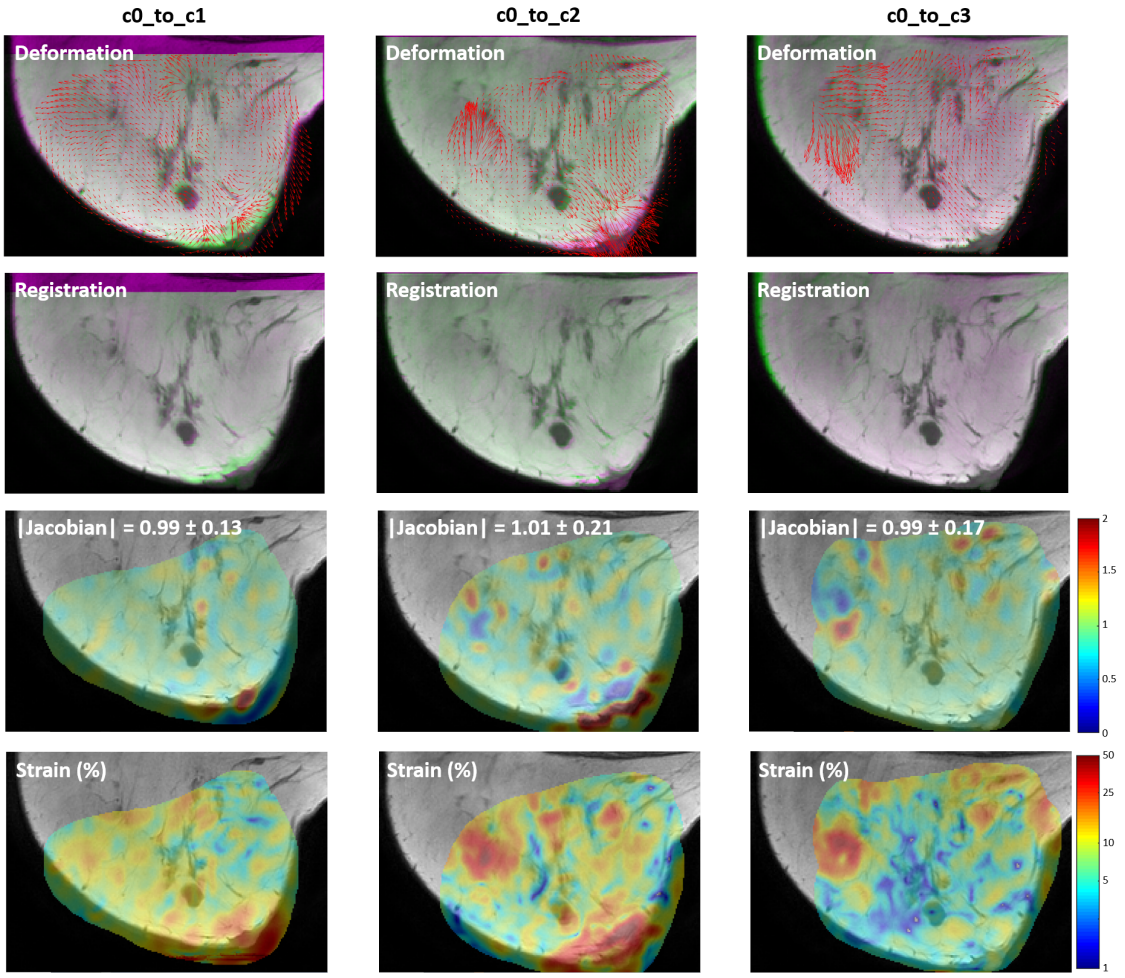

Figure 4.10.: First row) estimated deformation field superimposed to the overlaid original (green) and objective images (magenta). Second row) Image registration dramatically reduces the amount of mismatching features. Third row) The voxel-wise calculation of the determinant of the Jacobian matrix associated to the estimated deformation field reveals the regions where the incompressibility assumption was not respected. Fourth row) Maximum shear strain pattern generated on the breast tissue by the applied compression. Each column refers to the registration of the original image and each of the subsequent compressed states.

field (red arrows) obtained using the implemented non-rigid registration scheme shows the complex patterns caused by the three compressions. The estimated deformation produced a good overlapping between the objective image and the warped moving image in all three cases, as shown in the second row of Fig.4.10. Once again, the incompressibility assumption was globally fulfilled, with the voxel-wise calculated determinant of the

Jacobian matrix associated to each transformation being narrowly distributed around 1. Nevertheless, unlike the c0toc1 and c2toc3 case, in the c1toc2 case some of the voxel-values in the surrounding of the fibroadenoma move far away from the mean value, indicating a possible folding of the deformation field. This is a known disadvantage of B-Spline based non-rigid registration techniques [204], which can produce locally unreliable estimates of the deformation field. The calculated maximum shear strain confirms the complex deformation pattern generated in the surrounding of the fibroadenoma, with each consecutive deformation having a smaller contribution in light of the reduced applied compression as a consequence of tissue nonlinearity.

4.4. Discussion

A list of the main results reported in this chapter is presented in Table 4.4

Main results
A non-rigid image registration strategy was optimised to estimate the local strain generated by a pressurised tumour into its surrounding soft tissue. The quality of the retrieved deformation field was validated in silico through simulated realistic ground truth deformations of a real image of a tumour.
The registration strategy was found to produce accurate deformation estimates in a phantom setting, *in vivo* preclinical images and patient data.

Table 4.4.

In this chapter we have presented the use of a non-rigid image registration strategy to estimate the strain generated by a pressurised solid tumour onto its surrounding soft tissue. The registration method was initially tested and optimised *in silico* on real images subjected to realistic deformations. The image registration proved capable of recovering the ground truth deformation field in the case of radial and incompressible deformations, which represent the main characteristics expected from the mimicked tumour expansion. At the same time, the employed strategy might struggle to correctly estimate more complex tissue displacements that can be encountered *in vivo*, i.e. sliding, limitations that are exacerbated if the amount of features in the ROI is not adequate.

The optimised method was then used to estimate the strain generated by an inflated balloon onto the phantom material from the MR images acquired during the inflation experiments. An adequate alignment between the objective and the registered images at the different inflation states suggests an appropriate recovery of the radial expansion of

the balloon. The alignment between the objective and registered images at the different inflation states supports the quality of the estimate of the spherical deformation caused by the balloon. The intensity of the associated circumferential strain in the periphery of the balloon is enough to probe a nonlinear stress/strain response of soft tissue, as well as of the employed plastisol mixture, as expected from the literature and as empirically assessed in Chapter 5. This is especially true when 0.3 and 0.4 mL are injected in the catheter line.

Mouse and patient images were finally used to test the registration method in real scenarios, where more complex deformations can occur. In both cases, the soft tissue around the tumour was compressed and the generated strain in the tumour rim was estimated. While this was successfully achieved with the patient data, the subcutaneously implanted tumours in the murine models left very few millimetres of tissue around the tumour mass to assess the strain distribution. Nonetheless, both murine datasets allowed a sufficient appraisal of the intra-tumoural strain distribution.

Unlike the phantom case, the registration failed to warp the undeformed state (c0) to match all the other compressed cases in both the mouse and patient images; in these cases, the magnitude of the deformation sets a limit to the reconstruction method, so that it was required to register each state to its consecutive one and to combine the deformation fields. This leads to an accumulation of the errors from each estimate, which, combined with interpolation errors arising from moving each deformation field into the space grid of the image in the subsequent compression state, may affect the accuracy of the total strain estimation further. Even though this uncertainty cannot be avoided, it must be taken into consideration when large deformations are involved.

5. Phantom Material Characterisation

Plastisol was identified in Chapter 3 as a suitable material to replicate the mechanical properties of soft tissue. One of the crucial requirements for the phantom employed to validate the theory developed in Chapter 2 is to display a variation in shear modulus when subjected to strains comparable to those generated by a real pressurised tumour. Different mixtures can in fact be made using different plastisol and softener concentrations, hence producing samples characterised by distinct rheological behaviours [196]. The nonlinearity of the stress/strain curve was characterised empirically through a uni-axial compression test, which helped identify the ideal plastisol concentration required to produce a sufficient change in shear modulus for the inflation experiments. Macro- and micro-compressions, similar to those generated in phantoms in the MRE experiments, were employed to characterise the mechanical behaviour of the phantom material. Since the mathematical framework developed in Chapter 2 was based on a modified version of the Mooney-Rivlin constitutive equation, the capability of this model to predict the mechanical behaviour of the phantom material was assessed. The use of fractional calculus may be adequate to account for any viscous response of the phantom material when subjected to cyclic compression, which was ignored in the analytical formulation developed in Chapter 2.

In the first section of this chapter we will provide an overview of the models found in the literature to describe the general viscoelastic behaviour of soft tissue exposed to cyclic dynamic loading. In Section 5.2, the details of the rheological experiment designed to characterise the mechanical properties of the phantom material employed for the MRE experiments are reported. The mathematical model used to fit the acquired data will also be explained, together with the details of the minimisation process. Section 5.3 will present the results obtained comparing samples containing 0 % and 1 % w/v silica gel, focusing on how the presence of the tracking particles results in an increased nonlinearity of the sample. In Section 5.4 we will show how the modified Mooney-Rivlin and Fung exponential model can predict the viscoelastic behaviour of the material at different PVC concentrations. The best fitting parameters will be presented and a simplified version of the two models will also be proposed, to account for parameter coupling. In addition, the estimated parameters from each model will be used to calculate the shear modulus of the

investigated samples. Finally, the best phantom composition for the MRE experiments will be discussed and the assumptions behind the proposed models will be re-evaluated.

5.1. Model Tissue Viscoelasticity

Biological tissue is usually modelled as a viscoelastic material [45], therefore showing both elastic and viscous characteristics when subjected to deformation. In the case of a homogeneous purely elastic material, the simpler constitutive equation relating one-dimensional shear stress and strain is given by

$$\sigma_{12}(t) = \mu \varepsilon_{12}(t) \tag{5.1}$$

where μ represents the shear modulus of the sample. In the same way, in a Newtonian medium characterised by a purely viscous behaviour, the stress is proportional to the strain rate:

$$\sigma_{12}(t) = \eta \frac{d\varepsilon_{12}}{dt} \tag{5.2}$$

where η represents the viscosity parameter. In the particular test case of dynamic loading, in which a viscoelastic material is subjected to a cyclic strain defined as a complex quantity $\varepsilon^*_{12} = \varepsilon_0 e^{i\omega t}$, the corresponding complex stress will be characterised by the same angular frequency ω, but will accumulate a phase delay δ:

$$\sigma^*_{12} = \sigma_0 e^{i(\omega t + \delta)} = G^* \varepsilon^*_{12} \tag{5.3}$$

Here we have introduced the complex dynamic modulus G^*, defined as

$$G^* = \frac{\sigma_0}{\varepsilon_0} e^{i\delta} = \frac{\sigma_0}{\varepsilon_0} \cos(\delta) + i \frac{\sigma_0}{\varepsilon_0} \sin(\delta) \tag{5.4}$$

The real part of G^* is referred to as the storage modulus G' and is a measure of the stored energy, while the imaginary part, corresponding to the out of phase response and accounting for energy dissipation, is called the loss modulus G'', such that

$$G^* = G' + iG'' \tag{5.5}$$

Using a mechanical analogue, a viscoelastic material can be described using a combination of Hookean springs (elastic component) and Newtonian dampers or dash-pots (viscous component). The simplest models proposed are the Maxwell and the Kelvin-Voigt models. The former consists in a connection of the two elements in series and its constitutive equation is given by:

$$\frac{d\varepsilon_{12}}{dt} = \frac{\sigma_{12}}{\eta} + \frac{1}{\mu} \frac{d\sigma_{12}}{dt} \tag{5.6}$$

Here, both storage and loss modulus display a dependence on the vibration frequency

$$G^* = \frac{\mu(\omega\eta)^2}{\mu^2 + (\omega\eta)^2} + i\frac{\mu^2\omega\eta}{\mu^2 + (\omega\eta)^2} \qquad \text{with} \qquad \begin{cases} G' = \frac{\mu(\omega\eta)^2}{\mu^2+(\omega\eta)^2} \\ G'' = \frac{\mu^2\omega\eta}{\mu^2+(\omega\eta)^2} \end{cases} \tag{5.7}$$

The Kelvin-Voigt model, instead, connects a spring and a dash-pot in parallel, producing the following constitutive equation:

$$\sigma_{12} = \mu\varepsilon_{12} + \eta\frac{d\varepsilon_{12}}{dt} \tag{5.8}$$

In this case, the complex dynamic modulus assumes a particularly simple form, where the storage modulus equals the material shear modulus and the loss modulus is linearly dependent on the vibration frequency:

$$G^* = \mu + i\omega\eta \qquad \text{with} \qquad \begin{cases} G' = \mu \\ G'' = \omega\eta \end{cases} \tag{5.9}$$

While the Maxwell equation was found more suitable to model fluids [51, 241], the Kelvin-Voigt model was an attractive option for different soft tissue tests using elastography [51, 79, 51, 242]. Nevertheless, several researchers have reported shortcomings of the Kelvin-Voigt model in predicting stress relaxation [243] and the frequency dependent complex modulus of more complex viscoelastic media, such as soft tissue [244, 245, 246, 247]. Analysis of several biological components, ranging from individual cells [248] to excised liver tissue [249] have shown that both storage and loss shear modulus present a frequency dependence that can be described with a power law: $G', G'' \propto \omega^\alpha$.

5.1.1. Fractional Viscoelastic Models

Fractional calculus models have been proposed as a simple and effective way to represent the viscoelastic properties of complex systems like soft tissue [250]. These models rely on the replacement of the time derivatives in the constitutive equations with fractional order derivatives, D_t^α, where α defines the non-integer order of the time derivative. The advantage of this formalism consists in the possibility to continuously interpolate the fractional order in the intermediate range occupied by viscoelastic materials: between 0, descriptive of purely elastic solids, and 1, typical of Newtonian fluids. The mechanical interpretation of fractional models is given by the replacement of one or more springs or dash-pots, that describe "classical" solid and fluids, with a network of spring-pots, defined as an infinite ladder of springs and dash-pots, providing a link connecting these empirical models and observation to the molecular theories of polymer solids [244, 246].

In some cases, the non-integer order derivative can lead to an unintuitive behaviour, inherently different from that expected from models containing integer times derivatives, such as the Maxwell and the Kelvin-Voigt models. In the case of the simple spring-pot models introduced in the previous section, by applying a constant strain from time $t = 0$, defined by the strain step function $\varepsilon_0 U(t)$, where ε_0 is the strain magnitude and $U(t)$ is a unit step function

$$U(t) = \begin{cases} 1, & t > 0 \\ 0, & t \leq 0 \end{cases} \tag{5.10}$$

it is possible to test the stress relaxation typical of a viscoelastic material. The resulting stress function $G(t)$ is called the relaxation modulus and is calculated as

$$G(t) = \mu e^{-\frac{t}{\tau}} \qquad \text{for} \qquad \text{Maxwell} \tag{5.11a}$$

$$G(t) = \mu + \eta\delta(t) \qquad \text{for} \qquad \text{Kelvin-Voigt} \tag{5.11b}$$

where $\tau = \eta/\mu$ is the relaxation time and $\delta(t)$ is the Dirac delta function. While, as explained earlier, the Kelvin-Voigt model shows limitation to capture the stress relaxation of many viscoelastic materials, the simple exponential law provided by the Maxwell model is usually not sufficient to describe the more complex behaviour observed in nature. A fractional order constitutive equation can instead provide a more realistic expression for this behaviour through the following power law [251]:

$$G(t) = \frac{\mu}{\Gamma(1-\alpha)} \left(\frac{t}{\tau}\right)^{-\alpha} \quad \text{for} \quad \sigma_{12}(t) = X_\alpha D_t^\alpha \varepsilon_{12}(t) \quad \text{with} \quad \begin{cases} \lim\limits_{\alpha \to 0} X_\alpha = \mu \\ \lim\limits_{\alpha \to 1} X_\alpha = \eta \end{cases} \tag{5.12}$$

Fractional order viscoelasticity models have shown increased accuracy in modelling tissue mimicking materials [252, 253], ovine artery [254], canine liver [249] and have been used to describe the wave behaviour in human MRE experiments on healthy brain and liver [255], as well as on breast lesions [256]. The correct modelling of the elastic and viscous properties of tissue, in fact, becomes particularly important in dynamic elastography imaging techniques, which rely on application of cyclical mechanical forces at a normally monochromatic frequency, and a more accurate material model can increase both the specificity and sensitivity of the clinical diagnosis [257].

In the following sections of this chapter, a viscoelastic model will be developed and used to fit the rheological data acquired from different material samples through the use of a rheometer. While the elastic stress/strain relationship of the material will be described

using a hyperelastic law, the same stress tensor, subjected to fractional derivative, will be employed to reproduce the viscous response of the samples to the applied macro- and micro-compressions.

5.2. Rheological Data Acquisition & Processing

In order to identify a hyperelastic model capable to characterise the viscoelastic behaviour of the chosen phantom material, we set up a rheological test where material samples were subjected to a uniaxial harmonic micro-compression, similar to the conditions generated by the propagating waves used in MRE, superimposed with an additional macro-compression, to characterise the nonlinear response of the selected material when different plastisol concentrations were used.

5.2.1. Sample preparation

Given the necessity to add tracking particles to the phantom in order to estimate the deformation applied by the inflated balloon onto the otherwise featureless matrix, a first rheometric experiment was designed to assess the impact generated by the scattered trackers on the mechanical properties of the phantom material. For this case, three cuboidal samples using a 70 % PVC mixture were prepared. Sample A1 was used as control, while sample B1 contained a 1 % w/v of trackers. Sample A2 followed the same preparation protocol as sample A1 but was obtained using a different PVC batch, to account for batch variability.

A second experiment was then carried out to investigate the stress-strain nonlinearity under different plastisol concentrations. In this case we prepared three samples using 70 %, 80 % and 90 % concentration of plastisol and 1 % w/v of trackers. The details of the samples employed in both the experiments are listed in Table 5.1

		Initial height (±0.5 mm)	Trackers **(% w/v)**	**Plastisol (%)**	**Batch (no.)**
Experiment 1	Sample A1	38	0	70	1
	Sample B1	39.5	1	70	1
	Sample A2	39.5	0	70	2
Experiment 2	Sample A	38	1	70	3
	Sample B	38	1	80	3
	Sample C	37.5	1	90	3

Table 5.1.: Sample details.

5.2.2. Testing protocol

For the two experiments, each sample was positioned between the parallel plates of a BOSE Electroforce 5500 controlled stress rheometer. The height was adjusted to bring the top plate in contact with the top surface of the cuboid. This instrument allows to

apply a compression in the vertical direction ($\sigma_{(3,3)} = \sigma$), keeping the other directions stress-free ($\sigma_{(1,1)} = \sigma_{(2,2)} = 0$), and to simultaneously measure the displacement as well as the load applied on the sample. The tested samples were in turn preconditioned by applying an initial 6 mm compression for 5 min. Afterwards, each sample was repositioned between the plates, compressed to the desired level and subjected to six cycles of 0.5 mm harmonic micro-deformations along the direction of compression at increasing frequencies for a pre-determined period between 40 s and 1 min. This procedure was repeated four times with different levels of compression while alternating the samples to let them relax back to their original shape. At the end of the test, each sample was repositioned and six cycles of 4 mm harmonic macro-compressions were applied around a mean compression of 6 mm for the first experiment and a mean of 5 mm for the second experiment, using the same set of frequencies as in the micro-deformation case. Given the wide range of frequencies investigated and the number of data points for each frequency cycle, a single data acquisition for each sample was deemed sufficient for an accurate modelling of the material viscoelastic behaviour. The details of the protocol are summarstised in Table 5.2, where all compressions refer to the original sample height, while an illustration of the experimental setup and an example of the acquired data are reported in Fig.5.1.

Experiment 1								
Compression		**Frequency (Hz)**	0.1	0.5	1	2	5	10
Micro	5 % 10 % 15 % 20 %	**Duration (s)**	100	40	40	40	40	60
		Sampling freq (kHz)	0.1	0.5	0.5	1	1.25	1
Macro	10 %							
Experiment 2								
Compression		**Frequency (Hz)**	0.1	0.5	1	2	5	10
Micro	7 % 13 % 20 % 26 %	**Duration (s)**	100	40	40	40	40	60
		Sampling freq (kHz)	0.1	0.5	0.5	1	1.25	1
Macro	13 %							

Table 5.2.: Details of the protocol used for the rheological tests.

5.2.3. Data Analysis and Modelling

To model the stress generated by the uni-axial sinusoidal compression, it is convenient to decompose the Cauchy stress tensor into a deviatoric component and a component containing the hydrostatic pressure p, following Eq.2.11:

$$\boldsymbol{\sigma} = \boldsymbol{\sigma}' + p\mathbb{1} \tag{5.13}$$

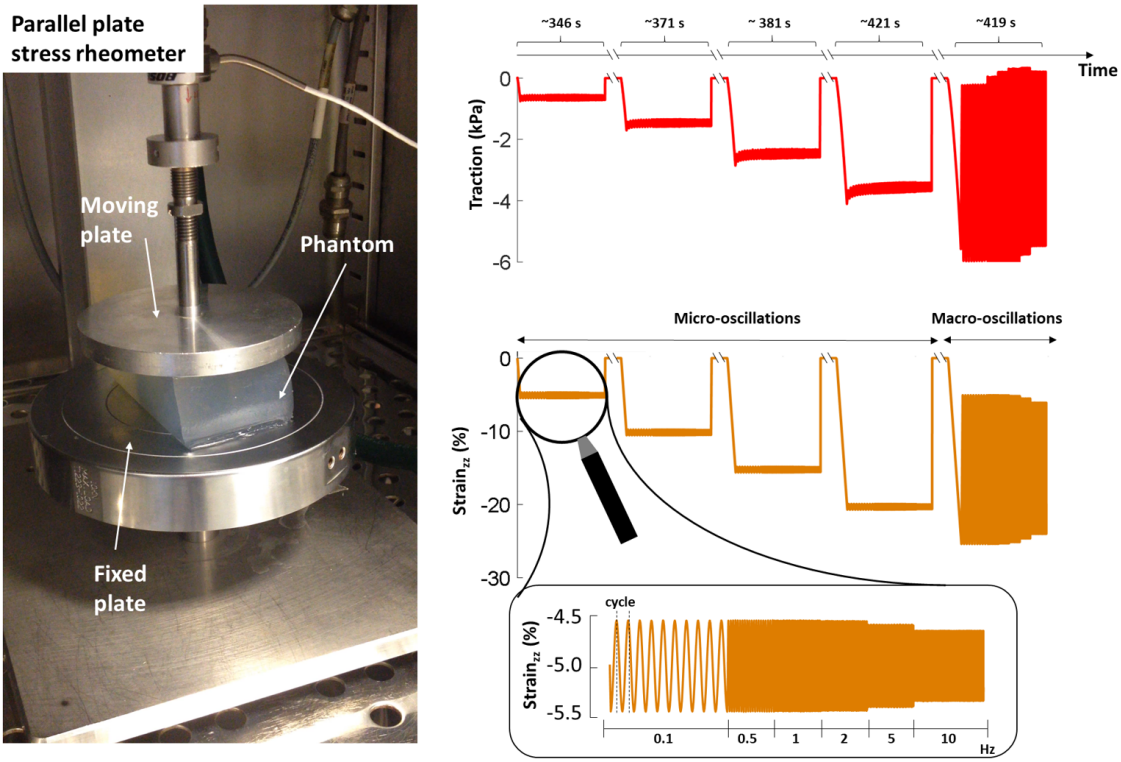

Figure 5.1.: Illustration of the experimental setup used for the viscoelastic characterisation of the phantom material (left). The moving plate was used to apply a fixed vertical compression on the sample and the load was measured through an integrated sensor. For each compression level, the phantom was subjected to four consecutive micro-oscillation and one macro-oscillation test (right). Each of those tests consisted in the application of a series of oscillatory compression cycles centred around the selected compression level at different frequencies, as presented in the zoomed panel.

In order to account for the elastic and viscous behaviour of the material, following the formulation used in Section 2.2, we have assumed a linear superposition of the small-amplitude harmonic deformation on top of the elastic macro-deformation of the sample generated through the rheometer. This assumption was motivated by the separation in scale between the two deformations, with a 0.5 mm amplitude of the micro-oscillations, typically an order of magnitude smaller than the applied macro deformation (5-25 %). Using this assumption, we postulated that $\boldsymbol{\sigma}'$ can be decomposed into the sum of a purely elastic and a viscous component, $\boldsymbol{\sigma}'_e$ and $\boldsymbol{\sigma}'_v$, where the first term captures the stress generated by the elastic macro-compression and the second term accounts for the time-dependent response of the material when the small-amplitude oscillations are additionally applied:

$$\boldsymbol{\sigma}' = \boldsymbol{\sigma}'_e + \boldsymbol{\sigma}'_v \tag{5.14}$$

It follows from above that the PK2 stress tensor can also be written as the sum of an elastic component, S_e and a viscous one, S_v, as:

$$\begin{aligned} \boldsymbol{S} &= \boldsymbol{S}' + pJ\boldsymbol{C}^{-1} \\ &= \boldsymbol{S}'_e + \boldsymbol{S}'_v + pJ\boldsymbol{C}^{-1} \end{aligned} \tag{5.15}$$

The elastic part of $\boldsymbol{S}'$ can be calculated from a chosen strain energy density function W_e in terms of $\boldsymbol{C}$ and its invariants, as presented in Eq.2.63, which is repeated here for simplicity:

$$\boldsymbol{S}'_e = 2\frac{\partial W_e}{\partial I_{\hat{\mathrm{C}}}} J^{-\frac{2}{3}} \left[-\frac{I_{\mathrm{C}}}{3}\boldsymbol{C}^{-1} + \mathbb{1} \right] + 2\frac{\partial W_e}{\partial II_{\hat{\mathrm{C}}}} J^{-\frac{4}{3}} \left[-\frac{2II_{\mathrm{C}}}{3}\boldsymbol{C}^{-1} + I_{\mathrm{C}}\mathbb{1} - \boldsymbol{C} \right] \tag{5.16}$$

Given the uni-axial compression employed and under the assumption of incompressible isotropic material, from the displacement measurements we can calculate the stretch ratio in the vertical direction $\lambda_3 = \Delta h/h = \lambda$, where h is the height of the sample and Δh is its variation under compression, as well as the ones in the in-plane directions: $\lambda_1 = \lambda_2 = \lambda^{-1/2}$. The deformation gradient and the right Cauchy-Green deformation tensor can then be directly calculated from the measured displacement using

$$\boldsymbol{F} = \begin{pmatrix} \frac{1}{\sqrt{\lambda}} & & \\ & \frac{1}{\sqrt{\lambda}} & \\ & & \lambda \end{pmatrix}, \qquad \boldsymbol{C} = \begin{pmatrix} \frac{1}{\lambda} & & \\ & \frac{1}{\lambda} & \\ & & \lambda^2 \end{pmatrix} \tag{5.17}$$

We have chosen to model the viscoelastic behaviour of the tested samples using fractional calculus, as explained in Section 5.1. In the absence of a known model capable of better capturing the viscous response of the employed material, we employed the same hyperelastic law in both the elastic and viscoelastic part of the total PK2 stress tensor, with the latter further subjected to a fractional order time derivative:

$$\mathrm{S}'_e = \mathrm{S}'_e(\boldsymbol{\mu}) \tag{5.18a}$$

$$\mathrm{S}'_v = \mathrm{S}'_v(\boldsymbol{\delta}) = D_t^{\alpha}\mathrm{S}'_e(\boldsymbol{\delta}) \tag{5.18b}$$

where $\boldsymbol{\mu}$ and $\boldsymbol{\delta}$ are the arrays of material parameters characterising the elastic and viscous behaviour of the material, while D_t^{α} represents the Caputo fractional derivative of order α [258], defined as

$$D_t^{\alpha} f(t) = \frac{1}{\Gamma(1-\alpha)} \int_0^t \frac{1}{(t-\tau)^{\alpha}} \partial_t f(\tau) d\tau \tag{5.19}$$

The deviatoric part of the total PK2 can therefore be modelled as:

$$\boldsymbol{S}'(\boldsymbol{\mu}, \boldsymbol{\delta}) = \boldsymbol{S}'_e(\boldsymbol{\mu}) + D_t^{\alpha}\boldsymbol{S}'_e(\boldsymbol{\delta}) \tag{5.20}$$

With the developed formulation, it is now possible to model the deviatoric part of the Cauchy stress tensor, defined in Eq.5.14 as the sum of an elastic and viscous component, using the relationship $\boldsymbol{\sigma}'(\boldsymbol{\mu}, \boldsymbol{\delta}) = J^{-1}\boldsymbol{F}\boldsymbol{S}'(\boldsymbol{\mu}, \boldsymbol{\delta})\boldsymbol{F}^T$:

$$\begin{aligned}\boldsymbol{\sigma}' &= \boldsymbol{\sigma}'_e(\boldsymbol{\mu}) + \boldsymbol{\sigma}'_v(\boldsymbol{\delta}) \\ &= J^{-1}\boldsymbol{F}\boldsymbol{S}'_e(\boldsymbol{\mu})\boldsymbol{F}^T + J^{-1}\boldsymbol{F}\boldsymbol{S}'_v(\boldsymbol{\delta})\boldsymbol{F}^T\end{aligned} \tag{5.21}$$

To work out the total Cauchy stress tensor, $\boldsymbol{\sigma} = \boldsymbol{\sigma}' + p\mathbb{1}$, measured by the rheometer, the hydrostatic pressure p must still be evaluated. To do so, we can exploit the fact that the only stress applied in the rheometric experiments is in the (3,3) direction, because the load is applied along the z-direction on the z-surface. This allows to focus on the component $\sigma_{(3,3)} = \sigma'_{(3,3)} + p$. If we then multiply the stress tensor by the unit vector directed along one of the other two orthogonal directions, say $\boldsymbol{n}_x = (1, 0, 0)^T$, then the result would be zero:

$$\begin{aligned}\boldsymbol{\sigma} \cdot \boldsymbol{n}_x &= \boldsymbol{0} \\ (\boldsymbol{\sigma}' + p\mathbb{1}) \cdot \boldsymbol{n}_x &= \boldsymbol{0}\end{aligned} \tag{5.22}$$

The hydrostatic pressure can then be calculated from Eq.5.22

$$p = -[\sigma'_{e(1,1)}(\boldsymbol{\mu}) + \sigma'_{v(1,1)}(\boldsymbol{\delta})] \tag{5.23}$$

which can be used in combination with the isochoric part of the Cauchy stress tensor in Eq.5.21 to obtain:

$$\begin{aligned}\boldsymbol{\sigma} &= \boldsymbol{\sigma}'_e(\boldsymbol{\mu}) + \boldsymbol{\sigma}'_v(\boldsymbol{\delta}) + p\mathbb{1} \\ &= \boldsymbol{\sigma}'_e(\boldsymbol{\mu}) + \boldsymbol{\sigma}'_v(\boldsymbol{\delta}) - [\sigma'_{e(1,1)}(\boldsymbol{\mu}) + \sigma'_{v(1,1)}(\boldsymbol{\delta})]\mathbb{1}\end{aligned} \tag{5.24}$$

After some simplifications, the (3,3) component of the Cauchy stress tensor can be expressed as:

$$\sigma_{(3,3)} = [\sigma'_{e(3,3)}(\boldsymbol{\mu}) - \sigma'_{e(1,1)}(\boldsymbol{\mu})] + [\sigma'_{v(3,3)}(\boldsymbol{\delta}) - \sigma'_{v(1,1)}(\boldsymbol{\delta})] \tag{5.25}$$

which represents the traction applied on the loaded surface and where $\boldsymbol{\mu}$ and $\boldsymbol{\delta}$ are the free parameters to be estimated from the rheological data fitting.

5.2.4. Parameter Fitting

Our approach to determine the free parameters expressed in Eq.5.25 involves the fitting of the measured traction to the (3,3) component of the Cauchy stress tensor obtained from the compression information using the selected hyperelastic model. For a more complete

insight into the generated nonlinear viscoelastic response, the micro- and macro-oscillatory tests carried out at different compression levels were fit simultaneously. The best estimate was obtained by minimising the objective function that accounts for the difference between the experimental data and the predicted values through linear least squares regression, carried out using the Matlab built-in function `lsqlin`. Given the oscillatory nature of the data, the objective function was defined as the L2-norm of the difference between the Fourier spectrum obtained for the modelled traction and the measured one, normalised over the latter. In detail, for each sample we name t_{ij}^{D} the set of traction data measured in the direction of compression at all time points of the frequency cycle j (for the analysis we have excluded the data points corresponding to the initial loading of the sample) and level of compression i; more specifically, j ranges from 1 to 6 as we have investigated 6 vibration frequencies, while i goes from 1 to 5, as it accounts for the four compression levels chosen for the micro-oscillation tests and the only compression level employed in the macro-oscillation test. In the same way, we name $t_{ij}^{M} = \sigma'_{ij(3,3)}(\tilde{\boldsymbol{\mu}}) - \sigma'_{ij(1,1)}(\tilde{\boldsymbol{\mu}})$ the modelled traction expressed in Eq.5.25, where $\tilde{\boldsymbol{\mu}} = [\boldsymbol{\mu}, \boldsymbol{\delta}]$ is the array containing the combination of the free parameters to be estimated, such that $\boldsymbol{\sigma}'(\tilde{\boldsymbol{\mu}}) = \boldsymbol{\sigma}'_{e}(\boldsymbol{\mu}) + \boldsymbol{\sigma}'_{v}(\boldsymbol{\delta})$. The sum of squares of the difference between the Fourier coefficients $\mathcal{F}(t^{D})$ and $\mathcal{F}(t^{M})$ of the measured and modelled traction defines the objective function for the minimisation process, as well as the fitting error, and is computed as

$$\text{error}_{\%} = 100 \times \sqrt{\sum_{i,j,k} \frac{|\mathcal{F}(t_{ij}^{D})_k - \mathcal{F}(t_{ij}^{M})_k|^2}{|\mathcal{F}(t_{ij}^{D})_k|^2}} \tag{5.26}$$

where the normalisation factor is such that the error reaches 100 % when all free parameters are equal to zero. While this error function does not account for a phase shift between model and data, no shift was observed when comparing the best model prediction with the acquired measurements.

The remaining parameter α, which represents the order of the Caputo fractional derivative, was instead fixed prior to proceeding with the linear regression. The range between $\alpha = 0$ (Hooke's Law) and $\alpha = 1$ (Newton's fluid model) was iteratively investigated, seeking the value that produced the best fit with a ± 0.005 precision.

5.3. Scattered Tracking Particles Increase Material Nonlinearity

Composite materials can have significantly different properties from those of their individual constituents; therefore, the first rheological test aimed at investigating the impact of the addition of motion trackers on the PVC-based sample matrix. We have

initially tried to fit the rheological data with the simple Neo-Hookean material law

$$W_e^{NH} = \mu_1(I_{\hat{\mathrm{C}}} - 3) \tag{5.27}$$

At the same time, we have also attempted modelling the rheological behaviour of the material using the modified version of the Mooney-Rivlin hyperelastic law proposed in Section 2.4, with a polynomial strain energy function truncated to the second order:

$$W_e^{MR} = \mu_1(I_{\hat{\mathrm{C}}} - 3) + \mu_2(II_{\hat{\mathrm{C}}} - 3)^2 \tag{5.28}$$

In contrast to the Neo-Hookean model, a Mooney-Rivlin law can generally produce a better fit of experimental data at the expense of adding an empirical constant. The term containing the second unimodular invariant has been squared to better capture the nonlinear behaviour observed in the data. In both models, plastisol was considered isotropic and incompressible, following the assumptions of Leclerc *et al.* (2012) for the same material [197].

We then used the traction data recorded during the initial loading of the samples prior to the micro-oscillation cycles carried out at the highest compression to quantify the associated nonlinear response of the material (Fig.5.2). Second-order polynomial curves produced a good fit of each of the three datasets: nevertheless, while sample A1 and sample B1 showed a similar linear coefficient, the coefficient scaling the quadratic term was 2.8 times larger in the latter case, highlighting a more nonlinear stress-strain response produced by the presence of the particles at the compression range explored. The quadratic curve used to fit the data from sample A2, instead, showed an intermediate nonlinearity, 1.8 times higher than the corresponding sample A1, as well as a much higher slope, underlining the variability introduced by the use of a different plastisol batch.

The traction data measured from sample A1 and B1, obtained from the same PVC batch in the presence and absence of deformation trackers, were then fitted using the incompressible form of the Neo-Hookean model and of the modified Mooney-Rivlin model, as explained in section 5.2. In the two cases, the elastic part of PK2 in Eq.5.18 assumes the following forms:

$$\mathrm{S}_e'^{NH} = 2\mu_1 \left[\mathbb{1} - \frac{1}{3} I_{\mathrm{C}} \mathbf{C}^{-1}\right] \tag{5.29}$$

$$\mathrm{S}_e'^{MR} = 2\mu_1 \left[\mathbb{1} - \frac{1}{3} I_{\mathrm{C}} \mathbf{C}^{-1}\right] + 4\mu_2 \left(II_{\mathrm{C}} - 3\right) \left[I_{\mathrm{C}} \mathbb{1} - \mathbf{C} - \frac{2}{3} II_{\mathrm{C}} \mathbf{C}^{-1}\right] \tag{5.30}$$

For the viscous terms, S_v^{NH} and S_v^{MR}, the same equations were subjected to fractional derivative and the parameters $\boldsymbol{\mu} = [\mu_1, \mu_2]$ were replaced by the viscous ones, $\boldsymbol{\delta} = [\delta_1, \delta_2]$.

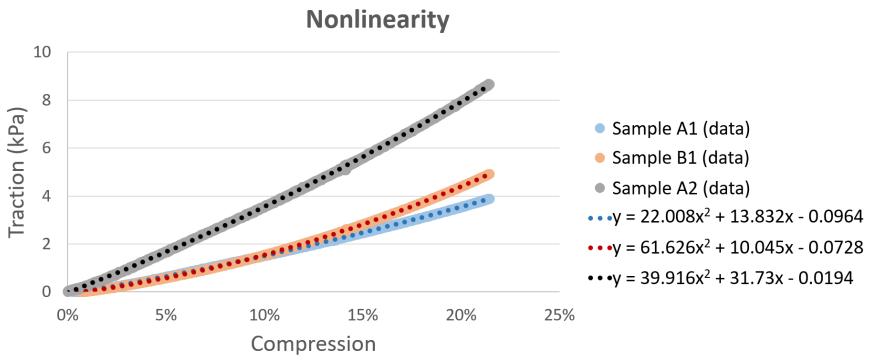

Figure 5.2.: Under the investigated level of compression, the traction data measured from sample B1, which contains motion trackers, show a higher material nonlinearity than sample A1 and A2. The different batch used for sample A2 produced a steeper curve than for sample A1, but a similar nonlinearity. The data are taken from the loading process that leads roughly to a 20 % compression.

5.3.1. Parameter Optimisation

Fig.5.3 shows the error contour for the order α of the fractional derivative that minimised the distance between the data and the model for both the material laws employed. All curves present a global minimum at small values of the fractional derivative order, suggesting a mildly viscous material. The minimising parameters were $\alpha = 0.04$ for the control sample when each model was used and $\alpha = 0.12$ and $\alpha = 0.05$ for the sample containing tracking particles fitted with the Neo-Hookean and the modified Mooney-Rivlin law, respectively. An example of the agreement between the data and the model is presented in Fig.5.4. The selected case corresponds to the best fit of the data obtained with the sample containing the tracking particles using the modified Mooney-Rivlin law, producing a 2.85 % error. Both in the micro- and in the macro-oscillation case, the model could correctly replicate the initial offset generated at different compressions, hence capturing the nonlinear response of the material; furthermore, it successfully reproduced the oscillations generated at the various frequencies, even those where the number of data points per cycle is scarce. In the same way, also the amplitude of the oscillations was well recovered. Finally, the viscous part of the modified Mooney-Rivlin model proved also capable of capturing the relaxation behaviour typical of viscoelastic materials.

The search for the best value of the parameter α led to a very shallow minimum in the fitting error, which keeps roughly constant over values of α that span over a range between approximately 0.04 and 0.2. A closer investigation of the best free parameters estimated at those α values was carried out separately for the two samples for both models. In the absence of trackers, μ_1 and δ_1 appeared coupled in both the Neo-Hookean and the modified Mooney-Rivlin case (Fig.5.5-A1,-A2), so that when the former grows with the increase of α, the latter decreases. The quadratic terms, instead, given the mild nonlinearity of the

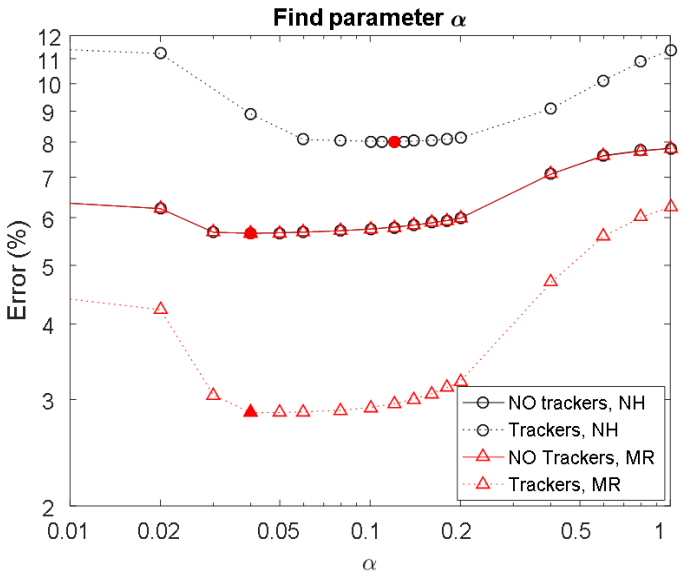

Figure 5.3.: The fractional derivative order that returned the minimised fitting error was investigated for both the Neo-Hookean (black) and the modified Mooney-Rivlin (red) model. While in the absence of trackers the two curves are identical, in their presence the latter provides a better fit of the rheological data. The minimum error in each curve is highlighted using a filled red symbol, however all the curves present a very shallow minimum region that goes roughly from $\alpha = 0.04$ to $\alpha = 0.2$.

pure PVC-material under the considered compressions, appear unnecessary to describe its rheological behaviour and the corresponding parameter values are negligible.
In the presence of tracking particles, instead, the quadratic terms become relevant and the same coupling is visible for both the linear and quadratic parameters (Fig.5.5-A2,-B2).

In light of the parameter coupling, the mean values between the two linear parameters, $(\mu_1 + \delta_1)/2$, and between the two quadratic ones, $(\mu_2 + \delta_2)/2$, were considered, rather than the individual parameters. The average of these combined parameters, calculated over the α range going from 0.04 to 0.2, are reported in Fig.5.6, together with the average error. The bar graph reveals how, in the control case, both models can equally well characterise the material in the absence of trackers, producing the same average error; the quadratic terms appear, in fact, not to be required to fit the data and their value is very close to zero, while the linear terms are equivalent. On the other hand, the nonlinearity introduced by the trackers is such that the Neo-Hookean model fails to accurately reproduce the data, with the average error rising to 8 %. The quadratic terms of the modified Mooney-Rivlin model, instead, grant a superior approximation, reducing the average fitting error to 3.0 %.

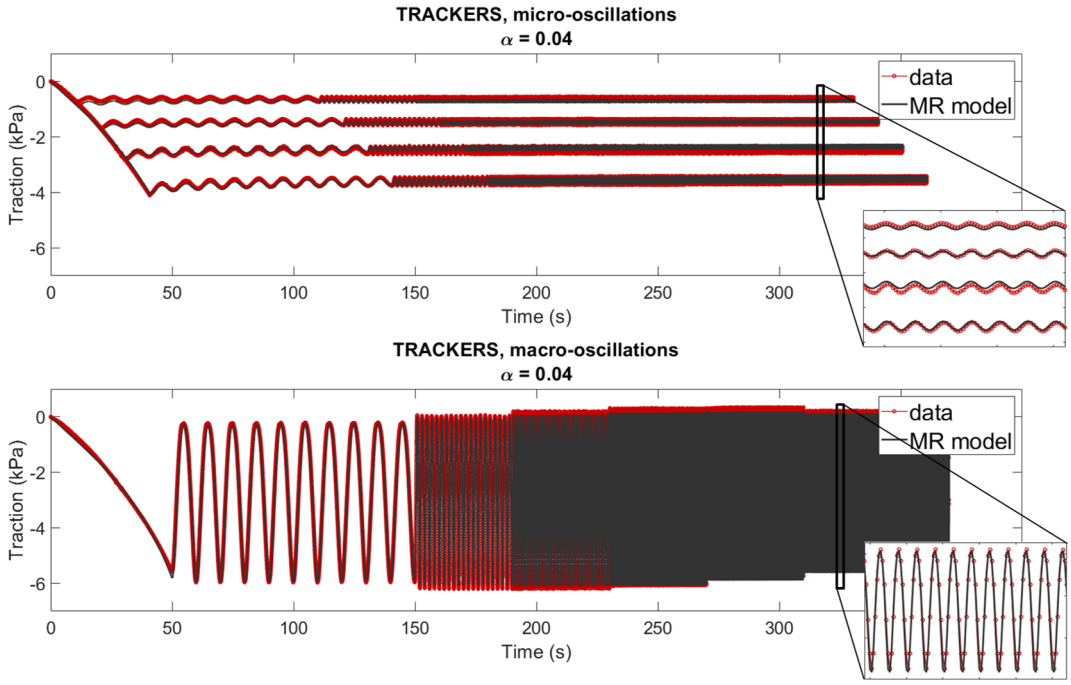

Figure 5.4.: Each sample was compressed to different levels and subjected to various sets of micro and macro-oscillations at different frequencies. Here, the data (red) obtained from the sample containing trackers were fitted to the modified Mooney-Rivlin model (black), with the best agreement obtained for the fractional derivative order $\alpha = 0.04$. Overall the model proved able to reproduce the induced oscillations even at the highest employed frequency. The nonlinear increase in traction was also captured, as well as the relaxation process visible over the explored time-frame.

5.4. Mooney-Rivlin and Fung Models Can Predict the Viscoelastic Behaviour of the Material at Different PVC Concentrations

The second experiment aimed to investigate how the stress-strain nonlinearity of the material is affected by the PVC concentration in the mixture used to prepare the phantoms. Compared to the first experiment, in this case the maximum compression range was extended to reach ~25 %, to better probe the nonlinear response of the material. The traction data recorded during the loading of the samples to the highest compression level were fitted to a quadratic curve (see Fig.5.7), which provided a good approximation in all three cases. The parameter multiplying the quadratic term of the fitting curve, indicative of the nonlinear stress/strain relationship of the material, showed a linear dependence on the plastisol concentration (Pearson's $r^2 = 0.9913$).

From the first experiment, we have shown that the nonlinear behaviour of the sample containing tracking particles is better described by a higher order strain energy density

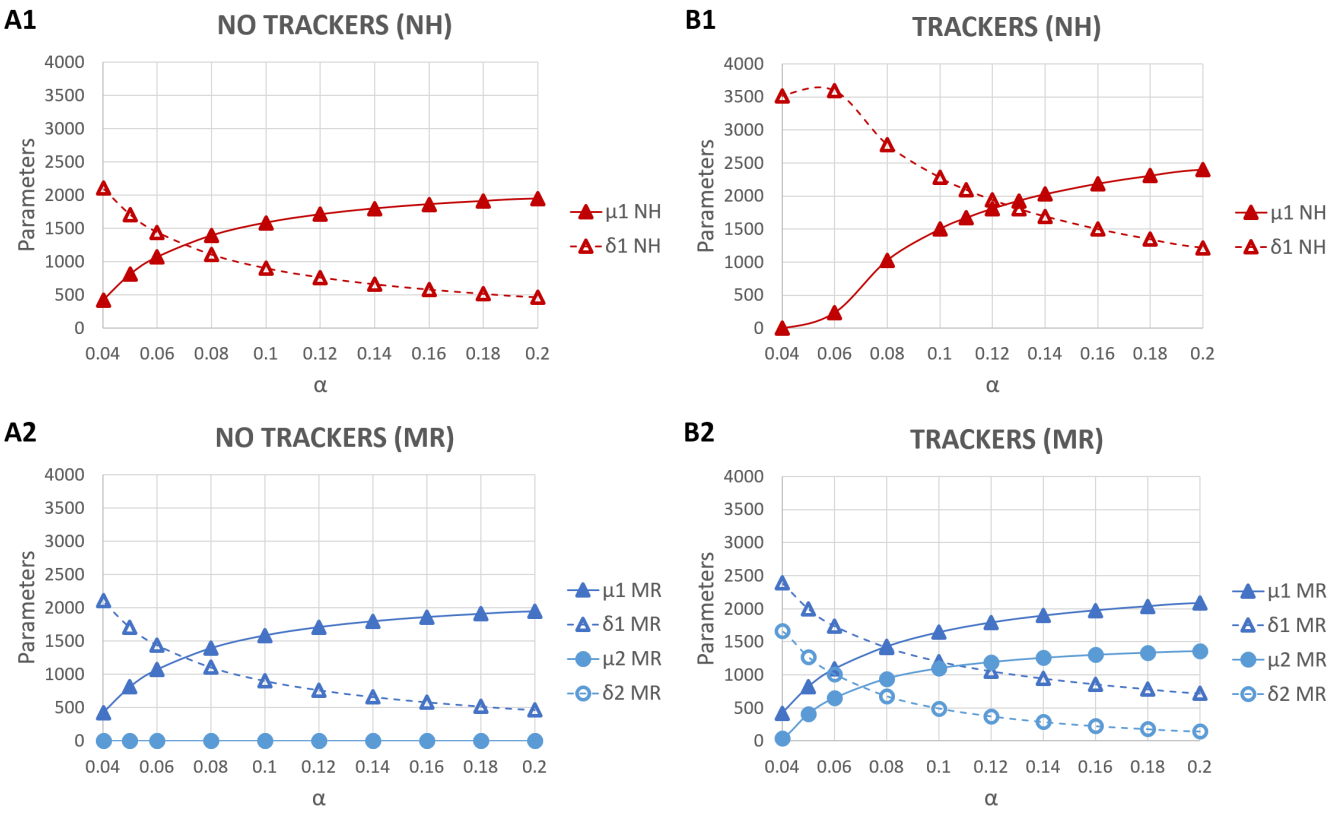

Figure 5.5.: Parameter trend at the variation of the fractional derivative order α in the absence (A1,A2) and presence (B1,B2) of trackers. The parameters that model the elastic and viscoelastic part of the two models show opposite and complementary trends.

function, like the proposed quadratic version of the Mooney-Rivlin law. Here, in addition, we have attempted to use Fung's exponential strain energy density function in its incompressible form, presented in Eq.2.58. When big strains are considered, the linear term can be neglected, further reducing the function to

$$W = \frac{\mu_1}{\mu_2}\left(e^{\mu_2(I_{\hat{\mathrm{C}}}-3)} - 1\right) \tag{5.31}$$

with the set of parameters $\boldsymbol{\mu} = [\mu_1, \mu_2]$ replacing c and b from Eq.2.58. Calculating $\partial W/\partial I_{\hat{\mathrm{C}}}$ and $\partial W/\partial II_{\hat{\mathrm{C}}}$ and substituting in the deviatoric part of Eq.5.16, we obtain the elastic part of the PK2 stress tensor for the exponential Fung law:

$$\mathrm{S}_e'^{FUNG} = \mu_1\left(e^{\mu_2(I_{\mathrm{C}}-3)}\right)\left[\mathbb{1} - \frac{1}{3}I_{\mathrm{C}}\mathrm{C}^{-1}\right] \tag{5.32}$$

Consistent with the Neo-Hookean and modified Mooney-Rivlin cases, the same stress tensor, subjected to the time fractional derivative, was used to model the viscous part of PK2.

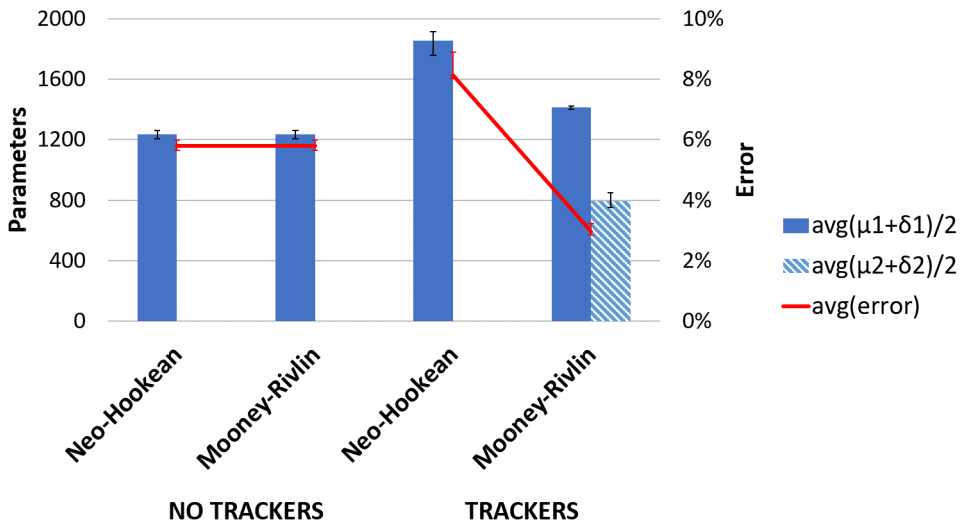

		$\frac{1}{N}\sum_{\alpha=0.04}^{\alpha=0.2}\frac{\mu_1+\delta_1}{2}$	$\frac{1}{N}\sum_{\alpha=0.04}^{\alpha=0.2}\frac{\mu_2+\delta_2}{2}$	$\frac{1}{N}\sum_{\alpha=0.04}^{\alpha=0.2}\text{error}_{\%}$
NO TRACKERS	Neo-Hookean	1238 Pa	-	5.8 %
	Mooney-Rivlin	1238 Pa	3.5×10^{-8} Pa	5.8 %
TRACKERS	Neo-Hookean	1858 Pa	-	8.1 %
	Mooney-Rivlin	1414 Pa	795 Pa	3.0 %

Figure 5.6.: The bar graph presents the best fitting parameters obtained from the tested samples in the presence and absence of trackers using both the Neo-Hookean and modified Mooney-Rivlin model. Each value, reported also in the table underneath, represents the average, over a fractional derivative order going from 0.04 to 0.2, of the mean value between the coupled parameters. The error bars show the range of values over the investigated α's. The same procedure is used to display the minimisation error.

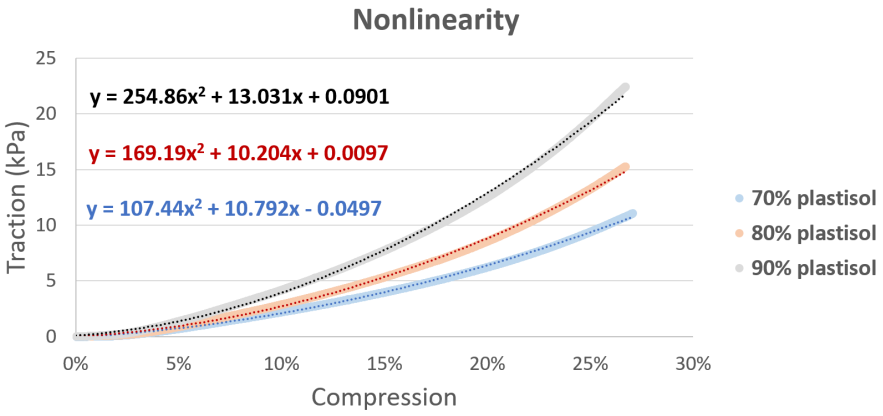

Figure 5.7.: The nonlinearity of the stress/strain response of the material increases with the plastisol concentration, as underlined by the increasing value of the parameter scaling the quadratic term of the fitting curve. Again, the data are taken from the loading process that leads to a compression slightly higher than 25 %.

For the fitting process, the material parameters in the viscous term were named $\boldsymbol{\delta} = [\delta_1, \delta_2]$.

5.4.1. Parameter Optimisation

For both the modified Mooney-Rivlin and the exponential constitutive law, the minimum fitting error was measured for a fractional derivative order lower than 0.2, confirming the mild viscosity of the material at all the investigated PVC concentrations (see Fig.5.8-A,B). Nonetheless, as in the first experiment, the minimisation curves were very shallow in the

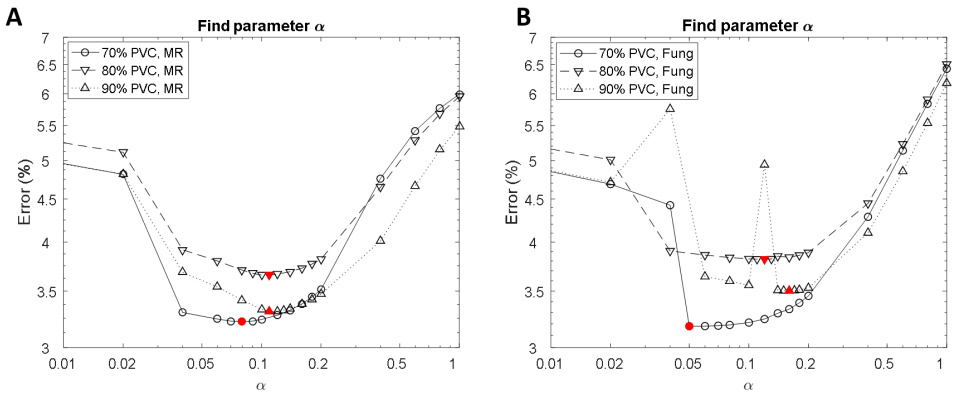

Figure 5.8.: Data from different PVC concentration are modelled by equally small fractional derivative orders. The best fit was obtained for a range of α values that roughly goes from 0.05 to 0.2 by both the modified Mooney-Rivlin (A) and the Fung hyperelastic law (B). The actual minimum α_{min} is indicated by a filled symbol. Both models show a good agreement with the data, with a fitting error smaller than 4 % in the selected region.

region of the minimum, which roughly goes from $\alpha = 0.05$ and $\alpha = 0.2$.
Again, Fig.5.9-A suggests a coupling between the elastic and viscous parameters, both for the linear and the quadratic terms of the modified Mooney-Rivlin model. In the Fung model, the parameters that scale the exponential term, μ_1 and δ_1, and those that control the exponential growth, μ_2 and δ_2, show different behaviours as a function of α (Fig.5.9-B). Similar to the Mooney-Rivlin case, the best estimate of δ_1 decreases with the increase of the fractional derivative order, balancing μ_1. However, this is not true for the best estimate of μ_2 and δ_2: while the first parameter keeps constantly around 1 at the increase of the fractional derivative order, hence not changing its contribution to the modelling of the nonlinear behaviour of the material, δ_2 follows a positive linear trend as a function of α, which gets more pronounced at higher PVC concentrations.

The best estimate of the parameters is plotted in Fig.5.10. In this case, the parameters of the modified Mooney-Rivlin model have been treated in the same way as in the previous experiment, reporting the average, over the α range going from 0.04 to 0.2, of the mean value between μ_1 and δ_1 and between μ_2 and δ_2. For the Fung model, instead, given the non-

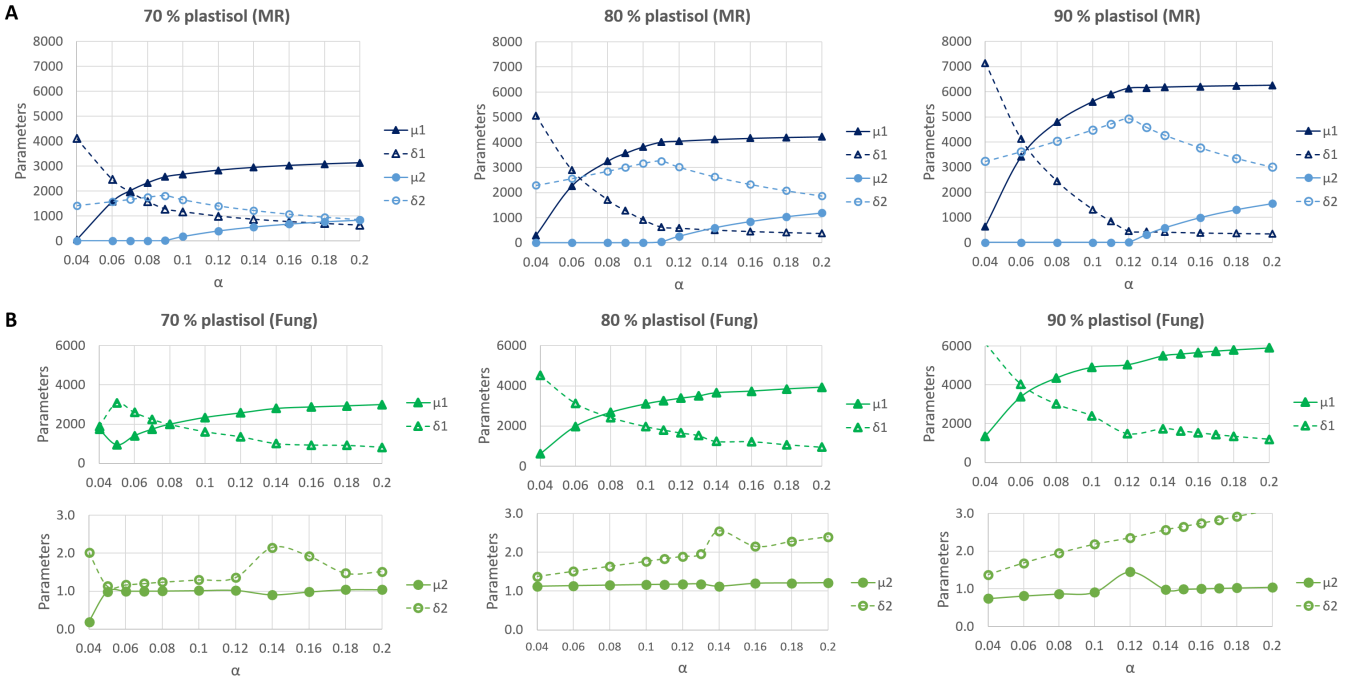

Figure 5.9.: A) Using the Mooney-Rivlin model, the elastic and viscous parameters show opposite and complementary trends over the considered α range at different plastisol concentrations. B) With the Fung model, while μ_1 and δ_1 appear coupled, μ_2 and δ_2 display non-complementary trends: while the former keeps constant for all samples, the latter increases linearly with the fractional derivative order, with a slope directly proportional to the plastisol concentration

constant trend of μ_2 and δ_2 over the same α range, we have reported the values obtained at $\alpha = \alpha_{min}$. Also, in the light of the coupling, the mean value between μ_1 and δ_1 was considered, while μ_2 and δ_2 have been treated individually. Minimisation errors constantly lower than 4 % suggest that both models provided a accurate approximation of the data for all three PVC concentrations, with the Mooney-Rivlin law slightly outperforming the exponential law at higher PVC concentrations.

5.4.2. Model Simplification to Account for Parameter Coupling

Seeking a unique parameter estimation, to circumvent the parameter coupling we have attempted to reduce the number of estimated constants by using one single set of two parameters, $\boldsymbol{\mu} = [\mu_1, \mu_2]$ in the Mooney-Rivlin model. The same was done for the coupled parameters in the Fung model, using the same constant μ_2 to scale both the elastic and viscous part of the fitting function, hence reducing the number of fitting parameters to three: μ_1, μ_2 and δ_2. The minimisation process for both the simplified versions of the models returned a clear minimum at a unique value of α between 0.08 and 0.09 for all samples (see Fig.5.11-A,B).

The new best estimates of the free parameters, obtained at $\alpha = \alpha_{min}$ are reported in Fig.5.12.

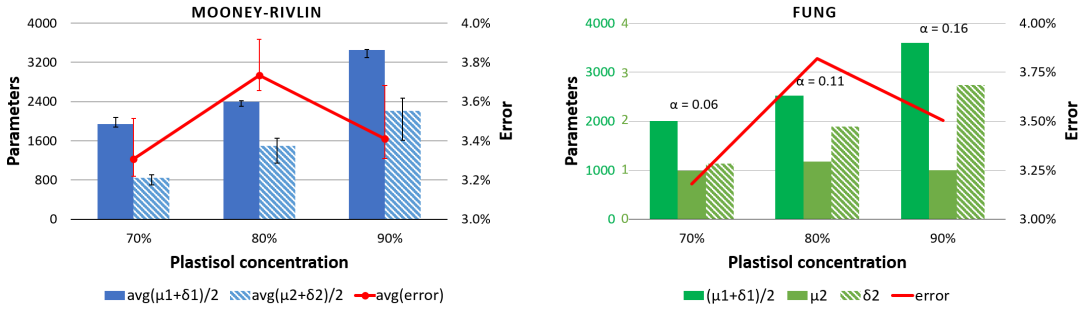

Model	Plastisol	$\frac{1}{N}\sum_{\alpha=0.04}^{\alpha=0.2}\frac{\mu_1+\delta_1}{2}$	$\frac{1}{N}\sum_{\alpha=0.04}^{\alpha=0.2}\frac{\mu_2+\delta_2}{2}$		$\frac{1}{N}\sum_{\alpha=0.04}^{\alpha=0.2}\text{error}_{\%}$
	70 %	1953 Pa	872 Pa		3.22 %
Mooney-Rivlin	80 %	2320 Pa	1648 Pa		3.66 %
	90 %	3381 Pa	2358 Pa		3.31 %
		$(\mu_1+\delta_1)/2$	μ_2	δ_2	$\text{error}_{\%}$
	70 %	2006 Pa	0.99 Pa	1.14 Pa	3.18 %
Fung	80 %	2517 Pa	1.18 Pa	1.89 Pa	3.82 %
	90 %	3592 Pa	1.00 Pa	2.74 Pa	3.50 %

Figure 5.10.: Estimated best parameters and corresponding fitting error at the three investigated PVC concentrations using the modified Mooney-Rivlin (left) and Fung law (right). In this case, given the non constant trend followed by the sum of the coupled parameters in the Fung model over the fractional order going from 0.04 to 0.2, only the estimates obtained at the fractional derivative order that minimised the error are considered. For the Mooney-Rivlin model, instead, the average value of the parameters and the fitting error are reported, with the error bars showing the range of values over the investigated αs. The parameter values and errors are also reported in the table underneath.

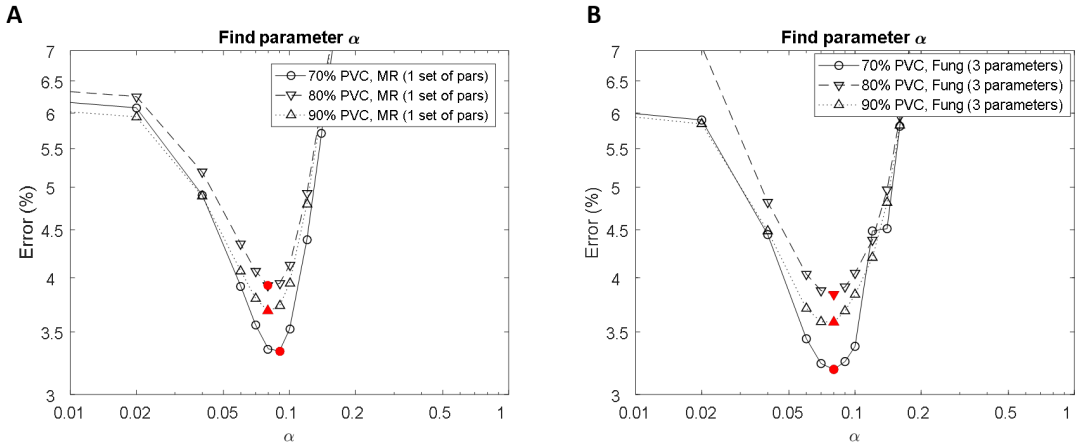

Figure 5.11.: Best fractional order to model the traction data measured for the 70 %, 80 % and 90 % PVC samples using the simplified version of the modified Mooney-Rivlin law (A) and the Fung law (B).

Compared to the four-parameter case, this simplified form of the Mooney-Rivlin model affected only marginally the quality of the fit, with a maximum increase in the fitting error by 0.37 % in the sample made with the highest plastisol concentration. While the

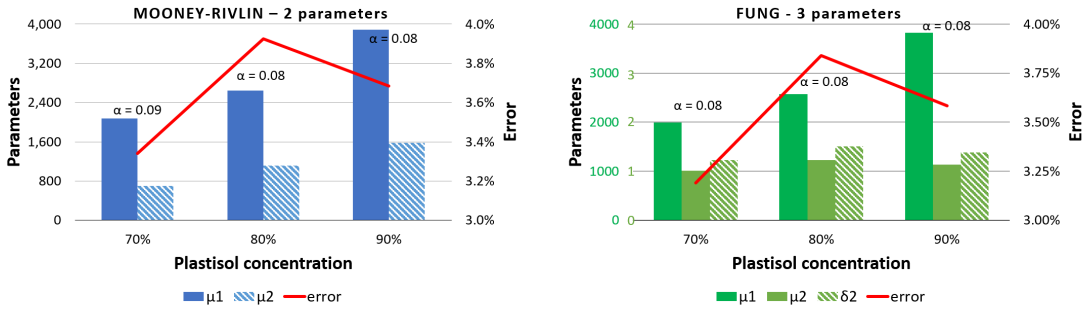

Model	Plastisol	μ_1	μ_2		error$_{\%}$
Mooney-Rivlin 2 parameters	70 %	2078 kPa (+6.4 %)	698 kPa (-19.9 %)		3.34 % (+0.12 %)
	80 %	2648 kPa (+14.1 %)	1118 kPa (-32.2 %)		3.92 % (+0.27 %)
	90 %	3883 kPa (+14.8 %)	1575 kPa (-33.2 %)		3.68 % (+0.37 %)
		μ_1	μ_2	δ_2	
Fung 3 parameters	70 %	1990 (-0.8 %)	1.01 kPa (+2.3 %)	1.23 (+8.2 %)	3.19 % (+0.01 %)
	80 %	2575 kPa (+2.3 %)	1.23 (+4.3 %)	1.50 (-20.6 %)	3.84 % (+0.02 %)
	90 %	3823 kPa (+6.4 %)	1.13 (+13.5 %)	1.39 (-49.3 %)	3.58 % (+0.08 %)

Figure 5.12.: Estimated best parameters and corresponding fitting error for the three investigated PVC concentrations using the simplified version of the modified Mooney-Rivlin (left) and Fung law (right). The associated fractional derivative order is also reported. The parameter values and errors are shown in the table underneath, together with their percentage variation with respect to the estimates in Fig.5.10.

new μ_1 differs from the mean of the corresponding elastic and viscous best parameter estimates by at most 14.8 %, the variation between the new quadratic parameter and the mean $(\mu_2 + \delta_2)/2$ from the previous version is instead more pronounced, with a decrease of 19.9 % in the sample containing the lowest plastisol concentration and ~33 % for the other two. The parameter reduction in the Fung model does not produce a significant error increase in any of the samples, either. In the simplified law, however, δ_2 does not appear to follow a particular trend, oscillating around 1.37 throughout the various plastisol concentrations, unlike in the four-parameter equivalent, where δ_2 showed a linear growth with the increase of plastisol in the mixture.

5.4.3. Linearised Shear Modulus

Following the mathematical framework presented in Section 2.3.2 in the limit of small strain, the material parameters of both the modified Mooney-Rivlin and the Fung law can be used to estimate the shear modulus μ of the material under different plastisol concentrations using Eq.2.68. Using the form of the Mooney-Rivlin constitutive law proposed in Eq.5.28 to describe the elastic response of the material, the linearised shear modulus is expressed as

$$\mu_e^{MR} = \lim_{a\to 0} \frac{E_{12}}{\sigma_{12}} = \lim_{a\to 0} 2\left(\frac{\partial W}{\partial I_{\hat{\mathrm{C}}}} + \frac{\partial W}{\partial II_{\hat{\mathrm{C}}}}\right) = \lim_{a\to 0} 2\left(\mu_1 + 2\mu_2(II_{\hat{\mathrm{C}}} - 3)\right) = 2\mu_1 \tag{5.33}$$

where $\lim_{a\to 0} II_{\hat{\mathrm{C}}} = 3$. Assuming that the total Mooney-Rivlin strain energy density function W, characterising both the elastic and viscoelastic behaviour of the material, is composed of the linear combination of an elastic and viscous term

$$W = W_e(I_{\hat{\mathrm{C}}}, II_{\hat{\mathrm{C}}}) + W_v(I_{\hat{\mathrm{C}}}, II_{\hat{\mathrm{C}}}, \partial_t^\alpha I_{\hat{\mathrm{C}}}, \partial_t^\alpha II_{\hat{\mathrm{C}}}) \tag{5.34}$$

and given the small fractional order observed in all sample, W_v can be equalised to W_e, however keeping the parameters δ_1 and δ_2. In fact, while for a non-integer fractional derivative order a more complicated viscoelastic behaviour could be predicted, as shown in Eq.5.12, for α close to zero $\boldsymbol{S}'_v$ is expected to behave as a purely elastic term. Under these circumstances, the same procedure presented in Eq.5.33 can be applied to the second term of the constitutive law in Eq.5.34, producing $\mu_v^{MR} = 2\delta_1$. The linearised shear modulus is then given by the combination of μ_e^{MR} and μ_v^{MR}:

$$\mu^{MR} = \mu_e^{MR} + \mu_v^{MR} = 2(\mu_1 + \delta_1) \tag{5.35}$$

In the case of the simplified Mooney-Rivlin equation, the same parameter μ_1 was employed to scale both the elastic and viscous term of the model. Consequently, the linearised shear modulus is given by

$$\mu^{MR_{(2\text{ parameters})}} = 2(\mu_1 + \mu_1) = 4\mu_1 \tag{5.36}$$

The same procedure was applied to calculate the linearised shear modulus in the case of the Fung model. Considering the constitutive law presented in Eq.5.31, we can calculate μ_e^{FUNG}:

$$\mu_e^{\mathrm{FUNG}} = \lim_{a\to 0} 2\left(\frac{\partial W}{\partial I_{\hat{\mathrm{C}}}} + \frac{\partial W}{\partial II_{\hat{\mathrm{C}}}}\right) = \lim_{a\to 0} 2\left(\mu_1 e^{\mu_2(II_{\hat{\mathrm{C}}}-3)}\right) = 2\mu_1 \tag{5.37}$$

Accounting for the viscous term, consistently to what done for the modified Mooney-Rivlin model, the linearised shear modulus is given by

$$\mu^{\mathrm{FUNG}} = \mu_e^{\mathrm{FUNG}} + \mu_v^{\mathrm{FUNG}} = 2(\mu_1 + \delta_1) \tag{5.38}$$

In the same way, the linearised shear modulus for the simplified version of the Fung model is given by

$$\mu^{\mathrm{FUNG}_{(3\text{ parameters})}} = 2(\mu_1 + \mu_1) = 4\mu_1 \tag{5.39}$$

The plot of the calculated shear modulus as a function of the plastisol concentration in Fig.5.13 revealed a quadratic trend, regardless of the employed model. However, while the difference between the estimated μ from each model is minimum for the sample made with 70 % of plastisol, the gap becomes wider with the increase of the plastisol concentration, where the stress/strain nonlinearity becomes more pronounced. Nonetheless, even in

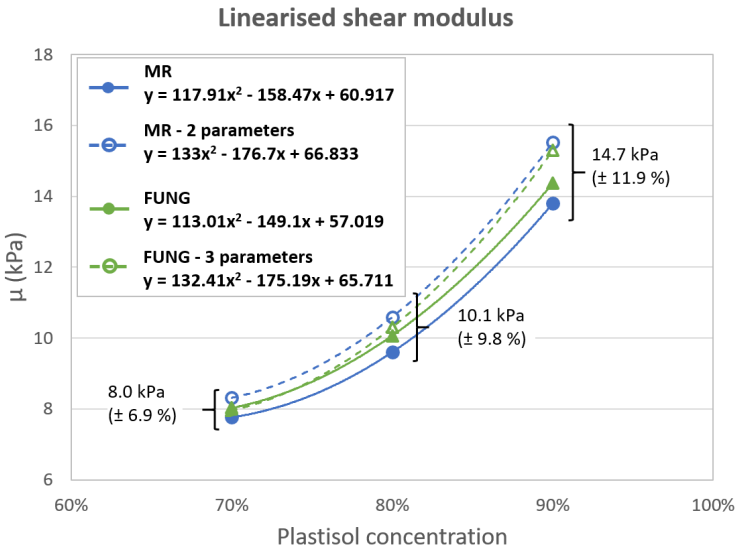

Figure 5.13.: All the four models generate a similar estimate of the linearised shear modulus of the three investigated samples, producing a similar quadratic dependence on the plastisol concentration.

the 90 % PVC sample, the estimated values of μ differ at most by less than 12 % from the associated mean value.

5.5. Discussion

A list of the main results reported in this chapter is presented in Table 5.3.

Main results
Tracking particles increase the nonlinearity of the plastisol samples. The quadratic term in the modified Mooney-Rivlin model can better fit the rheological data.
Consistently with the literature, a higher plastisol-to-softener ratio in the sample leads to an increased nonlinear stress-strain response. Both the modified Mooney-Rivlin law and the Fung law produce a close prediction of the rheological data.
Due to the low viscosity of the material at the investigated frequencies, a coupling between the parameters scaling the elastic and viscous terms of the PK2 stress tensor was observed. It was therefore possible to reduce the number of parameters employed in the models, using the same ones to model both the elastic and viscous components, without impacting the fitting quality.
The shear modulus of the sample was found to follow a second-order polynomial growth with the plastisol concentration. A trade-off between realistic stiffness and high nonlinearity was given by an 80 % plastisol concentration.

Table 5.3.

Here we have characterised the soft plastic mixture used to build the soft tissue-mimicking phantom cuboids by analysing the impact of the tracking particles on its material properties, as well as the effect of the plastisol concentration on its nonlinear stress-strain response.

From the first experiment, we could see that, in the absence of motion trackers, the same mixture made from two different plastisol batches generated a linear correlation between the applied compression and the associated measured traction. As a matter of fact, while the batch variability can represent a relevant source of variation in the material properties, it does not seem to have a significant impact on the nonlinearity.

Despite the rheological behaviour of the pure material having been reported as nonlinear in the literature [197], the limited strain applied in the first experiment was possibly not sufficient to escape the linear region of the stress-strain curve. The interaction of the scattered particles with the sample matrix, instead, produced a nonlinear stress response at compression levels higher than ~15 %. This result is ideal for the purpose of modelling the signature stiffness variation generated by the mimicked growing tumour, as it allows

to generate a change in the probed shear modulus without requiring large applied strains, that could damage the material (see Section 3.3.2).
A progressive increment in the nonlinearity of the stress-strain curve was further obtained increasing the plastisol concentration used to prepare the samples in the second rheological experiment. This result reflects the findings of Hungr *et al.* (2012) obtained investigating different PVC mixtures [196], although the undisclosed plastisol/softener ratio for both their and our reference premixed blend does not allow a direct comparison. Nevertheless, since under the assumption of incompressibility the shear modulus and Young's modulus can be related by the scaling equation $E = 3\mu$, the values of the linearised shear modulus extracted from the various hyperelastic models employed to characterise our PVC mixtures compare well with the Young's modulus reported for their "soft" mixture.

At the same time, we have investigated the rheological response of the chosen soft plastic material to uniaxial harmonic micro- and macro-compressions to identify a constitutive law capable of describing the viscoelastic behaviour of the samples when exposed to mechanical conditions similar to those experienced during the MRE experiments.
For the modelling of the stress experienced by the samples under the measured strain, we have developed a mathematical framework where the PK2 tensor has been conveniently decomposed into a term containing the hydrostatic pressure p and a deviatoric term $\boldsymbol{S}'$; the latter has in turn been considered as the linear combination of an elastic part, $\boldsymbol{S}'_e$, and a viscous one, $\boldsymbol{S}'_v$, modelled using a fractional order derivative. Using the proposed formulation, both the selected Neo-Hookean and modified Mooney-Rivlin hyperelastic laws could equally well fit the rheological data obtained from the investigated control sample in the absence of tracking particles. Given the scarce nonlinearity generated at a 70 % PVC concentration, in fact, the quadratic parts of the modified Mooney-Rivlin model became irrelevant, effectively reducing the model to the simpler Neo-Hookean form. The quadratic components present in W^{MR} were instead required to reproduce the nonlinear response introduced by the trackers, which could not be captured as accurately by just a linear function of $I_{\hat{\mathrm{C}}}$.

The need for a more complex hyperelastic law became more urgent when the rheological data from the second experiment were modelled, as the nonlinear behaviour of the employed samples was more pronounced. The Fung model has been suggested in the literature to model the nonlinear stress/strain response of breast tissue subjected to macro-deformations [50]; here it was employed as a valid alternative to the modified Mooney-Rivlin constitutive equation for the rheological characterisation of the phantom material in the presence of tracking particles. In all the samples used for the second experiment, both the Fung and the modified Mooney-Rivlin model reached a minimum error for

low values of the fractional derivative order α, ranging approximately between 0.05 and 0.2, indicating a consistently mild viscosity of the material. This was true regardless of the plastisol concentration and the material law employed for the data fitting, suggesting that, unlike the elastic properties of the material, its viscous response does not seem to be affected by the composition of the PVC mixture. Under an experimental point of view, this provides the advantage of a lessened dampening of the propagating shear waves during the MRE experiments, although it may not accurately reproduce the viscoelastic behaviour of soft tissues, which have been reported to exhibit non-negligible viscosity [45]. Given the almost purely elastic behaviour, it is understandable that the fitting error for both the modified Mooney-Rivlin and the Fung models kept relatively small even for fractional derivative orders closer to 1: the progressive decrease of the parameters involved in the modelling of the viscous response of the material, as opposed to the growth of the parameters scaling the elastic terms of the stress tensors associated to the increase of α, in fact, makes the purely elastic part of the model increasingly dominant, which is sufficient to still provide a good fit.

In light of the balance between the parameters over the investigated α range, the free parameters scaling the elastic and viscous parts of the two models appear not-identifiable and coupled, such that an equally good fit can be obtained with a different fractional derivative order at the expense of the magnitude of one or the other set of parameters. For this reason, it was not possible to carry out an analysis of the single parameters, but it was preferred to consider the average between μ_1 and δ_1 for the Neo-Hookean law, as well as between μ_2 and δ_2 for the modified Mooney-Rivlin model. Both average values showed a constant trend over the selected α range, as presented in Fig.5.14 for the first experiment.

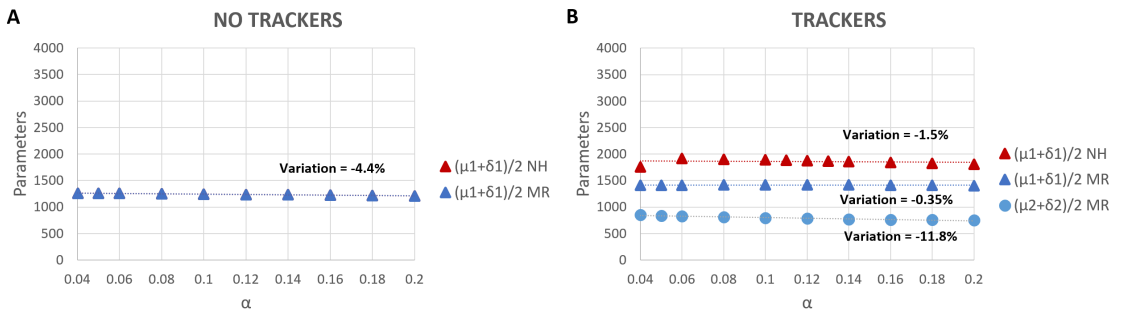

Figure 5.14.: All the four models generate a similar estimate of the linearised shear modulus of the three investigated samples, producing a similar quadratic dependence on the plastisol concentration.

A mathematical explanation for this parameter coupling can be given considering the small α values experimentally estimated. Having used the same equation for both the elastic and viscoelastic part of the deviatoric PK2 tensor, S'_v assumes the same form as

its elastic counterpart when the fractional derivative order is equal to zero, making the scaling parameters $\boldsymbol{\mu}$ and $\boldsymbol{\delta}$ redundant:

$$\boldsymbol{S}' = \boldsymbol{S}'_e(\boldsymbol{\mu}) + \boldsymbol{S}'_v(\boldsymbol{\delta}) = \boldsymbol{S}'_e(\boldsymbol{\mu}) + D_t^0 \boldsymbol{S}'_e(\boldsymbol{\delta}) = \boldsymbol{S}'_e(\boldsymbol{\mu}) + \boldsymbol{S}'_e(\boldsymbol{\delta}) \tag{5.40}$$

This approximation can be be considered valid also for the low values of α that minimise the objective function, hence permitting to halve the number of free constants in the case of the polynomial strain energy function. The same was only possible for the scaling parameters μ_1 and δ_1 in the Fung model, while μ_2 and δ_2, which followed non-complementary trends, have been treated separately. The acquisition of more data and the addition of a different kind of rheometric experiments could help with the practical identifiability of a unique set of parameters, however such an analysis falls outside the scope of this project.

In this chapter we have shown that the modified Mooney-Rivlin model proved capable of reproducing the viscoelastic properties of the PVC mixture employed to make the phantoms, hence justifying the use of the mathematical framework to analytically calculate the apparent shear modulus variation caused by an inflated thick-shelled sphere presented in Section 2.4. The Fung model displayed a similar accuracy in capturing the rheological behaviour of the investigated samples and the intrinsic shear modulus of the material, calculated using the various models, was found comparable at all the investigated PVC concentrations. Despite a higher nonlinearity was observed in the sample made using a 90 % plastisol mixture, which would result in a more pronounced variation in shear modulus when the material is compressed, hence facilitating its experimental detection, for the inflation experiments it was decided to use phantoms made with an 80 % plastisol mixture. This choice was dictated by the concomitant attempt to keep the shear modulus as close as possible to the values of healthy soft tissue, i.e. generally much lower than 10 kPa for breast, liver and brain. An 80 % plastisol concentration represented a reasonable trade-off.

In the next chapter, the reconstructed apparent shear modulus of the characterised material and its variation when subjected to spherical macro-deformation will be reported and the patterns generated around the tumour-mimicking inclusion will be compared with those numerically calculated in Chapter 2.

6. Experimental Investigation

The results presented in Chapter 2 of this thesis have demonstrated a close mathematical understanding of the impact generated by a pressurised tumour on the biomechanical properties of the surrounding soft tissue and of the local quantification of its apparent shear modulus through shear waves. In Chapter 3 we have shown the details of the implementation and execution of an inflation experiment in a phantom suitable to investigate the correlation between the experimentally measured variation in G' measured through MRE and its analytical prediction. The proposed experiment was reproduced three times, to assess its reproducibility and provide more convincing evidence of the theorised relationship, and the obtained results will be presented and discussed throughout this chapter. Section 6.1 of this chapter will provide a short introduction on the mathematical background underlying the employed elastography reconstruction technique of the wave data obtained through MRI. Afterwards, we will present the various results obtained for each replicate of the inflation experiment, where all outcomes are treated in parallel. Initially we will focus on the estimation of the local k-vector direction from the wave images and will devise a method to determine the local deformation probed by the waves, to differentiate between compression and tension. Subsequently we will show the voxel-wise local reconstruction of the apparent G' in a ROI around the inclusion and provide a comparison between the background G' obtained through the three experiments and the values analytically calculated from the fitting of the pressure data reported in Section 3.3. The experimental estimation of the generated shear modulus anisotropy around the inclusion will then be compared with the patterns predicted using the developed analytical framework. Finally, the details of our first attempt to replicate the presented experiment using a tissue sample will be given and the preliminary results obtained will be shown. The chapter will conclude with a discussion on the factors that produce the inequalities between the probed deformation and the associated changes in apparent modulus, as well as on the differences from the patterns expected from the analytical calculations in both phantom and tissue experiments. Two metrics will also be proposed in an attempt to qualitatively express the reliability of the obtained patterns.

6.1. MRE Reconstruction Method

At each given inflation state, wave images reporting the associated 3D micro-displacement generated are acquired at eight consecutive time points, evenly sampling the wave cycle. The Fourier transform is carried out for each voxel, recovering the complex harmonic displacement $\boldsymbol{u}_{\mathbb{C}}$, which is then used to solve Eq.2.50a introduced in Section 2.2 and reported here:

$$\rho\omega^2\boldsymbol{u}_{\mathbb{C}} + \nabla_{\boldsymbol{x}} \cdot (\boldsymbol{\mathcal{G}}^* : \nabla_{\boldsymbol{x}}\boldsymbol{u}_{\mathbb{C}} + p_{\mathbb{C}}\mathbb{1}) = 0 \tag{6.1}$$

Here the complex shear modulus $\boldsymbol{\mathcal{G}}^*$, which accounts for both the storage and loss modulus, i.e. $\boldsymbol{\mathcal{G}}^* = \boldsymbol{\mathcal{G}}' + i\boldsymbol{\mathcal{G}}''$, represents the unknowns of the equations, together with the hydrostatic pressure $p_{\mathbb{C}}$. The pressure term cannot be neglected, as it would lead to errors in the shear modulus reconstruction [259], however it can be removed by taking the curl of Eq.6.1, limiting the inverse problem to the estimation of $\boldsymbol{\mathcal{G}}^*$[73].This local reconstruction method relies on the fact that the curl of a scalar potential is zero, reducing Eq.6.1 to the following form:

$$\begin{aligned} \nabla_{\boldsymbol{x}} \times \left[\rho\omega^2\boldsymbol{u}_{\mathbb{C}} + \nabla_{\boldsymbol{x}} \cdot (\boldsymbol{\mathcal{G}}^* : \nabla_{\boldsymbol{x}}\boldsymbol{u}_{\mathbb{C}} + p_{\mathbb{C}}\mathbb{1})\right] = \\ \rho\omega^2\nabla_{\boldsymbol{x}} \times \boldsymbol{u}_{\mathbb{C}} + \nabla_{\boldsymbol{x}} \times \nabla_{\boldsymbol{x}} \cdot (\boldsymbol{\mathcal{G}}^* : \nabla_{\boldsymbol{x}}\boldsymbol{u}_{\mathbb{C}}) + \nabla_{\boldsymbol{x}} \times p_{\mathbb{C}}\mathbb{1} = \\ \rho\omega^2\nabla_{\boldsymbol{x}} \times \boldsymbol{u}_{\mathbb{C}} + \nabla_{\boldsymbol{x}} \times \nabla_{\boldsymbol{x}} \cdot (\boldsymbol{\mathcal{G}}^* : \nabla_{\boldsymbol{x}}\boldsymbol{u}_{\mathbb{C}}) = 0 \end{aligned} \tag{6.2}$$

If we assume that both $\boldsymbol{\mathcal{G}}'$ and $\boldsymbol{\mathcal{G}}''$ keep locally constant, by further denoting $\boldsymbol{q} = \nabla_{\boldsymbol{x}} \times \boldsymbol{u}_{\mathbb{C}}$ and observing that $\nabla_{\boldsymbol{x}} \times \nabla^2_{\boldsymbol{x}}\boldsymbol{u}_{\mathbb{C}} = \nabla^2_{\boldsymbol{x}}(\nabla_{\boldsymbol{x}} \times \boldsymbol{u}_{\mathbb{C}})$, we can rewrite the set of complex wave equations as

$$\rho\omega^2\boldsymbol{q} + \boldsymbol{\mathcal{G}}^* : \nabla^2_{\boldsymbol{x}}\boldsymbol{q} = 0 \tag{6.3}$$

A solution can now be obtained by solving the least squares minimisation problem

$$\Sigma = \frac{1}{2}\left[\left(\boldsymbol{\mathcal{G}}^*\nabla^2_{\boldsymbol{x}}q_x + \rho\omega^2 q_x\right)^2 + \left(\boldsymbol{\mathcal{G}}^*\nabla^2_{\boldsymbol{x}}q_y + \rho\omega^2 q_y\right)^2 + \left(\boldsymbol{\mathcal{G}}^*\nabla^2_{\boldsymbol{x}}q_z + \rho\omega^2 q_z\right)^2\right] \tag{6.4a}$$

$$\frac{\partial\Sigma}{\partial\boldsymbol{\mathcal{G}}^*} = 0 \tag{6.4b}$$

This leads to the complex equation that allows a direct reconstruction of the complex shear modulus for each voxel:

$$\boldsymbol{\mathcal{G}}^* = -\rho\omega^2\frac{\nabla^2_{\boldsymbol{x}}q_xq_x + \nabla^2_{\boldsymbol{x}}q_yq_y + \nabla^2_{\boldsymbol{x}}q_zq_z}{\left(\nabla^2_{\boldsymbol{x}}q_x\right)^2 + \left(\nabla^2_{\boldsymbol{x}}q_y\right)^2 + \left(\nabla^2_{\boldsymbol{x}}q_z\right)^2} \tag{6.5}$$

Under the assumption of isotropic material, all the components of $\boldsymbol{\mathcal{G}}^*$ are assumed to be equal and the tensors $\boldsymbol{\mathcal{G}}'$ and $\boldsymbol{\mathcal{G}}''$ can be considered as simple scaling factors replaced by the scalars G' and G'', which become the unknowns of Eq.6.5. As explained in Section

2.4, these scalars represent the component of the elastic and viscous tensors $\mathcal{G}'$ and $\mathcal{G}''$ probed by the propagating shear waves.
Here, a $5 \times 5 \times 5$ voxel reconstruction window was used for a first and third order polynomial fitting to analytically calculate the first and third order derivatives for the central voxel required to solve the wave equations. Because of the increased order of derivatives, the employed MRE reconstruction results exhibit an enhanced sensitivity to data quality[73]. SNR from elastography data obtained from phantoms is generally higher due to a controlled material homogeneity. Nevertheless, as presented throughout the following sections of this chapter, wave attenuation affects data quality, as noise has a more relevant impact on smaller harmonic displacements, which become more complicated to be correctly identified from the MR images of the propagating waves; therefore, smoothing of the wave images was required. In this case, a Gaussian filter with σ =1.5 voxel and using a 5 voxel support was applied.

6.2. Circumferential Strain Generates Apparent Anisotropy in Phantoms

As explained in Chapter 3, for each of the three replicates of the inflation experiment, the phantom containing the Foley catheter was positioned onto the designated support and into the bore of the MR scanner. The electromagnetic transducer was used to generate the shear waves required to probe the rheological response of the material around the balloon inflated with water. Imaging of the wave propagation around the inclusion allows the reconstruction of the shear modulus G' probed locally by the propagating waves.

6.2.1. Local Wave Propagation Determines the Probed Deformation

The shear waves generated through the electromagnetic transducer are imaged using MRE, which quantifies the displacement generated in the x-,y- and z-direction at eight different time points. An example of this micro-deformation is presented in Fig.6.1-A. Despite the strong wave attenuation shown in Fig.6.1-B, the wave-generated displacement is still detectable in the chosen ROI. Given the difficulty to generate plane waves with the developed setup, local knowledge of the direction of propagation of the wave is required to determine the probed macro-deformation associated with the balloon inflation. The calculation of the gradient of the complex displacement generated by the waves allows the voxel-wise estimation of the direction of the k-vector, which relates to the sensed apparent shear modulus. The red arrows in Fig.6.1-C show the wave behaviour around the inclusion. The mean k-vector however, shown as a green arrow, points roughly in the same direction at all considered inflations. Given the different directionality of the mean direction of propagation of the shear waves in the selected ROI throughout different

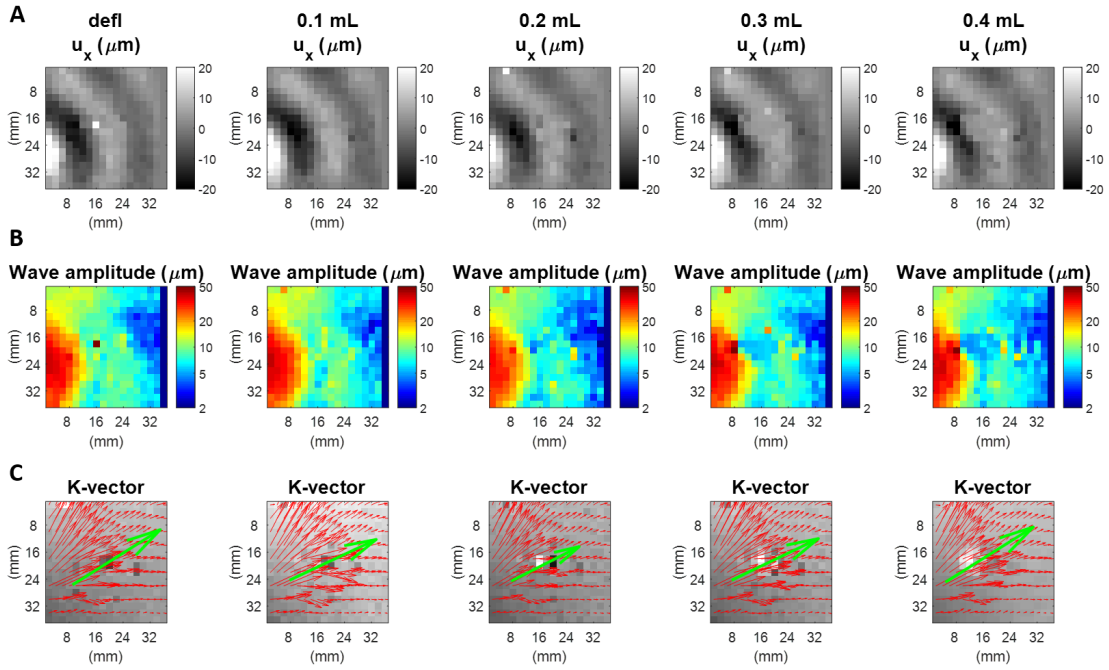

Figure 6.1.: The MR images of the wave displacement (A), the associate wave amplitude (B) as well as the local estimation of the k-vector (red arrows in C) is presented for each investigated inflation state. The green arrows represent the mean k-vector direction over the selected ROI.

replicates of the experiment, the green arrows will be used as reference to unravel the Cartesian images and to generate a polar representation of the measured variation in G' around the inclusion. An exhaustive explanation of this approach, employed to get a better intra- and inter-experiment comparison, will be given in Section 6.2.2.

The voxel-wise projection of the calculated right Cauchy-Green strain tensor on the direction of the k-vector, $\boldsymbol{CK} \cdot \boldsymbol{K}$, returns an estimate of the local deformation probed by the waves, an intuitive representation of which is shown in Fig.6.2-A.For each voxel, the k-vector magnitude has been normalised to compensate for wave attenuation. Values greater than 1 correspond to a sensed tension, while values smaller than 1 are obtained in the case of compression, when the angle θ between the k-vector direction and the local deformation vector is such that $\cos\theta < \cos\frac{\pi}{4}$ (see Fig.6.2-B). It is to be noted that, due to normalisation over the k-vector magnitude, such measurement is solely dependent on the magnitude of the projection of the right Cauchy-Green strain tensor on the local direction of propagation of the shear waves and it is not influenced by their attenuation. Using the deformation fields obtained from the registration of the MR images of the inclusion in its different states, shown in Fig.6.3, it is possible to generate an in-plane representation of the deformation sensed by the probing waves (Fig.6.4). The overlaid mean k-vector direction is added to help the visualisation of symmetries with respect to the main direction of

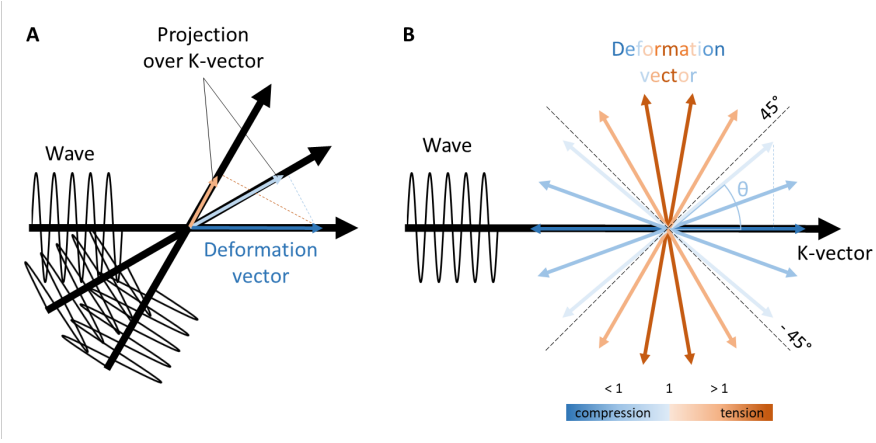

Figure 6.2.: A) Shear waves probe the material shear modulus along their direction of propagation, identified by the k-vector. This is comparable, in the case of a macro-deformation, to the projection of the deformation field onto the k-vector using $\boldsymbol{CK}\cdot\boldsymbol{K}$. B) For a spherical deformation, the angle between the deformation vector and the k-vector determines the magnitude of the probed material displacement and allows to differentiate between compression and tension.

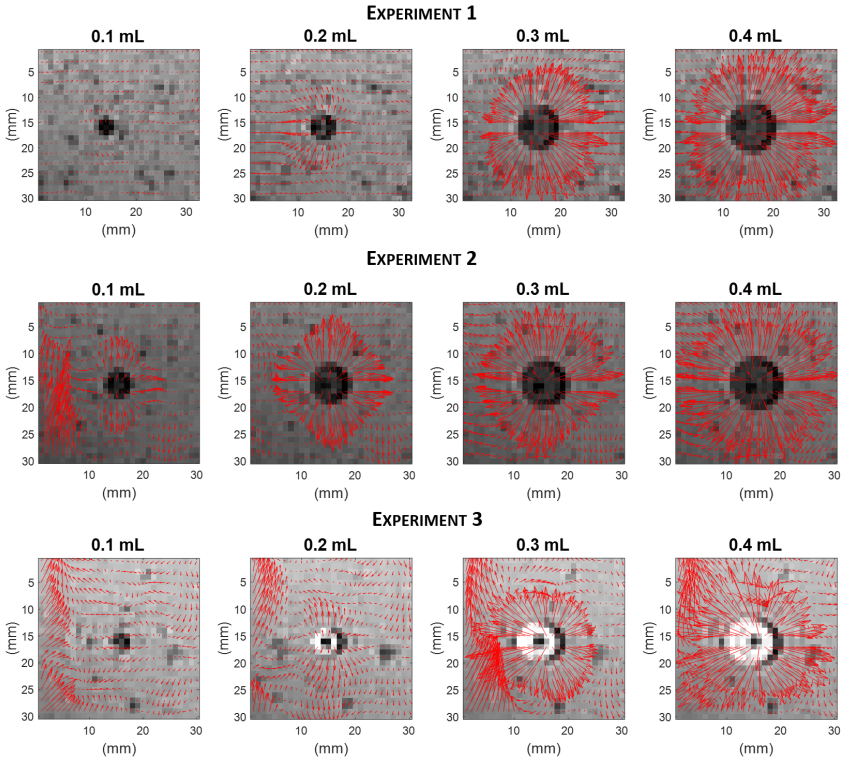

Figure 6.3.: Estimated macro-deformation using the implemented image registration strategy. The deformation field (red arrows, not to scale), relating the deflated balloon to each inflation state, shows a magnitude and directionality comparable with the spherical inflation of the inclusion.

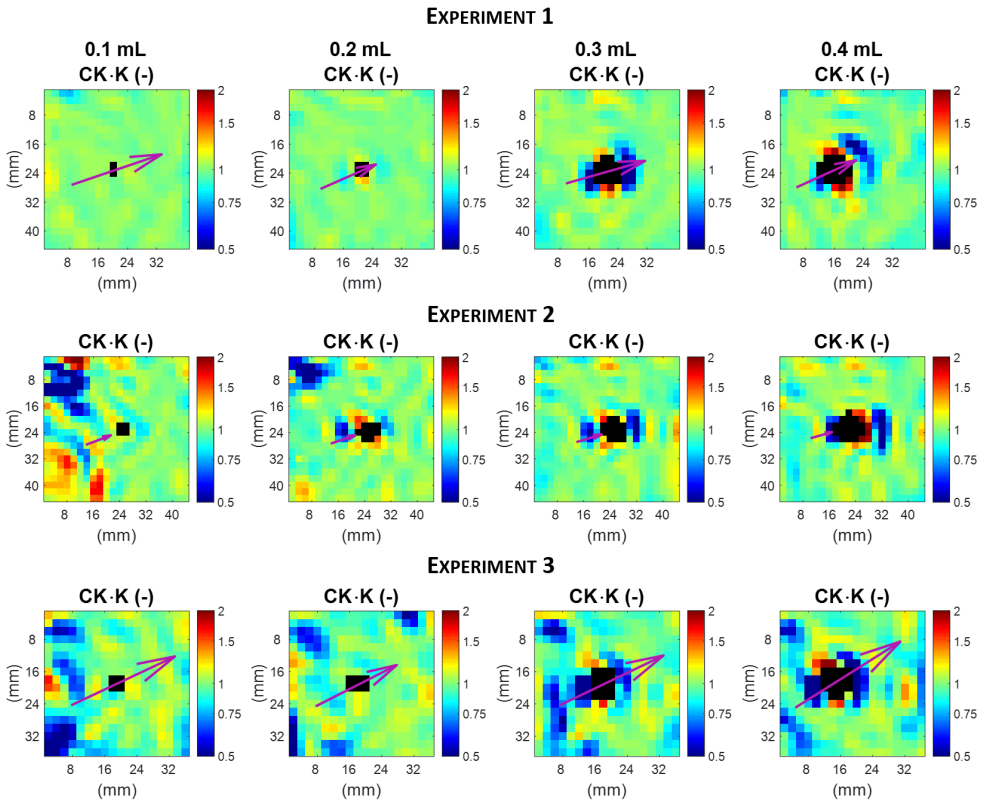

Figure 6.4.: In-plane Cartesian representation of the calculated $\boldsymbol{CK} \cdot \boldsymbol{K}$. The overlaid arrows represent the mean direction of propagation of the shear waves.

propagation of the waves. The obtained images show a clear compression probed at the leading and trailing edge of the inclusion, and a tension on the sides in all the experiments carried out.

6.2.2. Reconstructed Shear Modulus and Shear Modulus Variation from MRE Data

The shear modulus G' was reconstructed from the shear wave images using the MRE reconstruction strategy explained in Section 6.1. An example of the reconstructed mechanical parameter for various inflation states is presented in Fig.6.5-A, where the location of the inclusion can be clearly identified by the small values. The reconstruction focused on a limited ROI around the inclusion, as wave attenuation made the G' estimation away from the wave-source less reliable. The average background shear modulus, calculated averaging the reconstructed values from three in-plane slices sampling the centre of the inclusion from the 3D stack and masking out the inclusion and its immediate surroundings, is consistent throughout the phantoms used for the various replicates of the experiment and under different inflation levels (Fig.6.5-B); furthermore, the background shear modu-

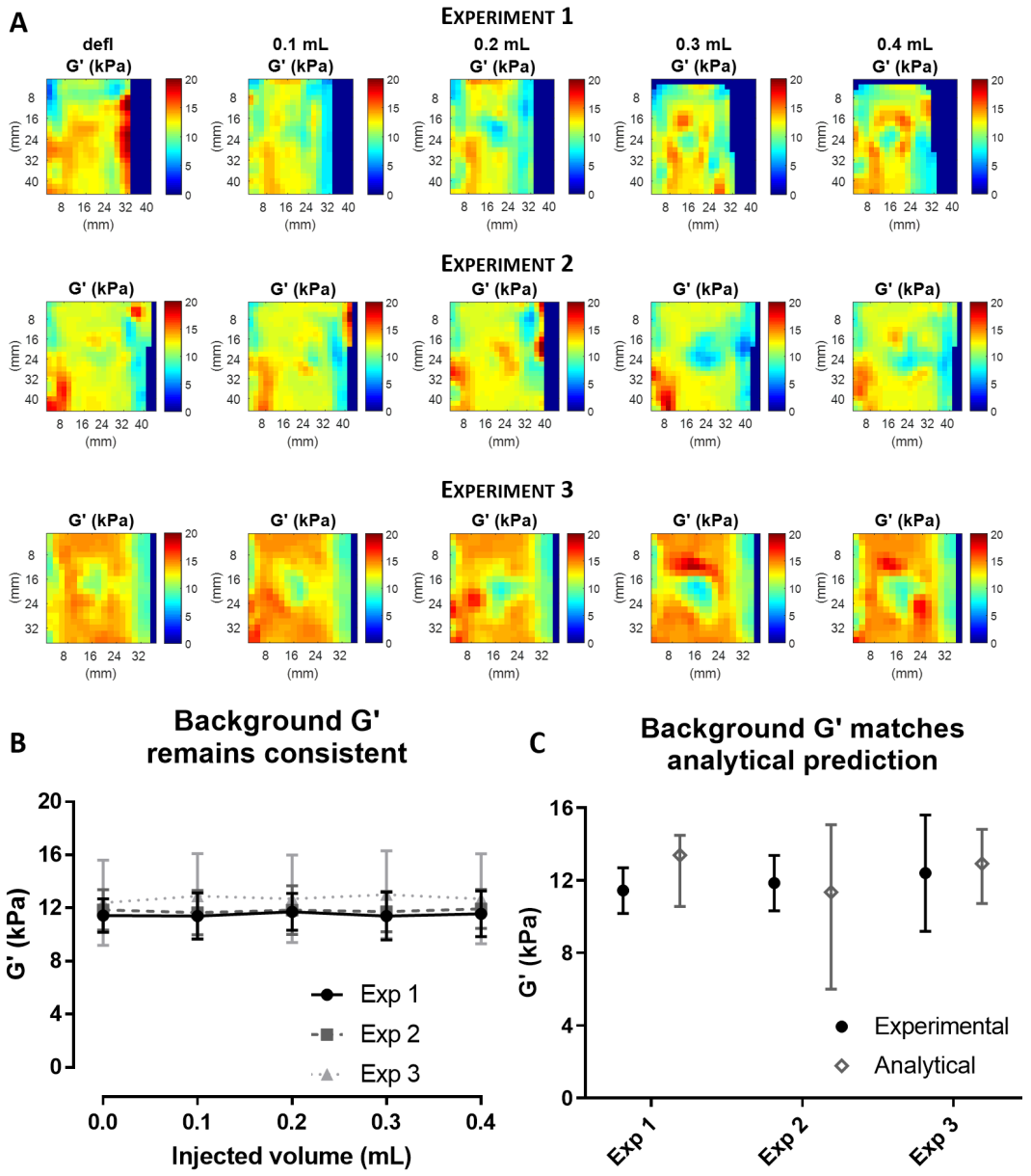

Figure 6.5.: A) Reconstructed shear modulus at different inflations. B) Background shear modulus reported as mean ± s.d. C) Comparison between background shear modulus reconstructed for the deflated cases and the analytical calculations using the best estimate of the material parameters obtained by fitting the pressure curve associated to each experiment. In this case, the error bars correspond to the values obtained when fitting the highest and lowest pressures measured throughout the different replicas of each experiment, as presented in Table 3.2.

lus reconstructed from each employed phantom is comparable to the values analytically predicted from the best fit of the inflating pressures (Fig.6.5-C).

The voxel-wise ratio between the reconstructed shear modulus at each inflation state and that of the deflated balloon returns the relative shift in shear modulus generated by the applied spherical deformation. Given the different spatial domains where the data are acquired, it is necessary to map the MRE image of the deflated balloon into the deformed configuration. This extra step is carried out by interpolating the deformation fields that connect the deflated state to the inflated ones, obtained from the nonrigid registration of the corresponding high resolution anatomical images (see Fig.6.3), into the voxel-grid used for the MRE images; image warping is then performed using the built-in Matlab function `imwarp`. The variation patterns obtained experimentally are presented in Fig.6.6, where the inclusion has been masked out.

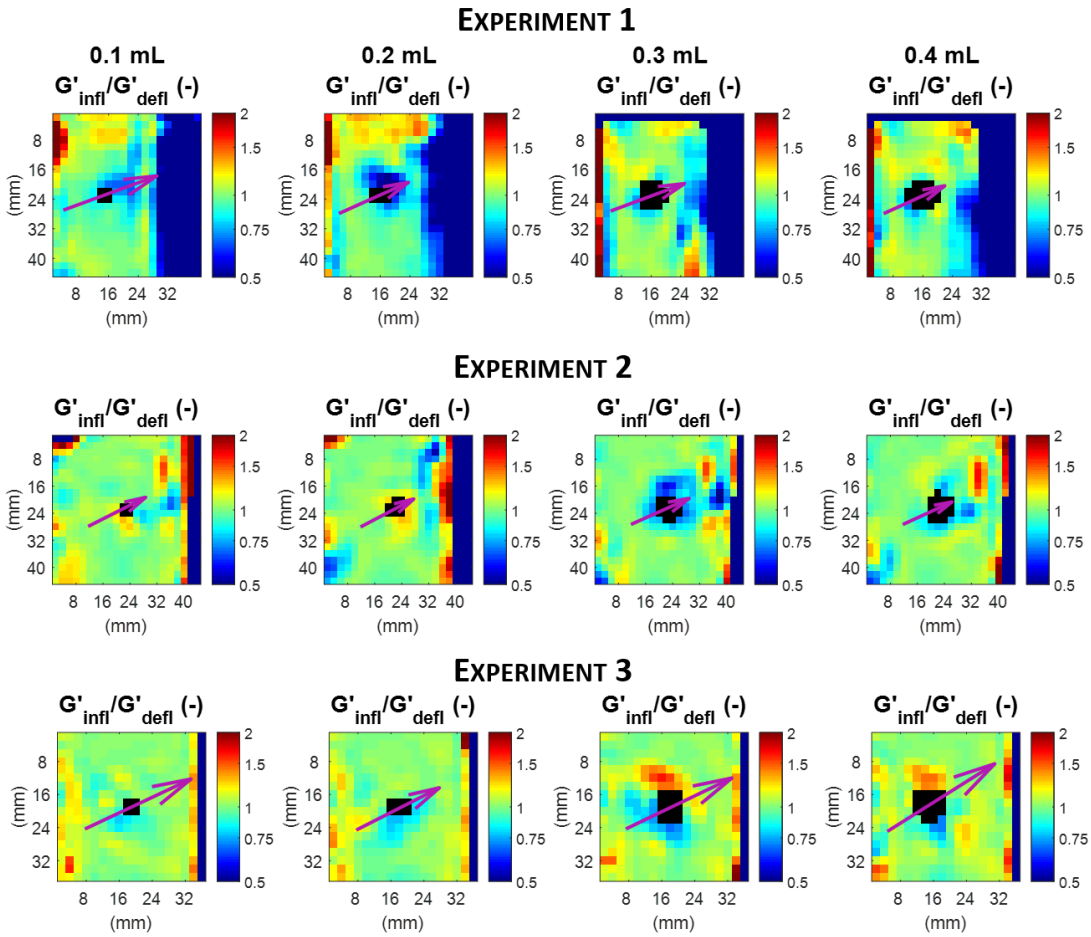

Figure 6.6.: Relative change in shear modulus between the various inflated states and the deflated case. The overlaid arrows show the mean direction of the propagating waves.

Given the non-trivial wave propagation, the Cartesian representation of the variation in shear modulus around the inflated balloon employed so far does not offer an easy comparison among different experiments, as well as with the corresponding analytical

results. For this reason, we have devised a new representation of the inclusion and its surroundings based on radial coordinates, which is presented in Fig.6.7. In the proposed

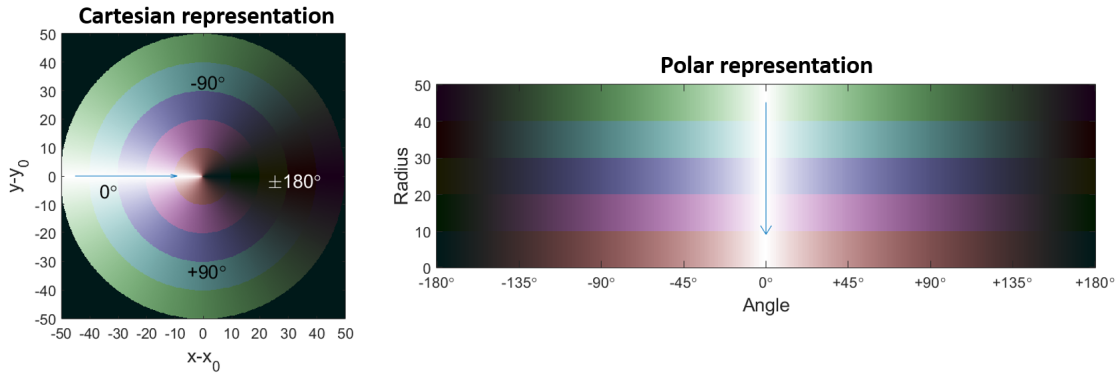

Figure 6.7.: Example of Cartesian representation of the inclusion where circular regions at different radial distances from the centre of the inclusion are showed with different colours (left). A better visualisation, independent on the mean direction of propagation of the waves, is obtained through the "unravelling" of the image following the perimeter of each circular region (right).

images, all voxels located at a fixed radial distance in the undeformed configuration from the centroid of the segmented inclusion are "unravelled" on the x-axis following the polar angle, defined with respect to the direction of the mean k-vector calculated in the selected ROI. With the new representation, the understanding of the deformation probed by the propagating waves is simpler, with a compression expected in the regions around a 0° and 180° angle from the direction of the mean k-vector and a tension around ±90°.

Fig.6.8 shows the direct comparison between the polar representation of the probed deformation (left), $\boldsymbol{CK} \cdot \boldsymbol{K}$, and the generated relative G' variation obtained experimentally (middle). A further comparison with the analytically predicted patterns for the same inflation levels assuming a simple plane wave propagation is also proposed (right). In this last case, the employed material parameters were obtained from the fitting of the pressure data measured for each experiment using the modified Mooney-Rivlin material law carried out in Section 3.3.4. The experimentally generated variations in shear modulus presents several elements in common with the probed deformation patterns (see arrows), especially at higher inflation levels; however, the location of the detected changes do not always match those of the applied deformation. At lower inflation levels, instead, despite no major variation is expected, this is not always found in the experimental pattern. Furthermore, overall the patterns seem to present a better agreement starting from one or two voxels away from the interface between the inclusion and the surrounding phantom material. On the other hand, in spite of a simplification on the wave propagation, the patterns

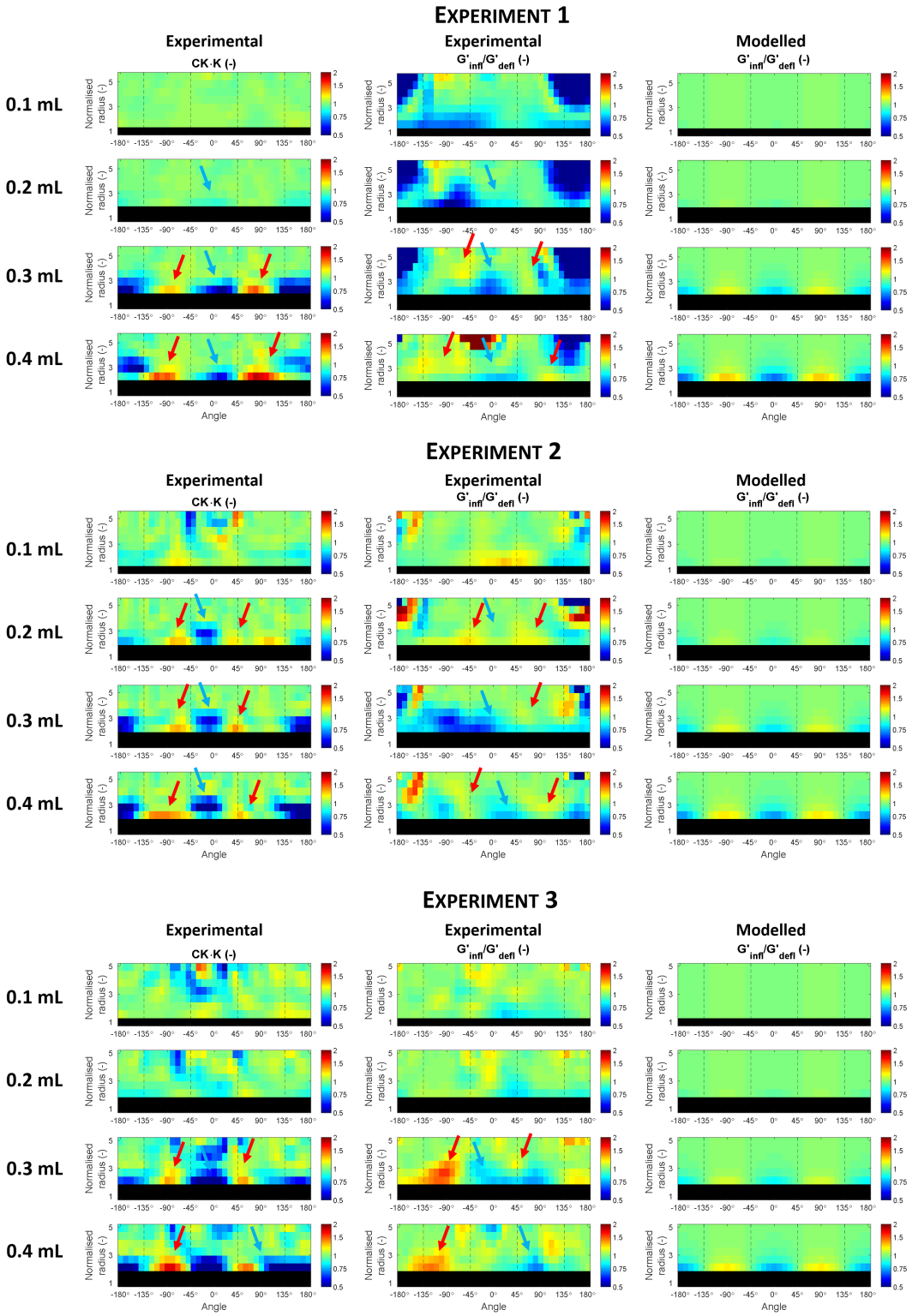

Figure 6.8.: Polar representation of the probed deformation (left), calculated using the local k-vector estimated from the wave images, compared with experimental (middle) and analytical (right) relative shear modulus variation at the four inflation levels investigated through three replicas of the inflation experiment. The common elements in the generated patterns are highlighted with arrows. The balloon region is blacked out.

associated to the probed deformation displayed tension/compression at the exact locations of the predicted shift in apparent shear modulus at all the investigated inflations.

6.3. Preliminary *Ex Vivo* Experiments Using Bovine Tissue Sample

The results obtained from the phantom experiments have shown a correlation between the applied deformation and the viscoelastic response of the phantom; furthermore, similar patterns have been analytically predicted, confirming a theoretical understanding of the observed alteration of shear modulus of soft tissue generated by pressurised tumour expansion. Unlike the plastic material used to make the phantoms, however, real tissue presents a more convoluted stiffness distribution, as well as additional challenges that could be neglected in the experiments presented so far. Aiming to bridge the developed analytical considerations to *in vivo* tissue, we have reproduced the same experiment *ex vivo* using a bovine tissue sample. Here we introduce the details of the implementation of the experiment, followed by a presentation of the first obtained results.

6.3.1. Experiment Implementation

A suitable sample was sought to reproduce the proposed experiment *ex vivo* using real tissue. The ideal sample would be able to withstand inflations comparable to those employed in the phantom experiment and the generated stress must increase nonlinearly with the applied strain, hence leading to a variation in the measured apparent shear modulus under sufficient inflation. Furthermore, blood vessels and nerves around the inserted balloon should provide additional features to help the image registration method estimate the applied deformation. Three different tissue samples were tested: ovine liver, ovine leg and bovine joint, obtained from a local abattoir. Analysis of the inflation pressure revealed that only the latter was capable of withstanding higher inflation levels employed; for the other two cases, a sudden decrease in pressure was associated to the rupture of the tissue (see Fig.6.9), as explained in Section 3.3. Given the fragility of the other samples, the bovine tissue sample was employed for the inflation experiment. To avoid undesired ruptures, however, the balloon inflation was reduced to a range going from 0.15 ml to 0.35 ml in steps of 0.05 ml.

The protocol used to carry out the inflation experiment was essentially the same as the one presented in Section 3.4. Nevertheless, a few corrections needed to be applied due to the time dependent deterioration of the tissue sample compared to stability of the PVC mixture. Exposure to air leads to tissue dehydration, which can alter its biomechanical properties and compromise the shear modulus measurements with respect to the deflated state. For this reason, immediately prior to the acquisition of the MRE and anatomical

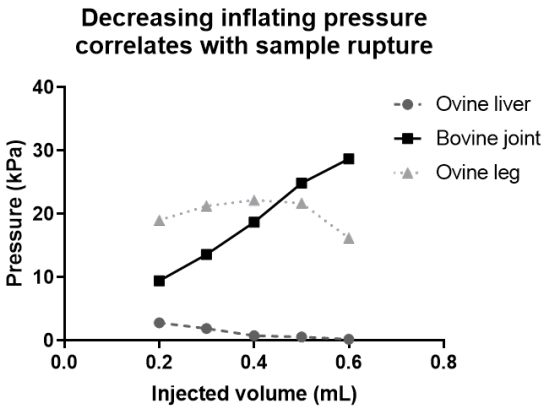

Figure 6.9.: Unlike the other two samples, the bovine joint proved capable of sustaining the stress generated by the balloon inflation without rupturing.

images, the sample was sprayed with water and loosely wrapped in a thin plastic film, to help keep the sample hydrated without changing the boundary conditions. Aiming to reduce the acquisition time, an NSA of 2, instead of 4, was used; while this effectively halves the acquisition time, the SNR is reduced by a factor $\sqrt{2}$. Finally, gadolinium was added to the water used to inflate the balloon in a 0.3 mM concentration, to provide a better contrast from the tissue sample. Under these conditions, one successful experiment was carried out, the results of which are reported in the following section.

6.3.2. Initial Results

The inflating pressure measured at the selected inflation volumes and the associated radial stretch are presented in Table 6.1.

	0.15 mL	0.20 mL	0.25 mL	0.30 mL	0.35 mL
Pressure (kPa)	22.0	26.8	32.0	35.4	19.2
Stretch (-)	1.55	1.79	1.86	2.04	2.18

Table 6.1.: Inflating pressure (kPa) and radial stretch (-) measured from the bovine tissue sample

The modified Mooney-Rivlin material law in the form $W = \mu_1/2\,(I_{\hat{\mathbf{C}}} - 3) + \mu_2/2\,(II_{\hat{\mathbf{C}}} - 3)^2$ was fitted to the acquired data in the way explained in Section 3.3 (see Fig.6.10). The best estimate of the parameters and the results of the tests carried out to quantify the quality of the fit are shown in Table 6.2.

μ_1 (kPa)	μ_2 (kPa)	r^2	SSR
18.4	0.4	0.98	0.007

Table 6.2.: Bovine tissue sample pressure data fitting

A Pearson's correlation coefficient of 0.98 indicates a good correlation between the observed

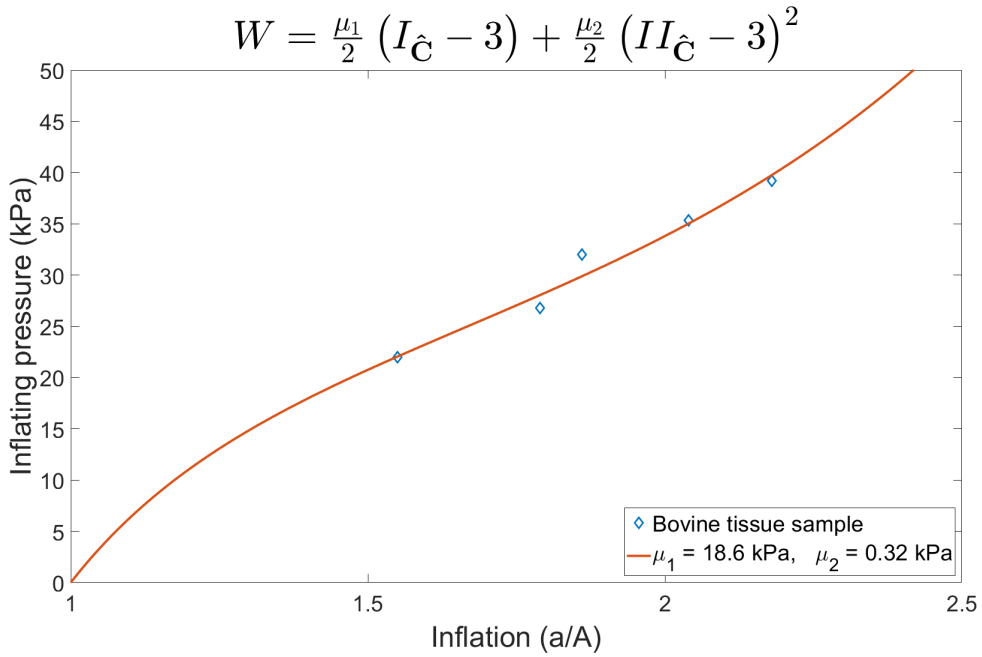

Figure 6.10.: The modified Mooney-Rivlin model provides a good fit of the pressure data acquired experimentally.

and expected values. Using Eq.2.68, the linearised shear modulus of the tissue sample could be calculated from the material parameters and was equal to 18.4 kPa.

The in-plane images presented in Fig.6.11-top show the location and size of the inclusion at the different inflation states. Fig.6.11-middle reports the displacement $\boldsymbol{u}_x$ generated by the propagating shear waves, the amplitude of which is displayed in Fig.6.11-bottom. The shear modulus of the tissue was estimated from the wave data using the reconstruction method presented in Section 6.1. The reconstructed G' for the various inflation states of the balloon is shown in Fig.6.12-A. With respect to the phantom experiments, a more inhomogeneous shear modulus distribution was observed in the bovine tissue sample. Again, the mean value of the background G' around the inclusion was estimated for the different injected volumes (Fig.6.12-B), where the region corresponding to the location of the inclusion and its immediate surroundings was masked out. While the mean G' value remains roughly the same, it is to be noticed that the standard deviation of the G' distribution is on average equal to the 30 % of the mean value and on average 2.4 times larger than in the phantom cases. Compared to the phantom experiments, in this case data filtering produced an overestimation of the background shear modulus (26 ± 10 kPa), which exceeded the value retrieved from the fitting of the inflating pressure. When no filtering was applied, the background value (19 ± 5 kPa), obtained from the image of the deflated balloon, was in better agreement with the analytical prediction obtained from the model (Fig.6.12-C).

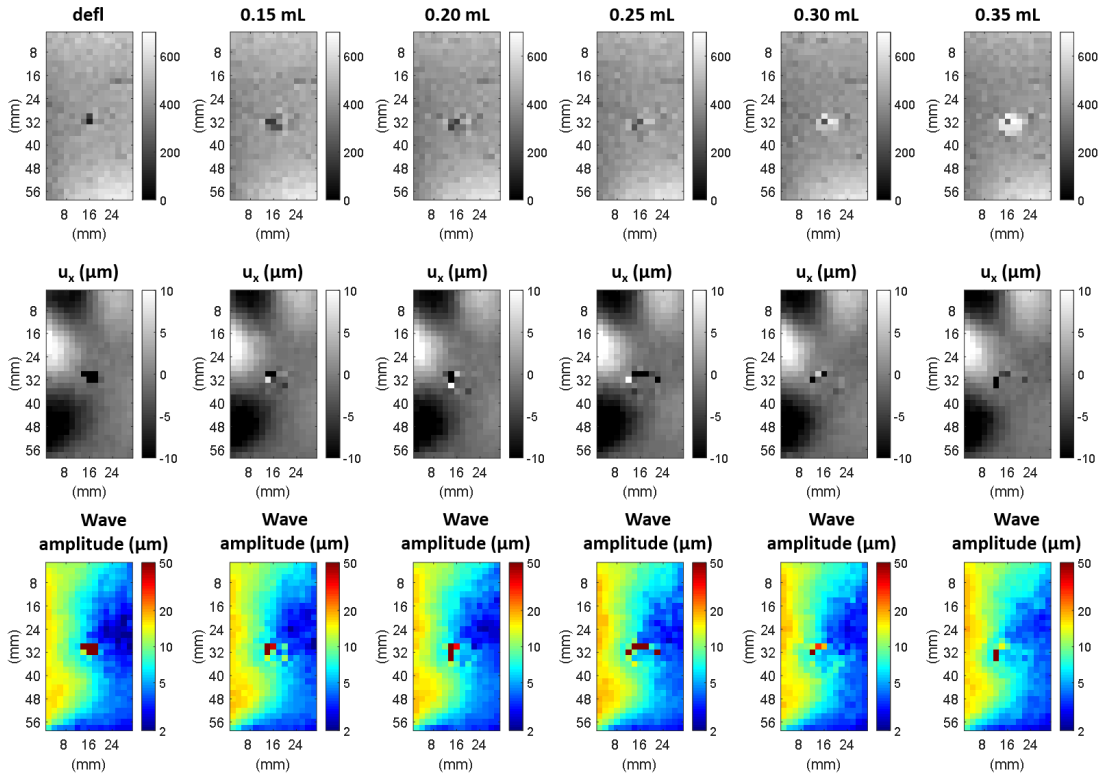

Figure 6.11.: Top) Magnitude images of the inclusion at different inflation levels. Middle) Wave images acquired through MRE. Bottom) The wave amplitude fades quickly while moving away from the wave source.

The voxel-wise ratio between the shear modulus reconstructed at each inflated state and the one obtained from the deflated case was compared with the numerically predicted patterns in Fig.6.13. Similarities with the probed deformation, calculated through $\boldsymbol{CK} \cdot \boldsymbol{K}$, were also sought and pointed out with arrows. The analytical predictions, based on the assumption of plane waves propagating unidirectionally through an homogeneous medium, revealed an expected softening at the leading and rear edge of the inclusion and a material stiffening on the sides, corresponding to the -135° to -45° and 45° to 135° regions. These patterns have been numerically calculated using the material parameters estimated from the fitting of the pressure data. Compared to the analytical estimates, the experimentally measured patterns are more convoluted and do not always correspond to the predictions; however the G' variation appears consistent throughout the various inflation states in most of the regions. The increasing reduction in shear modulus in the -45° to 45° region is possibly the most evident feature and it well correlates with the theory. The interpretation of the calculated $\boldsymbol{CK} \cdot \boldsymbol{K}$ appears more challenging, nonetheless a few areas in common with the measured G' variation are pointed out with arrows.

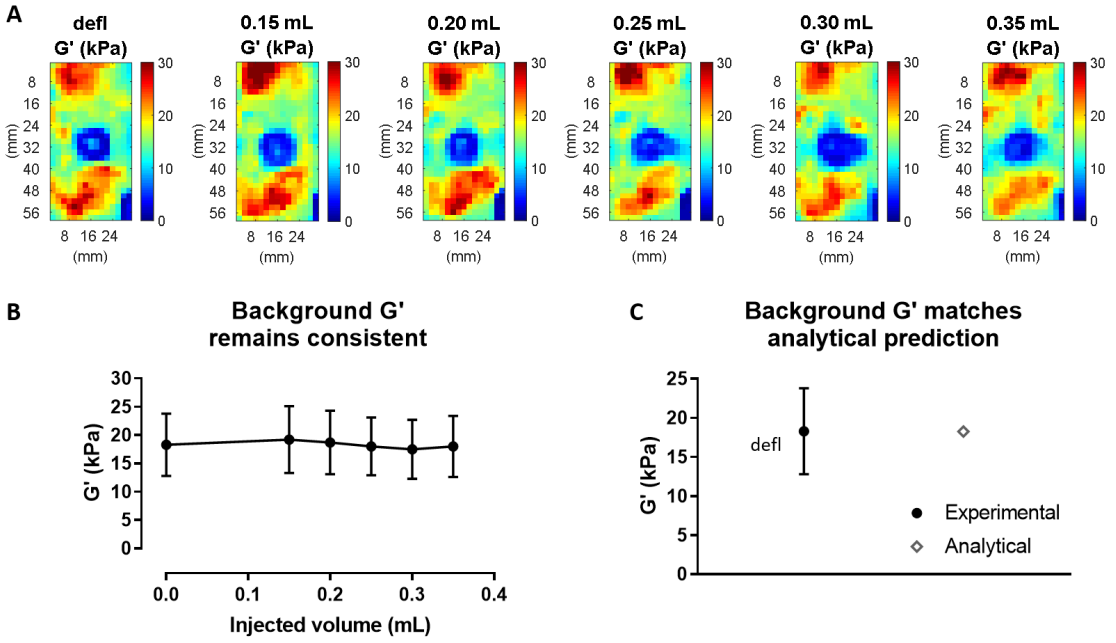

Figure 6.12.: The reconstructed shear modulus shows a heterogeneous distribution around the inclusion (A), as confirmed by the large standard deviation measured for each case (B). The mean value, however, remains roughly constant. A comparison between the reconstructed background G' and the value analytically calculated shows a good correlation.

6.4. Discussion

A list of the main results reported in this chapter is presented in Table 6.3.

In this chapter we have presented the results obtained from three replicates of the inflation experiment performed in phantoms to demonstrate an experimental correlation between the applied spherical macro-deformation and the resulting apparent variation in shear modulus. As explained previously, the term "*apparent*" indicates the probing of the nonlinear variation in G' along the direction of propagation of the shear waves when the sample is subjected to a macro-deformation, compared to the intrinsic shear modulus of the material in the undeformed state. In the ideal case analytically investigated in Chapter 2, we have assumed plane waves in the form $\boldsymbol{u} = u_y \hat{\boldsymbol{e}}_{\boldsymbol{y}} = \delta y \sin(k_x x)\, \hat{\boldsymbol{e}}_{\boldsymbol{y}}$, which describes a wave propagating in the x-direction and polarised along the y-direction. Such simple waves allows the detection of perfectly symmetric patterns at both sides of an axisymmetically deformed sphere; nevertheless, this situation is more complicated to reproduce experimentally. Material inhomogeneities can in fact reflect or refract the waves to different directions, while the proximity between the wave source and the balloon is such that the approximation of a planar wave front is difficult to achieve. The use of a wider piston, however, allows to reduce the curvature of the wave front, as shown in

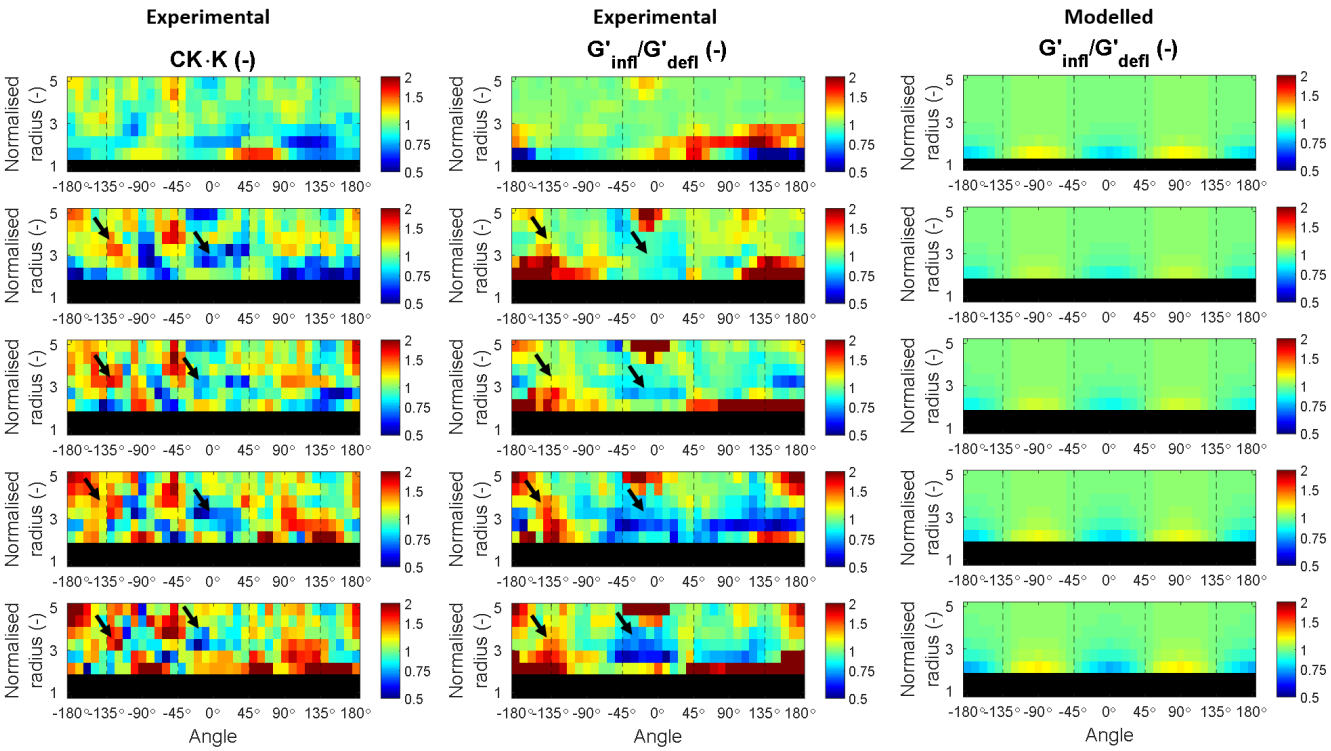

Figure 6.13.: The empirical $\boldsymbol{CK} \cdot \boldsymbol{K}$ (left) and G' variation (centre) show a very convoluted pattern, however some matching features are pointed out with arrows. The increasing softening in the -45°÷45° region also correlates with the analytical predictions (right).

Fig.6.1-A. The macro-deformation field estimated from the nonrigid registration of the high resolution MR images of the inclusion, on the other hand, provides an adequate approximation of a spherical inflation used for the analytical modelling. In light of these experimental limitations, the local calculation of the k-vector direction from the wave complex displacement grants an understanding of the deformation probed by the waves through the voxel-wise calculation of $\boldsymbol{CK} \cdot \boldsymbol{K}$. This devised measurement provides an easy differentiation between compression and tension, as well as a quantification that can be directly compared to the measured relative variation in shear modulus. Despite the more complex wave propagation patterns, the probed deformation closely resembles the expected one when phantoms were used, with a compression at the front and rear end of the inclusion and a tension sensed on the sides.

To quantify the shift in G' caused by the generated circumferential strain, a shear modulus map was reconstructed for each inflation state. To this goal, a vibration frequency of 210 Hz was employed. From Fig.6.1-A it is possible to make out the size of the inclusion, comparable to half the resulting wavelength of the propagating waves. While a longer mechanical excitation period would lead to a higher phase accumulation (see Eq.1.3),

Main results
A original approach to allow a better visual comparison between the patterns produced at different inflation states and through various experiments was conceived.
To deduce the local deformation sensed by the generated probing waves, a novel metric, $\boldsymbol{CK} \cdot \boldsymbol{K}$, was devised, to account for more complex wave behaviours. The produced pattern showed a good correlation with the model predictions at various inflation states.
The apparent G' reconstruction from MRE data also showed a promising agreement with the analytically produced patterns, however an improved reconstruction strategy is needed to better deal with the artifacts at the interface between the balloon and the surrounding material.
A preliminary *ex vivo* experiments helped to identify the challenges to be expected in the translation to an *in vivo* setting.

Table 6.3.

hence producing an improved wave image quality, the diffraction limit allows only to resolve objects of commensurable size to that of the associated wavelength. Due to the limited reconstruction window required for a local shear modulus quantification, the calculation of the local derivative estimates would also be more affected by noise in the case of long wavelengths, making the use of higher frequencies preferable. However, given the correlation between the vibration frequency and the wave amplitude attenuation as a function of the penetrated distance, a trade-off is required.

A similar reconstructed background shear modulus was obtained throughout the three replicas of the experiment, confirming the reproducibility of the phantom production, as well as the accuracy of the analytical predictions. These measures were obtained masking out the inclusion and its immediate surroundings from the reconstructed maps. This exclusion was motivated by presence of water inside the balloon, which does not support the propagation of shear waves, hence resulting in the reconstruction of meaningless values. In the absence of displacement, in fact, the stack of images sampling the different points of the wave cycle will be dominated by noise, which is interpreted as a high frequency oscillation during the reconstruction process, hence leading to the reconstruction of very low values. The use of finite differences with one-sided approximation, rather than the currently employed polynomial fitting method aimed at calculating the derivatives for the central pixel of the reconstruction window, can help tackle this problem. Furthermore, the

assumption of local homogeneity for both $\mathcal{G}'$ and $\mathcal{G}''$ throughout the chosen reconstruction window, required to simplify Eq.6.2 into Eq.6.3, is clearly not respected at the interface between the balloon and the surrounding PVC phantom, leading to underestimations[260]. Susceptibility artifacts and a limited image resolution, compared to the size of the inclusion, can exacerbate this issue. This underestimation seems to generally become more prominent with the increase in size of the balloon, which will then reflect into an estimated relative softening, or reduced stiffening, when compared to the unaffected values of the voxels around the inclusion in the deflated state.

Despite these limitations, the images showing the polar representation of the relative change in shear modulus present a reasonable agreement with the probed deformation in terms of apparent anisotropic pattern. This is true especially at higher strains, where the nonlinear tissue response is more prominent. This agreement is also found with the numerically calculated patterns in the simplified case of a perfectly spherical inflation and of unidirectional plane waves. Most of the regions that do not show a comparable response, however, can be traced back to locations in the shear modulus maps where the reconstruction appears heavily affected by the presence of the inclusion, i.e. 0.3 mL inflation from experiment 2 and 3 or 0.2 mL inflation from experiments 2, shown in Fig.6.5-A and Fig.6.6. The almost perfect agreement between the numerical patterns and the $\boldsymbol{CK} \cdot \boldsymbol{K}$, in fact, suggests that the differences in the experimentally measured variations should be ascribed to reconstruction issues rather than to the reliability of the estimate of the deformation field or the estimation of the correct local k-vector direction. Despite showing very similar patterns, the intensities of the probed deformations, $\boldsymbol{CK} \cdot \boldsymbol{K}$, and of the predicted variations in shear modulus do not follow a perfect one-to-one correlation; this was expected, as the Mooney-Rivlin model does not involve a linear relationship between the applied strain and the resulting variation in shear modulus. A more similar intensity is seen between the experimental and predicted change in G'; nonetheless, the employed constitutive equation does not seem capable to reproduce the patterns empirically measured further away from the inclusion, leading to the argument that a different material law might better represent the tissue response in the presence of low strains.

The MRE reconstruction employed in this study attempts to estimate the shear modulus of the probed sample solving the wave equation presented in Eq.6.1, valid for wave propagation in a linear viscoelastic material. This condition is accepted under the assumption that the strain created by the waves is small enough to produce a linear stress response. The application of a macro-deformation would then change the wave behaviour and the associated wavelength lengthening or shortening would lead to the reconstruction of an anisotropic shear modulus distribution. The incorporation of the correct material law in the reconstruction process, on the other hand, would permit to account for the nonlinear

response of the sample to an applied macro-deformation, hence allowing to reconstruct the intrinsic shear modulus of the material independently of the probing direction. This approach might find applicability in many cases where the bias introduced by a macro-deformation might be undesired (i.e. liver and heart compression during the respiratory and cardiac cycle or external compression during a breast exam) and a recent paper has looked into the development of a mathematical framework to be employed in liver elastography[86]. Additional work is still under development within our group to undo the effects of a spherical deformation and reconstruct the intrinsic shear modulus of the material. Promising results have been published in different conference proceedings[261, 162], an overview of which will be given in Chapter 7.

Quantitative Representation of Data Quality

The employed MRE reconstruction technique is very sensitive to data quality[51], which directly depends on the quality of the acquired wave displacement. As mentioned previously, because of the viscous dampening caused by the material, wave attenuation plays a non negligible role in the MRE reconstruction from the experimentally acquired MRE data. A smaller displacement, in fact, would make the local wavelength estimation more sensitive to noise, leading to less reliable estimates. The loss in amplitude A at the wave propagation distance Δx can be expressed, for many soft tissues, as a power law dependent on the vibration angular frequency ω[67]:

$$A(x + \Delta x) = A(x)e^{-\alpha(\omega)\Delta x} = A(x)e^{-\alpha_0 \omega^{\eta} \Delta x} \tag{6.6}$$

where α_0 and η are tissue dependent attenuation parameters. At the chosen 210 Hz frequency, wave propagation experienced a significant attenuation throughout the few mm that separate the inclusion from the wave source, hence requiring the use of a considerably high vibration amplitude. This enhanced attenuation is the result of an elevated viscosity of the phantom, which contradicts the findings from the rheological material characterisation. It has to considered, however, that the rheometric tests presented in Chapter 5 have been carried out using a maximum vibration frequency of 10 Hz, much lower than the 210 Hz employed to acquire the MRE images. At such low frequencies, the viscous response of the material was much less pronounced, leading to an underestimation of the impact of viscosity on the inflation experiment.

When the relative shear modulus variation is considered, however, both the wave amplitude image A_j in the inflated state j and reference deflated case A_0 need to be taken into account, the combination of which gives an understanding of the local trustworthiness of the generated images. To make such quality metric comparable throughout different inflations within a single experiment, each amplitude image has been divided by the

maximum value measured throughout the various inflations, $\max(A_i)$, in an ROI around the inclusion, and the voxel-wise product of the normalised wave amplitude from the reference and deformed image has been calculated for each inflation, in the following way:

$$(\text{combined relative wave amplitude})_j = \frac{A_j A_0}{\max(A_i)^2} \times 100 \quad \text{with} \quad i = [0, 1, ..., N],\ j = i \backslash \{0\}$$

where the index i indicates the inflation level, including the deflated state. Values close to 100 % signify a similar amplitude in both the deflated and inflated cases and little attenuation with respect to the region in the ROI closest to the wave source.

Another source of uncertainty in the MRE reconstruction is given by the presence of additional frequencies other than the selected vibration frequency in the wave images. The acquisition of 8 data points for each wave cycle allows the voxel-wise detection of the real and imaginary components of the displacement occurring at the main vibration frequency and at the first couple of upper harmonics. Given a working frequency of 210 Hz and in the light of Eq.6.6, any contribution from upper harmonics can be reasonably neglected; however, because of the use of a limited number of time samples, noise and reconstruction artefacts, usually related to high frequency perturbations, will add up to the energy of the Fourier coefficients associated to upper harmonics. The percentage ratio between such contributions and the magnitude of the Fourier coefficients representative of the actual vibration frequency offers an indicative metric of the local quality of the acquired wave data and hence of the reconstructed G'. Unlike the wave amplitude, a value closer to 0 % suggest a higher data quality. Again, the voxel-wise product of the upper harmonic contribution for the inflated case j and the deflated one, after being conveniently warped into the current configuration, produces a metric of the quality of the reconstructed relative shift in shear modulus around the inclusion:

$$(\text{contribution from upper harmonics})_j = \left(\sum_{k=1}^{M} \frac{|c_k|}{|c_0|} \times 100 \right)_j \quad \text{with} \quad j = [1, ..., N]$$

where c_k are the complex Fourier coefficients associated to the upper harmonics, while c_0 refers to the main frequency.

An exemplary representation of the two metrics calculated around the inclusion for one of the phantom experiments is reported in Fig.6.14-A, with the corresponding polar plots in Fig.6.14-B. Both metrics associate a higher reliability to the leading edge of the balloon, at angles between the mean direction of propagation of the shear waves and the radial distance from the centroid of the inclusion ranging between $-45°$ and $45°$. In such region, given the proximity to the wave source, the combined relative amplitude is closer to its maximum value and the higher SNR improves the detection of the main vibration

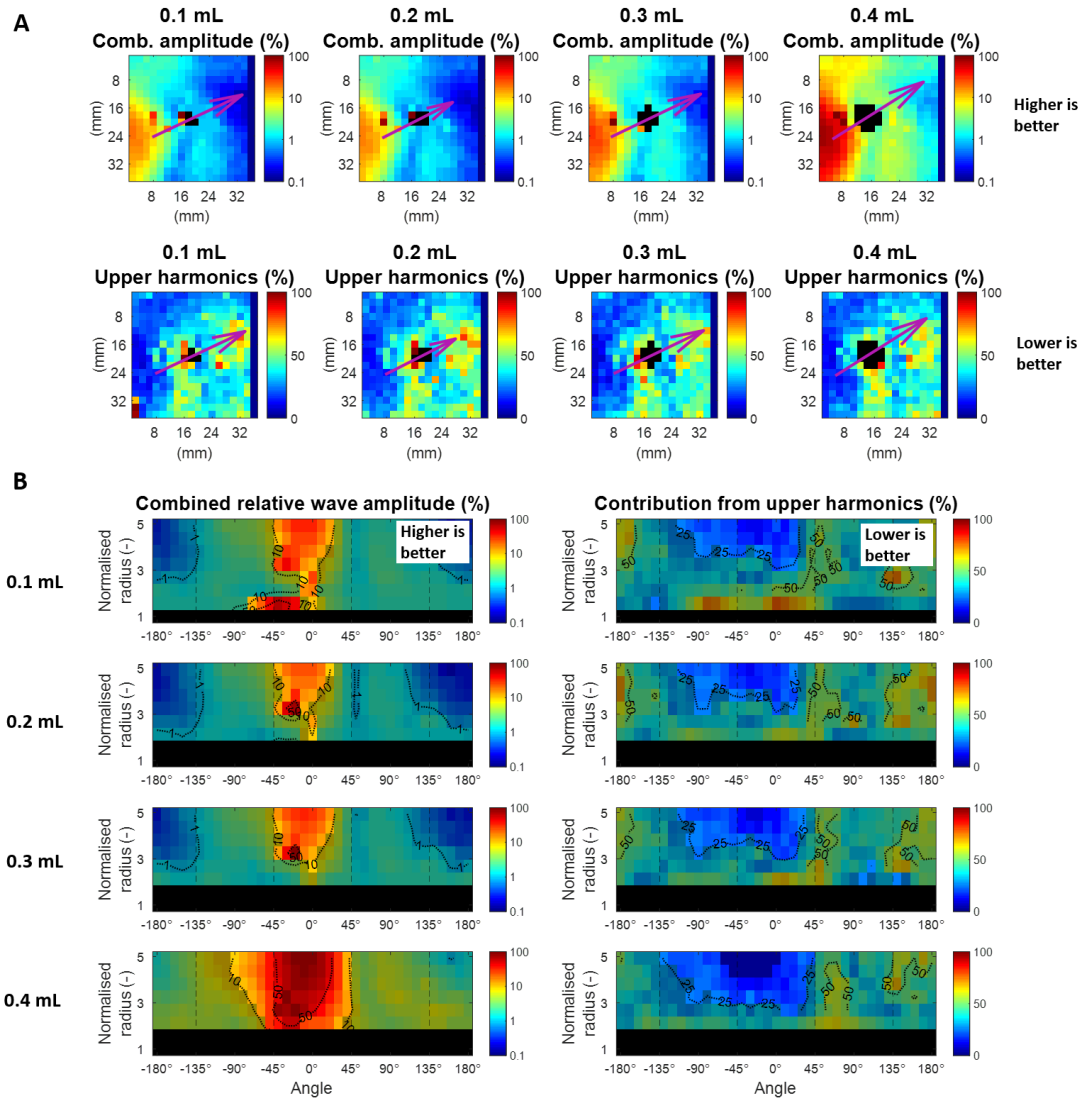

Figure 6.14.: Cartesian (A) and polar (B) representation of the two metrics devised to determine the local reliability of the measured variation in shear modulus at different inflation levels. In the polar representation, the less trustworthy regions (< 10 % and > 25 % respectively) are shaded out.

frequency, leading to a contribution from upper harmonics closer to 0 %. Interestingly, however, at these polar angles the data quality decreases at a very close radial distance from the inclusion, due to the presence of water in the balloon, that does not support shear wave propagation, hence affecting the wave image reconstruction in its immediate surroundings. Moving towards the ±180° angle, it is evident how both metrics show a sudden decrease in data quality, especially in the case of the combined relative amplitude, which drops by 1 to 2 orders of magnitude. Furthermore, given the quick wave attenuation at the trailing edge of the balloon, such a metric quickly approaches values close to 0.1 % at higher radial distances, in an opposite way to what was observed at the leading edge. The same decreasing trend is seen for the contribution from upper harmonics, with values that however rarely exceed 50 %. A similar data quality distribution is found for all the three replicas of the experiment (data not shown), as an indication of the trustworthiness of the relative shift in reconstructed shear modulus calculated at the different voxels around the inclusion and suggesting an overall reduced reconstruction quality when moving towards higher absolute polar angles. Here, the two threshold defining the local trustworthiness of the reconstructed shear modulus in Fig.6.14-B have been selected arbitrarily to give a general idea of the reliability of the reconstruction; however the actual relationship between each metric and the reconstruction quality, as well as the relevance of the impact of wave attenuation and upper harmonic contribution and their combination into a unique metric, should be further investigated. Nonetheless, these qualitative results clearly identify a region of higher trustworthiness, which coincides to the leading edge of the inclusion with respect to the propagating waves. The highest correlation between the analytical prediction and the shift in shear modulus measured in phantoms and especially in the tissue sample, were found nearby this region, and will be further discussed later in this section.

As mentioned, the employed curl-reconstruction method requires a higher measurement accuracy due to the increased order of differentiation of the wave displacement with respect to other techniques. To improve the quality of the acquired data, in the phantom study we have employed an NSA of 4, doubling the image SNR. Nevertheless, the acquisition time was also increased four times, making this approach acceptable in the case of phantoms, but less useful in real tissue investigations or with patients. To circumvent this problem, local MRE reconstruction strategies based on FEM have been proposed in the literature[260], which reduce the order of derivatives using an integration approach. Compared to the curl method, state-of-the-art local FEM methods showed a reduced sensitivity to noise in both phantom and anatomical data, although still presenting a strong dependence on the local homogeneity assumption.[260]. Global heterogeneous FEM approaches[259, 262], however, generally require regularisation of both the G' and hydrostatic pressure and,

although showing a comparable accuracy in phantoms, they present longer computational times and a higher parameter dependency[260].

Insights on *Ex Vivo* Experiments

Finally, we have shown the first results obtained performing the presented experiment on a soft tissue sample. The use of real tissue, rather than a polymer phantom, inherently generates additional complications that must be dealt with. While certain tissue samples proved too fragile, the bovine joint was capable to withstand the deformation generated by the inflated balloon. The main obstacle, however, was presented by the deterioration of the sample once exposed to air due to tissue dehydration. Here we have tackled this problem by spraying the sample with water and retaining the humidity with a plastic film. We have seen that this method was sufficient to keep the background shear modulus, estimated through MRE, constant over the total time required to perform the experiment. Nonetheless, the large variation of the reconstructed G' over the region surrounding the inclusion represents a second major concern, as it does not fully satisfy the assumption of local homogeneity requested by the employed MRE reconstruction method and can lead to inaccurate reconstructed values. Finally, the employed tissue samples did not present evident structures that could help the image registration process, which therefore relied only on the change in size of the inflated inclusion. The absence of additional features can lead to an inaccurate estimation of the deformation field farther away from the immediate proximity of the balloon; nevertheless, the analytical predictions have shown that, at higher radial distances from the centre of the inclusion, the applied deformations should be not sufficient to alter the measured apparent shear modulus from its background value. An unreliable local estimation of the deformation field can reflect on the calculation of $\boldsymbol{CK} \cdot \boldsymbol{K}$, which, however, in the presented case appears to be mainly affected by inaccuracies in the estimation of the k-vector from the wave images. Given the very quick wave attenuation through the ROI around the inclusion, in fact, the wave amplitude reaches values as low as $\sim 2\,\mu m$ on the trailing edge and on the sides of the inclusion, much lower than those measured in the phantom experiments. As explained previously, images of very small displacements are more affected by noise, hence making it difficult to capture the local wavelength and hence to reconstruct the correct shear modulus. This is particularly true for the reconstruction method employed, which relies on higher order derivative and is more sensitive to image quality. In this sense, halving the number of averages to reduce the acquisition time was expected to diminish the image SNR with respect to the phantom data. All these factors, combined, led to a more accurate G' reconstruction, and hence calculation of its variation, on the leading edge of the inclusion with respect to the mean k-vector direction. The experimentally measured softening, in fact, shows a good degree of consistency with the corresponding $\boldsymbol{CK} \cdot \boldsymbol{K}$, while, despite the simplifying assumptions

of tissue homogeneity and plane waves, both the pattern and the intensity trend closely match the analytical prediction in such regions. The modified Mooney-Rivlin material law employed, in fact, proved capable to capture the stress/strain response of the tissue, providing a good fit of the pressure data.
The increase of the wave amplitude can clearly improve the quality of the MRE data without incrementing the acquisition time, hence increasing the overall reliability of the k-vector estimation and, consequently, of the reconstruction. This can be done either locating the inclusion closer to the wave source or increasing the vibration amplitude of the push/pull rod of the transducer. The latter has been attempted, however an intrinsic limit to the vibration amplitude exists and has been identified by the snapping of the moving part of the transducer that connects the push-pull rod to the solenoid. Locating the inclusion closer to the wave source, instead, is discouraged, as the boundary conditions would be inherently different from those used in the analytical model and a direct comparison would become less relevant. Additionally, given the higher intrinsic shear modulus of the tissue compared to that of the PVC phantoms, the same vibration frequency, 210 Hz, results in a longer wavelength, hence reducing the ability to clearly resolve the size of the generated variations in G', comparable to the size of the inclusion. While a higher vibration frequency would solve the problem, Eq.6.6 has shown that the damping would become even more pronounced, requiring an even higher input power that the employed transducer could not sustain.

These results have highlighted a series of technical limitations which arise when MR-elastography is translated to *in vivo* experiments and to clinical applications. Much effort has been and is currently being put to have a better control over the generated waves through the development of novel and more precise transducers for patient applications[66]. Following this direction, further work on the hardware used for the presented experiments is required to validate the proposed theoretical framework both *ex vivo* and *in vivo* and to further investigate the effects of tissue inhomogeneity on the reconstructed shear modulus.

7. Conclusions & Future Work

7.1. Summary

Throughout this thesis we have introduced a novel mathematical and experimental framework to characterise the apparent variation in shear modulus measured around a pressurised tumour through MRE. Under the assumption of linear elasticity, the reconstruction employed to estimate the mechanical properties of soft tissue from the MR images of the propagating shear waves does not account for its nonlinear stress/strain response when subjected to large deformations, leading to a biased reconstruction. In the particular case of a spherical inflation, an idealisation of the stress generated by a solid tumour expansion on the isotropic host tissue, we have demonstrated analytically and experimentally how this bias yields a signature pattern that can represent a valuable biomarker for tumour growth and expansion.

In Chapter 2 an analytical formulation to explain the impact of an underlying macro-deformation on the wave equation and on the quantification of the elasticity tensor $\mathcal{G}'$ in elastography was developed. Using a modified version of the Mooney-Rivlin constitutive law and approximating the tumour-host tissue ensemble with a thick-shelled sphere, it was also shown that the detected apparent variation in shear modulus is strongly dependent on the shear waves, the direction of propagation of which allows to probe different components of $\mathcal{G}'$. Using the developed mathematical results, a quantification and mapping of the theorised anisotropy as a function of the magnitude of the spherical deformation was then presented, showing the dependence on the mechanical parameters of the material law chosen to represent soft tissue rheology. These analytical findings present the first evidence of the hypothesised apparent signature pattern generated by the nonlinear response of an isotropic medium to the radial stress produced by a mimicked pressurised tumour. The intensity of the apparent shift in shear modulus showed a direct correlation with the inflation of the inclusion, suggesting the potential to use the estimation of apparent peri-tumoural anisotropy, detected through MRE, as a biomarker to assess tumour growth and expansion. Also, the generated patterns displayed little dependence on the strain energy density function chosen to model the elastic behaviour of soft tissue, indicating that the same pattern could be expected in different organs and different types of soft tissue, regardless of their rheological behaviour. More important is the correct

characterisation of the material parameters of the tissue, as a wrong estimate can falsely associate the detected anisotropy to a more or less intense underlying strain. The correct estimation of the deformation applied by the solid tumour is in fact crucial to retrieve the state of stress of the tumour; unlike this simplified forward situation, the deformation field cannot be directly assessed in a real tumour, as its unpressurised state is unknown, hence leading to further assumptions as described in the following section of this chapter.

To reproduce these findings in a phantom setting, we have identified a nonlinear viscoelastic isotropic material capable of sustaining deformations comparable to those found in a tumour environment, replicated through the use of a balloon-catheter. A description of the protocol to build the phantom and details of the steps involved in the designed inflation experiment have been reported in Chapter 3; the correct quantification of the radial stretch and the development of a pressure measuring system to monitor the radial stress generated by the inflated balloon onto the surrounding matrix were crucial aspects to relate the experimental findings to the equivalent conditions in the analytical framework. Furthermore, the pressure trend as a function of the radial stretch was accurately captured by the constitutive law selected in Chapter 2, hence supporting its application to describe the rheological behaviour of the phantom material as well.

A local estimate of the magnitude and directionality of the deformation applied by the inflated balloon is required to get an understanding of the expected variation in shear modulus around the inclusion. To this end, a nonrigid image registration strategy was implemented and its validation using an *in silico* ground truth model has been presented in Chapter 4. The addition of silica gel during the making of the plastisol phantom helped guiding the registration of the MR images of the balloon-catheter inflated to different levels, producing an accurate estimate of the generated deformation field. This strain estimation method was further tested on MR images of murine and human tumours, subjected to macro-deformations generated by external compressive forces.

Chapter 5 reported the viscoelastic characterisation of the soft plastic material selected to mimic soft tissue through a controlled stress rheometer. The required nonlinear stress/strain response was initially assessed, to ensure a variation in the apparent shear modulus measured through elastography. The addition of silica particles has been associated to an increased nonlinearity of the plastic cuboid without impacting its background shear modulus in the absence of forces, and, as expected from the literature, a rise in nonlinearity was positively correlated to the plastisol concentration too, for strains lower than 25 %. A mathematical model, based on different hyperelastic material laws, which makes use of fractional calculus to account for the viscoelastic response of the sample, was developed to fit the experimental data. While a first order polynomial constitutive equation proved incapable of approximating the rheological behaviour of the employed samples in the presence of tracking particles, both the modified Mooney-Rivlin law introduced

in Chapter 2 and the Fung-type exponential law produced a satisfactory fit of the data. The very mild viscoelasticity observed supported the decision to focus on the analytical investigation of the impact of a spherical macro-deformation on the apparent storage shear modulus G' estimated through MRE. The value of the linearised shear modulus of the plastisol material, calculated from the parameters associated from the best fits, was in good agreement with the same value extracted from the fitting of the pressure data using the modified version of the Mooney-Rivlin law; both of them represented a close approximation of the shear modulus empirically measured through MRE and presented in Chapter 6, further confirming the validity of the model.

Finally, in Chapter 6, experimental observations of the shear modulus anisotropy reconstructed from MRE data around the inflated inclusion have been shown. A qualitative comparison between the analytically predicted shift in shear modulus and the estimate of the local deformation probed by the waves has revealed similar patterns, the visualisation of which was facilitated by the use of a polar representation of the regions around the inclusion. These results represent an experimental validation of the analytical results presented in Chapter 2, confirming the potential employment of MRE to provide a novel biomarker for tumour stress. In order to bridge these findings to an *in vivo* setting, the results obtained from a first *ex vivo* experiment, carried out using a bovine tissue sample, have also been presented, which helped to identify new challenges associated to the translation to *in vivo* imaging. From the experiments, wave damping has also arisen as a major limitation for an accurate detection of the mechanical parameters of soft tissue through MRE. A method to assess the local quality of the reconstructed patterns from the analysis of the wave images, accounting for wave attenuation as well as for the presence of higher harmonics, has also been proposed. Given the anisotropic change in the shear modulus generated by a radial inflation, the presented metrics have helped identify specific regions around the inclusion where the measured shift in apparent shear modulus from the intrinsic value is more reliable.

7.2. Clinical Impact

The analytical predictions of an apparent shear modulus anisotropy around an inflated object confirmed the expected signature pattern generated by the tumour expansion against its surroundings. The experimental results provided a validation of the analytical findings under the controlled conditions offered by a phantom setting. These findings assume a crucial importance in the context of the FORCE project, as they demonstrate for the first time the need to account for the impact of tumour-associated forces in the MRE reconstruction of the material properties of soft tissue. The relevance of these results lies in the quantitative explanation of the observed patterns and provides evidence of the potential to use MRE to detect changes in the shear modulus of soft tissue caused

by tumour expansion, and therefore to indirectly estimate forces in cancer through the analysis of the signature pattern reconstructed around a pressurised tumour.

Knowledge of peri-tumoural anisotropy permits recovery of underlying radial stretch

A novel method to estimate tumour pressure from the MRE measurement of the anisotropic shear modulus distribution in the peri-tumoural region, given the assumption of an appropriate material law that relates the applied strain to the associated stress, is currently under development in our group, in parallel to the work carried out for this thesis. While in Chapter 2 it was shown that knowledge of the deformation gradient $\boldsymbol{F}$, under the choice of a specific constitutive equation, can be used to predict the associated shift in shear modulus as probed by the shear waves, in an opposite way, a known deformation field can be incorporated in the inverse solution of the wave equation, hence allowing to effectively "undo" the apparent anisotropy effect and to reconstruct the intrinsic shear modulus of the material associated to the undeformed case. This was recently demonstrated by Capilnasiu *et al.* (2018) in PVA samples subjected to different levels of uni-axial compression and using the same modified version of the Mooney-Rivlin material law presented in this report[86]. Fovargue *et al.* (2018) have extended this work to the case of the radial stretch generated by an expanding sphere onto its surroundings. Using a FEM simulation of a spherical deformation of a Neo-Hookean material, we have shown the possibility to undo the bias and to reconstruct the intrinsic shear modulus of the medium[162]. Knowing the expected apparent variation generated by a spherical inflation, an objective function defined as the voxel variance within an annular region around the inclusion was designed, to iteratively seek the radial stretch that minimised its value (Fig.7.1-A). Given the material law describing the medium, the inflating pressure could be retrieved from the estimated radial stretch, showing an almost perfect recovery of the simulated one.

Correct modelling of tissue rheology is crucial in phantom experiments and clinical settings

While in an *in silico* situation the applied stretch is known, in clinical applications there is no prior knowledge of the underlying deformation field generated by the tumour. Assuming a spherical inflation, however, it becomes possible to iteratively find the radial stretch that minimises the shear modulus anisotropy in the same way as in the *in silico* case, provided the use of a suitable material law. This method was applied to the phantom data presented in this report, assuming Neo-Hookean elasticity and, as shown in Fig.7.1-B, the inflating pressures retrieved at the different inflation levels were comparable with the experimental measures[162]. This was especially true for higher inflation volumes since, as explained throughout this thesis, practical issue leading to low image SNR can increasingly affect the detection of the mild shear modulus anisotropy generated under

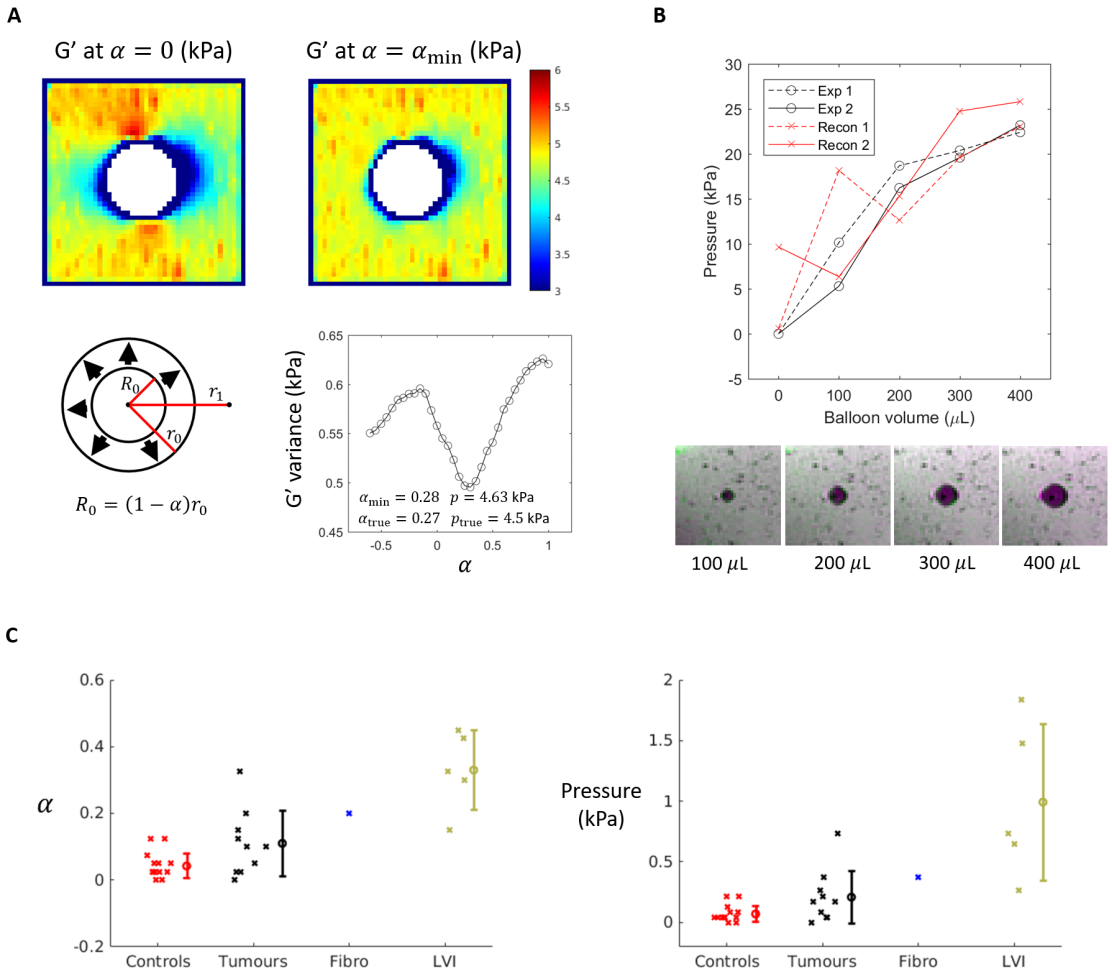

Figure 7.1.: A) Assuming a radial inflation, the iterative search for the scaling parameter α that minimises the voxel variance around the inclusion can be used to undo the anisotropic shear modulus pattern and retrieve the associated pressure *in silico*. B) The application of this method on the MRE data acquired through the inflation experiments allowed the recovery of pressures similar to those measured experimentally. C) This method can represent a non-invasive biomarker to gauge metastatic potential in breast cancer. Images A and B adapted with permission from Fovargue *et al.* (2018) [162], image C adapted with permission from Fovargue *et al.* (2018) [263].

low strains, leading to inaccurate inflation, and hence pressure, estimates.

Although in Chapter 5 it was shown that a higher order polynomial or an exponential strain energy density function could better capture the nonlinearity introduced by the use of the silica gel at the chosen plastisol concentration, Fig.2.1 revealed that, compared to a Neo-Hookean material law, the quadratic term introduced in the modified Mooney-Rivlin equation becomes relevant only for radial stretches larger than ~2.5; as the maximum radial stretch reported in the inflation experiments was ~2.6 (Fig.3.8), a Neo-Hookean

model was expected to provide reasonable pressure estimates with the advantage of using a simpler mathematical formulation.

Estimation of tumour pressure through MRE correlates with invasiveness in breast cancer

A first clinical application of this method was proposed in a recent study covering 15 malignant breast lesions and 1 breast fibroadenoma[263]. Here, Fovargue *et al.* (2018) have shown that a higher radial stretch and the corresponding elevated inflating pressure can differentiate tumours which presented lymphovascular invasion (LVI) from non-LVI breast lesions and from control undeformed soft tissue. While various simulated tumour sizes and shapes yielded consistent pressure curves[162], we have shown throughout this thesis that the correct assumption on the employed strain energy density function is absolutely crucial at higher applied strains, as it can lead to a pressure over- or underestimation, as reported in this clinical study. In this case, a Fung material law was assumed to model the rheological behaviour of the peri-tumoural tissue in breast, nevertheless the mathematical formulation presented in this report provides a framework that can be adapted to different tissues, given an accurate mechanical model of the soft tissue of interest. These results indicate that reconstruction of the total tumour stress through the analysis of the signature apparent shear modulus anisotropy can represent a non-invasive biomarker to gauge metastatic propensity, which can crucially help decide whether a cancer patient needs an immediate surgery or neoadjuvant chemotherapy. The presented results based on the framework proposed in this work, however, do not differentiate between solid stress and IFP, as the stress responsible for the deformation of the surrounding soft tissue can be ascribed to both factors. Nevertheless, since both solid stress and IFP have been directly associated to tumour aggressiveness and poor treatment efficacy, their combined effect is believed to correlate to the same features as well.

7.3. Limitations and Future Directions

The main limitations that affected the presented work are here summarised and potential solutions requiring further investigations are proposed.

- The mathematical framework developed in Chapter 2 was limited to the analysis of the impact of a spherical deformation onto the storage modulus as measured through MRE. While the loss modulus was not investigated, it can be expected that the tumour-generated strain introduces a loading bias on the reconstruction of G'' as well. Nevertheless, a low viscosity, such as the one observed for the material employed for the inflation experiments, can lead to an overestimation of the viscous modulus through the chosen MRE reconstruction[260], making the quantification unreliable. This problem is expected to vanish in *in vivo* studies, due to a stronger

viscosity of real soft tissue, however the sensitivity of the employed reconstruction method to noise calls for further research in a more controlled environment. In this report, we have not observed a correlation between the plastisol concentration in the employed mixture and the viscous response of the material, quantified by the fractional derivative order. A phantom investigation using a different and more viscous material could then shed light on the impact on tumour-generated forces on the measurement of the viscous properties of the surrounding soft tissue through MRE. Analytic results will have to follow.

- In Chapter 6 the underestimated reconstruction of G' from the inflation experiment in the immediate proximity of the balloon was discussed. This is a common problem of many local direct MRE reconstruction methods, due to the violation of the homogeneity assumption in the presence of large discontinuities, which can lead to fluctuations of both components of G^*. This artifact in the immediate vicinity of the inclusion, where the analytically calculated patterns have highlighted the need for a more accurate quantification of G', as the strain is larger and the apparent anisotropy is more pronounced; the quick fading to the background value only a few mm away from the inclusion, in fact, makes its detection more prone to errors dependent on the quality of the acquired data. The local FEM reconstruction method proposed by Fovargue *et al.* has shown the capability to better handle the presence of discontinuities, producing an accuracy near inclusion boundaries close to that obtained from a global method, without the need for parameter regularisation and at a reduced computational cost[260]. Although it is plausible that such a reconstruction method could provide a more accurate comparison between the predicted and measured shift in shear modulus, further improvements on the image acquisition scheme could also increase the accuracy of the reconstructed values. That said, in the imaging protocol used for the acquisition of the phantom data, SNR was already increased to the detriment of the data collection time, while MRE resolution is comparable to that used in clinical settings, hence making the investigation of this path a less favoured choice. Furthermore, the discontinuity is anticipated to have a less significant impact in real tumour cases, as, unlike in the phantom, both the tumour and the surrounding tissue support the propagation of shear waves and the transition of biomechanical properties from one tissue to the other is expected to be smoother.

- While the radial stretch of a thick-walled sphere can represent a reasonable approximation of tumour growth, the plane wave propagation has proven more challenging to achieve in a phantom and can represent a serious limitation *in vivo*, due to the higher material heterogeneity. In this report, in addition to the analytical predictions,

we have presented a comparison between the experimentally measured variation in shear modulus and a metric devised to quantify the direction and intensity of the deformation probed by the shear waves, $\boldsymbol{CK} \cdot \boldsymbol{K}$. These experimental patterns account for the complex wave direction around the inclusion and provide a better appraisal of the cause-effect relationship between the regions where tension/compression is expected and the corresponding impact on the material properties. Incorporation of the empirical wave pattern into the analytical formulation could produce a more accurate model of the experimental conditions, providing further insights on its implications in more complicated *in vivo* cases.

- Wave attenuation has proven to be a major issue in the inflation experiments carried out in this project. Such problem is a direct consequence of the viscosity of the phantom material at higher vibration frequencies, which, as shown in Eq.6.6, can lead to a non-negligible attenuation even in the case of a mildly viscous material. The higher chosen frequency was required to reduce the wavelength to the size of the inclusion, given the elevated shear modulus of the employed samples, higher than the values normally reported for healthy soft tissue. Despite being a good representation of the conditions encountered also in the employed tissue sample, an increased damping makes the identification of the wave displacement more subjected to noise, which can impact the MRE reconstruction, especially when the local curl method presented previously is used. Unfortunately, the setup employed here to generate the waves was not capable of withstanding the mechanical stress experienced when a higher power was used for a 210 Hz vibration frequency. Therefore, an improved wave propagation would require a re-design of the setup. Promising results have been achieved by this group in phantoms and in patients through the use of a newly-proposed gravitational transducer capable of generating a cleaner frequency spectrum, with no upper harmonics[66]; this transducer, however, was tested and employed only at frequencies lower than 100 Hz, therefore its performances at higher vibration frequencies are yet to be assessed.
  The use of a softer phantom material would, on the other hand, provide a better solution, as the shear modulus of the employed plastisol mixture was higher than that expected from soft tissue, in order to enhance its nonlinear stress/strain response. The ranges of shear moduli encountered *in vivo* in breast or liver tissues are much lower than those experimentally achieved here, and normally lower frequencies, in the order of 50 to 100 Hz, are sufficient. In this sense, plastisol was proposed as the ideal material for the inflation experiment presented in this study, in light of its nonlinearity, robustness and simple production method; nevertheless, as highlighted through this list of limitations, the identification of a different material characterised

by an increased viscosity and associating a sufficient nonlinearity to a reduced shear modulus would provide a better approximation of the mechanical properties of soft tissue and permit a more accurate study of the apparent changes generated by mechanical stresses.

7.4. Conclusions

To summarise, the presented work has proposed a mathematical framework to quantify the theorised anisotropic shear modulus distribution caused by tumour-associated forces in the surrounding host tissue, as measured through MRE. An inflation experiment using a soft tissue-mimicking material was then carried out to validate the analytical formulation through MRE data. The results presented in this report represent a significant step towards the development of a non-invasive method to measure and monitor intra- and peri-tumoural stresses as a biomarker for tumour progression and treatment efficacy.

A. The Material Derivative

In continuum mechanics, the time rate of change of a physical quantity of a material element moving at a velocity v is given by the material derivative. For a function $\psi(\boldsymbol{x}, t)$, its material derivative in an Eulerian coordinate system is defined as

$$\begin{aligned}\frac{D}{Dt}\psi(\boldsymbol{x}, t) &= \frac{\partial}{\partial t}\psi(\boldsymbol{x}, t) + \sum_{i=1}^{3} v_i \frac{\partial}{\partial x_i}\psi(\boldsymbol{x}, t) \\ &= \frac{\partial}{\partial t}\psi(\boldsymbol{x}, t) + \boldsymbol{v}(\boldsymbol{x}, t) \cdot \nabla_{\boldsymbol{x}}\psi(\boldsymbol{x}, t)\end{aligned} \tag{A.1}$$

In a Lagrangian coordinate system, with an observer fixed at the initial reference frame, the material derivative of the same function, expressed this time as $\psi(\boldsymbol{X}, t)$, is just a time derivative:

$$\frac{D}{Dt}\psi(\boldsymbol{X}, t) = \frac{\partial}{\partial t}\psi(\boldsymbol{X}, t) \tag{A.2}$$

A.1. The Material Derivative of a Volume Integral

Let Φ be a volume integral of a continuous differential function $\phi(x, y, z, t)$ defined in the current domain Ω_t at time t

$$\Phi(t) = \int_{\Omega_t} \phi(x, y, z, t)\, d\Omega \tag{A.3}$$

Its material derivative, highlighting the rate of change in a moving volume as a function of time, is given by

$$\frac{D\Phi}{Dt} = \int_{\Omega_t} \frac{\partial \phi}{\partial t}\, d\Omega + \int_{\Gamma_t} \left(\phi v_x n_x + \phi v_y n_y + \phi v_z n_z\right)\, d\Gamma \tag{A.4}$$

where Γ_t defines the surface of the volumetric domain Ω_t, $\boldsymbol{v}(t) = \left(\frac{dx}{dt}, \frac{dy}{dt}, \frac{dz}{dt}\right)^T$ is the velocity and $\hat{\boldsymbol{n}} = \left(n_x, n_y, n_z\right)^T$ is a unit vector normal to the surface. This equation can be written more concisely as

$$\frac{D\Phi}{Dt} = \int_{\Omega_t} \frac{\partial \phi}{\partial t}\, d\Omega + \int_{\Gamma_t} \phi \boldsymbol{v} \cdot \hat{\boldsymbol{n}}\, d\Gamma \tag{A.5}$$

Here, the first integral represents the rate of change inside a fixed volume, while the second integral describes the convective transfer through its surface. Applying Gauss theorem, the material derivative of a volume integral can be expressed in its final form

$$\frac{D\Phi}{Dt} = \int_{\Omega_t} \left(\frac{\partial \phi}{\partial t} + \frac{\partial (\phi v_x)}{\partial x} + \frac{\partial (\phi v_y)}{\partial y} + \frac{\partial (\phi v_z)}{\partial z} \right) d\Omega \tag{A.6}$$

or, in a more compact way

$$\frac{D\Phi}{Dt} = \int_{\Omega_t} \left(\frac{\partial \phi}{\partial t} + \nabla_{\boldsymbol{x}} \cdot (\phi \boldsymbol{v}) \right) d\Omega \tag{A.7}$$

Importantly, in a Lagrangian system, where $\Omega_t = \Omega_0$ for all t, the material derivative is simply given by

$$\frac{D}{Dt} \int_{\Omega_0} \phi(x, y, z, t)\, d\Omega = \int_{\Omega_0} \frac{\partial}{\partial t} \phi(x, y, z, t)\, d\Omega \tag{A.8}$$

B. The Reynolds Transport Theorem

The Reynolds transport theorem is useful to formulate the basic equations of quantum mechanics. Using the material derivative (Eq.A.6), we can express the z-component of the vector representing the linear momentum of a body as

$$\frac{D}{Dt}\int_{\Omega_t} \rho v_z \, d\Omega = \int_{\Omega_t} \left(\frac{\partial(\rho v_z)}{\partial t} + \frac{\partial(\rho v_z v_x)}{\partial x} + \frac{\partial(\rho v_z v_y)}{\partial y} + \frac{\partial(\rho v_z v_z)}{\partial z} \right) d\Omega \tag{B.1}$$

Ignoring the integral, the integrand on the right-hand side of Eq.B.1 can be expanded as follows

$$\begin{aligned} &\frac{\partial \rho}{\partial t} v_z + \rho \frac{\partial v_z}{\partial t} + v_z \left(\frac{\partial(\rho v_x)}{\partial x} + \frac{\partial(\rho v_y)}{\partial y} + \frac{\partial(\rho v_z)}{\partial z} \right) + \rho v_x \frac{\partial v_z}{\partial x} + \rho v_y \frac{\partial v_z}{\partial y} + \rho v_z \frac{\partial v_z}{\partial z} \\ &= v_z \left(\frac{\partial \rho}{\partial t} + \frac{\partial(\rho v_x)}{\partial x} + \frac{\partial(\rho v_y)}{\partial y} + \frac{\partial(\rho v_z)}{\partial z} \right) + \rho \left(\frac{\partial v_z}{\partial t} + v_x \frac{\partial v_z}{\partial x} + v_y \frac{\partial v_z}{\partial y} + v_z \frac{\partial v_z}{\partial z} \right) \end{aligned} \tag{B.2}$$

Under the assumption of continuity of mass (Eq.2.15), we find that the first term on the right-hand side of the equality is equal to zero, hence the integrand in Eq.B.1 can be replaced with what is left of Eq.B.2, returning

$$\frac{D}{Dt}\int_{\Omega_t} \rho v_z \, d\Omega = \int_{\Omega_t} \rho \left(\frac{\partial v_z}{\partial t} + v_x \frac{\partial v_z}{\partial x} + v_y \frac{\partial v_z}{\partial y} + v_z \frac{\partial v_z}{\partial z} \right) d\Omega \tag{B.3}$$

By noticing that the terms between brackets on the right-hand side of the equality are nothing else than the material derivative of v_z, the Reynolds transport theorem can be written as

$$\frac{D}{Dt}\int_{\Omega_t} \rho v_z \, d\Omega = \int_{\Omega_t} \rho \frac{Dv_z}{Dt} \, d\Omega \tag{B.4}$$

C. Simplification to Linearised Elastic Wave Equations

C.1. Linearisation of Perturbed PK1 Stress Tensor

Here we simplify the set of perturbed Equations 2.40 using a perturbation theory. Starting by explicitly writing the dependence of the PK1 tensor on the perturbed macro-deformation $\boldsymbol{u} = \boldsymbol{U} + \boldsymbol{u}_\varepsilon$ and pressure $p = P + p_\varepsilon$

$$\boldsymbol{P} = \boldsymbol{P}\left(\boldsymbol{F}(\boldsymbol{U} + \boldsymbol{u}_\varepsilon), \frac{\partial \boldsymbol{F}(\boldsymbol{U} + \boldsymbol{u}_\varepsilon)}{\partial t}, P + p_\varepsilon\right) \tag{C.1}$$

we can linearise the PK1 stress tensor by expanding about the current state $\boldsymbol{U}$ using the directional derivative. A truncation of the second order terms in the Taylor expansion leads to the following form:

$$P_{ij}(\boldsymbol{U} + \boldsymbol{u}_\varepsilon) = P_{ij}(\boldsymbol{U}) + \underset{①}{D[P_{ij}(\boldsymbol{F})][\boldsymbol{u}_\varepsilon]} + D\left[\underset{②}{P_{ij}\left(\frac{\partial \boldsymbol{F}}{\partial t}\right)}\right][\boldsymbol{u}_\varepsilon] + \underset{③}{D[P_{ij}(P)][p_\varepsilon]} + \mathcal{O}(h^2) \tag{C.2}$$

Using the chain rule[163], the directional derivative in ① can be expressed as

$$D[P_{ij}(\boldsymbol{F})][\boldsymbol{u}_\varepsilon] = \frac{\partial P_{ij}}{\partial F_{mn}} : D[F_{mn}][\boldsymbol{u}_\varepsilon] \tag{C.3}$$

Using the definition given in Eq.2.42, the directional derivative on the right-hand side of Eq.C.3 can be written as follows:

$$\begin{aligned} D[F_{mn}][\boldsymbol{u}_\varepsilon] &= \lim_{h\to 0} \frac{F(\boldsymbol{U} + h\boldsymbol{u}_\varepsilon)_{mn} - F(\boldsymbol{U})_{mn}}{h} \\ &= \lim_{h\to 0} \frac{(\nabla_X(\boldsymbol{U} + h\boldsymbol{u}_\varepsilon) + \mathbb{1})_{mn} - (\nabla_X \boldsymbol{U} + \mathbb{1})_{mn}}{h} \\ &= \lim_{h\to 0} \frac{\nabla_X(h\boldsymbol{u}_\varepsilon)_{mn}}{h} \underset{\text{L'Hôpital rule}}{\approx} (\nabla_X \boldsymbol{u}_\varepsilon)_{mn} \end{aligned} \tag{C.4}$$

In the same way, the chain rule applies to ② in Eq.C.2, giving

$$D\left[P_{ij}\left(\frac{\partial \boldsymbol{F}}{\partial t}\right)\right][\boldsymbol{u}_\varepsilon] = \frac{\partial P_{ij}}{\partial\left(\frac{\partial F_{mn}}{\partial t}\right)} : D\left[\frac{\partial F_{mn}}{\partial t}\right][\boldsymbol{u}_\varepsilon] \tag{C.5}$$

where

$$\begin{aligned} D\left[\frac{\partial F_{mn}}{\partial t}\right][\boldsymbol{u}_\varepsilon] &= \lim_{h\to 0}\left(\frac{\partial F(\boldsymbol{U}+h\boldsymbol{u}_\varepsilon)_{mn}}{\partial t} - \frac{\partial F(\boldsymbol{U})_{mn}}{\partial t}\right)\Big/ h \\ &= \lim_{h\to 0}\left(\frac{\partial(\nabla_X(\boldsymbol{U}+h\boldsymbol{u}_\varepsilon)+\mathbb{1})_{mn}}{\partial t} - \frac{\partial(\nabla_X \boldsymbol{U}+\mathbb{1})_{mn}}{\partial t}\right)\Big/ h \\ &= \lim_{h\to 0}\left(\frac{\partial \nabla_X(h\boldsymbol{u}_\varepsilon)_{mn}}{\partial t}\right)\Big/ h \underset{\text{L'Hôpital rule}}{\approx} \left(\nabla_X \frac{\partial \boldsymbol{u}_\varepsilon}{\partial t}\right)_{mn} \end{aligned} \tag{C.6}$$

Lastly, we can express ③ as

$$D[P_{ij}(P)][p_\varepsilon] = \frac{\partial P_{ij}}{\partial P} : D[P][p_\varepsilon] \tag{C.7}$$

where the directional derivative on the right-hand side of Eq.C.7 can be rewritten as

$$\begin{aligned} D[P][\boldsymbol{X}] &= \lim_{h\to 0}\frac{P(\boldsymbol{X}+h\boldsymbol{X})-P(\boldsymbol{X})}{h} \\ &= \lim_{h\to 0}\frac{P+hp_\varepsilon - P}{h} \approx p_\varepsilon \end{aligned} \tag{C.8}$$

Substituting Eq.C.4, C.6 and C.8 in Eq.C.3, C.5 and C.7, respectively, we obtain a new version of ①, ② and ③ which, once replaced in Eq.C.2, returns the linearisation of the perturbed version of $\boldsymbol{P}$

$$\boldsymbol{P}(\boldsymbol{U}+\boldsymbol{u}_\varepsilon) \approx \boldsymbol{P}(\boldsymbol{U}) + \nabla_{\boldsymbol{F}}\boldsymbol{P} : \nabla_{\boldsymbol{X}}\boldsymbol{u}_\varepsilon + \nabla_{\frac{\partial \boldsymbol{F}}{\partial t}}\boldsymbol{P} : \nabla_{\boldsymbol{X}}\frac{\partial \boldsymbol{u}_\varepsilon}{\partial t} + \frac{\partial \boldsymbol{P}}{\partial P}p_\varepsilon \tag{C.9}$$

Using Eq.2.8, we can finally substitute $\frac{\partial \boldsymbol{P}}{\partial P}$ with $J\boldsymbol{F}^{-T}$, hence obtaining

$$\boldsymbol{P}(\boldsymbol{U}+\boldsymbol{u}_\varepsilon) \approx \boldsymbol{P}(\boldsymbol{U}) + \nabla_{\boldsymbol{F}}\boldsymbol{P} : \nabla_{\boldsymbol{X}}\boldsymbol{u}_\varepsilon + \nabla_{\frac{\partial \boldsymbol{F}}{\partial t}}\boldsymbol{P} : \nabla_{\boldsymbol{X}}\frac{\partial \boldsymbol{u}_\varepsilon}{\partial t} + p_\varepsilon J\boldsymbol{F}^{-T} \tag{C.10}$$

C.2. Linearisation of Perturbed Jacobian

The same perturbation analysis can be used to linearised the Jacobian of the perturbed macro-deformation, $J(\boldsymbol{U}+\boldsymbol{u}_\varepsilon)$. Again, Taylor's expansion of J around the macro-deformation $\boldsymbol{U}$ is written as

$$J(\boldsymbol{U}+\boldsymbol{u}_\varepsilon) = J(\boldsymbol{U}) + D[J][\boldsymbol{u}_\varepsilon] + \mathcal{O}(h^2) \tag{C.11}$$

with a truncation of the second order terms $O(h^2)$. Using the chain rule and remembering Eq.C.4, the directional derivative in Eq.C.11 is expressed as

$$\begin{aligned} D[J][\boldsymbol{u}_\varepsilon] &= \nabla_F J : D[\boldsymbol{F}][\boldsymbol{u}_\varepsilon] \\ &= \nabla_F J : \nabla_X \boldsymbol{u}_\varepsilon \end{aligned} \tag{C.12}$$

Replacing Eq.C.12 in Eq.C.11 and knowing that $\nabla_F J = J\boldsymbol{F}^{-T}$, it follows that

$$\begin{aligned} J(\boldsymbol{U} + \boldsymbol{u_\varepsilon}) &\approx J(\boldsymbol{U}) + J\boldsymbol{F}^{-T} : \nabla_X \boldsymbol{u}_\varepsilon \\ &\approx J(\boldsymbol{U}) + JF^{-1}_{ji}\frac{\partial (u_\varepsilon)_j}{\partial X_i} \\ &\approx J(\boldsymbol{U}) + J\frac{\partial X_i}{\partial x_j}\frac{\partial (u_\varepsilon)_j}{\partial X_i} \approx J(\boldsymbol{U}) + J\frac{\partial (u_\varepsilon)_j}{\partial x_j} \end{aligned} \tag{C.13}$$

or, more compactly

$$J(\boldsymbol{U} + \boldsymbol{u_\varepsilon}) \approx J(\boldsymbol{U})\,(1 + \nabla_{\boldsymbol{x}} \cdot \boldsymbol{u}_\varepsilon) \tag{C.14}$$

Since the mass must be conserved at all times, both $J(\boldsymbol{U} + \boldsymbol{u_\varepsilon}) - 1 = 0$ and $J(\boldsymbol{U}) - 1 = 0$ are valid. It then follows that

$$\begin{aligned} J(\boldsymbol{U} + \boldsymbol{u}_\varepsilon) - 1 &\approx J(\boldsymbol{U}) + J(\boldsymbol{u})\nabla_{\boldsymbol{x}} \cdot \boldsymbol{U}_\varepsilon - 1 \\ &\approx (J(\boldsymbol{U}) - 1) + J(\boldsymbol{U})\nabla_{\boldsymbol{x}} \cdot \boldsymbol{u}_\varepsilon \\ &\approx J(\boldsymbol{U})\nabla_{\boldsymbol{x}} \cdot \boldsymbol{u}_\varepsilon = 0 \end{aligned} \tag{C.15}$$

As a consequence, $\nabla_{\boldsymbol{x}} \cdot \boldsymbol{u}_\varepsilon = 0$. Replacing this in Eq.C.14, we obtain the linearisation of the Jacobian of the perturbed macro-deformation:

$$J(\boldsymbol{U} + \boldsymbol{u}_\varepsilon) \approx J(\boldsymbol{U}) \tag{C.16}$$

Bibliography

[1] World Health Organization. *World Health Statistics 2018 : Monitoring Health For The SDGs*. Tech. rep. 2018.

[2] American Cancer Society. "Cancer Facts & Figures 2018". In: *American Cancer Society* (2018).

[3] J. Ferlay et al. "Cancer incidence and mortality patterns in Europe: Estimates for 40 countries and 25 major cancers in 2018". In: *European Journal of Cancer* 103 (Nov. 2018), pp. 356–387.

[4] J. Ferlay et al. "Cancer incidence and mortality worldwide: Sources, methods and major patterns in GLOBOCAN 2012". In: *International Journal of Cancer* 136.5 (Mar. 2015), E359–E386.

[5] F. Bray et al. "Global cancer statistics 2018: GLOBOCAN estimates of incidence and mortality worldwide for 36 cancers in 185 countries". In: *CA: A Cancer Journal for Clinicians* 68.6 (Nov. 2018), pp. 394–424.

[6] B. W. Stewart and C. P. Wild. *World Cancer Report 2014*. Tech. rep. 2014.

[7] G. W. Prager et al. "Global cancer control: Responding to the growing burden, rising costs and inequalities in access". In: *ESMO Open* 3.2 (2018), pp. 1–10.

[8] World Health Organization. *Guide to early cancer diagnosis*. 2017.

[9] World Health Organization. *National cancer control programmes: policies and managerial guidelines*. 2002.

[10] International Agency for Research on Cancer. *Breast cancer screening - IARC Handbooks of Cancer Prevention, Volume 15*. 2016, p. 469.

[11] D. Stockton et al. "Retrospective study of reasons for improved survival in patients with breast cancer in east Anglia: earlier diagnosis or better treatment." In: *BMJ (Clinical research ed.)* 314.7079 (Feb. 1997), pp. 472–5.

[12] M. Kriege et al. "Efficacy of MRI and Mammography for Breast-Cancer Screening in Women with a Familial or Genetic Predisposition". In: *New England Journal of Medicine* 351.5 (July 2004), pp. 427–437.

[13] J. S. Drukteinis et al. “Beyond mammography: New frontiers in breast cancer screening”. In: *American Journal of Medicine* 126.6 (June 2013), pp. 472–479.

[14] E. J. Granader, B. Dwamena, and R. C. Carlos. “MRI and Mammography Surveillance of Women at Increased Risk for Breast Cancer”. In: *Academic Radiology* 15.12 (Dec. 2008), pp. 1590–1595.

[15] C. Kuhl. “The Current Status of Breast MR Imaging Part I. Choice of Technique, Image Interpretation, Diagnostic Accuracy, and Transfer to Clinical Practice”. In: *Radiology* 244.2 (Aug. 2008), pp. 356–378.

[16] N. S White et al. “Diffusion-weighted imaging in cancer: Physical foundations and applications of restriction spectrum imaging”. In: *Cancer Research* 74.17 (Sept. 2014), pp. 4638–4652.

[17] L. Bartella and W. Huang. “Proton (1H) MR Spectroscopy of the Breast”. In: *RadioGraphics* 27.suppl_1 (Oct. 2007), S241–S252.

[18] T. Barrett. “What is Multiparametric-MRI of the Prostate and Why Do We Need It ?” In: *Journal of Imaging and Interventional Radiology* 1 (Oct. 2015), pp. 1–5.

[19] T. A. Krouskop et al. “Elastic moduli of breast and prostate tissues under compression”. In: *Ultrasonic Imaging* 20.4 (Oct. 1998), pp. 260–274.

[20] A. Samani, J. Zubovits, and D. Plewes. “Elastic moduli of normal and pathological human breast tissues: An inversion-technique-based investigation of 169 samples”. In: *Physics in Medicine and Biology* 52.6 (Mar. 2007), pp. 1565–1576.

[21] R. L. Siegel, K. D. Miller, and A. Jemal. “Cancer statistics, 2019.” In: *CA: A Cancer jJurnal for Clinicians* 69.1 (Jan. 2019), pp. 7–34.

[22] M. B. Barton, R. Harris, and S. W. Fletcher. “Does this patient have breast cancer? The screening clinical breast examination: Should it be done? How?” In: *Journal of the American Medical Association* 282.13 (Oct. 1999), pp. 1270–1280.

[23] M. Yin et al. “Assessment of hepatic fibrosis with magnetic resonance elastography.” English. In: *Clinical gastroenterology and hepatology : the official clinical practice journal of the American Gastroenterological Association* 5.10 (Oct. 2007), 1207–1213.e2.

[24] S. L Friedman. “Liver fibrosis – from bench to bedside”. In: *Journal of Hepatology* 38 (Jan. 2003), pp. 38–53.

[25] J. M. Llovet et al. “Hepatocellular carcinoma”. In: *Nature Reviews Disease Primers* 2 (Apr. 2016), p. 16018.

[26] J. A. Talwalkar and P. S. Kamath. “Influence of Recent Advances in Medical Management on Clinical Outcomes of Cirrhosis”. In: *Mayo Clinic Proceedings* 80.11 (Nov. 2005), pp. 1501–1508.

[27] R. A. Standish et al. “An appraisal of the histopathological assessment of liver fibrosis”. In: *Gut* 55.4 (Apr. 2006), pp. 569–578.

[28] P. Martus et al. “MR-elastography reveals degradation of tissue integrity in multiple sclerosis”. In: *NeuroImage* 49.3 (Feb. 2009), pp. 2520–2525.

[29] K. M. Pepin, R. L. Ehman, and K. P. McGee. “Magnetic resonance elastography (MRE) in cancer: Technique, analysis, and applications”. In: *Progress in Nuclear Magnetic Resonance Spectroscopy* 90-91 (Nov. 2015), pp. 32–48.

[30] W. Xu et al. “Cell Stiffness Is a Biomarker of the Metastatic Potential of Ovarian Cancer Cells”. In: *PLoS ONE* 7.10 (Oct. 2012). Ed. by Surinder K. Batra, e46609.

[31] L. Huwart et al. “Liver fibrosis: non-invasive assessment with MR elastography”. In: *NMR in Biomedicine* 19.2 (Apr. 2006), pp. 173–179.

[32] M. C. Murphy et al. “Preoperative assessment of meningioma stiffness using magnetic resonance elastography.” In: *Journal of neurosurgery* 118.3 (Mar. 2013), pp. 643–8.

[33] M. C. Murphy et al. “Measuring the Characteristic Topography of Brain Stiffness with Magnetic Resonance Elastography”. In: *PLoS ONE* 8.12 (Dec. 2013). Ed. by Gareth Robert Barnes, e81668.

[34] I. Sack et al. “Non-invasive measurement of brain viscoelasticity using magnetic resonance elastography”. In: *NMR in Biomedicine* 21.3 (Apr. 2008), pp. 265–271.

[35] R. Sinkus et al. “High-resolution tensor MR elastography for breast tumour detection.” In: *Physics in medicine and biology* 45.6 (2000), pp. 1649–1664.

[36] A. Kolipaka et al. “MR elastography as a method for the assessment of myocardial stiffness: Comparison with an established pressure-volume model in a left ventricular model of the heart”. In: *Magnetic Resonance in Medicine* 62.1 (July 2009), pp. 135–140.

[37] I. Sack et al. “MR elastography of the human heart: Noninvasive assessment of myocardial elasticity changes by shear wave amplitude variations”. In: *Magnetic Resonance in Medicine* 61.3 (Mar. 2009), pp. 668–677.

[38] Y. K. Mariappan et al. “MR elastography of human lung parenchyma: Technical development, theoretical modeling and in vivo validation”. In: *Journal of Magnetic Resonance Imaging* 33.6 (June 2011), pp. 1351–1361.

[39] J. A. Talwalkar et al. “Feasibility of In Vivo MR Elastographic Splenic Stiffness Measurements in the Assessment of Portal Hypertension”. In: *American Journal of Roentgenology* 193.1 (July 2009), pp. 122–127.

[40] S. F. Bensamoun et al. “Stiffness imaging of the kidney and adjacent abdominal tissues measured simultaneously using magnetic resonance elastography”. In: *Clinical Imaging* 35.4 (July 2011), pp. 284–287.

[41] Y. Shi et al. “Feasibility of using 3D MR elastography to determine pancreatic stiffness in healthy volunteers”. In: *Journal of Magnetic Resonance Imaging* 41.2 (Feb. 2015), pp. 369–375.

[42] L. Debernard, J.Y. Hogrel, and S.F. Bensamoun. “M.P.5.09 Non-invasive assessment of muscle stiffness with magnetic resonance elastography”. In: *Neuromuscular Disorders* 19.8-9 (Sept. 2009), pp. 629–630.

[43] M. M. Bahn et al. “Development and application of magnetic resonance elastography of the normal and pathological thyroid gland in vivo”. In: *Journal of Magnetic Resonance Imaging* 30.5 (Nov. 2009), pp. 1151–1154.

[44] S. K. Venkatesh, M. Yin, and R. L. Ehman. “Magnetic resonance elastography of liver: Technique, analysis, and clinical applications”. In: *Journal of Magnetic Resonance Imaging* 37.3 (Mar. 2013), pp. 544–555.

[45] Y. C. Fung. *Biomechanics : mechanical properties of living tissues*. Springer-Verlag, 1993, p. 568.

[46] J. D. Humphrey. *Cardiovascular solid mechanics : cells, tissues, and organs*. Springer, 2002, p. 757.

[47] A. P. Sarvazyan et al. “Biophysical Bases of Elasticity Imaging”. In: *Acoustical Imaging*. Springer, Boston, MA, 1995, pp. 223–240.

[48] A. R. Skovoroda et al. “Quantitative analysis of the mechanical characteristics of pathologically changed soft biological tissues”. In: *Biophysics* 40.6 (1995), pp. 1359–1364.

[49] M. Zhang, Y. P. Zheng, and A. F. T. Mak. “Estimating the effective Young’s modulus of soft tissues from indentation tests - Nonlinear finite element analysis of effects of friction and large deformation”. In: *Medical Engineering and Physics* 19.6 (Sept. 1997), pp. 512–517.

[50] P Wellman et al. “Breast tissue stiffness in compression is correlated to histological diagnosis”. In: *Harvard BioRobotics Laboratory Technical Repor* (1999), pp. 1–15.

[51] R. Sinkus et al. “Imaging anisotropic and viscous properties of breast tissue by magnetic resonance-elastography”. In: *Magnetic Resonance in Medicine* 53.2 (2005), pp. 372–387.

[52] D. R. Veronda and R. A. Westmann. “Mechanical characterization of skin-Finite deformations”. In: *Journal of Biomechanics* 3.1 (Jan. 1970), pp. 111–124.

[53] G. T. Mase, R. E. Smelser, and G. E. Mase. *Continuum mechanics for engineers*. 1999.

[54] Y. K. Mariappan, K. J. Glaser, and R. L. Ehman. “Magnetic Resonance Elastography: a Review”. In: *Clinical Anatomy* 23.5 (2010), pp. 497–511.

[55] S. A. Goss, R. L. Johnston, and F. Dunn. “Comprehensive compilation of empirical ultrasonic properties of mammalian tissues”. In: *The Journal of the Acoustical Society of America* 64.2 (Aug. 1978), pp. 423–457.

[56] T. L. Chenevert et al. “Elasticity reconstructive imaging by means of stimulated echo MRI”. In: *Magnetic Resonance in Medicine* 39.3 (Mar. 1998), pp. 482–490.

[57] A. Samani et al. “Measuring the elastic modulus of ex vivo small tissue samples”. In: *Physics in Medicine and Biology* 48.14 (July 2003), pp. 2183–2198.

[58] P. A. Hardy et al. “Imaging articular cartilage under compression - Cartilage elastography”. In: *Magnetic Resonance in Medicine* 53.5 (May 2005), pp. 1065–1073.

[59] D. B. Plewes et al. “Visualization and quantification of breast cancer biomechanical properties with magnetic resonance elastography”. In: *Physics in Medicine and Biology* 45.6 (June 2000), pp. 1591–1610.

[60] A. Samani, J. Bishop, and D. B. Plewes. “A constrained modulus reconstruction technique for breast cancer assessment”. In: *IEEE Transactions on Medical Imaging* 20.9 (2001), pp. 877–885.

[61] R. Muthupillai et al. “Magnetic resonance elastography by direct visualization of propagating acoustic strain waves.” In: *Science (New York, N.Y.)* 269.5232 (1995), pp. 1854–1857.

[62] Z. T. H. Tse et al. “Magnetic resonance elastography hardware design: a survey.” In: *Proceedings of the Institution of Mechanical Engineers. Part H, Journal of engineering in medicine* 223.4 (2009), pp. 497–514.

[63] J. Chen, C. Ni, and T. Zhuang. “Imaging mechanical shear waves induced by piezoelectric ceramics in magnetic resonance elastography”. In: *Chinese Science Bulletin* 51.6 (Mar. 2006), pp. 755–760.

[64] J. Braun, K. Braun, and I. Sack. “Electromagnetic actuator for generating variably oriented shear waves in MR elastography”. In: *Magnetic Resonance in Medicine* 50.1 (July 2003), pp. 220–222.

[65] P. Asbach et al. “Assessment of liver viscoelasticity using multifrequency MR elastography”. In: *Magnetic Resonance in Medicine* 60.2 (Aug. 2008), pp. 373–379.

[66] J. H. Runge et al. “A novel magnetic resonance elastography transducer concept based on a rotational eccentric mass: preliminary experiences with the gravitational transducer”. In: *Physics in medicine and biology* 64.4 (Feb. 2019), p. 045007.

[67] P. He. “Simulation of ultrasound pulse propagation in lossy media obeying a frequency power law”. In: *IEEE Transactions on Ultrasonics, Ferroelectrics, and Frequency Control* 45.1 (Jan. 1998), pp. 114–125.

[68] R. Muthupillai et al. “Magnetic resonance imaging of transverse acoustic strain waves.” In: *Magnetic resonance in medicine : official journal of the Society of Magnetic Resonance in Medicine / Society of Magnetic Resonance in Medicine* 36.2 (1996), pp. 266–274.

[69] A. Manduca et al. “Magnetic resonance elastography: Non-invasive mapping of tissue elasticity”. In: *Medical Image Analysis* 5.4 (2001), pp. 237–254.

[70] R. Muthupillai et al. “MRI visualization of acoustic strain waves: Effect of linear motion”. In: *Proc. ISMRM* 4 (1996), p. 1515.

[71] L. D. Landau and E. M. Lifshiftz. *Theory of Elasticity*. Butterworth-Heinemann, 1986, p. 187.

[72] K. J. Glaser, A. Manduca, and R. L. Ehman. “Review of MR elastography applications and recent developments”. In: *Journal of Magnetic Resonance Imaging* 36.4 (Oct. 2012), pp. 757–774.

[73] R. Sinkus et al. “Viscoelastic shear properties of in vivo breast lesions measured by MR elastography”. In: *Magnetic Resonance Imaging* 23.2 SPEC. ISS. (2005), pp. 159–165.

[74] D. Fovargue, D. Nordsletten, and R. Sinkus. “Stiffness reconstruction methods for MR elastography”. In: *NMR in Biomedicine* 31.10 (Oct. 2018), e3935.

[75] M. Honarvar, R. Rohling, and S. E. Salcudean. “A comparison of direct and iterative finite element inversion techniques in dynamic elastography”. In: *Physics in Medicine and Biology* 61.8 (Apr. 2016), pp. 3026–3048.

[76] A. L. McKnight et al. “MR elastography of breast cancer: Preliminary results”. In: *American Journal of Roentgenology* 178.6 (June 2002), pp. 1411–1417.

[77] J. Lorenzen et al. “MR elastography of the breast: Preliminary clinical results”. In: *RoFo Fortschritte auf dem Gebiet der Rontgenstrahlen und der Bildgebenden Verfahren* 174.7 (July 2002), pp. 830–834.

[78] T. Xydeas et al. “Magnetic resonance elastography of the breast: Correlation of signal intensity data with viscoelastic properties”. In: *Investigative Radiology* 40.7 (July 2005), pp. 412–420.

[79] R. Sinkus et al. “MR elastography of breast lesions: Understanding the solid/liquid duality can improve the specificity of contrast-enhanced MR mammography”. In: *Magnetic Resonance in Medicine* 58.6 (Dec. 2007), pp. 1135–1144.

[80] K. C. Siegmann et al. “Diagnostic value of MR elastography in addition to contrast-enhanced MR imaging of the breast - Initial clinical results”. In: *European Radiology* 20.2 (Feb. 2010), pp. 318–325.

[81] C. Balleyguier et al. “Value of whole breast magnetic resonance elastography added to MRI for lesion characterization”. In: *NMR in Biomedicine* 31.1 (Jan. 2018), e3795.

[82] S. K. Venkatesh et al. “MR elastography of liver tumors: Preliminary results”. In: *American Journal of Roentgenology* 190.6 (June 2008), pp. 1534–1540.

[83] P. Garteiser et al. “MR elastography of liver tumours: Value of viscoelastic properties for tumour characterisation”. In: *European Radiology* 22.10 (Oct. 2012), pp. 2169–2177.

[84] L. Xu et al. “Magnetic resonance elastography of brain tumors: Preliminary results”. In: *Acta Radiologica* 48.3 (Apr. 2007), pp. 327–330.

[85] E. C. Clarke et al. “Using static preload with magnetic resonance elastography to estimate large strain viscoelastic properties of bovine liver”. In: *Journal of Biomechanics* 44.13 (Sept. 2011), pp. 2461–2465.

[86] A. Capilnasiu et al. “Magnetic resonance elastography in nonlinear viscoelastic materials under load”. In: *Biomechanics and Modeling in Mechanobiology* (Aug. 2018), pp. 1–25.

[87] W. C. Yeh et al. “Elastic modulus measurements of human liver and correlation with pathology”. In: *Ultrasound in Medicine and Biology* 28.4 (Apr. 2002), pp. 467–474.

[88] R. K. Jain, J. D. Martin, and T. Stylianopoulos. “The Role of Mechanical Forces in Tumor Growth and Therapy”. In: *Annual Review of Biomedical Engineering* 16.1 (July 2014), pp. 321–346.

[89] R. K. Jain. “Normalizing tumor microenvironment to treat cancer: Bench to bedside to biomarkers”. In: *Journal of Clinical Oncology*. Vol. 31. 17. American Society of Clinical Oncology, June 2013, pp. 2205–2218.

[90] R. Kalluri and M. Zeisberg. “Fibroblasts in cancer”. In: *Nature Reviews Cancer* 6.5 (May 2006), pp. 392–401.

[91] R. Kalluri. “The biology and function of fibroblasts in cancer”. In: *Nature Reviews Cancer* 16.9 (Sept. 2016), pp. 582–598.

[92] I. Acerbi et al. “Human breast cancer invasion and aggression correlates with ECM stiffening and immune cell infiltration”. In: *Integrative Biology (United Kingdom)* 7.10 (Oct. 2015), pp. 1120–1134.

[93] N. Rath and M. F. Olson. “Regulation of pancreatic cancer aggressiveness by stromal stiffening”. In: *Nature Medicine* 22.5 (May 2016), pp. 462–463.

[94] L. Tao et al. “Cancer associated fibroblasts: An essential role in the tumor microenvironment”. In: *Oncology Letters* 14.3 (Sept. 2017), pp. 2611–2620.

[95] G. S. Karagiannis et al. “Cancer-Associated Fibroblasts Drive the Progression of Metastasis through both Paracrine and Mechanical Pressure on Cancer Tissue”. In: *Molecular Cancer Research* 10.11 (Nov. 2012), pp. 1403–1418.

[96] P. J. Wipff and B. Hinz. “Myofibroblasts work best under stress”. In: *Journal of Bodywork and Movement Therapies* 13.2 (Apr. 2009), pp. 121–127.

[97] P. J. Wipff et al. “Myofibroblast contraction activates latent TGF-β1 from the extracellular matrix”. In: *Journal of Cell Biology* 179.6 (Dec. 2007), pp. 1311–1323.

[98] M. H. Branton and J. B. Kopp. “TGF-β and fibrosis”. In: *Microbes and Infection* 1.15 (Dec. 1999), pp. 1349–1365.

[99] M. Egeblad, M. G. Rasch, and V. M. Weaver. “Dynamic interplay between the collagen scaffold and tumor evolution”. In: *Current Opinion in Cell Biology* 22.5 (Oct. 2010), pp. 697–706.

[100] D. T. Butcher, T. Alliston, and V. M. Weaver. “A tense situation: Forcing tumour progression”. In: *Nature Reviews Cancer* 9.2 (Feb. 2009), pp. 108–122.

[101] M. J. Paszek et al. “Tensional homeostasis and the malignant phenotype”. In: *Cancer Cell* 8.3 (Sept. 2005), pp. 241–254.

[102] J. M. Tse et al. “Mechanical compression drives cancer cells toward invasive phenotype”. In: *Proceedings of the National Academy of Sciences* 109.3 (Jan. 2012), pp. 911–916.

[103] P. Koumoutsakos, I. Pivkin, and F. Milde. “The Fluid Mechanics of Cancer and Its Therapy”. In: *Annual Review of Fluid Mechanics* 45.1 (Jan. 2013), pp. 325–355.

[104] P. Carmeliet and R. K. Jain. “Angiogenesis in cancer and other diseases”. In: *Nature* 407.6801 (Sept. 2000), pp. 249–257.

[105] R. K. Jain. “Normalization of tumor vasculature: An emerging concept in antiangiogenic therapy”. In: *Science* 307.5706 (Jan. 2005), pp. 58–62.

[106] B. J. Vakoc et al. “Three-dimensional microscopy of the tumor microenvironment in vivo using optical frequency domain imaging”. In: *Nature Medicine* 15.10 (Oct. 2009), pp. 1219–1223.

[107] H. Hashizume et al. “Openings between defective endothelial cells explain tumor vessel leakiness”. In: *American Journal of Pathology* 156.4 (Apr. 2000), pp. 1363–1380.

[108] C. H. Heldin et al. “High interstitial fluid pressure - an obstacle in cancer therapy.” In: *Nature reviews. Cancer* 4.10 (2004), pp. 806–813.

[109] M. A. Swartz and A. W. Lund. “Lymphatic and interstitial flow in the tumour microenvironment: Linking mechanobiology with immunity”. In: *Nature Reviews Cancer* 12.3 (Mar. 2012), pp. 210–219.

[110] A. J. Leu et al. “Absence of functional lymphatics within a murine sarcoma: a molecular and functional evaluation.” In: *Cancer research* 60.16 (Aug. 2000), pp. 4324–7.

[111] T. P. Padera et al. “Lymphatic metastasis in the absence of functional intratumor lymphatics.” In: *Science (New York, N.Y.)* 296.5574 (June 2002), pp. 1883–6.

[112] N. Isaka et al. “Peritumor Lymphatics Induced by Vascular Endothelial Growth Factor-C Exhibit Abnormal Function”. In: *Cancer Research* 64.13 (July 2004), pp. 4400–4404.

[113] T. Hoshida et al. “Imaging steps of lymphatic metastasis reveals that vascular endothelial growth factor-C increases metastasis by increasing delivery of cancer cells to lymph nodes: therapeutic implications.” In: *Cancer research* 66.16 (Aug. 2006), pp. 8065–75.

[114] N. Gjorevski and C. M. Nelson. “Endogenous patterns of mechanical stress are required for branching morphogenesis”. In: *Integrative Biology* 2.9 (Sept. 2010), pp. 424–434.

[115] E. W. Gomez et al. “Tissue geometry patterns epithelial-mesenchymal transition via intercellular mechanotransduction”. In: *Journal of Cellular Biochemistry* 110.1 (May 2010), pp. 44–51.

[116] Z. N. Demou. “Gene expression profiles in 3D tumor analogs indicate compressive strain differentially enhances metastatic potential”. In: *Annals of Biomedical Engineering* 38.11 (Nov. 2010), pp. 3509–3520.

[117] W. W. Kilarski et al. “Biomechanical regulation of blood vessel growth during tissue vascularization”. In: *Nature Medicine* 15.6 (June 2009), pp. 657–664.

[118] M. Kalli et al. “Solid Stress Facilitates Fibroblasts Activation to Promote Pancreatic Cancer Cell Migration”. In: *Annals of Biomedical Engineering* 46.5 (May 2018), pp. 657–669.

[119] S. S. Nathan et al. “Elevated physiologic tumor pressure promotes proliferation and chemosensitivity in human osteosarcoma”. In: *Clinical Cancer Research* 11.6 (Mar. 2005), pp. 2389–2397.

[120] G. R. DiResta et al. “Cell proliferation of cultured human cancer cells are affected by the elevated tumor pressures that exist in vivo”. In: *Annals of Biomedical Engineering* 33.9 (Sept. 2005), pp. 1270–1280.

[121] M. Hofmann et al. “Long-term lowering of tumour interstitial fluid pressure reduces Ki-67 expression”. In: *Journal of Biomechanics* 40.10 (Jan. 2007), pp. 2324–2329.

[122] S. S. Nathan et al. “Tumour interstitial fluid pressure may regulate angiogenic factors in osteosarcoma”. In: *Annals of the Academy of Medicine Singapore* 38.12 (May 2009), pp. 1041–1047.

[123] A. C. Shieh. “Biomechanical forces shape the tumor microenvironment”. In: *Annals of Biomedical Engineering* 39.5 (May 2011), pp. 1379–1389.

[124] M. W. Dewhirst and T. W. Secomb. “Transport of drugs from blood vessels to tumour tissue”. In: *Nature Reviews Cancer* 17.12 (Nov. 2017), pp. 738–750.

[125] Y. Boucher and R. K. Jain. “Microvascular Pressure Is the Principal Driving Force for Interstitial Hypertension in Solid Tumors: Implications for Vascular Collapse”. In: *Cancer Research* 52.18 (Sept. 1992), pp. 5110–5114.

[126] T. P. Padera et al. “Cancer cells compress intratumour vessels”. In: *Nature* 427.6976 (Feb. 2004), p. 695.

[127] T. Stylianopoulos et al. “Coevolution of solid stress and interstitial fluid pressure in tumors during progression: Implications for vascular collapse”. In: *Cancer Research* 73.13 (July 2013), pp. 3833–3841.

[128] A. I. Minchinton and I. F. Tannock. “Drug penetration in solid tumours”. In: *Nature Reviews Cancer* 6.8 (Aug. 2006), pp. 583–592.

[129] S. Goel et al. “Normalization of the Vasculature for Treatment of Cancer and Other Diseases”. In: *Physiological Reviews* 91.3 (July 2011), pp. 1071–1121.

[130] C. Voutouri et al. “Role of constitutive behavior and tumor-host mechanical interactions in the state of stress and growth of solid tumors”. In: *PLoS ONE* 9.8 (Aug. 2014). Ed. by Pankaj K. Singh, e104717.

[131] J. S. Young, C. E. Llumsden, and A. L. Stalker. "The significance of the "tissue pressure" of normal testicular and of neoplastic (Brown-Pearce carcinoma) tissue in the rabbit". In: *The Journal of Pathology and Bacteriology* 62.3 (July 1950), pp. 313–333.

[132] R. K. Jain and L. T. Baxter. "Mechanisms of heterogeneous distribution of monoclonal antibodies and other macromolecules in tumors: Significance of elevated interstitial pressure". In: *Cancer Research* 48.9 Supplement (Dec. 1988), pp. 7022–7032.

[133] L. T. Baxter and R. K. Jain. "Transport of fluid and macromolecules in tumors. I. Role of interstitial pressure and convection". In: *Microvascular Research* 37.1 (Jan. 1989), pp. 77–104.

[134] R. K. Jain, R. T. Tong, and L. L. Munn. "Effect of vascular normalization by antiangiogenic therapy on interstitial hypertension, peritumor edema, and lymphatic metastasis: Insights from a mathematical model". In: *Cancer Research* 67.6 (Aug. 2007), pp. 2729–2735.

[135] H. O. Fadnes, R. K. Reed, and K. Aukland. "Interstitial fluid pressure in rats measured with a modified wick technique". In: *Microvascular Research* 14.1 (July 1977), pp. 27–36.

[136] Y. Boucher et al. "Interstitial Hypertension in Superficial Metastatic Melanomas in Humans". In: *Cancer Research* 51.24 (Dec. 1991), pp. 6691–6694.

[137] P. P. Provenzano et al. "Enzymatic Targeting of the Stroma Ablates Physical Barriers to Treatment of Pancreatic Ductal Adenocarcinoma". In: *Cancer Cell* 21.3 (Mar. 2012), pp. 418–429.

[138] U. Ozerdem and A. R. Hargens. "A simple method for measuring interstitial fluid pressure in cancer tissues". In: *Microvascular Research* 70.1-2 (July 2005), pp. 116–120.

[139] K. E. DelGiorno et al. "Response to Chauhan et al.: Interstitial Pressure and Vascular Collapse in Pancreas Cancer-Fluids and Solids, Measurement and Meaning". In: *Cancer Cell* 26.1 (July 2014), pp. 16–17.

[140] V. P. Chauhan et al. "Compression of Pancreatic Tumor Blood Vessels by Hyaluronan Is Caused by Solid Stress and Not Interstitial Fluid Pressure". In: *Cancer Cell* 26.1 (July 2014), pp. 14–15.

[141] M. D. Nieskoski et al. "Separation of Solid Stress From Interstitial Fluid Pressure in Pancreas Cancer Correlates With Collagen Area Fraction". In: *Journal of Biomechanical Engineering* 139.6 (Apr. 2017), p. 061002.

[142] T. Hompland et al. “Interstitial fluid pressure and associated lymph node metastasis revealed in tumors by dynamic contrast-enhanced MRI”. In: *Cancer Research* 72.19 (Aug. 2012), pp. 4899–4908.

[143] R. Elmghirbi et al. “Toward a noninvasive estimate of interstitial fluid pressure by dynamic contrast-enhanced MRI in a rat model of cerebral tumor”. In: *Magnetic Resonance in Medicine* 80.5 (Nov. 2018), pp. 2040–2052.

[144] W.T- Shi et al. “Pressure dependence of subharmonic signals from contrast microbubbles”. In: *Ultrasound in Medicine & Biology* 25.2 (1999), pp. 275–283.

[145] F. Forsberg et al. “In vivo pressure estimation using subharmonic contrast microbubble signals: proof of concept”. In: *IEEE Transactions on Ultrasonics, Ferroelectrics and Frequency Control* 52.4 (Apr. 2005), pp. 581–583.

[146] T. Stylianopoulos. “The Solid Mechanics of Cancer and Strategies for Improved Therapy”. In: *Journal of Biomechanical Engineering* 139.2 (Jan. 2017), p. 021004.

[147] D. J. McGrail et al. “Osmotic Regulation Is Required for Cancer Cell Survival under Solid Stress”. In: *Biophysical Journal* 109.7 (Oct. 2015), pp. 1334–1337.

[148] C. Voutouri et al. “Hyaluronan-Derived Swelling of Solid Tumors, the Contribution of Collagen and Cancer Cells, and Implications for Cancer Therapy”. In: *Neoplasia* 18.12 (Dec. 2016), pp. 732–741.

[149] T. Stylianopoulos et al. “Causes, consequences, and remedies for growth-induced solid stress in murine and human tumors”. In: *Proceedings of the National Academy of Sciences* 109.38 (Sept. 2012), pp. 15101–15108.

[150] G. Helmlinger et al. “Solid stress inhibits the growth of multicellular tumor spheroids”. In: *Nature Biotechnology* 15.8 (Aug. 1997), pp. 778–783.

[151] G. Cheng et al. “Micro-environmental mechanical stress controls tumor spheroid size and morphology by suppressing proliferation and inducing apoptosis in cancer cells.” In: *PloS one* 4.2 (2009), e4632.

[152] C. J. Whatcott et al. “Desmoplasia in Primary Tumors and Metastatic Lesions of Pancreatic Cancer”. In: *Clinical Cancer Research* 21.15 (Aug. 2015), pp. 3561–3568.

[153] S. R. Eisenberg and A. J. Grodzinsky. “Swelling of articular cartilage and other connective tissues: Electromechanochemical forces”. In: *Journal of Orthopaedic Research* 3.2 (Jan. 1985), pp. 148–159.

[154] V. K. Lai et al. “Swelling of Collagen-Hyaluronic Acid Co-Gels: An In Vitro Residual Stress Model.” In: *Annals of biomedical engineering* 44.10 (2016), pp. 2984–2993.

[155] V. P. Chauhan et al. “Angiotensin inhibition enhances drug delivery and potentiates chemotherapy by decompressing tumour blood vessels”. In: *Nature Communications* 4.1 (Dec. 2013), p. 2516.

[156] T. Roose et al. “Solid stress generated by spheroid growth estimated using a linear poroelasticity model”. In: *Microvascular Research* 66.3 (Nov. 2003), pp. 204–212.

[157] M. Sarntinoranont, F. Rooney, and M. Ferrari. “Interstitial stress and fluid pressure within a growing tumor”. In: *Annals of Biomedical Engineering* 31.3 (Mar. 2003), pp. 327–335.

[158] C. P. Calderón and T. A. Kwembe. “Modeling tumor growth”. In: *Mathematical Biosciences* 103.1 (Feb. 1991), pp. 97–114.

[159] H. T. Nia et al. “Solid stress and elastic energy as measures of tumour mechanopathology”. In: *Nature Biomedical Engineering* 1.1 (Nov. 2017), p. 0004.

[160] G. Helmlinger et al. “Solid stress inhibits the growth of multicellular tumor spheroids”. In: *Nature biotechnology* 15.8 (Aug. 1997), pp. 778–783.

[161] *Force – Imaging the Force of cancer, www.force-imaging.org*.

[162] D. Fovargue et al. “Non-linear Mechanics Allows Non-invasive Quantification of Interstitial Fluid Pressure”. In: *ISMRM*. 2018.

[163] J. Bonet and R. D. Wood. *Nonlinear continuum mechanics for finite element analysis*. Cambridge University Press, 1997, p. 248.

[164] H. Mehrabian and A. Samani. “An iterative hyperelastic parameters reconstruction for breast cancer assessment”. In: *Proc. SPIE 6916, Medical Imaging 2008: Physiology, Function, and Structure from Medical Images*. Ed. by Xiaoping P. Hu and Anne V. Clough. Vol. 6916C. International Society for Optics and Photonics, Mar. 2008.

[165] A. Samani and D. Plewes. “A method to measure the hyperelastic parameters of ex vivo breast tissue samples”. In: *Physics in Medicine and Biology* 49.18 (Sept. 2004), pp. 4395–4405.

[166] J. J. O’Hagan and A. Samani. “Measurement of the hyperelastic properties of tissue slices with tumour inclusion”. In: *Physics in Medicine and Biology* 53.24 (Dec. 2008), pp. 7087–7106.

[167] M. Mooney. “A theory of large elastic deformation”. In: *Journal of Applied Physics* 11.9 (Sept. 1940), pp. 582–592.

[168] R. S. Rivlin and D. W. Saunders. “Large Elastic Deformations of Isotropic Materials. VII. Experiments on the Deformation of Rubber”. In: *Philosophical Transactions of the Royal Society A: Mathematical, Physical and Engineering Sciences* 243.865 (Apr. 1951), pp. 251–288.

[169] Y.C. Fung. "Elasticity of soft tissues in simple elongation". In: *American Journal of Physiology-Legacy Content* 213.6 (Dec. 1967), pp. 1532–1544.

[170] P. F. Gou. "Strain energy function for biological tissues". In: *Journal of Biomechanics* 3.6 (Nov. 1970), pp. 547–550.

[171] H. Demiray. "A note on the elasticity of soft biological tissues". In: *Journal of Biomechanics* 5.3 (May 1972), pp. 309–311.

[172] A. A. Oberai et al. "Linear and nonlinear elasticity imaging of soft tissue in vivo: Demonstration of feasibility". In: *Physics in Medicine and Biology* 54.5 (Mar. 2009), pp. 1191–1207.

[173] S. Goenezen, P. Barbone, and A. A. Oberai. "Solution of the nonlinear elasticity imaging inverse problem: The incompressible case". In: *Computer Methods in Applied Mechanics and Engineering* 200.13-16 (Aug. 2011), pp. 1406–1420.

[174] K. Takamizawa and K. Hayashi. "Strain energy density function and uniform strain hypothesis for arterial mechanics". In: *Journal of Biomechanics* 20.1 (Jan. 1987), pp. 7–17.

[175] R. W. Ogden. "Large Deformation Isotropic Elasticity - On the Correlation of Theory and Experiment for Incompressible Rubberlike Solids". In: *Proceedings of the Royal Society A: Mathematical, Physical and Engineering Sciences* 326.1567 (Feb. 1972), pp. 565–584.

[176] R. W. Ogden. *Non-linear elastic deformations*. Dover Publications, 1997, p. 532.

[177] P. Garteiser et al. "MR elastography of liver tumours: Value of viscoelastic properties for tumour characterisation". In: *European Radiology* 22.10 (Oct. 2012), pp. 2169–2177.

[178] E. L. Madsen and G. R. Frank. *Tissue mimicking elastography phantoms*. May 2008.

[179] K. Manickam, R. R. Machireddy, and S. Seshadri. "Characterization of biomechanical properties of agar based tissue mimicking phantoms for ultrasound stiffness imaging techniques". In: *Journal of the Mechanical Behavior of Biomedical Materials* 35 (July 2014), pp. 132–143.

[180] E. L. Madsen et al. "Tissue mimicking materials for ultrasound phantoms". In: *Medical Physics* 5.5 (Sept. 1978), pp. 391–394.

[181] E. L. Madsen, J. A. Zagzebski, and G. R. Frank. "Oil-in-gelatin dispersions for use as ultrasonically tissue-mimicking materials". In: *Ultrasound in Medicine & Biology* 8.3 (Jan. 1982), pp. 277–287.

[182] M. O. Culjat et al. "A Review of Tissue Substitutes for Ultrasound Imaging". In: *Ultrasound in Medicine & Biology* 36.6 (June 2010), pp. 861–873.

[183] T. J. Hall et al. “Phantom materials for elastography”. In: *IEEE Transactions on Ultrasonics, Ferroelectrics, and Frequency Control* 44.6 (Nov. 1997), pp. 1355–1365.

[184] K. J. Parker et al. “Tissue response to mechanical vibrations for "sonoelasticity imaging"”. In: *Ultrasound in Medicine and Biology* 16.3 (Jan. 1990), pp. 241–246.

[185] J. Oudry et al. “Copolymer-in-oil Phantom Materials for Elastography”. In: *Ultrasound in Medicine and Biology* 35.7 (July 2009), pp. 1185–1197.

[186] E. L. Madsen et al. “Tissue-mimicking agar/gelatin materials for use in heterogeneous elastography phantoms”. In: *Physics in Medicine and Biology* 50.23 (Dec. 2005), pp. 5597–5618.

[187] K. J. M. Surry et al. “Poly(vinyl alcohol) cryogel phantoms for use in ultrasound and MR imaging”. In: *Physics in Medicine and Biology* 49.24 (Dec. 2004), pp. 5529–5546.

[188] K. C. Chu and B. K. Rutt. “Polyvinyl alcohol cryogel: An ideal phantom material for MR studies of arterial flow and elasticity”. In: *Magnetic Resonance in Medicine* 37.2 (Feb. 1997), pp. 314–319.

[189] S. R. Stauffer and N. A. Peppast. “Poly(vinyl alcohol) hydrogels prepared by freezing-thawing cyclic processing”. In: *Polymer* 33.18 (Sept. 1992), pp. 3932–3936.

[190] C. M. Hassan and N. A. Peppas. “Structure and Applications of Poly(vinyl alcohol) Hydrogels Produced by Conventional Crosslinking or by Freezing/Thawing Methods”. In: *Biopolymers · PVA Hydrogels, Anionic Polymerisation Nanocomposites*. Berlin, Heidelberg: Springer Berlin Heidelberg, 2000, pp. 37–65.

[191] V. Pazos, R. Mongrain, and J. C. Tardif. “Polyvinyl alcohol cryogel: Optimizing the parameters of cryogenic treatment using hyperelastic models”. In: *Journal of the Mechanical Behavior of Biomedical Materials* 2.5 (Oct. 2009), pp. 542–549.

[192] J. Fromageau et al. “Characterization of PVA cryogel for intravascular ultrasound elasticity imaging”. In: *IEEE Transactions on Ultrasonics, Ferroelectrics, and Frequency Control* 50.10 (Oct. 2003), pp. 1318–1324.

[193] Jérémie Fromageau et al. “Estimation of polyvinyl alcohol cryogel mechanical properties with four ultrasound elastography methods and comparison with gold standard testings”. In: *IEEE Transactions on Ultrasonics, Ferroelectrics, and Frequency Control* 54.3 (Mar. 2007), pp. 498–508.

[194] G. Lamouche et al. “Review of tissue simulating phantoms with controllable optical, mechanical and structural properties for use in optical coherence tomography”. In: *Biomedical Optics Express* 3.6 (June 2012), p. 1381.

[195] S. Chatelin et al. “Anisotropic polyvinyl alcohol hydrogel phantom for shear wave elastography in fibrous biological soft tissue”. In: *IEEE International Ultrasonics Symposium, IUS*. Vol. 59. 22. IOP Publishing, Nov. 2014, pp. 1857–1860.

[196] Nikolai Hungr et al. “A realistic deformable prostate phantom for multimodal imaging and needle-insertion procedures”. In: *Medical Physics* 39.4 (Mar. 2012), pp. 2031–2041.

[197] Gwladys E. Leclerc et al. “Characterization of a hyper-viscoelastic phantom mimicking biological soft tissue using an abdominal pneumatic driver with magnetic resonance elastography (MRE)”. In: *Journal of Biomechanics* 45.6 (2012), pp. 952–957.

[198] G. A. Holzapfel. “Nonlinear Solid Mechanics: A Continuum Approach for Engineering Science”. In: *Meccanica* 37.4/5 (2002), pp. 489–490.

[199] P. Garteiser et al. “Rapid acquisition of multifrequency, multislice and multidirectional MR elastography data with a fractionally encoded gradient echo sequence”. In: *NMR in Biomedicine* 26.10 (Oct. 2013), pp. 1326–1335.

[200] T. Z. Pavan et al. “Nonlinear elastic behavior of phantom materials for elastography.” In: *Physics in medicine and biology* 55.9 (May 2010), pp. 2679–92.

[201] S. A. Narod. *Tumour size predicts long-term survival among women with lymph node-positive breast cancer*. Oct. 2012.

[202] E. L. Madsen et al. “Tissue-mimicking oil-in-gelatin dispersions for use in heterogeneous elastography phantoms”. In: *Ultrasonic Imaging* 25.1 (Jan. 2003), pp. 17–38.

[203] W. Li, B. Belmont, and A. Shih. “Design and Manufacture of Polyvinyl Chloride (PVC) Tissue Mimicking Material for Needle Insertion”. In: *Procedia Manufacturing*. Vol. 1. Elsevier, Jan. 2015, pp. 866–878.

[204] W. R. Crum, T. Hartkens, and D. L. G. Hill. “Non-rigid image registration: theory and practice”. In: *The British Journal of Radiology* 77.suppl_2 (2004), S140–S153.

[205] C. A. Pelizzari et al. “Accurate three-dimensional registration of CT, PET, and/or MR images of the brain.” In: *Journal of computer assisted tomography* 13.1 (1989), pp. 20–6.

[206] D. L. G. Hill et al. “Registration of MR and CT images for skull base surgery using point-like anatomical features”. In: *British Journal of Radiology* 64.767 (Nov. 1991), pp. 1030–1035.

[207] D. J. Hawkes et al. “Tissue deformation and shape models in image-guided interventions: A discussion paper”. In: *Medical Image Analysis* 9.2 (2005), pp. 163–175.

[208] L. Tang, G. Hamarneh, and A. Celler. “Co-registration of Bone CT and SPECT Images Using Mutual Information”. In: *2006 IEEE International Symposium on Signal Processing and Information Technology* (Aug. 2006), pp. 116–121.

[209] M. Auer, P. Regitnig, and G. A. Holzapfel. “An automatic nonrigid registration for stained histological sections”. In: *IEEE Transactions on Image Processing* 14.4 (Apr. 2005), pp. 475–486.

[210] X. Zhuang et al. “A registration-based propagation framework for automatic whole heart segmentation of cardiac MRI”. In: *IEEE Transactions on Medical Imaging* 29.9 (Sept. 2010), pp. 1612–1625.

[211] A. P. King et al. “Registering preprocedure volumetric images with intraprocedure 3-D ultrasound using an ultrasound imaging model”. In: *IEEE Transactions on Medical Imaging* 29.3 (Mar. 2010), pp. 924–937.

[212] M. Ferrant et al. “Serial registration of intraoperative MR images of the brain”. In: *Medical Image Analysis* 6.4 (2002), pp. 337–359.

[213] D. Rueckert et al. “Nonrigid registration using free-form deformations: application to breast MR images.” In: *IEEE Transactions on Medical Imaging* 18.8 (1999), pp. 712–21.

[214] M. H. Davis et al. “A physics-Based coordinate transformation for 3-D image matching”. In: *IEEE Transactions on Medical Imaging* 16.3 (June 1997), pp. 317–328.

[215] J. B. A. Maintz and M. A. Viergever. “A survey of medical image registration”. In: *Medical Image Analysis* 2.1 (1998), pp. 1–36.

[216] J. P. Thirion. “Image matching as a diffusion process: an analogy with Maxwell’s demons.” In: *Medical image analysis* 2.3 (1998), pp. 243–260.

[217] G. E. Christensen et al. “Automatic Analysis of Medical Images Using a Deformable Textbook”. In: *Computer Assisted Radiology* (1995), pp. 1–6.

[218] M. Bro-Nielsen and C. Gramkow. “Fast Fluid Registration of medical images”. In: *4th International Conference on Visualization in Biomedical Computing*. Springer Berlin Heidelberg, 1996, pp. 265–276.

[219] D.L. Collins et al. “Automatic 3D segmentation of neuro-anatomical structures from MRI”. In: *Information processing in medical imaging* 3 (1995), pp. 139–152.

[220] R. D. Eastman, N. S. Netanyahu, and J. Le Moigne. “Survey of image registration methods”. In: *Image Registration for Remote Sensing*. Vol. 21. 2011, pp. 35–76.

[221] C. R. Meyer et al. “Demonstration of accuracy and clinical versatility of mutual information for automatic multimodality image fusion using affine and thin-plate spline warped geometric deformations.” In: *Medical image analysis* 1.3 (1997), pp. 195–206.

[222] F. L. Bookstein. “Principal Warps: Thin-Plate Splines and the Decomposition of Deformations”. In: *IEEE Transactions on Pattern Analysis and Machine Intelligence* 11.6 (June 1989), pp. 567–585.

[223] M. Holden. “A review of geometric transformations for nonrigid body registration”. In: *IEEE Transactions on Medical Imaging* 27.1 (Jan. 2008), pp. 111–128.

[224] J. R. DeQuardo et al. “Landmark-based morphometric analysis of first-episode schizophrenia”. In: *Biological Psychiatry* 45.10 (1999), pp. 1321–1328.

[225] J. E. Downhill et al. “Shape and size of the corpus callosum in schizophrenia and schizotypal personality disorder”. In: *Schizophrenia Research* 42.3 (2000), pp. 193–208.

[226] W. S. Gharaibeh et al. “A geometric morphometric assessment of change in midline brain structural shape following a first episode of schizophrenia”. In: *Biological Psychiatry* 48.5 (2000), pp. 398–405.

[227] R. Bajcsy and S. Kovačič. “Multiresolution elastic matching”. In: *Computer Vision, Graphics, and Image Processing* 46.1 (1989), pp. 1–21.

[228] S. Timoshenko. *Theory Of Elasticity. 1st. Ed.* Mcgraw-Hill Book Company, Inc.; New York, 1934.

[229] W. Jaunzemis. *Continuum mechanics*. Macmillan, 1967.

[230] N. M. Grosland, R. Bafna, and V. A. Magnotta. “Automated hexahedral meshing of anatomic structures using deformable registration.” In: *Computer methods in biomechanics and biomedical engineering* 12.1 (Feb. 2009), pp. 35–43.

[231] A. Hagemann et al. “Biomechanical modeling of the human head for physically based, nonrigid image registration”. In: *IEEE Transactions on Medical Imaging* 18.10 (1999), pp. 875–884.

[232] B. K. P. Horn and B. G. Schunck. “Determining optical flow”. In: *Artificial Intelligence* 17.1-3 (1981), pp. 185–203.

[233] X. Pennec, P. Cachier, and N. Ayache. “Understanding the "Demon’s Algorithm": 3D non-rigid registration by gradient descent”. In: *International Conference on Medical Image Computing And Computer-Assisted Intervention (MICCAI)* 1679 (1999), pp. 597–605.

[234] U. Kjems et al. “Enhancing the multivariate signal of [15O] water PET studies with a new nonlinear neuroanatomical registration algorithm”. In: *IEEE Transactions on Medical Imaging* 18.4 (1999), pp. 306–319.

[235] F. P. M. Oliveira and J. M. R. S. Tavares. “Medical image registration : A review”. In: *Computer Methods in Biomechanics and Biomedical Engineering* 17.2 (Jan. 2014), pp. 73–93.

[236] W. Schroeder. “The ITK Software Guide Second Edition Updated for ITK version 2 . 4”. In: *FEBS Letters* 525 (2005), pp. 53–58.

[237] S. Klein and M. Staring. *elastix: The Manual*. 2015.

[238] D. P. Shamonin et al. “Fast parallel image registration on CPU and GPU for diagnostic classification of Alzheimer’s disease.” In: *Frontiers in neuroinformatics* 7.January (2013), p. 50.

[239] K. Marstal et al. “SimpleElastix: A User-Friendly, Multi-lingual Library for Medical Image Registration”. In: *IEEE Computer Society Conference on Computer Vision and Pattern Recognition Workshops*. 2016, pp. 574–582.

[240] S. Klein et al. “Adaptive stochastic gradient descent optimisation for image registration”. In: *International Journal of Computer Vision* 81.3 (Mar. 2009), pp. 227–239.

[241] E. E. W. Van Houten et al. “Elasticity reconstruction from experimental MR displacement data: initial experience with an overlapping subzone finite element inversion process”. In: *Medical Physics* 27.1 (Jan. 2000), pp. 101–107.

[242] L. Huwart et al. “Magnetic Resonance Elastography for the Noninvasive Staging of Liver Fibrosis”. In: *Gastroenterology* 135.1 (July 2008), pp. 32–40.

[243] H. T. Banks, S. Hu, and Z. R. Kenz. “A Brief Review of Elasticity and Viscoelasticity for Solids”. In: *Advances in Applied Mathematics and Mechanics* 3.01 (Apr. 2011), pp. 1–51.

[244] R. L. Bagley and P. J. Torvik. “A Theoretical Basis for the Application of Fractional Calculus to Viscoelasticity”. In: *Journal of Rheology* 27.3 (June 1983), pp. 201–210.

[245] T. L. Szabo and J- Wu. “A model for longitudinal and shear wave propagation in viscoelastic media”. In: *The Journal of the Acoustical Society of America* 107.5 (May 2000), pp. 2437–2446.

[246] B. Suki, A. L. Barabasi, and K. R. Lutchen. “Lung tissue viscoelasticity: a mathematical framework and its molecular basis”. In: *Journal of Applied Physiology* 76.6 (June 1994), pp. 2749–2759.

[247] L. S. Taylor et al. “Viscoelastic effects in sonoelastography: Impact on tumor detectability”. In: *IEEE International Ultrasonics Symposium, IUS* 2 (2001), pp. 1639–1642.

[248] B. Fabry et al. “Time scale and other invariants of integrative mechanical behavior in living cells”. In: *Physical Review E - Statistical Physics, Plasmas, Fluids, and Related Interdisciplinary Topics* 68.4 (Oct. 2003), p. 041914.

[249] M. Z. Kiss, T. Varghese, and T. J. Hall. “Viscoelastic characterization of in vitro canine tissue”. In: *Physics in Medicine and Biology* 49.18 (Sept. 2004), pp. 4207–4218.

[250] R. L. Magin. *Fractional calculus in bioengineering*. Begell House Publishers, 2006, p. 684.

[251] M. A. Matlob and Y. Jamali. “The concepts and applications of fractional order differential calculus in modelling of viscoelastic systems: A primer”. In: *Critical Reviews in Biomedical Engineering* (2018).

[252] Q. Chen et al. “Dynamic mechanical properties of agarose gel by a fractional”. In: *J Biomech Eng* 126.5 (2004), pp. 666–671.

[253] F. C. Meral, T. J. Royston, and R. Magin. “Fractional calculus in viscoelasticity: An experimental study”. In: *Communications in Nonlinear Science and Numerical Simulation* 15.4 (Apr. 2010), pp. 939–945.

[254] D. Craiem and R. L. Armentano. “A fractional derivative model to describe arterial viscoelasticity.” In: *Biorheology* 44.4 (2007), pp. 251–63.

[255] D. Klatt et al. “Noninvasive assessment of the rheological behavior of human organs using multifrequency MR elastography: a study of brain and liver viscoelasticity”. In: *Physics in Medicine and Biology* 52.24 (Dec. 2007), pp. 7281–7294.

[256] B. Robert et al. “A new rheological model based on fractional derivatives for biological tissues”. In: *Proceedings - IEEE Ultrasonics Symposium*. Vol. 1. IEEE, 2006, pp. 1033–1036.

[257] R. Sinkus et al. “MR elastography of breast lesions: Understanding the solid/liquid duality can improve the specificity of contrast-enhanced MR mammography”. In: *Magnetic Resonance in Medicine* 58.6 (Dec. 2007), pp. 1135–1144.

[258] M. Caputo. “Linear Models of Dissipation whose Q is almost Frequency Independent-II”. In: *Geophysical Journal of the Royal Astronomical Society* 13.5 (Nov. 1967), pp. 529–539.

[259] E. Park and A. M. Maniatty. “Shear modulus reconstruction in dynamic elastography: Time harmonic case”. In: *Physics in Medicine and Biology* 51.15 (Aug. 2006), pp. 3697–3721.

[260] D. Fovargue et al. “Robust MR elastography stiffness quantification using a localized divergence free finite element reconstruction”. In: *Medical Image Analysis* 44 (Feb. 2018), pp. 126–142.

[261] D. Fovargue et al. “Using non-linear tissue biomechanics to infer static forces within tissue: towards quantifying IFP”. In: *ISMRM*. 2017.

[262] M. Honarvar et al. “Sparsity regularization in dynamic elastography”. In: *Physics in Medicine and Biology* 57.19 (Oct. 2012), pp. 5909–5927.

[263] D. Fovargue et al. “Lymphovascular invasion correlates with elevated tumor pressure as quantified by MR Elastography: initial results from a breast cancer trial”. In: *ISMRM*. 2019.